Development of GEM Detectors for the ALICE TPC Upgrade and Study of Particle Production at LHC Energies

By

RAJENDRA NATH PATRA

PHYS04201304008

Variable Energy Cyclotron Centre, Kolkata

A thesis submitted to the

Board of Studies in Physical Sciences

In partial fulfillment of requirements

for the Degree of

DOCTOR OF PHILOSOPHY

of

HOMI BHABHA NATIONAL INSTITUTE

March, 2019

Homi Bhabha National Institute [1]

Recommendations of the Viva Voce Committee

As members of the Viva Voce Committee, we certify that we have read the dissertation prepared by Rajendra Nath Patra entitled *"Development of GEM detectors for the ALICE TPC Upgrade and Study of Particle Production at LHC Energies"* and recommend that it may be accepted as fulfilling the thesis requirement for the award of Degree of Doctor of Philosophy.

Chairman	Prof. Subhasish Chattopadhyay	S. Chatt...	**Date:** 19/6/2019
Guide/Convener	Prof. Tapan K. Nayak	Tapan Nayak	**Date:** 19/6/2019
Examiner	Prof. Satyanarayana Bheesette	[signature]	**Date:** 19/6/19
Member 1	Dr. Tilak Ghosh	T. Ghosh	**Date:** 19/6/19
Member 2	Dr. Supriya Das	Supriya Das..	**Date:** 19/6/19.
Technology Adviser	Dr. Saikat Biswas	Saikat Biswas	**Date:** 19.6.19

Final approval and acceptance of this thesis is contingent upon the candidate's submission of the final copies of the thesis to HBNI.

I hereby certify that I have read this thesis prepared under my direction and recommend that it may be accepted as fulfilling the thesis requirement.

Date: 19/6/2019

Place: Kolkata

Tapan Nayak
Guide

[1] This page is to be included only for final submission after successful completion of viva voce.

STATEMENT BY AUTHOR

This dissertation has been submitted in partial fulfillment of requirements for an advanced degree at Homi Bhabha National Institute (HBNI) and is deposited in the Library to be made available to borrowers under rules of the HBNI.

Brief quotations from this dissertation are allowable without special permission, provided that accurate acknowledgment of source is made. Requests for permission for extended quotation from or reproduction of this manuscript in whole or in part may be granted by the Competent Authority of HBNI when in his or her judgment the proposed use of the material is in the interests of scholarship. In all other instances, however, permission must be obtained from the author.

Rajendra Nath Patra

Rajendra Nath Patra 19/06/2019

DECLARATION

I, hereby declare that the investigation presented in the thesis has been carried out by me. The work is original and has not been submitted earlier as a whole or in part for a degree / diploma at this or any other Institution / University.

Rajendra Nath Patra

Rajendra Nath Patra 19/06/2019

List of Publications arising from the thesis

Journal

1. **"Measurement of basic characteristics and gain uniformity of a triple GEM detector"**, Rajendra Nath Patra, Rama N. Singaraju, Saikat Biswas, Zubayer Ahammed, Tapan K. Nayak, Yogendra P. Viyogi, Nucl. Instr. Methods A **862** (2017) 25.

2. **"Characteristic study of a quadruple GEM detector and its comparison with a triple GEM detector"**, Rajendra Nath Patra, Rama N. Singaraju, Saikat Biswas, Yogendra P. Viyogi, Tapan K. Nayak, Nucl. Instr. Methods A **906** (2018) 37.

3. **"Characteristic study of a quadruple GEM detector in different electric field configurations"**, Rajendra Nath Patra, Rama Narayan Singaraju, Somnath Dalal, Saikat Biswas, Yogendra P. Viyogi, Tapan K. Nayak, Nucl. Instr. Methods A **936** (2019) 433.

4. **"Characterisations of GEM detector prototype"**, Rajendra Nath Patra, Amit Nanda, Sharmili Rudra, P. Bhattacharya, Sumanya Sekhar Sahoo, S. Biswas, B. Mohanty, T. K. Nayak, P. K. Sahu, S. Sahu, Nucl. Instr. Methods A **824** (2016) 501.

5. **"Particle identification studies with a full-size 4-GEM prototype for the ALICE TPC upgrade"**
ALICE TPC Collaboration, Nucl. Instr. Methods A **903** (2018) 215.

Conferences

1. **"Gain Uniformity and Characteristics Study of a Triple GEM Detector"**, Rajendra Nath Patra, Rama N. Singaraju, Saikat Biswas, Zubayer Ahammed, Tapan K. Nayak, Yogendra P. Viyogi, IEEE (NSS/MIC/RTSD) 2016, Conference Record, doi:10.1109/NSSMIC.2016.8069752

2. **"Time Resolution and Characteristic Studies of MWPC Detectors with Argon Based Gas Mixtures"**, Rajendra Nath Patra, R. N. Singaraju, S. Biswas, T. K. Nayak and Y. P. Viyogi, Springer Proceedings in Physics, **203** (2018) 509-512. doi:10.1007/978-3-319-73171_119

3. **"Study of a Triple GEM Detector Operated with Different Argon Based Gas"**, Rajendra Nath Patra,, R. N Singaraju, S. Biswas, Z. Ahammed, T. K. Nayak and Y. P. Viyogi, Springer Proceedings in Physics **203**, (2018) 821-823. doi:10.1007/978-3-319-73171_199

4. **"Characteristics of triple GEM detector for the ALICE TPC upgrade at CERN"**, Rajendra Nath Patra, R. N. Singaraju, S. Biswas, Z. Ahammed, T. K. Nayak, Y. P. Viyogi, Proceedings of the DAE-BRNS Symp. on Nucl. Phys. **61** (2016) 1050-1051.

5. **"Study of Multiwire Proportional Chambers MWPC detector using NIM and MANAS electronics"**, Rajendra Nath Patra, R.N. Singaraju, T. K. Ghosh, S. Biswas, T. K. Nayak,Y.P. Viyogi, Proceedings of the DAE-BRNS Symp. on Nucl. Phys. **61** (2016) 1052-1053.

6. "Framing and testing of large GEM foils for ALICE TPC upgrade". Rajendra Nath Patra, J. Hehner, D. Miskowiec, Proceedings of the DAE-BRNS Symp. on Nucl. Phys. **61** (2016) 1054-1055.

7. **"Assembly and Test Results of a 4-GEM Detector"**, Rajendra Nath Patra, R. N. Singaraju, T. K. Nayak, Y. P. Viyogi,
Proceedings of the DAE-BRNS Symp. on Nucl. Phys. **62** (2017) 1114-1115.

Rajendra Nath Patra
19/06/2019
Rajendra Nath Patra

Dedication

Achievement brings pleasure only when our dearest ones have a big delighted smile.

I dedicate this humble thesis to my beloved

Father and Mother

Without whom constant support, love, blessing and sacrifice this thesis would never have been completed.

Along with for strengthening me in hard times to my loving

Brother

ACKNOWLEDGEMENTS

First and foremost, I would like to express my deepest gratitude to my supervisor Prof. Tapan K. Nayak for giving me the opportunity to involve in such an exciting experiment. His guidance, encouragement, continuous motivation and support in all forms has made me a good researcher. I would like to express my heartfelt appreciation to the Senior Professor Dr. Y. P. Viyogi, VECC for his kind visits to my lab many times with new ideas and scientific suggestions towards my research goals. I am very fortunate to work with Shri R. N. Singaraju (Rama Sir), who is such a devoted person and he dedicated countless weekends for me. I take the opportunity to thank Dr. Saikat Biswas who trained me from the very first day of my research. His encouragements, valuable discussions, promoting for publications and good wishes are of worth to me.

I would like to express my sincere thanks to Prof. Subhasis Chattopadhyay, Group Head, for the valuable suggestions and constant support in all difficulties in my VECC life. I also like to acknowledge Dr. A. K. Dubey, Dr. Z. Ahammed, Partha Bhaskar and HEP Detector and Electronics laboratory persons in VECC who have helped me on many aspects during my research. My sincere thanks to Prof. Jane Alam (Dean Academy) and Dr. Tilak K. Ghosh (Dean Affairs) for their great help in all academic and nonacademic difficulties arising at VECC. I am also thankful to Dr. Supriya Das for valuable comments and suggestions about my research work.

I am highly thankful to Prof. Silvia Masciocchi, GSI for giving me the opportunity and arranging funds for my research work at GSI for the ALICE TPC upgrade project. I would like to express my heartiest thanks to Dr. Dariusz Miskowiec for guidance and close collaboration. I thank Joerg Hehner for his help and friendship during my stay at GSI.

I would also like to thank Dr. Rob Veenhof, RD51 Collaboration of CERN for fruitful scientific discussions, help in simulations and suggestions over email every time. I am also thankful to Dr. Christian J. Schmidt, GSI for insightful discussions during my GSI visits.

A big thank to all my seniors, juniors and friends for excellent discussions, scientific debates and lots of fun which helped during my journey at VECC.

I gratefully acknowledge UGC NET-JRF fellowship no. 201314-NETJRF-10484-1. I am also grateful to VECC for financial support to attend meetings and conferences.

Finally, I owe everything to my beloved parents and my loving brother for their patience as well as unconditional love and support towards the completion of my thesis.

Rajendra Nath Patra

Contents

Synopsis

The major physics goals of the ALICE (A Large Ion Collider Experiment) collaboration at the Large Hadron Collider (LHC) of CERN are to study the properties of a new form of high temperature and high energy density matter, called the quark-gluon plasma (QGP) [1, 2]. This form of matter can be created by colliding heavy-ions (such as Pb on Pb) at ultra-relativistic energies which is possible at the LHC. The QGP matter has been predicted to have existed only within few microseconds of the Big Bang. Quarks and gluons are the building blocks of normal hadronic matter, such as of protons and neutrons, which in turn form atoms. The strong interaction is responsible for binding the protons and neutrons together inside the atomic nuclei. According to quantum chromodynamics (QCD), which is the theory of strong interactions, the quarks and gluons cannot be isolated and are confined within the hadronic matter. At extreme conditions of temperatures and energy densities, the quarks and gluons may not remain bound or confined together within the hadrons and would form the QGP state. The ultra-relativistic heavy-ion collision experiments at the Relativistic Heavy-Ion Collider (RHIC) and LHC aim to study the formation of the QGP matter in the laboratory.

ALICE [3] is one of the four experiments at the LHC. It is a dedicated experiment for the precision measurements at different particles produced in high multiplicity environments of heavy-ion collisions. The LHC is capable of colliding proton-proton (pp), proton-lead (p-Pb), lead-lead (Pb-Pb) and other species. Since the year 2009, LHC has collided pp at highest center-of-mass energy of 13 TeV, p-Pb at $\sqrt{s_{\rm NN}}$ (center-of-mass energy per nucleon pair) of 8.02 TeV and Pb-Pb at $\sqrt{s_{\rm NN}}$ of 5.02 TeV. By measuring majority of the produced particles, ALICE has made extensive studies of the strong interaction of matter and addressed the phenomena related to the QGP formation. During LHC Run-1 and Run-2 periods from 2009 and till now, ALICE has addressed physics phenomena like collision centrality dependency of particle productions, study of identified particles, investigations of correlations and flow to investigation of QGP. The future physics goals of ALICE [4] in the next period of LHC running (Run-3) are the precise measurements of several different probes and emphasis will be on rare probes which require accumulation of a large number collision events and their precise analysis. To achieve the physics goals, high event statistics and high precision measurements are required. In Run-3 Pb-Pb collision rate will be increased to 50 kHz from the present 8 kHz rate. This increase has demanded for high rate capability measurements of all ALICE detectors, readout systems and data acquisition. During the long shutdown (LS2) period of 2019-2021, ALICE will upgrade the existing detectors by enhancing low-momentum tracking capability and excellent vertexing, and allowing data taking at substantially higher rates. ALICE will then be in a position to accumulate $\mathscr{L}_{int}$ (integrated luminosity) = 10 nb^{-1} of Pb–Pb collisions corresponding to 10^{11} interactions. This is the minimum needed to address the proposed physics programme with focus on rare probes both at low and high transverse momenta. For this purpose, ALICE is going through major upgrades of the detectors. Accordingly, the Inner Tracking System (ITS) and the TPC will be upgraded completely [5]. A new, high-resolution, low-material ITS will be installed to improve its tracking performance significantly. The present MWPC [6] based readout will be replaced with a new readout scheme, based on GEM [7] technology in TPC with capability for high rate data taking. The future data production in TPC will be 100 times higher than the present. Corresponding new electronics also will be installed for signal extraction from the new readout and for fast data transfer. Major part of the thesis consists of the study of the GEM detector for the TPC for future upgrade.

The ALICE TPC and its upgrade:

ALICE TPC is the main central barrel detector for charge particle tracking and particle identification (PID) [8]. The TPC consists of a 5 m long cylindrical chamber with 90 m^3 active volume. The central drift plane of the TPC divides the chamber into two halves which contains readout plane at the end in rϕ plane. The drift field of the TPC is 400 V/cm. The maximum drift time of the electrons is 100 μs for the gases used. During TPC Run-1 Ne/CO_2/N_2 90:10:5 (in 2009-2010), Ne/CO_2 90:10 (in 2011-2013) and in Run-2, Ar/CO_2 88:12 are used. A Magnetic field of B = 0.5 T is used in parallel to drift field for charge particles bending. The readout plane is divided into 18 trapezoidal sectors each has azimuthal coverage of 20 degree. Each sector is divided into inner readout chambers (IROC) and outer readout chambers (OROC) along the radial directions. The present readout is based on MWPC with gating grid to stop the ions going back to the drift volume. The present TPC with MWPC based readout has been performing quite satisfactorily.

In the upgrade scenario of the TPC [5], several R&D have been performed with GEM technology to fulfill future requirements. The major challenges for the new TPC will be to keep the ion back flow (IBF) < 1% at gas gain of 2000 with energy resolution (σ_E) = 12% for ^{55}Fe X-ray source. Therefore a quadruple GEM based design has been adopted for the TPC upgrade. In recent times, the focus has been on the detailed study of the quadruple GEM detectors as well as production and testing of IROC and OROC chambers for installation in LS2. My thesis work is based on the detailed studies of the triple and quadruple GEM detectors, quality assurance tests of the large size GEM foils and successful assembly and testing of the OROC chambers.

GEM detectors:

Gas Electron Multiplier (GEM) is a novel kind of micro-pattern gas detector (MPGD), invented by F. Sauli at CERN in 1997 [7]. A GEM foil consists of an insulator made of a 50 μm thick Kapton foil with 5 μm thick copper cladding on both sides and pierced by a regular array of holes. These perforated holes, having typically 70 μm diameter and separated by 140 μm pitch, are arranged in a hexagonal pattern. With application of few hundred of voltages ($\sim$ 350 V) very high electric field ($\sim$ 70 kV/cm) is created across the microscopic holes. Electrons, passing through this tiny holes, will have charge amplifications in presence of high field. The advantages of the GEM detector compared to other kinds of micro-pattern detectors are its high rate handling capability, low discharge probability, high gain, excellent position resolution, inherent ion suppression property and stable operation without ageing for long term use. These properties make GEM detectors most suitable for high energy physics (HEP) experiments. Many HEP experiments are opting for GEM detectors for all the major advantages compared to other gas detectors. The detail characteristic studies and development of the GEM detector are very important for its usefulness in HEP experiment. Triple GEM detectors are found useful in many HEP experiments for trigger and tracking purposes in case of high rate collisions. The quadruple GEM detector is useful in large drift chambers like in our TPC because of low IBF properties. As a part of the thesis work, we have assembled and tested both triple GEM and quadruple GEM detectors.

GEM has a very complicated geometry. Electric field for the GEM geometry is calculated numerically using field solving software. The drift velocity and diffusion of the electrons in different gas mixtures are calculated using Magboltz-11.2 [9] software. Gas ionization and avalanche formation are simulated using Garfield [10]. Limiting value of time resolutions of the GEM detector is also simulated.

Study of triple GEM detector:

A triple GEM detector consists of three GEM foils arranged in a particular fashion. We have assembled a triple GEM detector and undertaken a detailed test for studying the detector characteristics [11]. The drift gap, transfer gaps and the induction gap of the detector are kept as 3-2-2-2 mm, respectively. The detector was operated using Argon and CO_2 gas mixtures in proportions of 70:30 and 90:10 at atmospheric pressure. High voltage (HV) is applied through a voltage divider resistor chain for the required electric field of the detector to operate. The detector is tested with ^{55}Fe X-ray source, ^{106}Ru-Rh and ^{90}Sr β-source and cosmic muons, and energy spectrum for those are found. Gain and energy resolution have been calculated from the ^{55}Fe 5.89 keV X-ray spectrum. The effective gain of the detector is measured in the range of $10^3 - 10^4$ at operating region and resolution is found to be $\sim$ 20%. For efficiency measurement, trigger was provided by the coincidence signal of a set of three scintillators. The efficiency at plateau region was found to be $\sim$ 95%. Time resolution of the detector with the same trigger setup is measured and the obtained value is $\sim$ 10 ns. The overall performance of a large volume detector depends on gain, energy resolution and efficiency uniformity over the entire active region. Several factors, like variations in hole diameter, variations in gas gap due to inaccurate stretching, etc., can lead to non-uniform operation of the detector. In this work, a method has been used to scan for the gain and energy resolution over the entire active area of the detector. The RMS variations of gain and energy resolution are 8.8% and 6.7%, respectively over the entire area [11].

Study of quadruple GEM detector:

A quadruple GEM detector consists of four GEM foils arranged in a particular fashion. We have assembled a quadruple GEM detector and undertaken a detailed test for studying its characteristics [12]. The drift gap, transfer gaps and the induction gap of the detector are 4.8-2-2-2-2 mm, respectively. The detector has been operated using Argon and CO_2 gas mixtures in proportions of 70:30 and 90:10 at atmospheric pressure. The test procedure of this detector had been similar to triple GEM detector. Effective gain and energy resolution of the detector were measured and compared with the triple GEM results. It is found that to have similar gain, the individual GEM voltage ($\Delta V_{GEM-single}$) required in case of triple GEM detector is higher than that of a quadruple GEM detector. Detector operating with lower $\Delta V_{GEM-single}$ is expected to have more stable operation for long term use. It is observed that the quadruple GEM detector has poorer energy resolution compared to triple GEM detector. Similar result is also reported in literature because of having low IBF in quadruple GEM detector [5]. For the efficiency measurement, the trigger setup has been used similar to the triple GEM case. It is found that the main factor for the efficiency of the detector is its gain. We observed that the efficiency plateau is reached at a gain of $\sim$ 5000 for the specific electronics (NIM) setup used in the measurement.

The primary electrons produced in drift volume are guided by drift field (E_d) to transfer through the holes of the first GEM foil. Electron transparency as a function of E_d for Ar/CO_2 with 90:10 and 70:30 gas mixtures have been measured. The observation is that the transparency increases with E_d and attains an optimum value and then decreases again at higher E_d. The optimum transparency of the electrons for the Ar/CO_2 90:10 and 70:30 gas mixtures are found at drift field values of 750–1000 V/cm and 1000–1500 V/cm, respectively. Electron transparency has been further studied with changing of the GEM voltages. From these measurements, we can conclude that both drift field and field across the holes of the first GEM have important roles in electron transparency depending on the range of the field [12].

Time resolution of the quadruple GEM detector and its drift field dependency have been measured. Time resolution of the detector is found to be ~ 13 ns. It is found that time resolution does not improve further for E_d above 2 kV/cm.

Study of GEM detector is found to be important in HEP because of its usefulness in present and upcoming experiments as well as applications in different imaging techniques. A detailed detector simulation task has been taken up with proper electric fields and different gas mixtures. Tests of triple and quadruple GEM detectors have been carried out in the laboratory. The test results provide important inputs to the simulations. The tests have been performed using X-ray and β^- sources. Effective gain, energy and time resolution, efficiency and uniformity measurements for both the detectors are performed and compared. The advantages of quadruple GEM detector has been found to be its lower operation voltages ($\Delta V_{GEM-single}$) compare to triple GEM detector, which is preferable for long term stable operation of the detectors.

Study on the multi-wire proportional chamber:

As a part of this thesis work, a number of Multi-Wire Proportional Chambers (MWPC) were fabricated for the understanding of various detector characteristics. The detector contains a number of gold-coated tungsten wires (20 μm diameter) on the anode frame, with a pitch of 2.8 mm. This frame is placed between the cathode and readout planes. The gap between the anode and the cathode is 3 mm and the distance between anode and readout is also 3 mm. Detailed studies of MWPC in terms of gain, energy and timing resolution and efficiency measurements have been performed. The detector has been operated using Ar/CO_2 gas mixtures with 70:30 and 90:10 ratio. The efficiency of the detector was studied using ^{106}Ru-Rh β-source as well as a 3-fold cosmic ray muon trigger. Energy spectrum of ^{55}Fe X-ray source is obtained for the detector. The gain and energy resolution of the detector were calculated from the Gaussian fit of ^{55}Fe energy spectrum. The study showed the efficiency $\sim 94\%$ at the plateau and gas gain of $\sim 4 \times 10^3$ around the operating voltage for the 70:30 mixture. Time resolution of the detector is measured using ^{106}Ru-Rh β-source with both gas mixtures in different HV setting. Time resolution is obtained as of ~ 10 ns for Ar/CO_2 70:30 gas mixture. The results have been summarized in [13].

Preparation of the TPC upgrade:

The installation of the TPC in the ALICE cavern is scheduled to start in 2019. For the TPC, we need 36 numbers of both IROC and OROC chambers. The IROC and OROC consists of quadruple GEM foils in trapezoidal shape. My thesis work concentrated on the production and testing of OROCs. The GEM foils first go through a set of basic and advance quality assurance (QA) tests. Then the foils are framed and again QA tests are conducted. During the QA test the framed GEMs are checked optically using microscope and by the leakage current measurement in dry environment. OROCs have to pass gas tightness, gain and IBF mapping, irradiation test and foils leakage current measurement tests to make sure that they are ready to be used during TPC installation. All the test history are recorded into an electronic database. After this stage, the OROC final assembly is made.

Particle production at relativistic energy:

The comprehensive study of global observables in the collision provides valuable information for thermal and chemical analysis of the freeze-out conditions. Some of these observables include the multiplicity and rapidity distributions of charged and identified particles, momentum spectra, particle ratios, flow and the size of the fireball. The multiplicity of the produced particles depends on collision geometry, initial energy density and parton distribution. A Monte-Carlo (MC) based Glouber [14] model is used to calculate geometrical quantities like impact parameter and number of participating nucleons. Charged particle multiplicity $dN_{ch}/d\eta$ is compared with MC Glauber model to estimate number of participant N_{part} at different centrality classes. Multiplicity density study $(2/\langle N_{part}\rangle)dN_{ch}/d\eta$ is important for a direct comparison with pp($\bar{p}$) collisions. Charged particle multiplicity density study along with transverse energy density estimate Bjorken energy, the initial energy density of the fireball. In this thesis, a review on charged particle multiplicity study with different centrality and collision energy ($\sqrt{s_{\mathrm{NN}}}$) will be presented. The data from RHIC to LHC energies are compared for multiplicity density and initial energy density estimation of the fireball. Multiplicity computation using AMPT [15] model is also presented to compare with the data to determine its validation. The multiplicity $dN_{ch}/d\eta$ and initial energy density are estimated for future LHC energy at Run-3 in Pb-Pb collision at $\sqrt{s_{\mathrm{NN}}} = 5.5$ TeV. The estimation of $dN_{ch}/d\eta$ at $\sqrt{s_{\mathrm{NN}}} = 5.5$ TeV has a special importance for detector upgrade in Run-3.

Bibliography

[1] P. B. Munzinger and J. Stachel, The quest for the quark–gluon plasma, Nature **448** (2007) 302.

[2] K. Aamodt for ALICE Collaboration, Phys. Rev. Lett. **105** (2010) 252302.

[3] ALICE Collaboration, The ALICE experiment at the CERN LHC, Journal of Instr. **3** (2008) S08002.

[4] ALICE Collaboration, Upgrade of the ALICE Experiment: Letter Of Intent. CERN-LHCC-2012- 012 / LHCC-I-022. 2012. J. Phys. G: Nucl. Part. Phys. **41** (2014) 087001.

[5] ALICE Collaboration, Technical Design Report for the Upgrade of the ALICE Time Projection Chamber, ALICE-TDR-016, CERN-LHCC- 2013-020, 2014.

[6] G. Charpak *et al.*, The use of multiwire proportional counters to select and localized charge particles, Nucl. Instr. Methods **62**,(1968), 262.

[7] F. Sauli, GEM: a new concept for electron amplification in gas detectors, Nucl. Instr. Methods A **386** (1997) 531.

[8] ALICE Collaboration, Technical Design Report of the Time Projection Chamber. CERN/LHCC 2000-001. 2000.

[9] http://magboltz.web.cern.ch/magboltz

[10] R. Veenhof, Garfield, recent developments, Nucl. Instr. Methods A **419** (1998) 726.

[11] Rajendra Nath Patra *et al.*, Measurement of basic characteristics and gain uniformity of a triple GEM detector, Nucl. Instr. Methods A **862** (2017) 25.

[12] Rajendra Nath Patra *et al.*, Characteristic study of a quadruple GEM detector and its comparison with a triple GEM detector, Nucl. Instr. Methods A **906** (2018) 37.

[13] Rajendra Nath Patra *et al.*, Time Resolution and Characteristic Studies of MWPC Detectors with Argon Based Gas Mixtures, Springer Proceedings in Physics, **203** (2018) 509-512.

[14] M. Miller *et al.*, Ann. Rev. Nucl. Part. Sci. **57**, (2007) 205.

[15] Z.W. Lin, C.M. Ko, B.A. Li, B. Zhang, S. Pal, Phys. Rev. C **72** (2005) 064901.

List of Figures

List of Tables

Chapter 1

Introduction

The major goals of nuclear and particle physics experiments at ultra-relativistic energies are to study the fundamental constituents of matter and their basic interactions. Heavy-ion collisions at these energies create matter at extreme conditions of temperature and/or energy density, similar to what had been existed within few micro-seconds of the Big Bang. At these extreme conditions, the normal matter goes through a phase transition to a new state, called the quark-gluon plasma (QGP) [1–3]. The nature and the range of the strong interaction among the quarks and gluons are governed by the theory of Quantum Chromodynamics (QCD). For this reason, the QGP state is also known as the QCD plasma. Accelerator facilities at the Relativistic Heavy Ion Collider (RHIC) at Brookhaven National Laboratory (BNL) and the Large Hadron Collider (LHC) at CERN provide collisions of Au and Pb ions at extremely high energies. By analyzing a large number of particles emitted from the collision vertex, the experiments at RHIC and LHC have confirmed the formation of the QGP state in the laboratory.

The ALICE [4, 5] (A Large Ion Collider Experiment) at the LHC is a dedicated experiment for the study of QGP. During the first two phases of LHC data taking runs (Run-1 and Run-2) in the last ten years, the experiment has accumulated a large amount of Pb-Pb collision data and provided evidence for the formation of the QGP in the laboratory. The signals of the QGP are extracted by dedicated measurement of charged particles and their identification, photons, electrons and muons. In order to probe much deeper in to the understanding of QGP, the experiment is undergoing an upgrade for the third and fourth (Run-3 and Run-4) phases of data run. Run-3 and Run-4 will have higher energy Pb-Pb collisions with high luminosity. The experiment will take data at a rate of 50 kHz in Pb-Pb collisions, for which special dedicated detectors are required. The thesis consists of detector development for the ALICE upgrade.

Experiments at the large facilities need to be equipped with sensitive detectors in order to provide accurate measurements of particle identification and momenta of the particles. For example, the ALICE (A Large Ion Collider Experiment) at the LHC consists of several different types of detectors dedicated for the measurement of charged hadrons, photons, electrons and muons. The heart of the experiment is the large Time Projection Chamber (TPC), surrounded by a large magnet, for the charged particle tracking and particle identification. The TPC consists of a large gas volume which ionizes the charged particles traversing through it and the traces are measured by gas detectors. At present, the ALICE TPC includes multi-wire proportional chambers (MWPC) as the detection planes. In future, all the MWPC detectors will be replaced by much faster and more precise gas electron multiplier (GEM) detectors. The major part of the thesis is devoted to the research and development of GEM detectors and characterizing those using test setups in laboratory at VECC, Kolkata.

During Run-3, the per nucleon center-of-mass energy of Pb-Pb collisions will reach 5.5 TeV with a collision rate of 50 kHz. We have studied the particle production and global properties for these collisions and extract global properties. The last chapter of the thesis is dedicated to the study of particle production at the LHC.

In this chapter, we present a brief overview of the physics motivations of the thesis in terms of the Standar Model, QCD, QGP and basics of relativistic heavy-ion collisions. We discuss some of the experimental observables and conclude with the arrangement of the thesis.

1.1 Standard Model

The Standard Model (SM) of particle physics, proposed by Glashow, Salam and Weinberg [6–8] in 1970s, successfully explains the fundamental structure of the matter as well as the fundamental interactions. According to this theory, the elementary particles are categorized into three groups, namely quarks, leptons and gauge bosons. The property of the elementary particles and their mediators of the SM theory are summarized in Fig. 1.1. The quarks and leptons are spin half particles, *i.e.,* fermions, follow the Fermi-Dirac statistics. On the other side, the gauge bosons have integer spin and they follow the Bose–Einstein statistics. The six quarks in the SM are divided into three generations, up (u) and down (d) quarks, charm (c) and strange (s) quarks, top (t) and bottom (b) quarks. The leptons are also divided into three generations as electron (e) and electron neutrino (ν_e), the muon (μ) and muon neutrino (ν_μ) and the tau (τ) and tau neutrino (ν_τ). The gauge bosons are the mediators of the fundamental interactions - (1) gluon (g) for the strong force, (2) photon (γ) for the electromagnetic force and (3) $W^\pm$ and Z bosons for the weak force. The Higgs boson particle is responsible for generation of the mass of the elementary particles. Recent discovery of Higgs particle in 2012 by the ATLAS [9] and CMS [10] experiments in LHC is a big success of the SM theory.

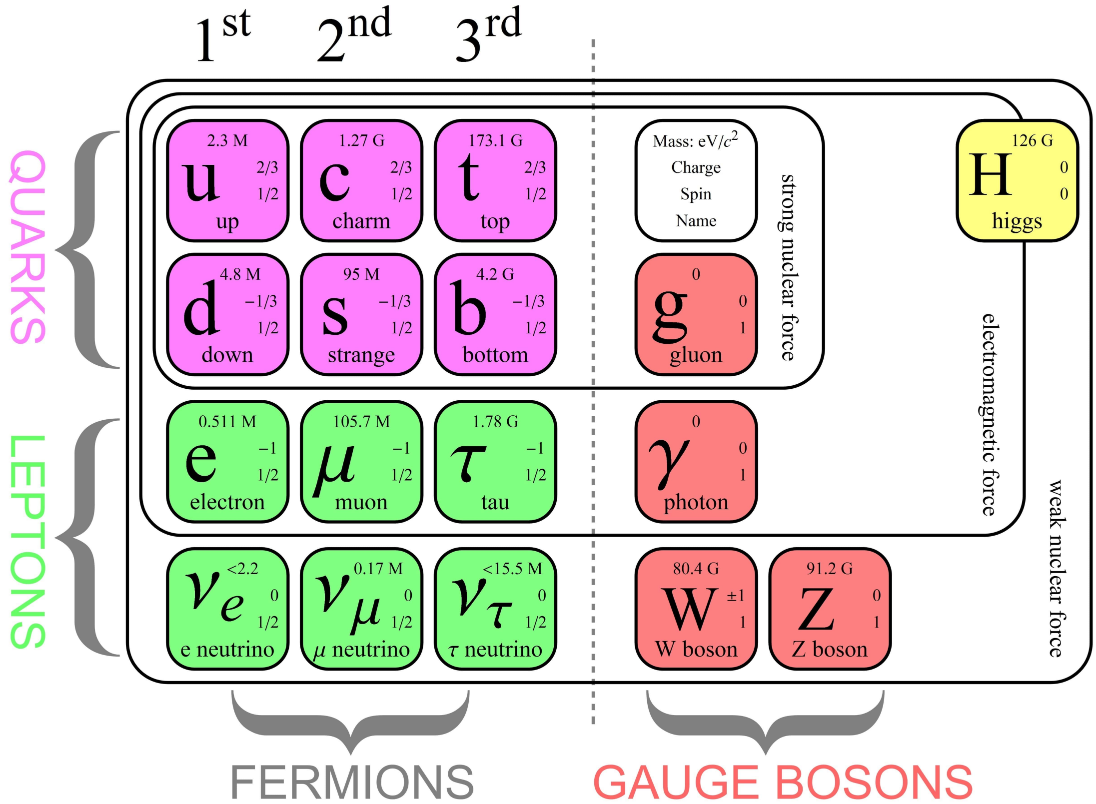

Figure 1.1: Standard model of particle physics: fundamental particles and mediators of the fundamental forces.

1.2 Quantum Chromodynamics

From the deep inelastic scattering experiment, we know that the proton and neutron are not the fundamental particles rather they are composed of quarks, which are held together by the mediation of the gluons. Quantum Chromodynamics (QCD) is the theory of the strong interactions among the quarks similar to the quantum electrodynamics (QED) for the interactions of the electrons. In QCD, the quarks have "colour" charge similar to the electrical charges in the leptons. The quarks have three different colour charges, namely red, green and blue whereas in QED only electric charge is observed. Gluons are self-interacting, unlike to the photons in QED. There are eight different gluons in the QCD. During the QCD interaction, the colour of the quarks can be changed by gluon exchange but the flavour of the quarks (u, d, c, s, t, b) remain unchanged.

The partonic interaction can be written as:

$$V(r) = -\frac{4}{3}\frac{\alpha_s}{r} + kr, \tag{1.1}$$

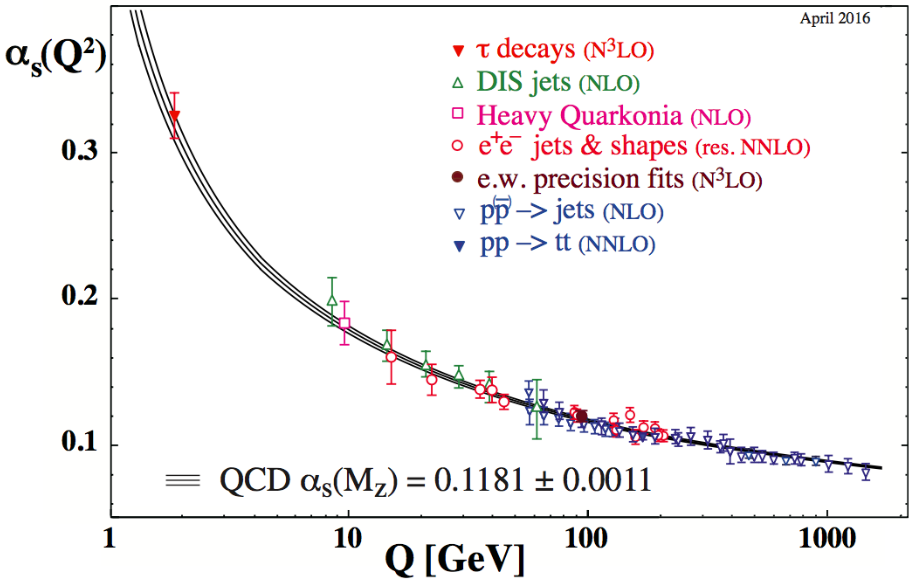

Figure 1.2: Coupling constant as a function of energy scale from different experimental results. The figure is adopted from [11].

where α_s is the strong coupling constant and k is the color string tension constant. The mathematical expression for the strong coupling constant is,

$$\alpha_s(Q^2) = \frac{12\pi^2}{(33 - 2N_f)\ln(Q^2/\Lambda^2_{QCD})}, \tag{1.2}$$

where Q^2 is the momentum transfer, N_f is the number of quark flavors (6) in the QCD, and Λ is the QCD scale parameter (∼200 MeV). The value of α_s can be estimated by perturbative QCD (pQCD) calculation and compared with the different experimental results as shown in Fig. 1.2. From the figure, it is observed that at large momentum transfer or small distance the effective coupling between the quarks decreases to such a low value that the interaction strength is weak and the quarks are in a quasi-free state. This feature of the QCD is called the *asymptotic freedom* [12–14].

The quarks are always confined within a hadron in a normal state of matter. At low momentum transfer or at large distance the coupling constant α_s is large and its value increases with increasing the separation distance between the quarks. Therefore it is impossible to separate the quarks to free. This property of the quarks in QCD is called the *confinement* [15].

1.3 Quark-Gluon Plasma: a new phase of matter

The asymptotic freedom of quarks predicts that at high density and (or) temperature the deconfined state of the quarks can be reached. The extreme state of the matter where quarks and gluons are de-confined is called Quark-Gluon Plasma (QGP) [15]. In cosmology, it is believed that such a QGP state did exist after few micro-seconds of the Big Bang. In 1974, T. D. Lee first proposed that by colliding heavy-ions at very high pressure and/or temperature [1], one can create an extended system of QGP.

For an ideal, massless noninteracting gas the thermodynamic relation is

$$\epsilon = \frac{\pi^2}{30} g(T) T^4, \tag{1.3}$$

where ϵ and T are energy density and temperature, respectively. g is the number of degrees of freedom of the constituents. For ultra-relativistic hadron gas of massless pions, the value of g is 3 for there isospin degrees of freedom. For the deconfined gas of gluons and massless quarks $g = (16 + 21/2\,.n_f)$, where n_f is the number of quark flavors. At very high temperature limit the ϵ/T^4 will approach to the free gas limit,

$$\frac{\epsilon_{SB}}{T^4} = \frac{\pi^2}{30}\left(16 + \frac{21}{2} n_f\right). \tag{1.4}$$

The lattice QCD calculation predicts a phase transition from a normal hadronic matter to a deconfined partonic state of QGP at high temperatures [16, 17]. According to the lattice QCD, the phase transition occurs at critical temperature (T$_c$) of $\sim 154 \pm 9$ MeV, corresponding energy density (ϵ_c) being ~ 0.5 GeV/fm^3 [17]. The lattice QCD calculation of transverse energy density as a function of temperature is shown in Fig. 1.3 for 2, 3 flavor QCD along with 2+1 flavor QCD, *i.e.,* two light quark and one heavier quark flavors. The sharp change of the ϵ/T^4 at the critical temperature T_c indicates the change of degrees of freedom at thecritical point is corresponding to the phase transition.

1.3.1 Space-time evolution of heavy-ion collisions

In relativistic heavy-ion collision, two nuclei are accelerated in the opposite direction to each other with almost the speed of light ($\beta \approx 1$). Such relativistic nuclei are Lorentz contracted along the beam direction. The space-time evolution of the collision of two relativistic nuclei is graphically shown in Fig. 1.4. The energy carried by the individual nucleons is deposited within a very small region in space and short duration of time. By generating such an incredibly hot and dense "fireball" of fundamental particles in the collision, the de-confined state of quarks and gluons can be reached. The fireball may take some time for subsequent interactions of quarks and gluons to reach a thermalized state called the quark-gluon plasma. The time required to reach

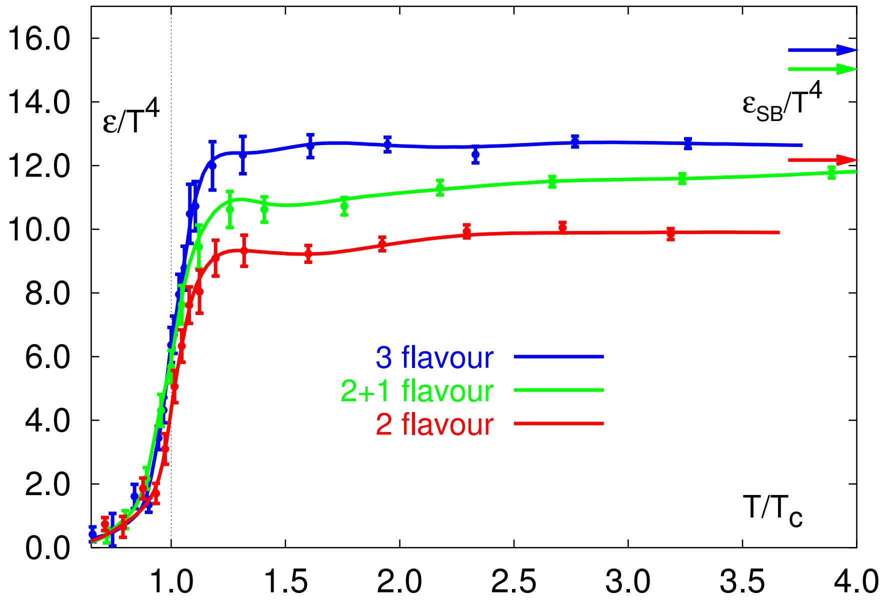

Figure 1.3: Lattice QCD prediction, the temperature dependence of energy density of QCD medium. Sudden change in the energy density below and above the critical temperature (T_c): an evidence of phase change [16].

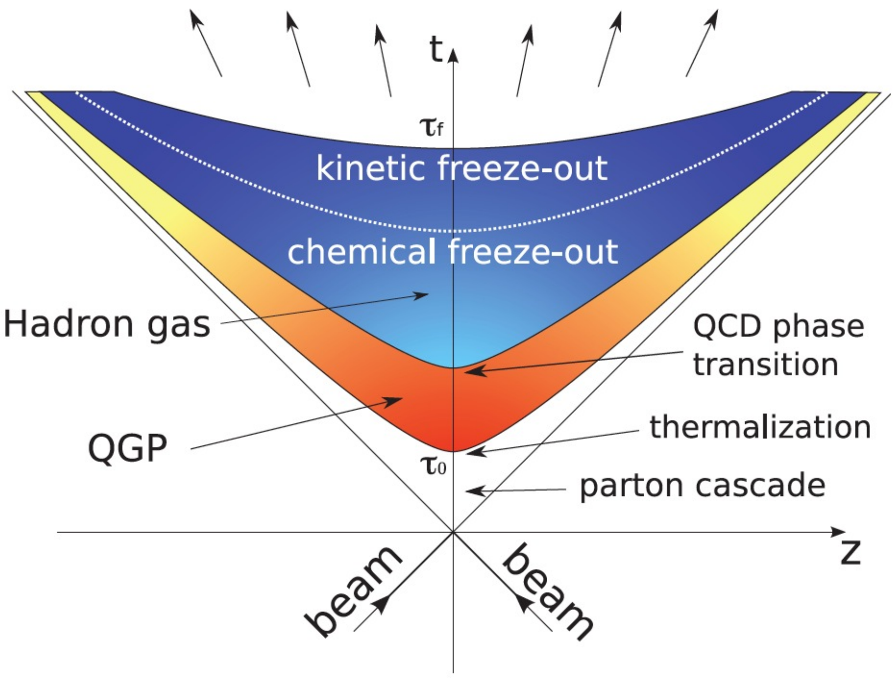

Figure 1.4: Schematic diagram of the space-time evolution through different stages of the relativistic heavy-ion collision.

the thermalized state is called proper time τ_0. The plasma lives for a very short time (about 10 fm/c) and during this time undergoes a rapid expansion in space. As a consequence, the QGP medium cools down at a rapid pace. Hadronization takes place once the temperature reaches the critical value. The expanding QGP medium has a phase transition from de-confined partonic state to the formation of the hadrons (to the hadron gas). The critical temperature at which the chemical composition of the medium is changing is called chemical freeze-out temperature T_{ch}. The composition of different particles gets determined at this time (at T_{ch}). After that, the hadrons keep continuing elastic collisions among themselves. The mean free path of the interaction of the hadrons are exceeding the dynamic size of the system at some moment and the elastic collision ceases. The temperature of such time is known as kinetic freeze-out temperature, T_{kin}. The hadrons are streamed out freely in all possible directions and reach the detector.

1.4 Experimental facilities for heavy-ion collisions

The first dedicated relativistic heavy-ion collision programs for QGP search was initiated at Lawrence Berkeley National Laboratory (LBNL) in the early 1970s. Gold ion beams of energy 1 AGeV is used as a projectile to collide with the target nuclei to reach a condition, where energy density few times higher than the normal nuclear matter was observed. The success of this experiment is followed by a series of experiments at Brookhaven National Laboratory (BNL) and at European Organisation for Nuclear Research (CERN) with higher projectile energy. The Alternating Gradient Synchrotron (AGS) at BNL started fixed target collision programme in 1986 with Oxygen and Silicon beam of $\sqrt{s_{\mathrm{NN}}} = 4.86$ GeV. The ASG started providing gold ion beam of the same $\sqrt{s_{\mathrm{NN}}}$ in 1991. The CERN ion program initiated at the SPS in 1986 with Oxygen beam of energy 60 and 200 GeV/nucleon. A series of experiments (NA44, NA45, NA49, NA50, NA52, NA60, WA97, WA98, etc) at Super Proton Synchrotron (SPS) at CERN have completed with a maximum collision energy $\sqrt{s_{\mathrm{NN}}} = 17.3$ GeV. The results for the anomalous J/Ψ suppression and the strangeness enhancement measurement at SPS was a signature of formation of QGP [18, 19].

A new dedicated accelerator facility for the QGP study, Relativistic Heavy Ion Collider (RHIC) at BNL became operational in 2000. Four experiments, BRAHMS, PHOBS, PHENIX, STAR, were dedicated to different physics observables for Au-Au collisions at $\sqrt{s_{\mathrm{NN}}} = 200$ GeV. Au-Au collisions within an energy range from $\sqrt{s_{\mathrm{NN}}} = 7.7$ GeV to 200 GeV allowed for a detail investigation about QGP formation and to map the QCD phase diagram. The beam energy scan program (BES-I) at RHIC successfully described the QGP phase diagram. RHIC also collided other ion species for the detailed study of the QGP phase.

The Large Hadron Collider (LHC) at CERN is the biggest accelerator facility in the world. It has a ring of 27 km circumstance. The highest possible center-of-mass energy for Pb-Pb collisions at the LHC is $\sqrt{s_{\mathrm{NN}}} = 5.5$ TeV. During the LHC Run-1 (2008-2013) and Run-2 (2015-2018) the Pb-Pb collision of energy $\sqrt{s_{\mathrm{NN}}} = 2.76$ TeV and $\sqrt{s_{\mathrm{NN}}} = 5.02$ TeV are achieved, respectively.

According to the future plan of the LHC, in next Run-3 (2021-2023) and Run-4 (2026-2029), it will reach to its maximum possible energy $\sqrt{s_{\rm NN}}$ = 5.5 TeV. Below I discuss some features of LHC and the four major experiments.

Two new accelerators are being constructed for studying the QGP phase transition. The FAIR (Facility for Anti-proton and Ion Research) at GSI, Darmstadt, Germany will have a fixed target beam at 20 GeV per nucleon. The NICA (Nuclotron-based Ion Collider fAcility) at Dubna, Russia will have Au and Au ions colliding at $\sqrt{s_{\rm NN}}$ = 4 GeV.

1.5 Large Hadron Collider and its experiments

The LHC is the largest collider machine ever built, located at European Organization for Nuclear Research (CERN) near Geneva, Switzerland. The LHC ring of circumference 26.7 km is at the border between the Switzerland and France, located underground between 50 m and 175 m depth. The successful operation of LHC began in November 2009.

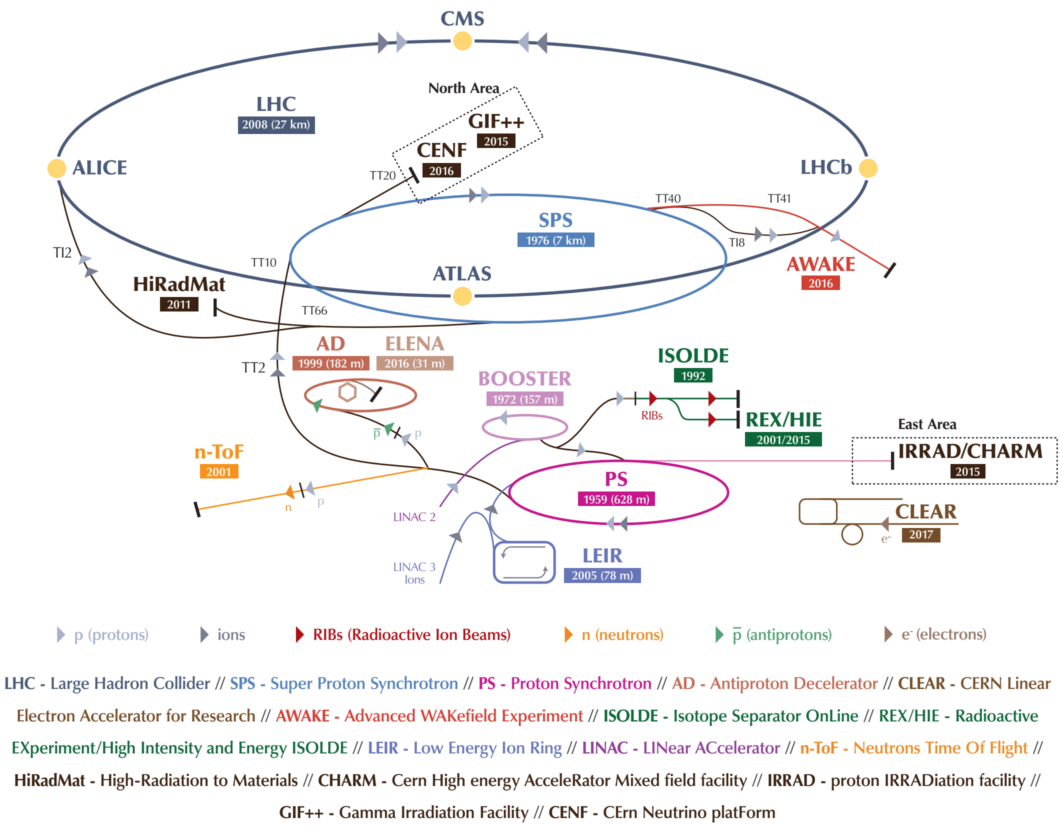

Figure 1.5: Schematic view of CERN accelerator complex and its four experiments. Figure is adopted from [20].

The full accelerator complex of the CERN is shown in Fig. 1.5. In the full LHC ring, it has 1232 dipole magnets for the purpose of bending two beams and 392 quadrupole magnets for focusing the beam near interaction points (IPs) where the collisions occur. For a proton beam, hydrogen atoms are stripped off electrons by applying an electric field, that is injected from a linear accelerator (LINAC-2) into the Proton Synchrotron Booster (PSB) with initial energy 50 MeV. In the PSB, the proton energy is increased to 1.4 GeV before passing to the Proton Synchrotron (PS) for further acceleration up to 25 GeV. The beam is then sent to Super Proton Synchrotron (SPS) before injection to the LHC with an energy 450 GeV. The LHC provides ion-beam facility also along with the proton-beam. Ions are first accelerated at LINAC-3 then it goes through the Low-Energy Injector Ring (LEIR), PS, SPS and then LHC.

The LHC has a successful Run-1 during 2009-2013 with highest centre-of-mass energy $\sqrt{s_{\rm NN}} = 8.0$ TeV for pp collisions, 5.02 TeV for p-Pb collisions and 2.76 TeV for Pb-Pb collisions. After a break for maintenance and upgrade, called Long Shutdown 1 (LS1), LHC started Run-2 in April 2015 and continued successfully up to December 2018 before the Long Shutdown 2 (LS2). In Run-2, LHC has data with highest centre-of-mass energy $\sqrt{s_{\rm NN}} = 13.0$ TeV for pp collisions, 8.16 TeV for p-Pb collisions, 5.02 TeV for Pb-Pb collisions with a new collision system Xe-Xe collision at $\sqrt{s_{\rm NN}} = 5.44$ TeV. During the LS2 2019-2020 LHC has planned for maintenance and upgrade of the accelerator as well as the experiments.

There are four experiments in LHC machine for different physics objectivities, named as ALICE, CMS, ATLAS, LHCb. All the four experiments have programs for QGP study.

- **ALICE (A Large Ion Collider Experiment)** is dedicated to the study of heavy-ion collisions in LHC. More details on ALICE experiments are given in Chapter 2.

- **ATLAS (A Toroidal LHC ApparatuS)** is the largest volume particle detector ever built. This is a general purpose detector. The main discovery of ATLAS is Higgs boson. ATLAS investigates the property of the Higgs particle and physics beyond the standard model.

- **CMS (Compact Muon Solenoid)** is the second general purpose particle detector. CMS study for Standard Model, Higgs boson, and beyond Standard Model physics. The physics goals are similar to ATLAS. However, CMS and ATLAS use different design of the detector and technique to study physics.

- **LHCb (Large Hadron Collider beauty)** is focused on heavy-flavor physics and in particular CP violation. In other experiments, detectors covering from all around the collision point, whereas in LHCb the detectors are placed in a 20 m long forward rapidity region.

1.6 Experimental observables of the QGP formation

The QGP signals are not unique and one needs to make a comprehensive study of all available probes in order to make any firm conclusion. Here, I present only a few of the selected observables.

1.6.1 Particle multiplicity and energy density

The charged particle pseudorapidity density $dN_{ch}/d\eta$ is the basic global property used in study in every particle physics experiment. The multiplicity of emitted particles provides important information about the collision geometry and has a strong dependence on the impact parameter. The particle production mechanism, *i.e.,* the soft scattering and the hard scattering are related to the collision energy. The pseudorapidity $dN_{ch}/d\eta$ distribution of the produced particles reflects the entropy of the system, and along with mean transverse momentum ($\langle p_{\mathrm{T}}\rangle$) measurement of the outgoing particles, this can be used to estimate the initial energy density of the system. The normalized charged particle pseudorapidity density $\frac{2}{\langle N_{part}\rangle}\langle dN_{ch}d\eta\rangle$ as a function of collision energy $\sqrt{s_{\mathrm{NN}}}$ is presented in Fig. 1.6 for the pp (p$\bar{p}$), p-A(d-A) and A-A collision systems [21]. The multiplicity follows a power law function, as^b. In heavy-ion collisions particle production is much steeper $b = 0.154$ than pp(p$\bar{p}$) collisions with $b = 0.103$. The measurement concludes that the particle production in heavy-ion collisions is not solely because of the multiple collisions undergone by the participating nucleons since the p-A(d-A) collisions also encounter multiple collisions.

The global observable, transverse energy density $dE_{\mathrm{T}}/d\eta$ are useful quantities to estimate the produced energy density in the collision. The $dE_{\mathrm{T}}/d\eta$ measurement in heavy ion collision confirms about the QGP formation. The initial energy density of the medium, within the Bjorken model [22], can be estimated from the measurement of $dE_{\mathrm{T}}/d\eta$, as,

$$\epsilon = \frac{1}{A_{\mathrm{T}}\tau_0}\frac{dE_{\mathrm{T}}}{dy} = \frac{1}{A_{\mathrm{T}}\tau_0}J(y,\eta)\frac{dE_{\mathrm{T}}}{d\eta}. \tag{1.5}$$

Where A_{T} is the overlapping area in the transverse plane, τ_0 is the proper time and $J(y,\eta)$ is the Jacobian of the transformation from pseudorapidity to rapidity.

The importance of the transverse energy density can be explained using the Fig.1.7, which shows the ratio $\langle dE_{\mathrm{T}}/d\eta\rangle/\langle dN_{ch}/d\eta\rangle$ as a function of $\sqrt{s_{\mathrm{NN}}}$. The result shows that at RHIC energies $\langle dE_{\mathrm{T}}/d\eta\rangle/\langle dN_{ch}/d\eta\rangle$ is almost saturated or weakly dependent on $\sqrt{s_{\mathrm{NN}}}$. The empirical extrapolation of the data to LHC energies is as shown in the gray band in the figure whereas the experimentally measured value indicates that an increase in the collision energy does not only increases of the particle production, but also the mean energy per particle [23].

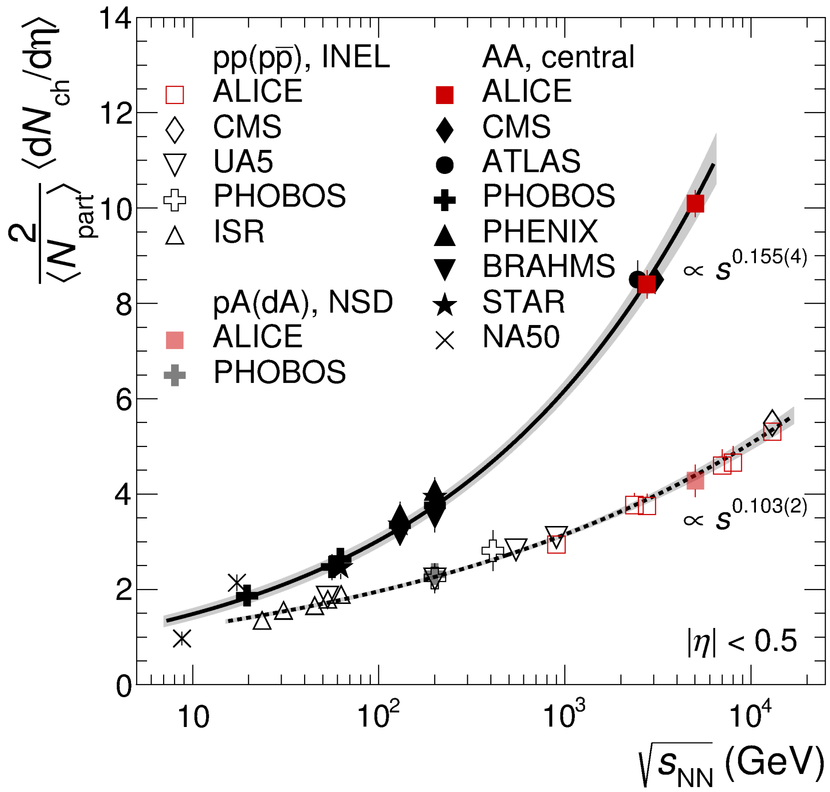

Figure 1.6: Charged particle pseudorapidity density variation with collision energy $\sqrt{s_{\rm NN}}$ for pp(p$\bar{p}$), p-A(d-A) and A-A collision systems. Figure is adopted from [21].

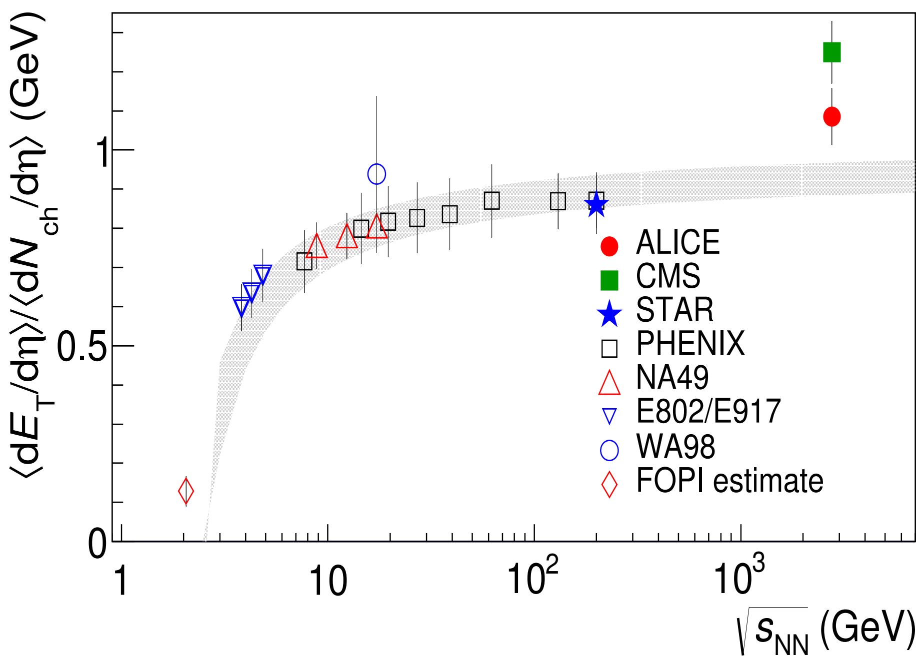

Figure 1.7: Energy dependence of the ratio of the mean transverse energy density over the mean charged particle density. Data from different experimental facilities. Figure is adopted from [23].

1.6.2 Nuclear modification factor (R_{AA})

To study QGP formation, comparison of the observables with a baseline system is necessary, such as proton-proton system where no QGP is expected to form. In heavy ion collisions, the partons with high p_{T} scatter in the partonic medium prior to hadronization. As a result degradation of the high p_{T} particles. To quantify it, a parameter called "nuclear modification factor" which is the ratio of the yield of the heavy ion collisions to that of the proton-proton collisions normalized by the total number of binary collisions is defined as,

$$R_{\mathrm{AA}} = \frac{1}{\langle N_{coll} \rangle} \frac{d^2 N_{\mathrm{AA}}/dydp_{\mathrm{T}}}{d^2 N_{pp}/dydp_{\mathrm{T}}}, \tag{1.6}$$

where $\langle N_{coll} \rangle$ is the average number of binary nucleon-nucleon collisions calculated using MC Glauber model. If the heavy ion collision is simply the superposition of many binary collisions, then R_{AA} is expected to be unity. If its value is lower than unity then it indicates high p_{T} hadrons production is suppressed due to the strongly interacting medium formation. The value R_{AA} for the charged hadrons as a function of p_{T} as measured in ALICE experiment for Pb-Pb 0-5% central collision of $\sqrt{s_{\mathrm{NN}}} = 2.76$ TeV is shown in Fig. 1.8 [24]. Data from highest RHIC energy is also presented for comparison. The observation of the high p_{T} (> 5 GeV/c) particle suppression suggest strong parton energy loss and therefore denser medium formation in LHC compared to RHIC. A strong dependency of p_{T} can found in the low momentum region ($p_{\mathrm{T}} \lesssim 2 - 2.5$ GeV/c) which is associated with thermal production. The peak indicates $\langle p_{\mathrm{T}} \rangle$ is shifting to higher value due to the collective effect of the medium. In the intermediate p_{T} region it is found that the proton is less suppressed than pion and kaon, which is due to collectivity and mass ordering effect.

1.6.3 Jet quenching

A jet is a high p_{T} quark or gluon fragmented into cluster of hadrons those are moving approximately same direction. If two jets are created in pp or e^+e^- collisions, they move back to back with almost same momentum. These are called dijet. However, in A-A collision if the dijets are produced close to the surface (medium dependency), then one jet is more probable to escape without interaction with the partonic medium. The other has to pass through the hot and dense medium through multiple interactions. Therefore, the second jet loses most of its energy or may even completely absorbed into the medium before fragmenting to hadrons. Two particles azimuthal co-relation for minimum bias pp and for central d-Au, Au-Au systems of $\sqrt{s_{\mathrm{NN}}} = 200$ GeV as measured by STAR experiment is shown in Fig. 1.9 [25]. The away side peak at $\Delta\phi = \pi$ is strongly suppressed for

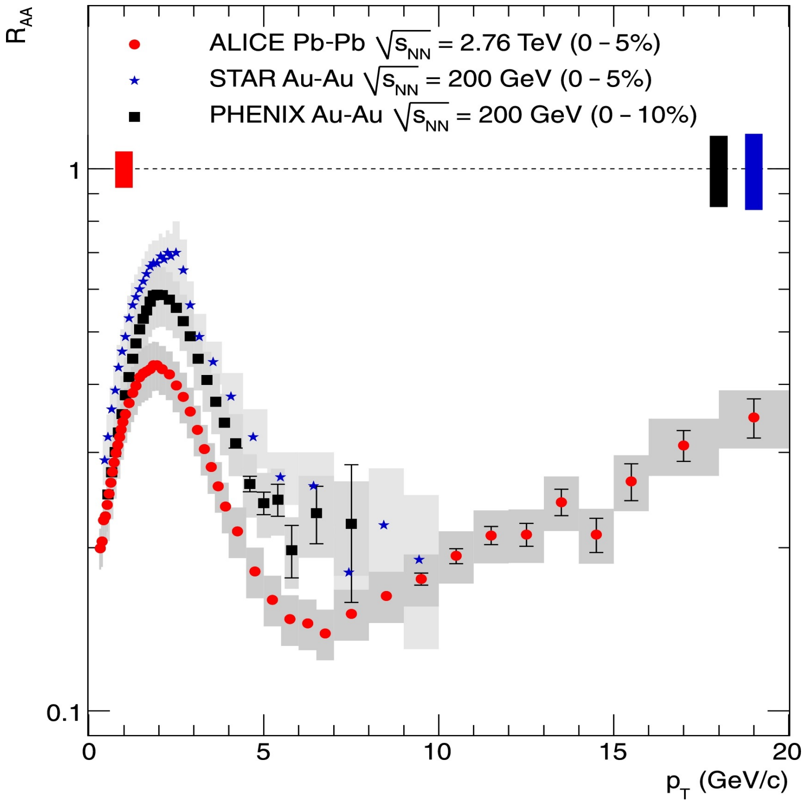

Figure 1.8: Nuclear modification factor R_{AA} as a function of p_{T}. Data from central Pb–Pb collisions at LHC and Au-Au collision at RHIC are compared. Figure is adopted from [24]

Au-Au case; however, a peak is found for pp and d-Au system. The away side peak suppression is the experimental evidence of jet quenching and hence the QGP medium formation.

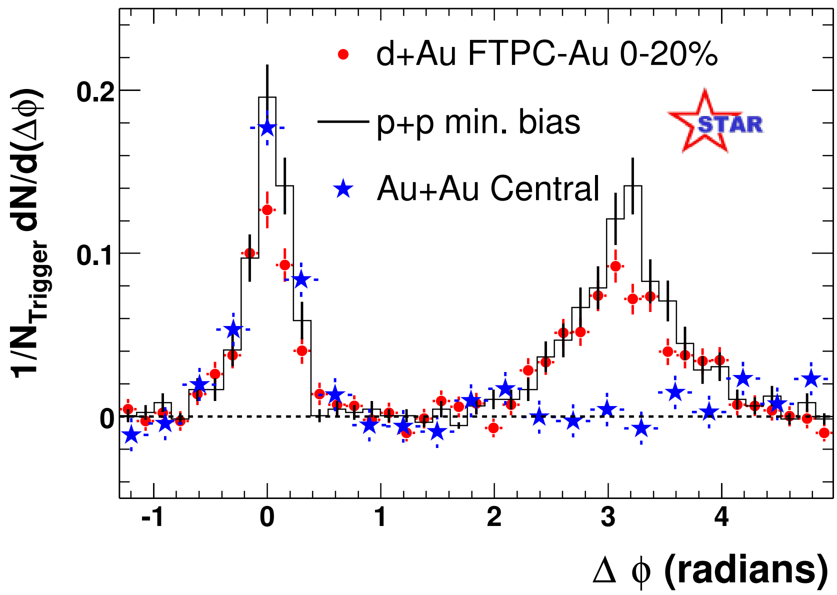

Figure 1.9: Di-hadron azimuthal co-relation for pp, d-Au and Au-Au collisions at $\sqrt{s_{\mathrm{NN}}} = 200$ GeV in STAR experiment [25].

1.6.4 J/Ψ suppression

The quarkoniums (or bottomoniums) are the bound states of quark anti-quark pairs like $c\,\bar{c}$ (or $b\,\bar{b}$). These particles are produced at the initial stage by the method of hard scattering. J/Ψ is the bound state of $c\,\bar{c}$ pair. The production of the J/Ψ is suppressed in A-A collisions due to the creation of the strongly interacting QGP medium. In a QGP medium colour charge of the charm quark c will be screened, called Debye screening, by all other quark, anti-quark and gluon colour charges of the plasma. Debye screening length λ_D, which decreases with increasing temperature of the medium, determines the range of the attractive interaction between c and $\bar{c}$. Therefore a $c\,\bar{c}$ pair could not form the J/Ψ particle in medium. The other important reason of the J/Ψ suppression is the string tension between the c and $\bar{c}$ vanishes because of deconfinement of the quarks in the matter. The $c\,\bar{c}$ dissociate to c and $\bar{c}$ and hadronize those quasi-free quarks as D-mesons ($c\,\bar{u}$, $c\,\bar{d}$) etc. R_{AA} is the measurement of the J/Ψ suppression provides insight into the QGP medium. The inclusive J/Ψ R_{AA} as reported by ALICE in Pb-Pb collisions at $\sqrt{s_{\mathrm{NN}}} = 2.76$ TeV [26] is shown in Fig. 1.10. The results of PHENIX experiment is also included in the figure for comparison [27]. R_{AA} is almost a factor of 3 larger for N$_{part} \geq 180$ in ALICE. The higher values of R_{AA} at LHC can be explained by recombination process of c, $\bar{c}$ into J/Ψ in the medium.

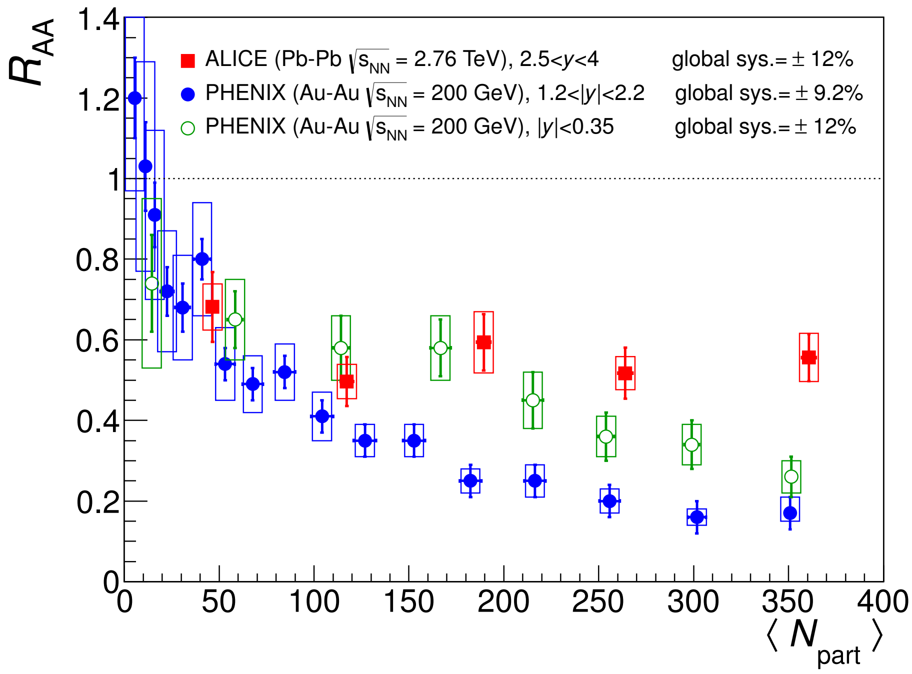

Figure 1.10: Nuclear modification factor R_{AA} of J/Ψ for Pb-Pb collisions measured in ALICE at $\sqrt{s_{\mathrm{NN}}} = 2.76$ TeV [26]. The results of PHENIX experiment are taken for comparison [27].

1.7 Motivation and organization of this thesis

The QGP formation and particle production mechanism are still not completely understood. In the future, ALICE is focusing on looking for a precise measurement of the rare processes at low and intermediate p_{T} regions, which require high statistics. The primary challenge for the ALICE TPC detector is its rate acceptance. The TPC with MWPC and gating grid based readout can handle at most 3.3 kHz where in LHC Run-3 Pb-Pb collision rate will be 50 kHz. Therefore, TPC upgrade is planned using the GEM readout. The advantages of GEM readout in TPC upgrade is discussed in Section 6.3.

The main motivation of this thesis is the development and characterization of the GEM detector keeping in mind of the ALICE TPC upgrade. GEM is also found very useful in other high-energy physics experiments like STAR, CMS and CBM in FAIR. Detailed study of triple GEM and quadruple GEM detectors are performed measuring its gain, energy resolution, time resolution and efficiency. Spatial uniformity is desired for the uniform operation of the large area GEM detector. The electric field configuration plays another important role in GEM characterization. Therefore, the optimization of the voltage difference across the GEM foils and the electric field within the gaps are necessary for the good operation of the GEM detector. A direct comparison of the triple GEM and quadrupole GEM results will be presented, which might help in choosing the right detector based on the experimental requirements. The testing methods, characterization and comparisons are discussed in Chapter 4. A gas simulation based on the Garfield software is performed for the limiting value of the time resolution is also described in that chapter.

A few MWPC detectors are fabricated and tested in our lab. The characterization of the detectors is performed using different electronics setup, namely NIM and MANAS. The test results are found important. The detailed testing methods are described in Chapter5.

For the TPC upgrade, GEM-based new readout chambers have to be ready at the earliest of the LHC long shutdown 2. All the chambers are produced in a period from July 2017 to October 2018. The assembling and testing of the chambers are done at different stations within the TPC upgrade collaboration. I am involved in TPC upgrade activity by performing the quality assurance test of the GEM foils, outer readout chambers (OROCs) assembly and test performances based on GSI, Darmstadt lab. All the successful OROCs are transported to CERN for the beam test and commissioning in the new TPC. The detail methods of the OROC preparation are described in Chapter 6.

A simulation on Pb-Pb collision at centre-of-mass energy $\sqrt{s_{\mathrm{NN}}} = 5.5$ TeV has been performed as a part of this thesis. In this study, the global property of the collision estimated like charged particle multiplicity, momentum distribution, the energy density at the early stage of the collision for LHC energy at Run-3. The AMPT model is used in the simulation study. The estimation of the charged particle multiplicity in Pb-Pb collisions at $\sqrt{s_{\mathrm{NN}}} = 5.5$ TeV is necessary to check with the limitation of the TPC particle acceptance. The results are described in Chapter 7.

The major findings of this thesis are summarized in Chapter 8.

Chapter 2

ALICE experiment and its upgrade

A Large Ion Collider Experiment (ALICE) is one of the four big experiments at the LHC [4, 5]. ALICE is a dedicated experiment for heavy-ion collisions; however, it takes data for pp, p-Pb collisions as well for reference studies. The main goal of the ALICE experiment is to pursue physics knowledge of strong interaction in nucleus-nucleus collision and characterization of the QGP medium formation which is formed in such collisions. ALICE became fully operational at the end of 2009 and took data till December 2018 before the declaration of the LHC long shutdown 2 (LS2). During the first phase of operation, ALICE has collected data corresponding to collision energies for pp: 0.9, 2.76, 7, and 8 TeV, Pb-Pb: 2.76 TeV and p-Pb collisions at 5.02 TeV and in the second phase data of pp maximum possible energy 13 TeV, Pb-Pb: 5.02 TeV, p-Pb: 8.16 TeV and with a new collision environment Xe-Xe: 5.44 TeV. This chapter will be described the details of the ALICE detectors, future goals of ALICE and its upgrade strategies.

2.1 ALICE detectors

The ALICE experiment is designed with the placement of many detectors at specific positions based on their physics goals. Schematic view of the ALICE detectors is shown in Fig. 2.1. The detectors may be classified into three categories as: central detectors, forward detectors and Muon spectrometer [28]. The central detectors are ITS, TPC, TRD, TOF, HMPID, PHOS, EMCAL [29–35] and the forward detectors include ZDC, PMD, FMD, T0, V0 and AD [36–39]. ACORDE detector is placed above the L3 magnet [40].

The central barrel detectors, namely ITS, TPC, TRD and TOF, have full azimuthal ($0 \leq \phi \leq 2\pi$) coverage with rapidity acceptance $|\eta| < 0.9$. The detectors are enclosed in the L3 solenoid magnet which provides a 0.5 T magnetic field. Let us go through these detector systems.

- **The Inner Tracking System (ITS)** is the innermost of the ALICE barrel detector [29].

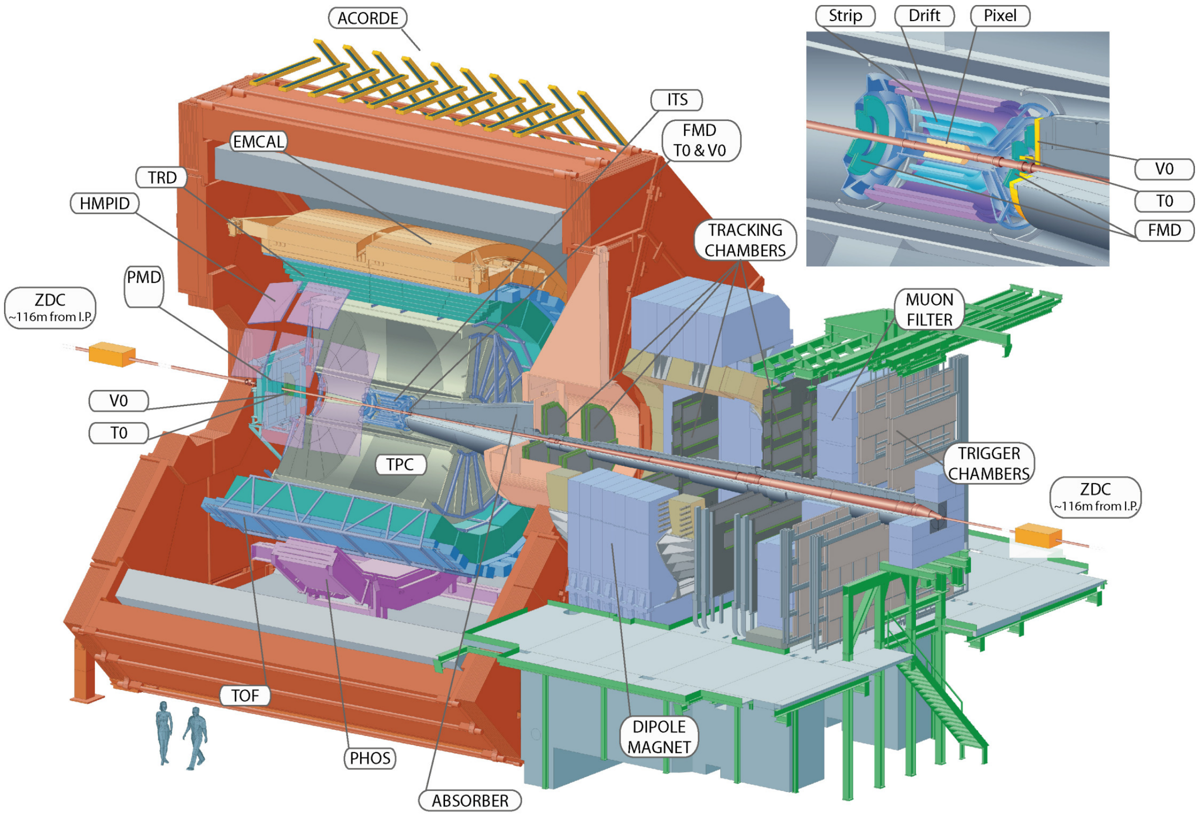

Figure 2.1: ALICE experiment labeled with all the detectors [41].

The detector is placed very close to the beam pipe, covering radius from 3.9 cm to 43 cm. Starting from the beam pipe to radially outward direction two Silicon Pixel Detector (SPD), two Silicon Drift Detector (SDD) and two Silicon Strip Detector (SPD) composed the full six layer ITS detector. The SPD is based on hybrid silicon pixels that consist of a two-dimensional matrix (sensor ladder) of reverse-biased silicon detector diodes. Each diode is bumped-bound on the readout chips which provide a binary output only. Therefore, the SPD provides only hit information of the particles and no dE/dx information. The first layer of the SPD has a pseudorapidity coverage of $|\eta| < 1.98$ which is together with Forward Multiplicity Detectors (FMD) used to measure the charged particle multiplicity. SPD has very high granularity for precise position determination of high track density ($50/\mathrm{cm}^2$). The SDD is the two intermediate layers of the ITS followed by the two outer most layers of the SSD. The outer four layers have analog readout. Particle identification of the low momentum particle ($p_{\mathrm{T}} < 100$ MeV/c) can be performed using ITS. Primary vertex (collision center) and secondary vertex determination of the decaying particle also the particle track construction can be done using the ITS.

- **Time Projection Chamber (TPC)** is the main central barrel detector in ALICE [30]. TPC is a gas-filled drift chamber currently using MWPC as readout. TPC has full azimuthal coverage with pseudorapidity coverage $|\eta| < 0.9$. $Ne/CO_2/N_2$, Ne/CO_2 or Ar/CO_2 gas mixtures are considered as active gas of the chamber from time-to-time. The inner radius of the chamber is about 85 cm and outer radius is about 250 cm with the active gas volume 90 m^3. The main purpose of TPC is the particle identification (PID) and momentum measurement at mid rapidity using energy deposition and track reconstruction of the incident particles. TPC can successfully measure particle momentum from 100 MeV/c up to 100 GeV/c. More discussion about ALICE TPC is given in Section 6.2.

• **Transition Radiation Detector (TRD)** is placed around the TPC, the radial position of the detector is in between 2.9 m and 3.68 m with pseudorapidity coverage $|\eta| < 0.84$ [31]. The main purpose of TRD is identification and tracking electrons of momentum above 1 GeV/c and pion rejection in this momentum range. The working principle of the detector is based on the transition radiation (photon) produced by relativistic electron crossing material of different dielectric constants. The radiator releases X-ray photon of energy range 1 to 30 keV. For the absorption of the X-ray photon Xe/CO_2 85:15 gas mixture is used as an optimum choice. The pion being heavier, it does not emit radiation below $\sim$ 100 GeV/c. Therefore, TRD has very efficient ($\approx$ 100%) pion rejection capability from electrons, that allows better measurement of the J/Ψ production through the di-electron channel.

• **Time Of Flight (TOF)** is a multi-gap resistive plate chamber (MRPC) detector segmented into 18 azimuthal sectors, each of these sectors is divided into 5 modules along the beam direction [32]. TOF is positioned at a radial position 370 cm from the primary vertex, *i.e.,* $z = 0$ with $|\eta| < 0.9$ and full azimuthal coverage. TOF has a good PID capability in the intermediate momentum range. The basic unit of TOF is a 10 gap-MRPC strip. Each strip has an active area 120×7.4 cm^2 and it is sub-divided into two rows of 48 pads of size 3.5×2.5 cm^2. The TOF has an ability to detect particles with 99.9% efficiency and an average total TOF time resolution of 80 ps can be achieved during normal running conditions. The PID is achieved in this detector by measuring the time-of-flight, which is the characteristic of each particle. The time-of-flight is the difference between the time of the hit measured by the TOF and the time of the interaction, that can be measured by the T0 detector. The TOF can provide more than 2σ π/K separation up to momentum 3 GeV/c and 3σ p/K separation up to 4 GeV/c in Pb-Pb collisions at $\sqrt{s_{\rm NN}} = 2.76$ TeV.

• **High Momentum Particle IDentification (HMPID)** is a ring imaging Cherenkov detector which covers only 5% of the central barrel phase space [33]. When a charged particle passes through the liquid C_6F_{14} (perflurohexane), it radiates Cherenkov light. The emitted lights are detected by a CsI coated photocathode of a multi-wire proportional chamber. The detector has good particle identification at high momentum range where TPC and TOF are unable. The detector is useful for the particle identification with p/K and K/p, on a track-by-track basis, up to

3 GeV/c and 5 GeV/c, respectively.

• **PHOton Spectrometer (PHOS)** is a high resolution electromagnetic calorimeter dedicated to precise measurement of the direct photon and neutral meson (π^0) yields in a p_T range up to 100 GeV/c [34]. The detector is located at a radial distance 4.6 m with azimuthal coverage of 220^o to 320^o and pseudorapidity acceptance $|\eta| < 0.12$. The detector is made of high granularity lead-tungsten scintillator crystals ($PbWO_4$). A Charged Particle Veto (CPV) is also placed in front of the PHOS to reject the charged particles.

• **ElectroMagnetic CALorimeter (EMCAL)** is installed for measurement of jet, high p_T photon and electron study [35]. The calorimeter also produces a fast, high-p_T trigger. The EMCAL is a lead-scintillator sampling calorimeter (1.44 mm Pb and 1.76 mm polystyrene scintillator in 77 layers) placed at about 4.5 m from the beam pipe. It has an azimuthal angle of 80^o to 180^o, almost opposite to the PHOS, with pseudorapidity coverage $|\eta| < 0.7$ which is about 23% of the phase space of the central region.

• **Zero Degree Calorimeter (ZDC)** is located on either side of the interaction point (IP) at a distance of 116 m along the beam direction [36]. The spectator nucleons that leave the IP can be estimated using ZDC; therefore, centrality classes can be determined indirectly. The ZDC consists of a neutron detector (ZN) placed at zero degree relative to LHC axis in between two beam pipe and proton detector (ZP) is placed externally to the outgoing beam pipe on the side where positive particles are deflected. In addition, two electromagnetic calorimeters (ZEM), located at 7 m from the IP, are used to distinguish between central and peripheral events.

• **Photon Multiplicity Detector (PMD)** provides the multiplicity and pseudorapidity distribution of photons [37]. The azimuthal anisotropy of the photons in the forward rapidity can be related to elliptic flow. PMD is placed at a distance 3.7 m from the IP in the direction of the A side of the ALICE (opposite to Muon Spectrometer). It has full azimuth with $2.3 < \eta < 3.9$ coverage. PMD is a preshower detector with an array of gaseous proportional counters. It consists of two identical proportional counter planes with a lead converter of thickness $3X_0$ in between them. The plane behind the converter is called preshower plane. A photon produces shower while passing through the converter. From the hit on several cells of the preshower plane, photons can be identified. The plane towards the IP is called Charged Particle Veto (CPV) plane and is used for improving the discrimination between charged hadrons and photons. The readout electronics of the detector is a Front End Electronics (FEE) board which contains four Multiplexed ANAlog Signal Processor (MANAS) chips, two inverting buffer amplifiers, two serial 12 bit ADC (AD7476) and a custom built ASIC called Muon Arm Readout Chip (MARC). Details about MANAS specification is given in Section 5.1.1. All the indigenous effort on PMD towards production testing and installation at ALICE cavern are made by Variable Energy Cyclotron Centre, Kolkata and ALICE-India group.

• **Forward Multiplicity Detector (FMD)** measures the charged particle multiplicity at very forward rapidity region ($-3.4 < \eta < -1.7$ and $1.7 < \eta < 5.0$) with full azimuthal coverage [38]. The FMD consists of 5 rings (3 inner rings and 2 outer rings) of silicon strip detector. The FMD has a total of 51,200 readout channels.

• **T0** is a fast timing and trigger detector. It has a time resolution of 50 ps [38]. T0 detector provides early trigger (wake up) to TRD and the precise start signal for the TOF. In addition, T0 detector measure approximate vertex determination within accuracy ± 1.5 cm. The T0 detector consist of two arrays of Cherenkov counters called T0A and T0C. T0A is located at about 3.6 m away from the IP with pseudorapidity coverage $4.5 < \eta < 5$. T0C is located at about 70 cm away from the IP opposite to T0A with pseudorapidity coverage $-3.3 < \eta < -2.9$.

• **V0** detector consists of two arrays of scintillator counters, named as V0A and V0C, installed on both sides of the ALICE collision vertex [38]. This detector provides minimum bias and centrality triggers for the central barrel detectors and rejection of beam gas events. V0A is located about 3.4 m from the ALICE vertex on the side opposite to the muon spectrometer with pseudorapidity coverage $2.8 < \eta < 5.1$, whereas, V0C is located on the other side of the vertex about a distance 90 cm with pseudorapidity coverage $-3.7 < \eta < -1.7$. The time resolution is of the order 1 ns for both the arrays.

• **ALICE Diffractive (AD)** is relatively new compared to other ALICE detector [39]. AD has been installed during LS1 for the second phase of the LHC run (Run-2). The AD consists of two stations, namely ADA at 17 m and ADC at 19.5 m on both sides of the interaction point. Each station has two layers of 4 plastic scintillators. The detector has the pseudorapidity coverage $-7.0 < \eta < -4.9$ for the C-side and $4.8 < \eta < 6.3$ for the A-side. The AD detector allows studying diffractive physics and photon-induced processes more efficiently at a very small angle concerning the beam pipe.

• **Muon Spectrometer** provides the complete spectrum of the charmonium state ($J/\Psi, \Psi'$) as well as bottomonium state ($\Upsilon, \Upsilon', \Upsilon''$) through their di-muon $\mu^+\mu^-$ detection [28]. The muon spectrometer covers full azimuth with a pseudorapidity range of $-4.0 < \eta < -2.5$ for acceptance of muons with $p_{\mathrm{T}} > 4$ GeV/c. This momentum cutoff is due to muons which pass through a front absorber made of carbon, concrete and steel. The front absorber cutoff all the background hadrons and photons by absorption. Behind the front absorber, the tracking system is made of 10 cathode pad/strip chambers arranged in 5 stations of 2 chambers each. A dipole magnet is located at about 7 m from the IP which allows the muon momenta to be reconstructed. An iron wall of

1.2 m located between tracking stations and trigger stations allow further reduction of low energy background in the trigger chambers. Both the trigger stations have 2 resistive plate chambers. MANAS chip has been used in the readout electronics. Saha Institute of Nuclear Physics, Kolkata from India and ALICE-India group made an extensive effort in building and testing the second tracking station.

- **ALICE Cosmic Ray Detector (ACORDE)** is an array of scintillators installed on top of the L3 magnet for the cosmic rays trigger. It has a pseudorapidity coverage ($|\eta| < 1.3$) over the azimuthal angle -60^o to 60^o. It provides a fast L0 trigger signal for the commissioning, calibration and alignment of the some of the ALICE tracking detectors mainly TPC, TOF, HMPID and ITS.

2.2 Future physics goals of ALICE

The ALICE detectors had excellent performance in LHC Run-1 and Run-2 and achieved many physics results [42]. ALICE has reported global features like charged particle multiplicity distributions, momentum spectra, initial energy density with different centrality classes and collision energies. Quarkonia suppression and enhancement, jet quenching, and direct photon measurement allowed to understand parton distribution function, parton kinematic and energy loss in the plasma phase. However, more precision measurements are desirable in rare processes.

The scientific programmes of ALICE in LHC Run-3 are described in a comprehensive Letter of Intent [43]. The future physics goal of ALICE is the precise measurement of the rare probes, their interaction with the medium and hadronization processes. The major physics interest is charm and beauty quark measurements, their in medium energy loss and thermalization. To address the heavy quark physics questions, measurements are required to low and intermediate p_{T} regions. Other studies would include anisotropy flow of charm mesons and baryons, quarkonia suppression and regeneration at low p_{T} (< 3 GeV/c) as a probe of the deconfined state of matter. The low mass di-lepton measurements are important since these infer about direct-photon spectrum in the p_{T} region of 1–5 GeV/c where the thermal contribution is expected to dominate. Measuring jets and their energy loss of the hard scattered partons in the QGP provides access to the properties of the strongly interacting medium. ALICE can provide physics information on jets by accurate track reconstruction at low p_{T} domain.

2.3 ALICE detectors upgrade

The luminosity in different collision system of the LHC during different run periods are given in Table 2.1. All those future physics investigations are required high statistics and low momentum scale. The future Pb-Pb collision rate will be increased to 50 kHz in Run-3 and Run-4 to achieve the required statistics. ALICE will accumulate $\mathscr{L}_{int}$(integrated luminosity) $\approx$ 10 nb^{-1} of Pb-Pb collisions corresponding to 10^{11} interactions. This is the minimum needed to address the proposed physics programme with focus on rare probes both at low and high p_{T}. The central barrel detectors are planned for a major upgrade to cope up with high rate particle production and enhancing its low-momentum vertexing and tracking capability. The upgrade will happen during the long shutdown-2 (LS2) in 2019-2021. The following two detectors: ITS and TPC will be fully upgraded with its readout and electronics. Whereas, Transition Radiation Detector (TRD), Time-Of-Flight (TOF) detector, PHOton Spectrometer (PHOS) and Muon spectrometer detectors will have only electronics upgrade.

System	Year	$\sqrt{s_{\mathrm{NN}}}$ (TeV)	$\mathscr{L}_{int}$
Run-1 (2019-2013) & Run-2 (2015-2018)			
Pb-Pb	2010-2011	2.76	$\sim 75\ \mu b^{-1}$
	2015	5.02	$\sim 250\ \mu b^{-1}$
	2018	5.02	$\sim 750\ \mu b^{-1}$
Xe-Xe	2018	5.44	$\sim 0.3\ \mu b^{-1}$
p-Pb	2013	5.02	$\sim 15\ nb^{-1}$
	2016	5.02, 8.16	$\sim 3\ nb^{-1}$, $\sim 25\ nb^{-1}$
pp	2009-2013	0.9, 2.76	$\sim 200\ \mu b^{-1}$, $\sim 100\ nb^{-1}$
		7, 8	$\sim 1.5\ pb^{-1}$, $\sim 2.5\ pb^{-1}$
	2015-2017	5.02	$\sim 1.3\ pb^{-1}$
	2018	13	$\sim 25\ pb^{-1}$
Run-3 (2021-2023)			
Pb-Pb	2021-2023	5.5	$\sim 6\ nb^{-1}$
Run-4 (2026-2029)			
Pb-Pb	2027-2029	5.5	$\sim 7\ nb^{-1}$

Table 2.1: The collision luminosity of the LHC during Run-1 and Run-2 and projected luminosity in Run-3 and Run-4.

- **ITS upgrade:** The current ITS has rate capability of 1 kHz whereas in future the rate capability will be about 100 kHz for Pb-Pb collisions. The current six layers readout will be replaced with seven layers detector with Monolithic Active Pixel Sensors (MAPS) [44]. The MAPS, are based on CMOS technology, have the sensor and the readout chip on the same silicon wafer instead of bump-bond of those. The new sensor will cut the material budget with the radiation length from 1.1%X_0 to 0.3%X_0 for the inner three layers and 0.9%X_0 for the outer four layers. The pixel size will be shrinking to 30×30 μm^2 at three inner layers where the existing size is 50×425 μm^2. This will improve by a factor of 3 the resolution for secondary vertices and extends its tracking capabilities to lower transverse momentum.

- **TPC upgrade:** The current TPC with MWPC and gating grid based readout has excellent particle tracking capability. However, with the existing readout TPC can take data with a maximum possible rate of 3.3 kHz. To overcome rate limitation Gas Electron Multiplier (GEM) based readout is chosen for the new TPC. The R&D of the GEM detector has proven that readout with four GEM stack can be a suitable choice for the TPC [45, 46]. All other performances like PID capability using dE/dx measurement and momentum resolution of the existing TPC will be restored. TPC upgrade activity is a part of this thesis. Therefore, detail description about ALICE TPC and its upgrade activity are described in Chapter 6.

- **Muon Forward Tracker (MFT) detector:** MFT is new Si-tracking detector designed to accurate vertexing capabilities of the Muon spectrometer [47]. MFT positioned before the front absorber of the Muon spectrometer with a pseudorapidity coverage $-3.6 < \eta < -2.45$. The MFT consists of two half-MFT cones. Each half-MFT cone includes of 5 layer half-disks positioned along the beam axis. The same CMOS monolithic technology as chosen for the new ITS will be implemented as the MFT pixel sensors.

- **Fast Interaction Trigger (FIT) detector:** As a part of the ALICE detector upgrade, the existing forward detectors T0, V0 and FMD detectors will be replaced by a single trigger detector Fast Interaction Trigger (FIT). The FIT upgrade aims to replace these detectors with a single detector system that can provide these functionalities at the higher collision rates. The FIT will provide forward trigger, luminosity and collision time measurement. It will also determine multiplicity, centrality, and reaction plane of heavy-ion collisions. The time measurement of the FIT will be used in TOF based particle identification for which time resolution < 50 ps is needed. The FIT detector will consist of two arrays Cherenkov quartz radiators with MCP-PMT sensors which have same functionality as T0 detector and single, large scintillator ring which is similar as V0 detector. The arrays will be placed on both sides of the IP. The detail description about FIT positioning and performances can be found in [48]

- **Readout and trigger upgrade:** The ALICE detectors and electronics systems are upgrading to handle the future interaction rate of 50 kHz in Pb-Pb and 200 kHz in pp and p-Pb collisions. The ALICE detectors readout methodology will be based upon a minimum-bias trigger (provided by the FIT detector) or continuously be readout to acquire all the events. This huge data volume of $\sim$ 3 TB/s will be reduced to 80 GB/s before sending to an online computing system and data storage. This process will be done by Common Readout Unit (CRU), trigger and timing distribution and control moderation [49]. The CRU forms an interface between the sub-detectors Front End Electronics (FEE), the trigger system and the detector data link (DDL) connecting to the online computing system (O^2). Data transmission between the sub-detector FEE and the CRUs will be based on the GBT links. CRU can multiplex, process and format the data depending on the detectors specification.

To summarize, in this chapter, the ALICE experiment and its sub-detectors are described. The future physics goal of the ALICE experiment is the precise measurement of the rare probes for which high statistics are required. ALICE will upgrade its detectors and readout system to accumulate a high rate (50 kHz) Pb-Pb collisions data in LHC Run-3 to address its future physics plan.

Chapter 3

Gaseous detectors in High-Energy Physics and GEM

Gaseous detectors have played a major role in nuclear and particle physics experiments. The low material budget, large volume production and relatively low cost make it a suitable choice for High-Energy Physics (HEP) experiments. The gaseous detectors such as wire chamber, GEM, Micromegas, RPC, etc. have very different geometrical structure. However, particle detections are based on the same basic principles. The general principle of the charged particle detection in a gaseous detector is described below. Then I will discuss different types of gas detectors. The Section 3.3 will present a general discussion about the development of GEM detector.

3.1 Principle of particle interactions in gaseous detector

Charged particles passing through matter lose energy due to electromagnetic interaction, bremsstrahlung, e^+e^- pair production and photo-nuclear interactions. In the relativistic energy range, the Coulomb interaction is the most dominating among others. However, for a light particle, like the electron, bremsstrahlung is equally important as Coulomb interaction in the relativistic energy regime. The interaction of the charged particle can be divided into two categories based on its energy exchange: elastic (*i.e.,* no energy exchange) and inelastic and ionization (*i.e.,* energy deposition). Energy deposition of a charged particle in inelastic collisions by mean of excitation or ionization of the atom or molecule as given below.

$$e^- + atom \rightarrow atom^* + e^- \rightarrow atom + \gamma + e^-$$

$$e^- + atom \rightarrow atom^+ + 2e^-$$

The average energy loss dE of a charged particle by means of excitation and ionization in a length dx inside the medium is given by *Bethe-Bloch formula* [50],

$$\frac{dE}{dx} = K\frac{Z}{A}\frac{z^2}{\beta^2}\left(\frac{1}{2}\ln\left[\frac{2m_e\gamma^2v^2W_{max}}{I^2}\right] - \beta^2 - \frac{\delta(\beta\gamma)}{2}\right), \tag{3.1}$$

where $K = 4\pi N_A r_e^2 m_e c^2 = 0.307$ MeV mol^{-1} cm^2.
Here $\delta(\beta\gamma)$ is *density effect* correction to ionization energy loss. The specific energy loss dE/dx for different charge particles in air is shown in Fig. 3.1. At nonrelativistic energy region, specific energy loss dE/dx is dominated by the $1/\beta^2$ factor and decreases with increasing energies until velocity about $v = 0.96c$ ($\beta\gamma = 4$), where a minimum is reached. A particle of this energy is called minimum ionizing particles (MIPs). It is important to note that all particles with the same charge have almost same dE/dx at minimum ionization.

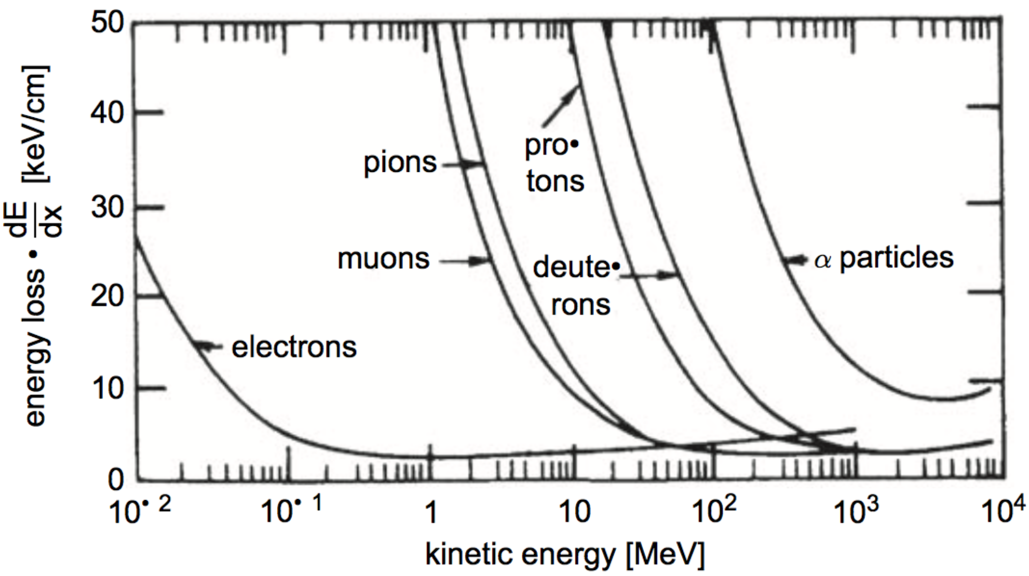

Figure 3.1: Specific energy loss of different charged particles in air [51].

3.1.1 Working principle of gaseous detectors

A schematic of parallel plate gas detector is shown in Fig. 3.2 to explain the basic working principle of the gaseous detector. When a charged particle passes through the detector, it produces primary ionization. The number of primary ionizations produced is proportional to the energy deposition within the gas volume as described in the *Bethe-Bloch formula*. The primarily produced electrons drift towards the anode in the presence of a drift electric field (few 100 V/cm − few kV/cm). However, those primary electrons are not sufficient to produce a detectable electric signal. Therefore, a charge avalanche is intended before collecting the electrons on the anode. A high electric field is applied (few tens of kV/cm) to accelerate electrons and have a cascade of secondary electrons before collecting them on the anode. The drift region and the avalanche region might be same or physically separate depending on the detector geometry and field configurations.

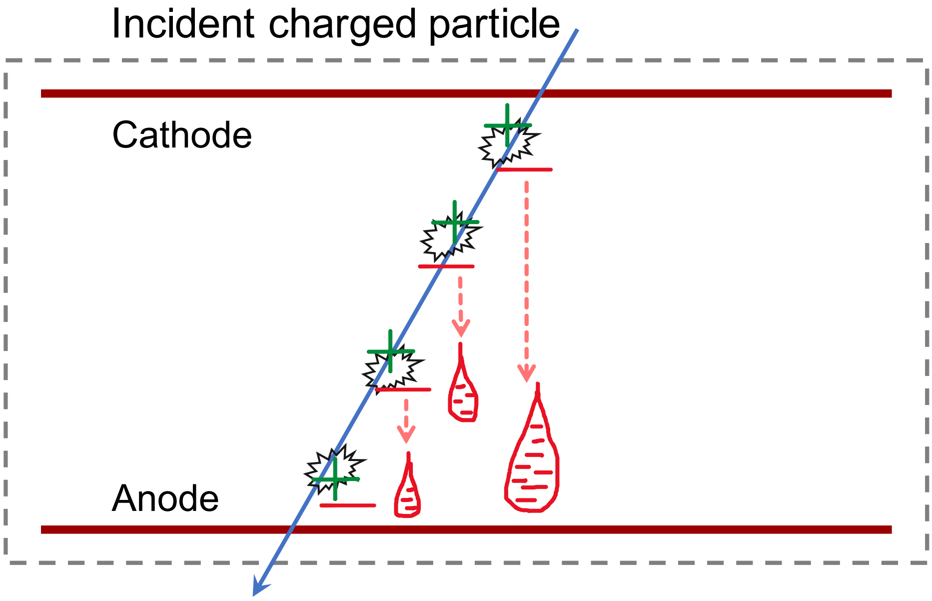

Figure 3.2: Working mechanism of a simple parallel plate gas detector.

3.2 Micro-pattern gaseous detector (MPGD)

Multi-wire proportional chamber (MWPC) is invented by G. Charpak and his collaborators in 1968 [52], for which G. Charpak was awarded Nobel Prize in Physics in 1992. Immediately after the discovery, MWPC revolutionized the field of HEP experiments. The development of gas detector technology followed the advance in accelerator facilities. The new facilities like RHIC and LHC have much more particle production rate than the limitation of the MWPC. The study found that the rate limitation is 10^4 Hz/mm^2 [53] due to its space charge effect. To overcome the particle rate limitation, a new technology, Micro-Pattern Gaseous Detectors (MPGDs) was invented, which revolutionized the field of HEP experiments.

Development of micro-pattern gaseous detector (MPGD) technology started in 1990 with the aim to achieve higher rate capability than MWPC. The invention of different micro-pattern gaseous detectors come from the industry of microelectronics and printed circuits technologies. The common feature of MPGDs is a structure with narrow amplification gap of typically 50-100 μm. MPGDs made a significant change in HEP experiments with its advantages like high rate capability, improved spatial and time resolution, radiation hardness, detector segmentations, simplified construction, large scale production and minimizing the power and cost. In the following section, a brief description of different kind of MPGDs are given.

The most successful design of MPGD are found (1) Micromegas and (2) GEM because of superior performance, operational stability against discharge, decoupled readout design and large scale manufacturing advances.

3.2.1 Micro-strip gas chamber (MSGC)

The first kind of MPGD technology is the Micro-Strip Gas Chamber (MSGC). The first MSGC is invented by A.Oed in 1988 [54]. Instead of wire, the detector is composed of the fine anode strips of 10 μm thick and the cathode strips (typically 50-200 μm) are printed on an insulator board. The anodes are separated by a few hundred microns in contrast of 2-5 mm gap in MWPC. The schematic design and electric field lines in an MSGC is shown in the left panel of Fig. 3.3. The

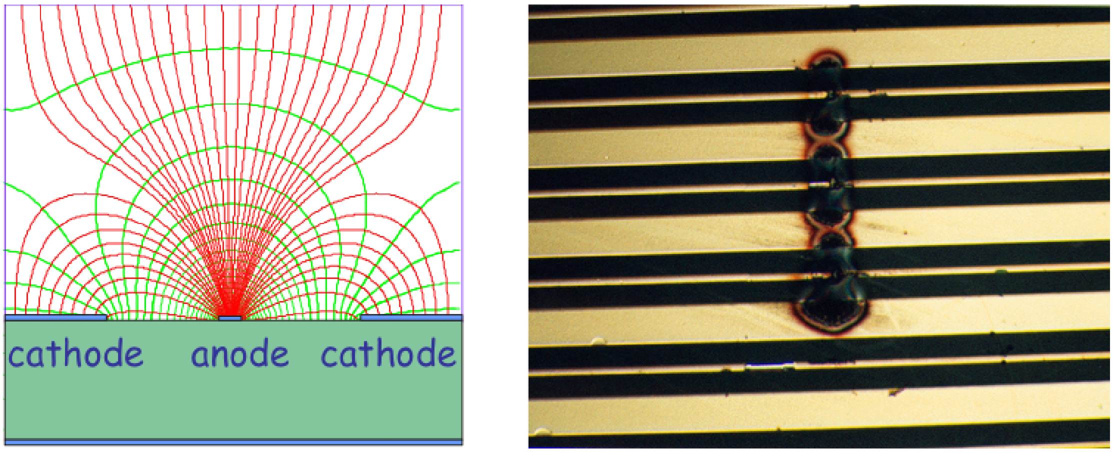

Figure 3.3: Schematic design of MSGCs in left panel and breakdown of strips due to discharges of MSGC in right panel.

ions are collected quickly by nearest cathode strips (within 100 μm), therefore no space charge issue as presented in MWPC. The detector has 10^3 times higher rate capability [55] as shown in Fig. 3.4 and better spatial resolution compared to MWPC. Unfortunately, MSGC suffers terribly from discharge, especially from heavily ionizing particles or high rate particles. The strips can have a breakdown or even have a short circuit because of heavy discharges as shown in Fig. 3.3. Therefore the MSGCs cannot be considered for high rate and long-time operation in particle physics experiment.

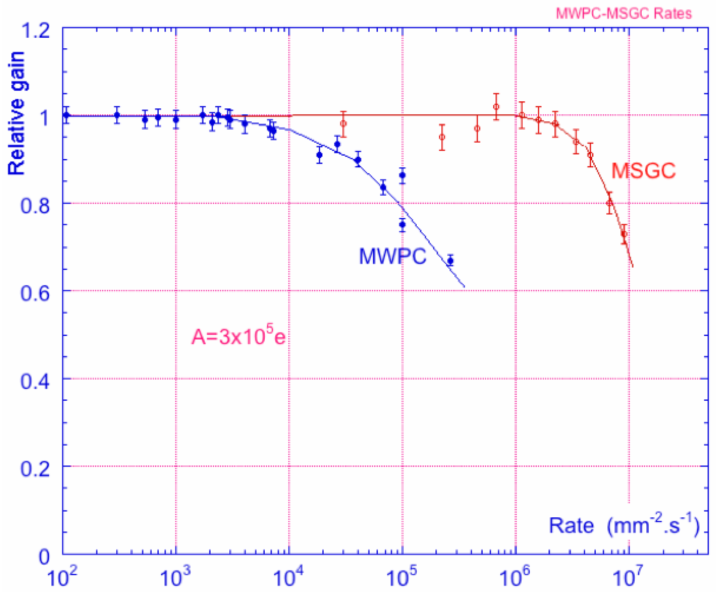

Figure 3.4: Gain as a function of particle rate for both the MWPC and the MSGC.

3.2.2 Micromegas

Micro-Mesh Gaseous Structure or Micromegas is a new kind of MPGD, introduced by Y. Giomataris in 1996 [56]. The principle of Micromegas detector is based on parallel plate geometry with an amplification gap between the micro-mesh and the readout plane. The detector has separate ionization region and amplification region. The gap of few mm between the drift plane and the micro-mesh is functions as ionization region. Whereas, a limited amplification is intended in a narrow gap of 50-100 μm in between the micro-mesh and the anode plane. The schematic design of the detector is shown in Fig. 3.5. A regularly spaced pillars are used in the amplification gap to keep it uniform over the space. A regular array of the spacers can be found in Fig. 3.6. The detector has excellent spatial and time resolution because of its fast charge collection and limited avalanche.

3.3 Development of Gas Electron Multiplier (GEM) detector

Gas Electron Multiplier (GEM) was introduced by F.Sauli in 1997 [57]. GEM is found to be very successful over a wide range of applications in nuclear and particle physics experiments, dark matter and rare event search, medical imaging and homeland security. The advantages of GEM detector like high gain, excellent position resolution, stable operation against discharge, radiation hardness and ion suppression factor make it an optimum choice for trigger and tracking devices

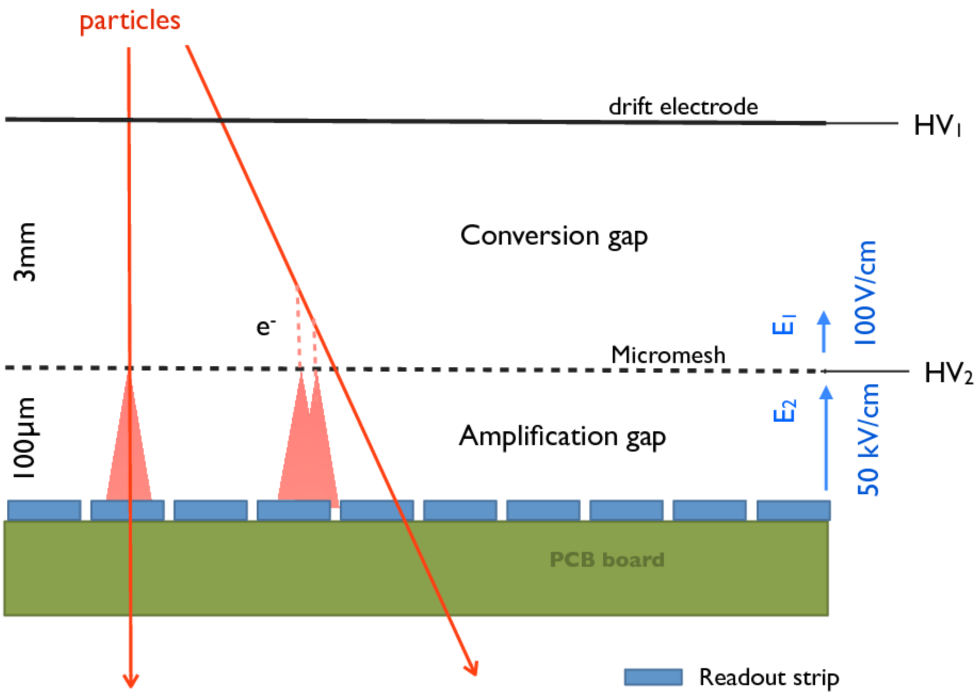

Figure 3.5: Schematic design with operating principle of Micromegas detector.

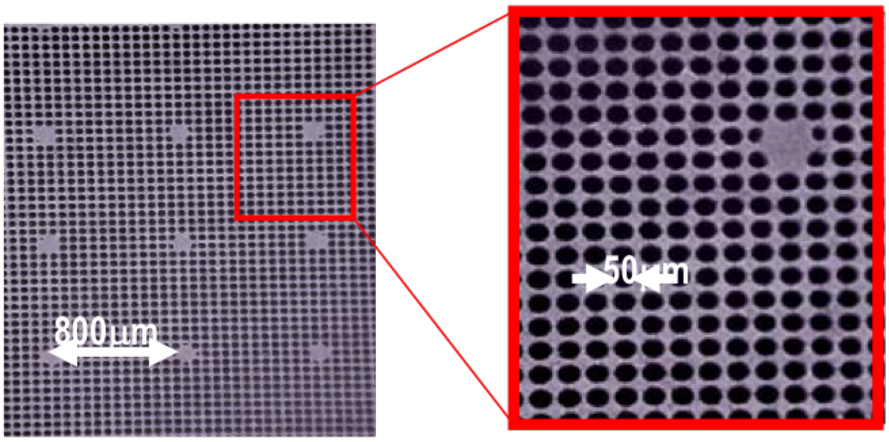

Figure 3.6: Picture of micro-mesh with spacers from top view.

in HEP experiment.

CERN has developed a special photolithographic technique of polyamide etching. Fabrication of GEM foil is based on polyamide etching technology. A GEM is a polyamide foil of thickness 50 μm with metal cladding from both side of thickness 5 μm having a regular array of holes in a hexagonal pattern. The polyamide foil is made of kapton and the metal is copper. The holes are perforated chemically in a bi-conical shape using photolithographic technique. Two photo-masks are placed with alignment from the top and bottom in double mask method. The foil is chemically etched from both sides. The GEM fabrication using double mask technology is shown in Fig. 3.7.

In the double-mask etching method, the main difficulties are in hole alignment, especially for large size (> 50 cm) GEM production. The RD51 collaboration at CERN has developed single-mask

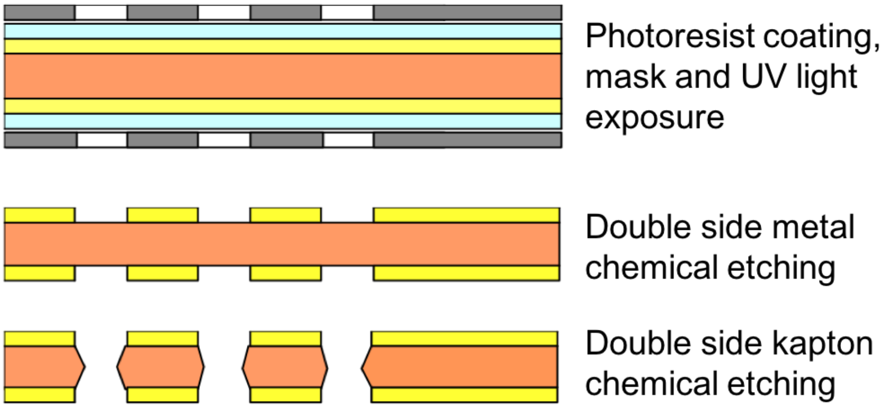

Figure 3.7: GEM foil fabrication steps using double-mask photolithographic technology.

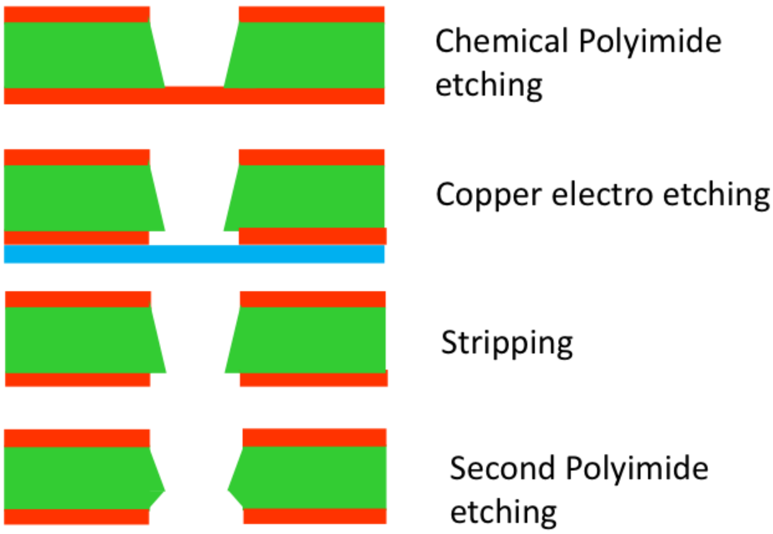

Figure 3.8: GEM foil fabrication steps using single-mask photolithographic technology.

technology [58] recently to make it possible of large scale ($\sim$ m^2) industrial production of GEM foils. In the single-mask method, only one photomask is used from the top of the copper plane. The etched polyamide functions as a mask for the bottom copper etching. The GEM fabrication using single-mask technology is shown in Fig. 3.8. Single mask method has simplified the GEM fabrication constraints, especially for large production area and production cost also decreased by an order of magnitude. The single-mask GEM foils have been used in large area detectors for example in ALICE, CMS and CBM experiments.

The holes of a standard GEM foil are bi-conical with inner and outer diameters of 50 μm and 70 μm, respectively, and the distance between two closest holes, pitch, is 140 μm. A photograph of a standard GEM foil using an electron microscope is shown in Fig. 3.9. GEM detectors with standard foils are used in most of the experiments. However, depending on the specific application

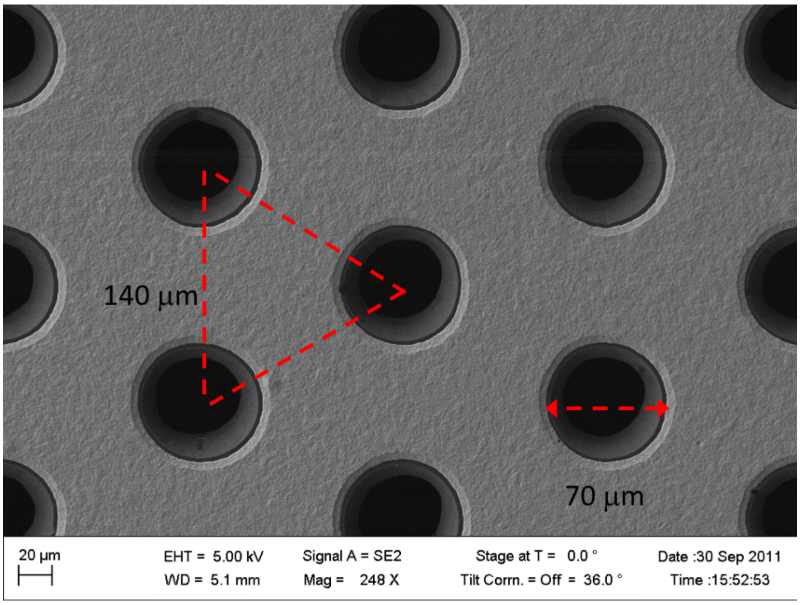

Figure 3.9: Electron microscope photograph of standard GEM foil on right.

the foils with different hole size and pitch are also found useful. In ALICE TPC, GEM foils of standard pitch and large pitch (280 μm) both will be used with a very special configuration to reduce the ion backflow (IBF). The photograph of the GEM foils with both standard pitch and large pitch are shown in Fig. 3.10.

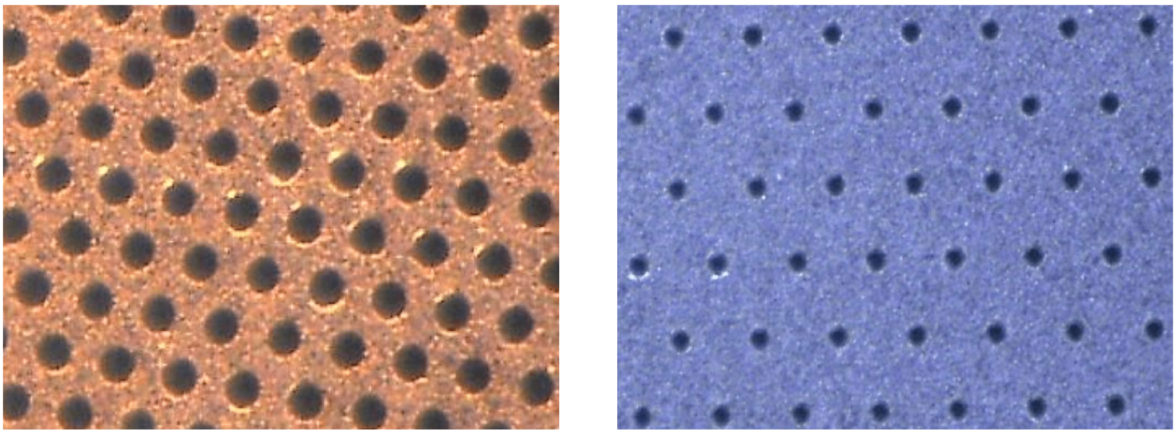

Figure 3.10: Photograph using optical microscope: standard pitch GEM foil in left panel and large pitch GEM foil in right panel with pitch 140 μm and 280 μm, respectively. Note the length scales are different.

A 3D graphical image of a standard GEM hole is shown in the left panel of Fig 3.11. With the application of voltage difference (ΔV_{GEM}) in between two metal surface separated by a tiny insulator (about 50 μm), a strong electric field (typically $50 - 70$ kV/cm) can be generated within the hole. The cross-sectional view of GEM hole with electric field lines is shown in the right panel of Fig. 3.11. When electrons pass through the hole in the presence of such a high electric field, an avalanche will be produced. Avalanche formation inside a GEM hole can be simulated using Garfield [59, 60] software as shown in Fig. 3.12.

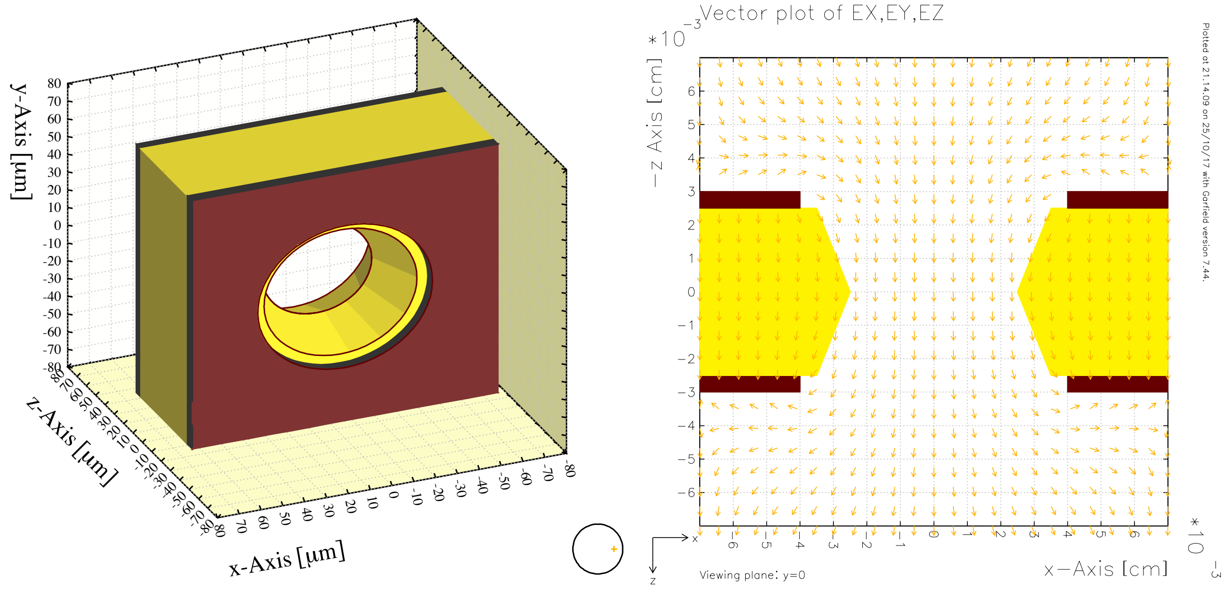

Figure 3.11: 3D view of a GEM hole in left panel. Electric field lines through the GEM holes in the right panel.

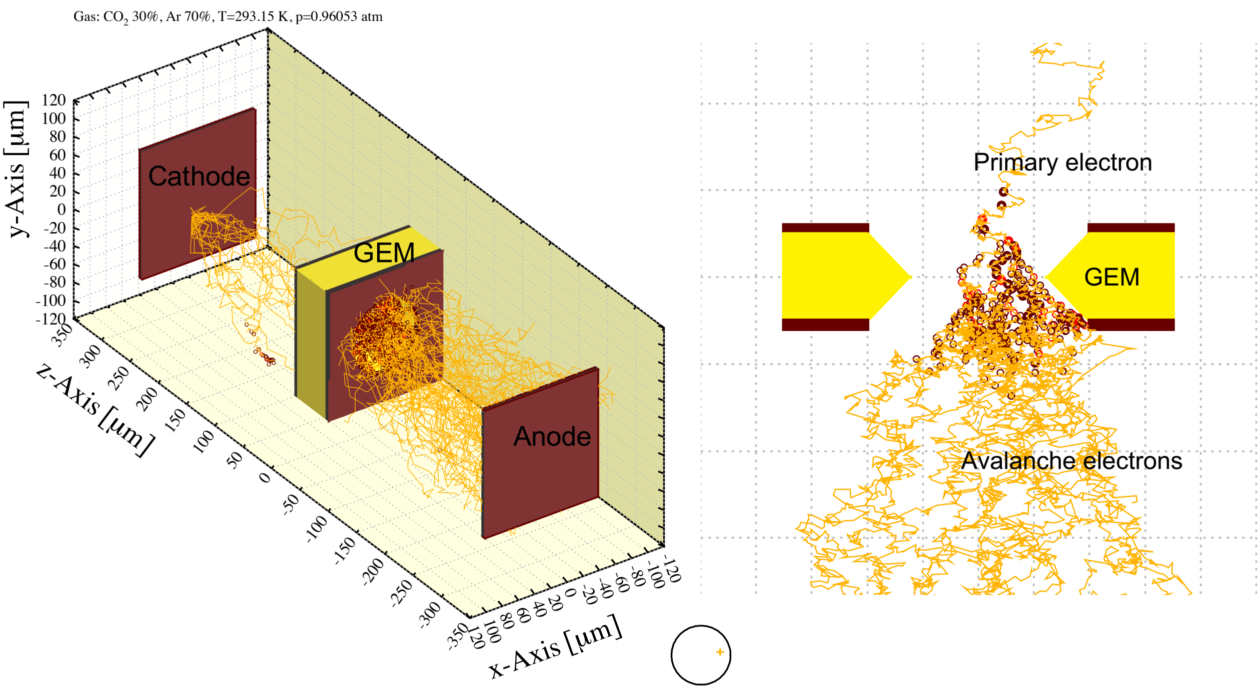

Figure 3.12: Simulation of electron avalanche within the GEM hole using Garfield.

Each hole of the GEM foil acts as an individual proportional counter. In a GEM detector, a stack of GEM foils is placed above a readout plane with a drift plane covered from the top.

The gap between the drift plane and the top GEM is called drift gap. The gap between two GEM is named as transfer gap and the gap between the last GEM and the readout plane is induction gap. The drift gap can be from few mm to few cm depending on the application whereas the transfer and induction gaps are constrained to $1-2$ mm. A schematic diagram of multi-stage avalanche and signal formation in a triple GEM detector is shown in Fig. 3.13. A

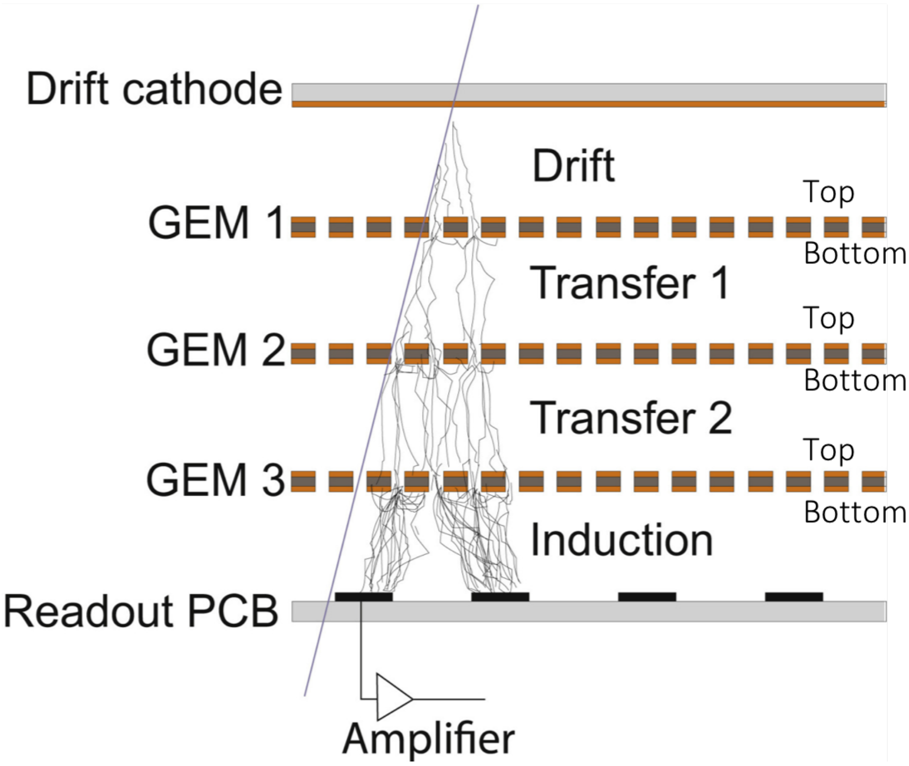

Figure 3.13: Multi-stage avalanche formations and charge collection in a triple GEM detector.

particle passing through the detector produces primary electron-ion pairs. The drift electric field guides the electron-ion pairs produced within the drift gap towards the first GEM where the first avalanche occurs. The secondary electrons produced in avalanche moved towards the second GEM foil. However, a fraction of the secondary electrons are collected on the bottom side of the first GEM foil. After reaching the second GEM, the electrons undergo another avalanche. The same procedure is repeated for the third GEM as shown in the figure after the final amplification the electrons travel through the induction gap and lastly collected on the readout plane. The electrons collected in the readout plane are processed with readout electronics for signal reconstruction and further detailed investigation.

The unique property of the GEM detector is decoupling of the amplification in many stages so that discharge probability and IBF becomes very low. The readout plane is also coupled separately in a GEM detector. Since charge multiplication region and the charge collection region are physically separated the readout electronics are safe from spark/discharge those can happen within the GEM holes.

This chapter can be summarized as gas detector has a broad range of applications in nuclear and particle physics experiments. The MPGD technology brings a new era in particle physics experiment and other applications. The GEM technology and its advantages make it much more useful in large size detector in big experiments compared to other gas detectors.

Chapter 4

Characterization of GEM detectors

Study of the GEM detector is very relevant because of its large scale applications in many world-wide HEP experiments with special importance for the upgrade of the ALICE TPC detector. A triple GEM detector and a quadruple GEM detector assembly and testing have been performed at Variable Energy Cyclotron Centre, Kolkata [61, 62]. This chapter will describe the assembly and test results for characterization both the GEM detectors. A method of spatial uniformity measurement of the GEM detector performances and importance of the electric field, along with a simulation study for the time resolution based on triple GEM detector will also be presented in this chapter.

4.1 Triple GEM detector

In this section, details of characterization of the triple GEM detector are discussed. At first, I will present the detector assembly, then setup details of the test including electronics. Then the test results for spectra using ^{55}Fe source, ^{106}Ru-Rh source and cosmic rays are presented. The method for spatial uniformity of the gain, energy resolution and efficiency measurement is also discussed.

4.1.1 Assembly of the detector

A prototype triple GEM detector of active area 10$\times$10 cm^2 is assembled. The materials of the detector, GEM foils, readout plane, readout connectors, edge frame, O-rings for gas tightness, nylon screws and nuts are procured from CERN, Geneva. Before assembly of the detector, all the different components are visually examined and good electrical connections of the readout plane are confirmed. It is crucial to confirm no electrical short between two copper layers of the GEM foils. The detector is constructed using a stack of three standard single-mask GEM foils followed by a drift (cathode) plane on the top, above the readout plane. The active part of the detector is covered by an edge frame made of G10 material and a kapton window from the top. To ensure the gas tightness of the detector rubber made O-rings are placed on the grooves of the edge frame. The schematic design of the detector assembly is shown in Fig. 4.1. Drift, transfer and the induction gaps are kept as $3-2-2-2$ mm, respectively in the present setup as shown in the figure. The readout plane has gold coated metallic strips in both $x-$ and $y-$direction. A total of 256 parallel strips are grouped into two connectors (128 strips to each) in both $x-$ and $y-$direction. The different components of the detector are shown in Fig. 4.2

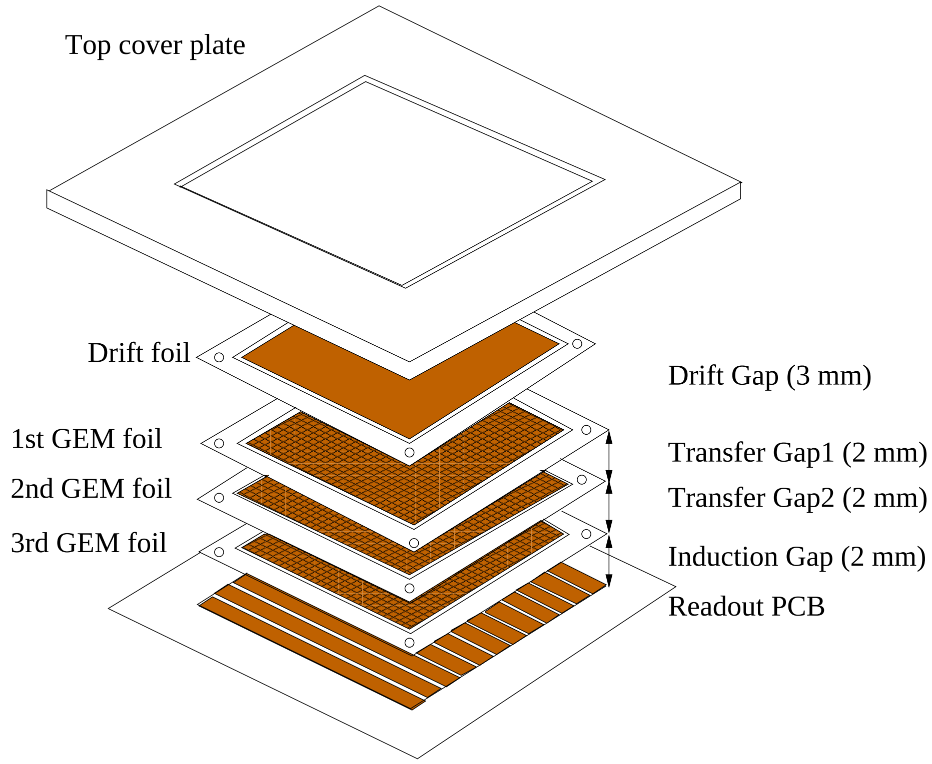

Figure 4.1: Schematic design of the triple GEM detector.

4.1.2 Test setup of the detector

Gas leakage test and gas setup

The first step of testing a gas detector is the gas tightness test. It is essential to ensure perfect tightness; otherwise, gas contaminants degrade the detector performances. In reality, some mi-

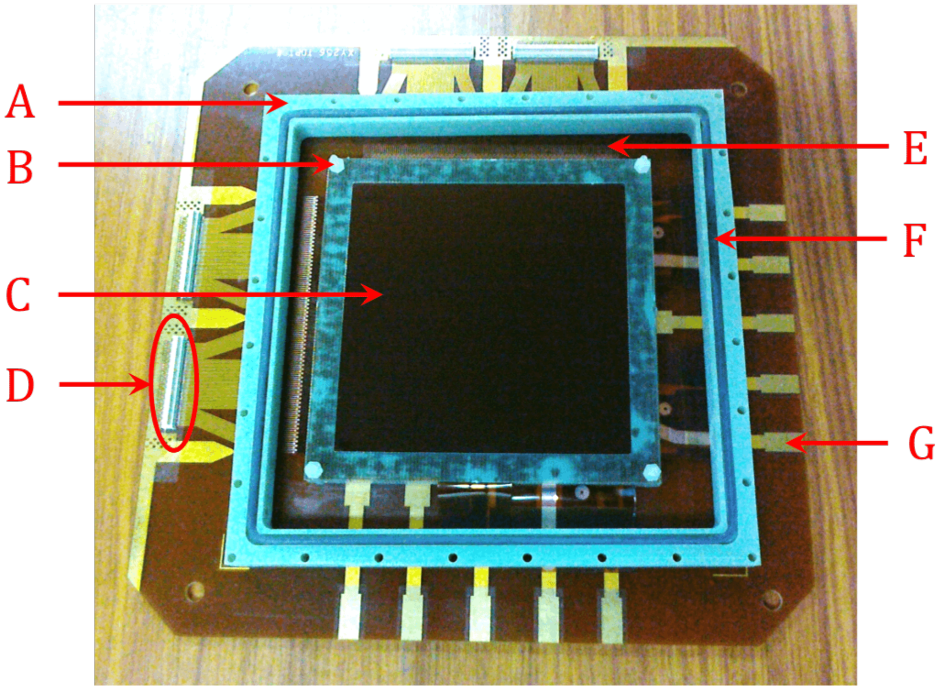

Figure 4.2: Components of the GEM detector: A - Edge frame, B - Nylon screw, C - GEM foil, D - Readout connector, E - readout strips, F - Gas tightness O-ring, G - HV strips for the GEM voltage supply.

croscopic gas leak might be present, but those are not harmful since the detector is operating in positive gas pressure. The detector is put in Ar/CO_2 gas inflow mode. A CO_2 gas leak detector is used for leak detection. No gas leak warning was found from the detector.

All the tests of the detector are performed in Argon and CO_2 gas mixtures in proportions of 90:10 and 70:30. Pre-mixed gas of research grade is used, instead of an online gas mixing unit. The advantages of the pre-mixing gas are to maintain a constant proportion of the gas components without using an active flow controller and ensures uniform performances of the detector because of the gas.

Voltage divider resistor chain

A voltage divider resistor chain is prepared to create the required electric field in the different gaps of the detector with the application of a negative high voltage (HV). The advantage of using a resistor chain is to bias the detector with the application of a single channel of the HV module. Another advantage is to maintain a constant electric field ratio between different gaps of the detector with the variation of the HV. That is helpful in avoiding unwanted electric field effect in the characterization of the detector. difficult to study different proportion of fields or absolute field values.

The disadvantage of this type resistor chain is the difficult to study different proportion of fields or absolute field values effect on the GEM detector. In that case, multiple HV modules are needed to change the electric field independently in the different region of the detector. In Section 4.2.8, independent drift field study with the help of two HV channels and a modified resistor chain are discussed in detail.

The voltage divider resistor chain used in the triple GEM detector is shown in Fig. 4.3. An RC filter circuit is coupled with the resistor chain to eliminate the AC noise from the supply voltage to the detector. The capacitor of low reactance value is used to bypass low-frequency AC noise to ground. Ohmic response of the resistor chain is tested with HV, which can be found in Fig. 4.4.

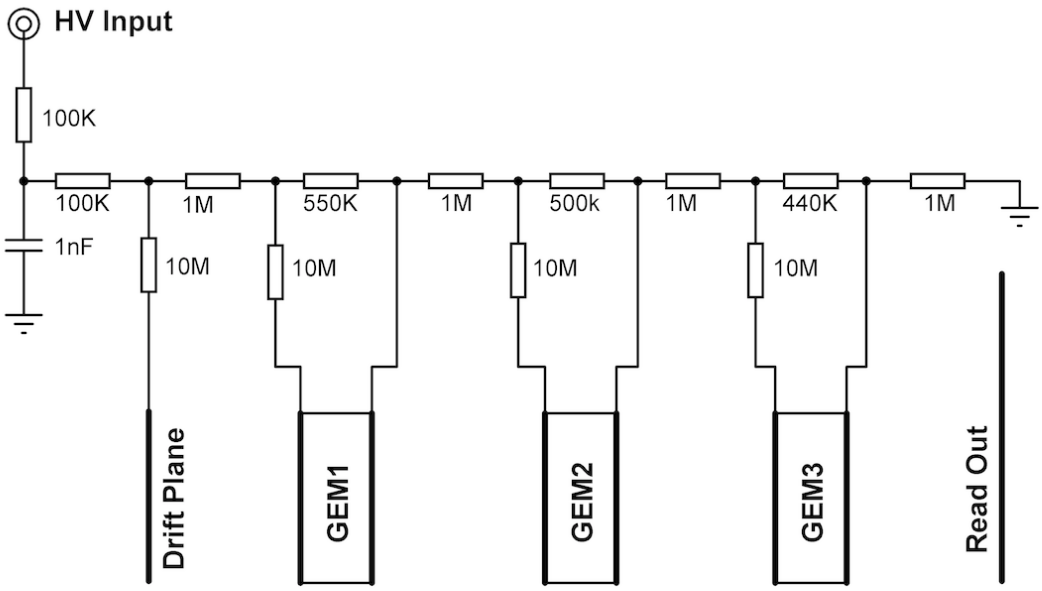

Figure 4.3: Voltage divider resistor chain of the triple GEM detector. The resistors values are in the unit of MΩ.

A linear relation between the HV and the current is observed.

All the electrical components of the detector are metal shielded to reduce noise pickup in the signal. The detector is biased with the application of HV through the voltage divider resistor chain. The electric field produced in different gaps of the detector can be calculated by the formula,

$$E = \frac{I_{div} R}{d}. \tag{4.1}$$

Where I_{div} is the current through the resistor chain monitored in the HV module. R is the resistance in a gap of width d. The block diagram of the electronics setup of the detector is shown in Fig. 4.5.

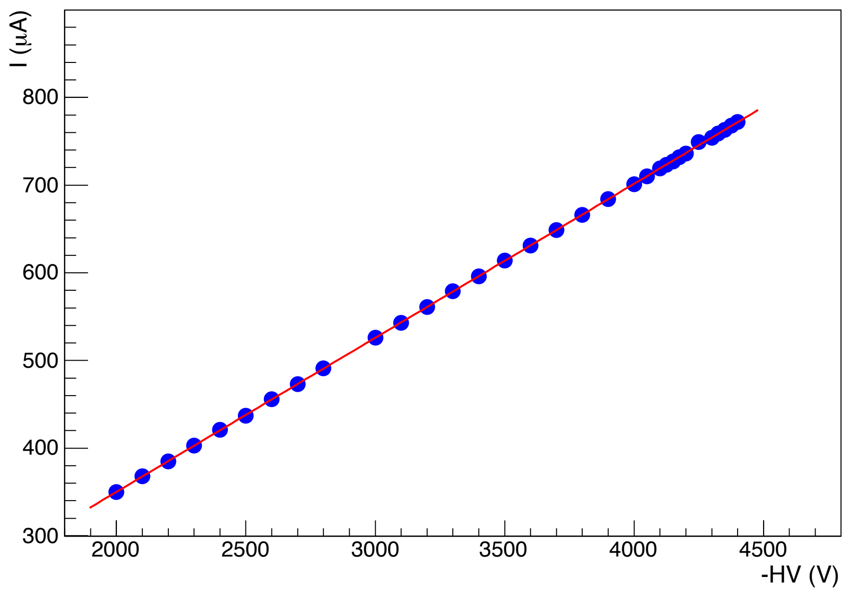

Figure 4.4: Ohomic characteristic of the voltage divider resistor chain. Current *vs.* voltage measurement.

Electronics setup

The GEM detector is powered by an HV module (model CAEN N470) and different electronic modules are used for the raw signal processing of the detector. For the energy spectrum of the detector with X-ray, β-ray and cosmic muon radiations, the electronics setup of which is shown in Fig. 4.5. The radioactive source is placed above the kapton window of the GEM detector. Since

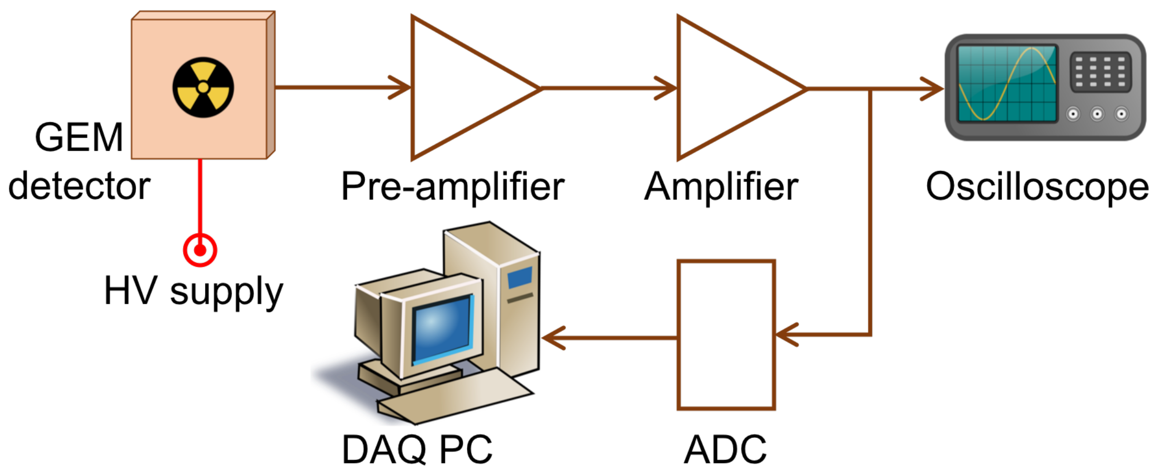

Figure 4.5: Electronics setup for the energy spectrum study of different radiations.

the kapton window and the drift plane are very thin ($\sim$ 50 μm), radiation can pass through it easily. The signal from the readout strips is collected using a sum-up board that goes to a charge sensitive pre-amplifier (ORTEC 142IH). The sensitivity of the pre-amplifier is 1 mV/fC as per specification. The pre-amplifier converts the input charge signal to an output signal of opposite polarity. In this case, the pre-amplifier output has a positive polarity. The output signal is fed to an ORTEC spectroscopy amplifier (ORTEC 572A). The integral time of the signal of the amplifier is set to 1 μs to collect the entire charge of the signal. During the integral time, no pileup event is expected since the radioactive sources are weak. The amplifier gain is set to 7.5-10X. The amplifier has both unipolar and bipolar output pulse option. The output of the amplifier is connected to an oscilloscope for the monitoring purpose of the GEM signal. The unipolar output of the amplifier is connected to an ADC module (model ORTEC ASPEC-927) which converts analog input to a digital signal. The ADC module can operate with both, gate and without gate mode. The gate mode is helpful for the signal detection with trigger whenever it is necessary. The ADC module is set to a 12-bit channel with a resolution of 2.44 mV/ADC channel. The digital output signal of the ADC is connected to a PC. Pre-installed MAESTRO software is used for processing the digital signal and store it up into PC memory for future analysis. No discriminator is used in signal processing. It is found that the ADC module was insensitive for voltage < 40 mV. Therefore, in the energy spectrum, no count is obtained at lower ADC channel.

The electronics modules used in the measurements are calibrated to avoid over/under estimation from the actual results. For the calibration of the pre-amplifier (ORTEC 142IH), a voltage test pulse of sharp rise time (20 ns) with a long decay tail (100 μs) similar to a detector pulse is generated from a pulse generator (BNC BH-1) to provide the test input of the pre-amplifier. In the test input of the pre-amplifier had a capacitor of value 1 pF which converts a voltage signal to a charge signal. Changing of the output voltages with respect to variation of the input voltage is observed in the oscilloscope for making calibration of the instrument. For the calibration of the ORTEC spectroscopy amplifier (ORTEC 572A), the input is fed by a voltage test pulse, similar to detector signal, from the pulse generator. The gain of the amplifier was set to any value between 2 to 15 using the coarse and fine gain adjustment with an internal jumper set to 0.1. The variation of the amplifier output with the input voltage is observed using a oscilloscope for the calibration. The calibration plot of the spectroscopy amplifier is shown in Fig. 4.6 for different set of gains of the amplifier module. The 12-bit ADC module (model ORTEC ASPEC-927) used in the measurement can accepts only unipolar pulses of positive polarity of 10 V maximum. A test pulse of variable voltage amplitude with large width (20 us) is generated using a function generator (Agilent 8111A) and fed to the ADC input. With variation the voltage of the input pulse between the range 0-10 V the output is filled in a range of 12-bit ADC. From this calibration procedure, ADC module was found perfectly linear throughout the range of the operations (12-bit).

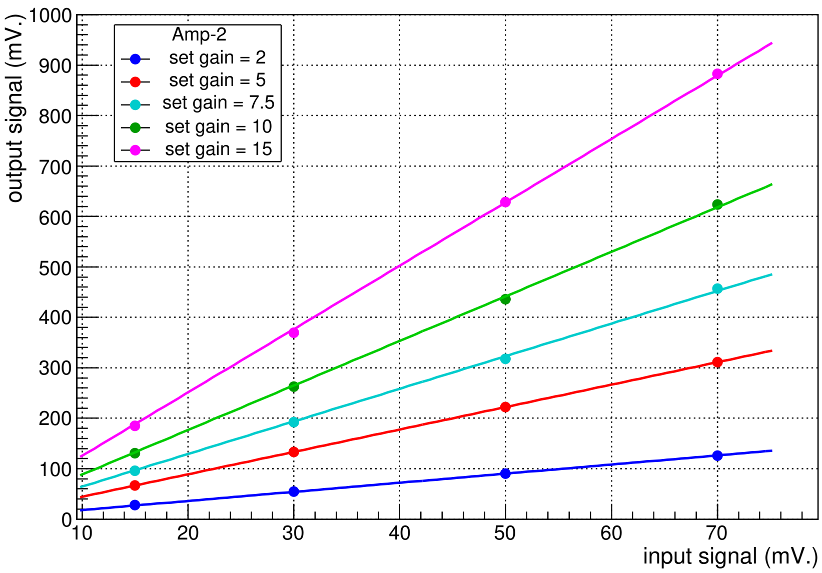

Figure 4.6: Gain calibration plot of the spectroscopic amplifier (ORTEC 572A).

4.1.3 Energy spectrum study

With the application of necessary HV and electronics setup for signal reading, the energy spectrum of different type of radiations is studied with the triple GEM detector. The measurements are performed with both the Ar/CO_2 gas mixtures. The test results of the individual sources are discussed below.

^{55}Fe X-ray spectrum

A ^{55}Fe radioactive source of low activity is used for the X-ray spectrum study. ^{55}Fe decays via electron capture process to ^{55}Mn with a half-life ($t_{1/2}$) 2.73 years. The vacancy produced in the K-shell by electron capture is filled by an electron from a higher atomic shell. In this process, K_α X-ray of energy 5.89 keV and K_β X-ray of energy 6.49 keV are emitted. K_α X-ray of energy 5.89 keV is most abundant radiation of the ^{55}Fe source. The relative intensity of these two X-rays are 25:3.3. These two energy peaks can be separated easily using a Silicon detector as shown in Fig. 4.7. However, it is difficult to distinguish those two energy peaks in a gaseous detector because of its energy resolution limitation.

The obtained energy spectrum of the ^{55}Fe X-ray source of the triple GEM detector in Ar/CO_2 70:30 gas is shown in Fig. 4.8. The huge counts at very low ADC channels are associated with the noise followed by a small peak and the 5.89 keV energy peak. The small peak at lower ADC channel in the figure is called Argon escape peak. K-shell binding energy of Ar is 3.206 keV. K-shell release a characteristic X-ray of energy ($\sim$ 3 keV) equal to the energy difference between

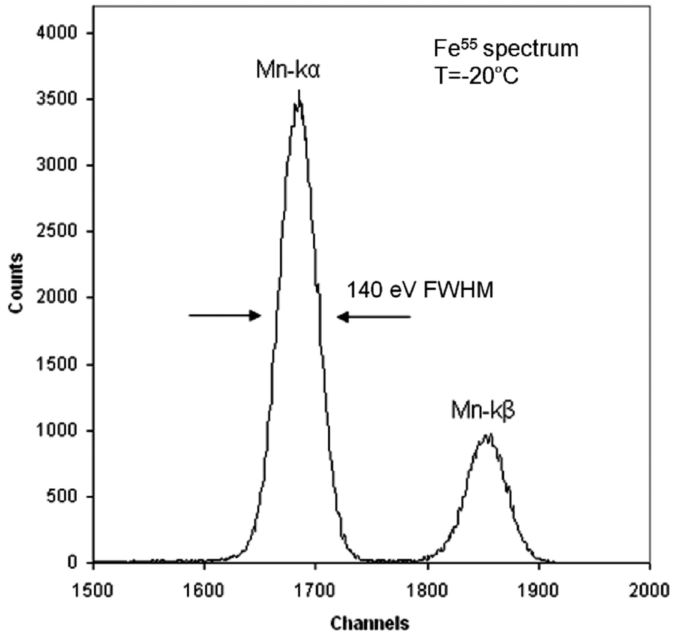

Figure 4.7: The energy spectrum of ^{55}Fe X-ray source of a Silicon detector. Both K_α and K_β peaks are clearly separated [63].

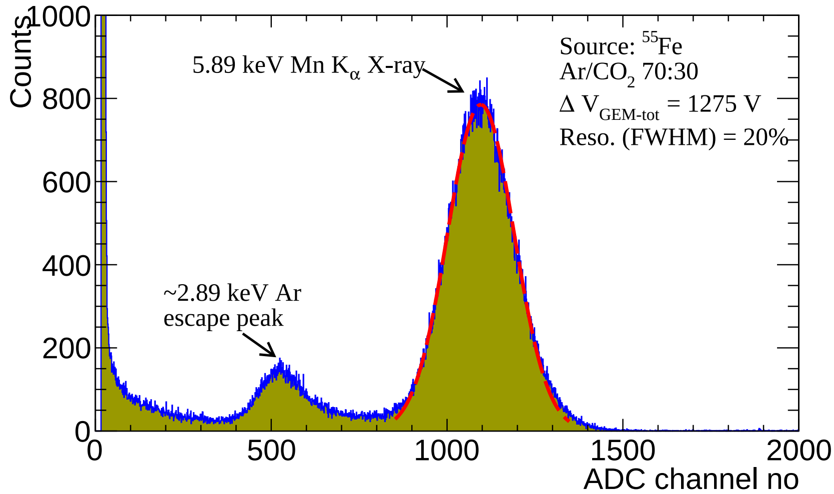

Figure 4.8: The obtained energy spectrum of the ^{55}Fe X-ray source of the triple GEM detector. The peak at ∼2.89 keV correspond to the Ar escape peak. The main photopeak correspond to the K_α X-ray of energy 5.89 keV.

K-shell and higher shells (L- or M-shell). The released X-ray has a lower absorption cross-section as shown in Fig. 4.9. Therefore it has a finite probability of escape from the detector volume and the small peak corresponding to the deposited energy of ∼ 2.89 keV is called Ar escape peak. The main photopeak corresponding to the full energy deposition of K_α 5.89 keV is also mentioned in the figure. The main photopeak is fitted with a Gaussian function. The mean ADC of the Gaussian fit is used in the gain calculation of the detector. The detail about gain calculation is discussed later in this section.

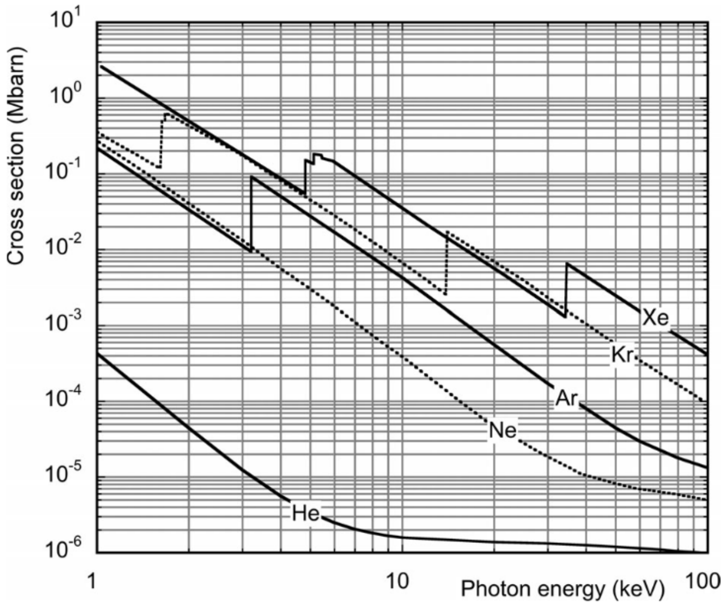

Figure 4.9: Photon total cross-section for noble gases.

Cosmic muon and ^{106}Ru-Rh β-spectrum

Cosmic rays are high-energy particles, mostly protons (90%), helium nuclei (9%) and electrons (1%) that comes from the outer space. These tiny particles undergo through nuclear interaction with the atmospheric nuclei. Most of the secondaries are pions (charged and neutral). Charged pions decay into muons via weak interactions, such as –

$$\pi^+ \rightarrow \mu^+ \nu_\mu$$

$$\pi^- \rightarrow \mu^- \bar{\nu}_\mu$$

and the $\mu^\pm$ can travel a long distance through the atmosphere since they are less interactive. The mean energy of the muons at the sea level is $\approx$ 4 GeV [64]. Therefore, these relativistic muons can pass through us easily.

The obtained energy spectrum of the cosmic muon is shown in Fig. 4.10. A gated ADC spectrum is taken otherwise the MPV at a lower ADC channel can be overlapped with the noise. The relativistic muons are showing a continuum energy spectrum. The spectrum follows the Landau distribution nicely.

Ruthenium-106 (^{106}Ru) is a β^- emitter with a half-life ($t_{1/2}$) of 371.5 days. It decays to Rhodium-106 (^{106}Rh) which is also a β^- emitter with a half-life of 30.1 seconds only. This means that they have the same activity in the sample. The β^- endpoint energy of ^{106}Ru-Rh source is 3.54 MeV. The electron release from the source is in the relativistic regime and hence they show

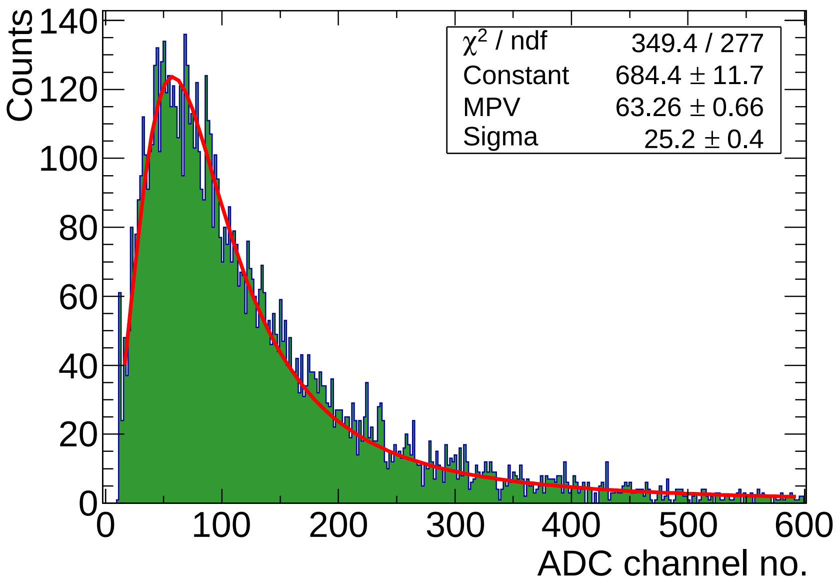

Figure 4.10: Cosmic muon spectrum of the triple GEM detector at 4400 V. The spectrum with Ar/CO_2 70:30 gas.

a MIP like distribution in the spectrum. The gated spectrum of the ^{106}Ru-Rh source is shown in Fig. 4.11. A Landau distribution with a long tail, characteristic of the MIP, is observed in the energy spectrum.

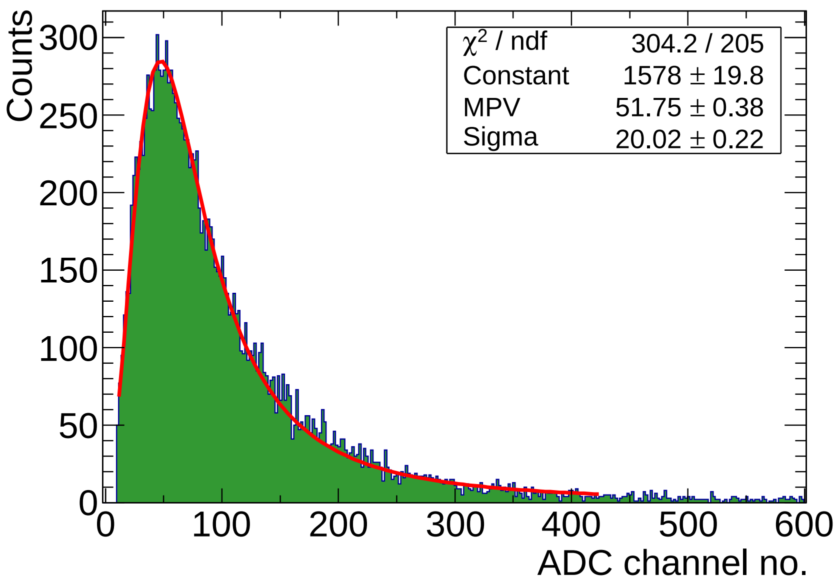

Figure 4.11: ^{106}Ru-Rh β^--spectrum of the triple GEM detector at 4400 V. The spectrum with Ar/CO_2 70:30 gas.

4.1.4 Efficiency measurement

The efficiency measurement of a detector is essential for determining the range of the operating voltage of the detector. The efficiency measurement setup of the triple GEM detector is shown in Fig. 4.12. In this setup, three scintillator detectors are used to provide external three-fold (3F) coincidence trigger. Two small scintillators are put on the top of the GEM detector. The

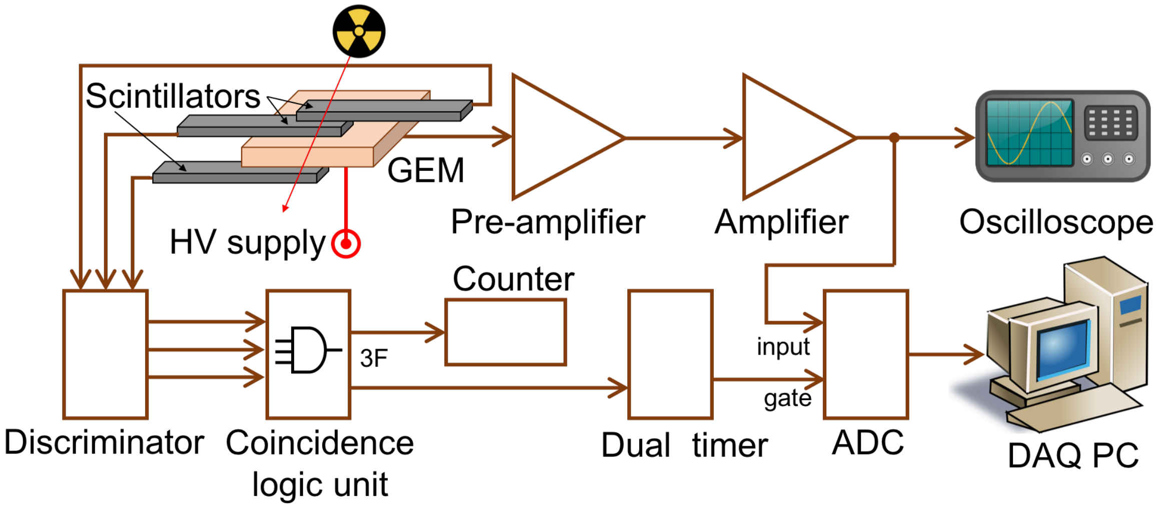

Figure 4.12: Electronics setup for the efficiency measurement of the triple GEM detector.

big scintillator is placed below the GEM. The three scintillators have a common overlap area for triggering a real event when a particle passes through it. The laboratory setup picture of the efficiency measurement is shown in Fig. 4.13. The dimension of the small scintillators are ($2.5\times2.5\times0.2$ cm^3) and the big scintillator is ($7\times9\times1$ cm^3). The using of the small scintillators have an advantage. It increases the 3F trigger rates significantly of the ^{106}Ru-Rh source because of low material budget. A 4-channels HV module (model CAEN N470) is used for biasing the scintillator PMTs. The output signals of the scintillators are connected to a discriminator module. The discrimination level is set to 25-30 mV to avoid noise trigger which may produce a false coincidence. The output of the discriminator is a NIM logic signal which is fed to a quad coincidence logic unit to have a 3F coincidence signal. One of the 3F outputs is connected to a counter where the other provides a gate for the ADC. The detector signal is processed in a similar way as described in Fig. 4.5. The detector signal with the 3F gate is processed in ADC and saved.

Cosmic muon and ^{106}Ru-Rh are both used as a trigger source for the efficiency measurement of the detector. Cosmic muons can pass the scintillators and the detector material easily. However, the penetration power of the ^{106}Ru-Rh β^- particle is tested for the detector material as the particles have energy of few MeV only. For this test, a three-fold (3F) scintillators setup is used with both side copper laminate FR4 sheets placed in between as shown in Fig. 4.14. It is found

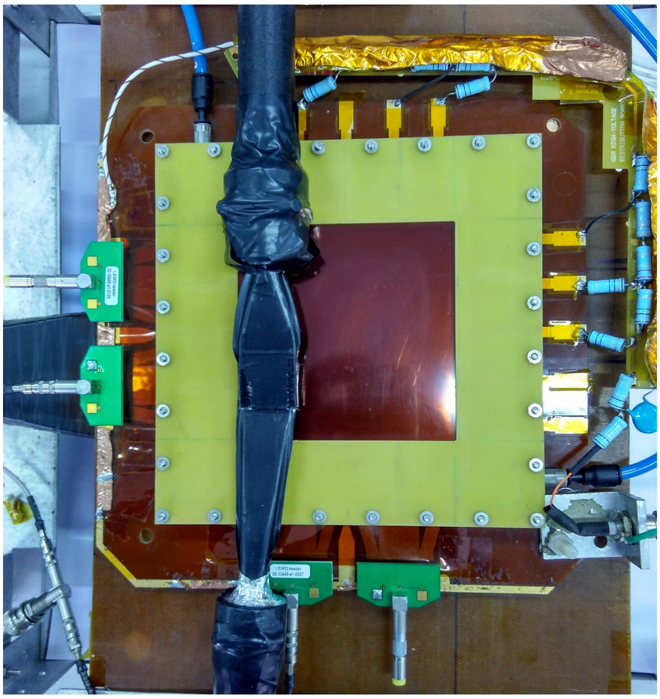

Figure 4.13: Photograph of the efficiency measurement setup of the triple GEM detector.

that a good fraction of the β^- particles can pass the material which is indeed thicker than the material budget of the GEM detector.

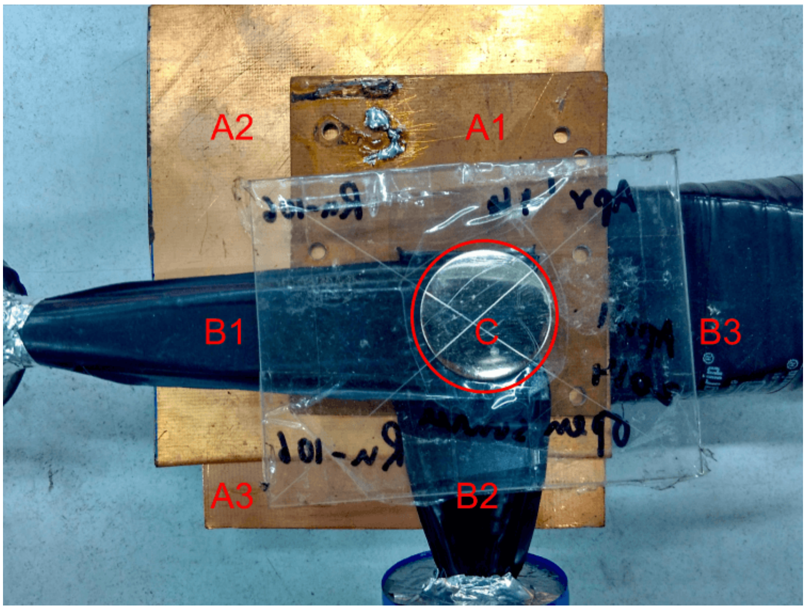

Figure 4.14: Photograph of the β^- penetration test using ^{106}Ru-Rh source. A1, A2, A3 are both side copper laminated FR4 sheets, B1 and B2 are two small scintillators on top. B3 is big scintillator at bottom.

The efficiency of the detector is defined as,

$$\mathcal{E} = \frac{no.\ of\ hits\ in\ the\ detector\ with\ 3F\ gate}{no.\ of\ 3F\ counts}. \tag{4.2}$$

The efficiency ($\mathcal{E}$) as a function of the applied voltage of the detector by using cosmic muons and ^{106}Ru-Rh source is shown in Fig. 4.15. Ar/CO_2 70:30 gas mixture is used in this measurement.

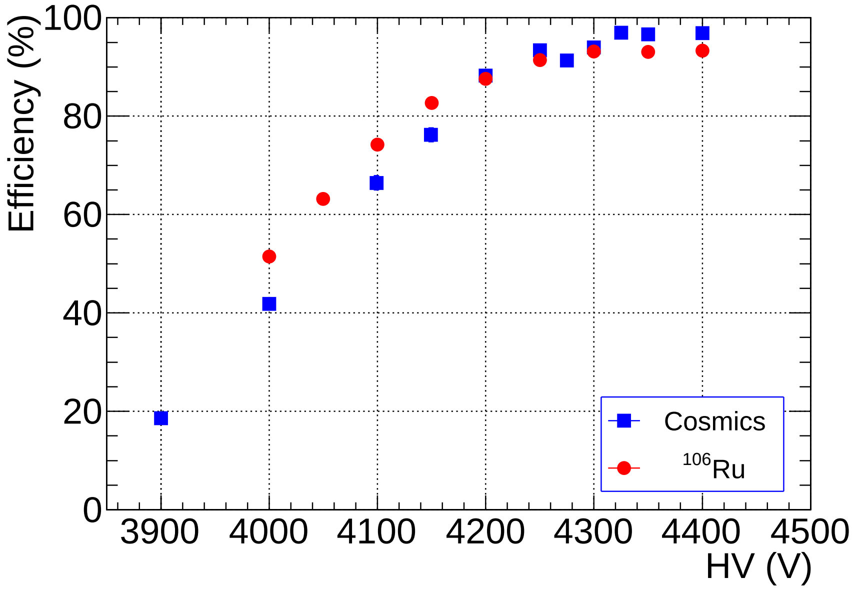

Figure 4.15: Efficiency measurement of the triple GEM detector as a function of applied HV. The efficiency is obtained by using cosmic muon and ^{106}Ru-Rh source with Ar/CO_2 70:30 gas. Statistical errors are small and within the symbol size.

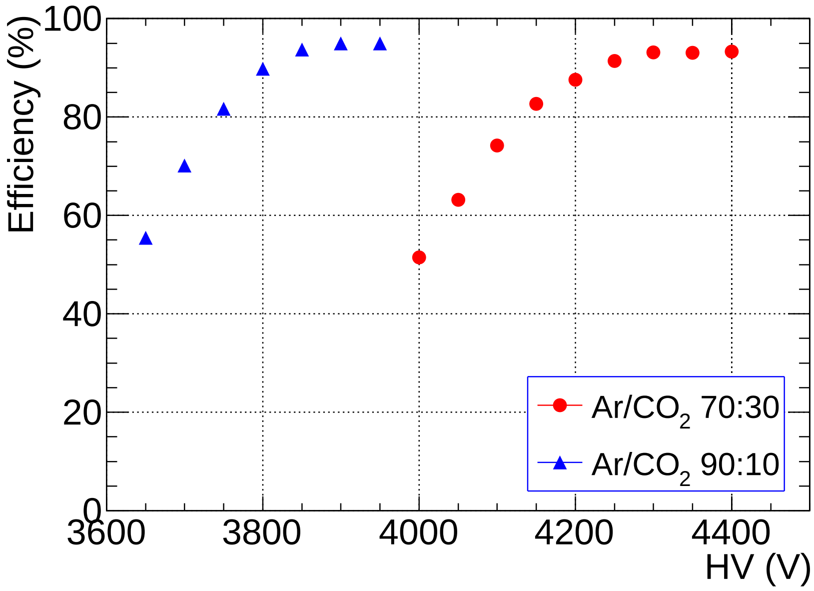

Figure 4.16: Efficiency measurement of the triple GEM detector as a function of applied HV. The efficiency is obtained by using ^{106}Ru-Rh source with Ar/CO_2 90:10 and 70:30 gas. Statistical errors are small and within the symbol size.

The efficiency ($\mathcal{E}$) results for the cosmic muons and ^{106}Ru-Rh are very similar and falls one above other. With increasing the HV from 3900 V the efficiency started gradually increasing from 20%.

Beyond the voltage 4300 V the efficiency reaches to a plateau of value $\sim$ 95% as found in the figure. It is noted that the efficiency measurement using ^{106}Ru-Rh is a much faster and convenient method than it could be thought of.

Efficiency measurements of the triple GEM detector with Ar/CO_2 90:10 and 70:30 gas mixtures are shown in Fig. 4.16. In this measurement, ^{106}Ru-Rh β^--source has been used to provide the trigger. Similar efficiency plateau is achieved in Ar/CO_2 90:10 gas at a much lower voltage compared to 70:30 gas mixture. The reason is understood quite well because of a significant fraction of quencher (CO_2), which is used in 70:30 mixture. The operating voltage of the detector is found to be 3850 V and 4300 V for the 90:10 and 70:30 gases, respectively, from the figure.

4.1.5 Gain and energy resolution measurement

Effective gain

Gain is one of the important parameters to measure in any gas detector. The effective gain (G_{eff}) of a GEM detector is calculated using the following formula,

$$G_{eff} = \frac{M.K_{ele}}{N_p.q_e}, \tag{4.3}$$

where M is the ADC mean value of the Gaussian fit of the main peak of 5.9 keV X-ray as shown in Fig. 4.8. K_{ele} is the electronic gain factor from the pre-amplifier and the amplifier. N_p is the number of total primary electrons produced by full energy deposition of 5.9 keV X-ray in the drift volume and q_e is the charge of the electron.

The total number of primary electrons produced in a gas mixture can be calculated by the weighted contribution of the component gases in the mixture as given in the following formula,

$$N_p = E_\gamma \left(\frac{\%(Ar)}{W_{Ar}} + \frac{\%(CO_2)}{W_{CO_2}} \right), \tag{4.4}$$

where E_γ is the photon energy and W_i is the average energy per ion pair of the specific gas component. The value of N_p is calculated to be 220 and 212 for Ar/CO_2 90:10 and 70:30 gas mixtures, respectively.

The energy spectrum of ^{55}Fe is taken with different HV setting for the gain scan. Figure 4.17 shows the effective gain as a function of HV for both the gas mixtures [65, 66]. The gain increases with HV and it has an exponential trend as expected for the gas detector. For the 90:10 gas mixture, the gain curve is shifted downside in HV with respect to the 70:30 gas mixture. This makes sure that the detector has a higher effective gain in Ar/CO_2 90:10 gas w.r.t. to 70:30 gas for the same applied voltage. The gain of the detector is proportional to the Townsend coefficient of the respective operating gas. Townsend coefficient for different gas mixtures as a function of the electric field is shown in Fig. 6.4, which imply that Ar/CO_2 90:10 has a higher value of Townsend coefficient compared to 70:30 gas mixture.

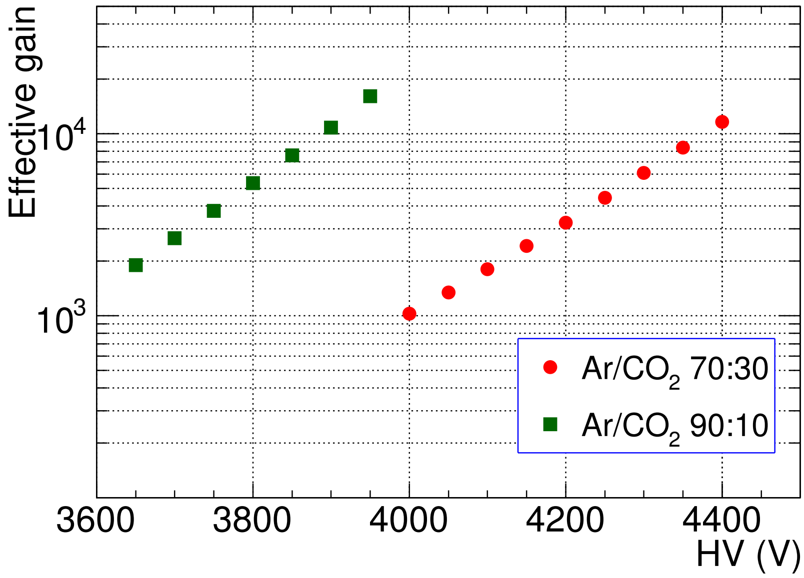

Figure 4.17: Effective gain of the triple GEM detector as a function of HV for both Ar/CO_2 90:10 and 70:30 gas mixtures. Statistical errors are small and within the symbol size.

Energy resolution

The energy resolution of a detector is the measurement of its ability to resolve two energy peaks that are close together. The resolution of the energy spectrum depends on the factors, statistical fluctuation of the primary electrons, avalanche fluctuations and electronic noise (ENC). The energy resolution expression can be written as

$$\left(\frac{\sigma_E}{E}\right)^2 = \left(\frac{\sigma_N}{N}\right)^2_{primary\,ele.} + \left(\frac{\sigma_M}{M}\right)^2_{avalache} + f(ENC). \tag{4.5}$$

The resolution expression can be written in terms of the average number of primary electrons N, Fano factor F, and average gain $\bar{A}$ as,

$$\left(\frac{\sigma_E}{E}\right) = \sqrt{\frac{1}{N}\left(F + \frac{1}{\bar{A}}\right)} + f(ENC). \tag{4.6}$$

The energy spectrum of the photon is always Gaussian in nature. The Full width at half maximum (FWHM) and the standard deviation of the Gaussian distribution follow the relation, $\Delta E_{FWHM} = 2.35\sigma_E$. The statistical limit of energy resolution for the 5.9 keV photon is $\left(\frac{\sigma_E}{E}\right)_{FWHM} = 2.35\left(\frac{\sigma_E}{E}\right) \approx 7 - 8\%$ for the typical value of $F = 0.2$ in gas. The measured value is always three times higher than the theoretical limit of the energy resolution.

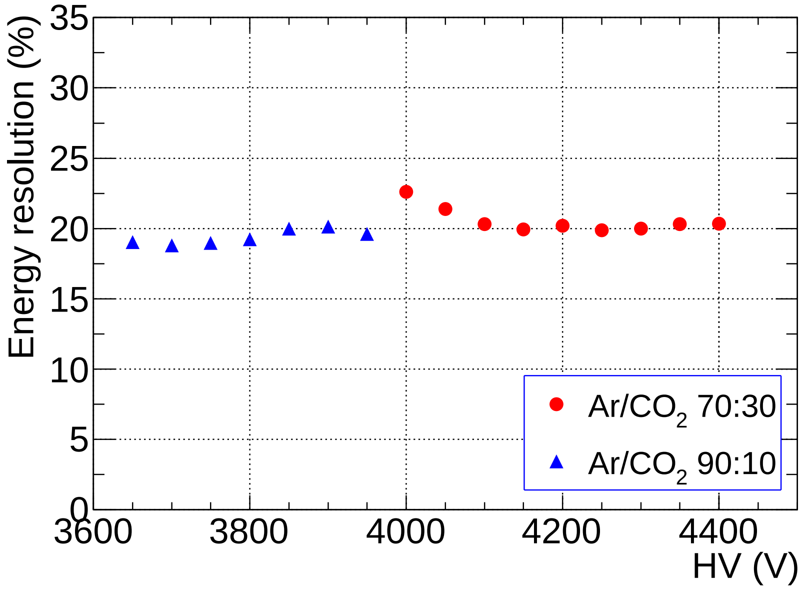

Figure 4.18: Energy resolution of the triple GEM detector as a function of HV for both Ar/CO_2 90:10 and 70:30 gas mixtures. Statistical errors are small and within the symbol size.

The energy resolution (in terms of FWHM) as a function of HV is shown in Fig. 4.18. The resolution is measured for both the Ar/CO_2 gas mixtures. From the figure, it can be observed that energy resolution has a bit lower value ($\sim$ 18%) for 90:10 gas w.r.t. resolution ($\sim$ 20%) of 70:30 gas [61, 66]. It can also be observed that the resolution has little variation over the range of the voltage studied. The energy resolution has a little dependency on gas mixtures as explained in Equation 4.6.

4.1.6 Time resolution measurement

The time resolution of the GEM detector is the determination of the spread in signal formation time for different events. The signal formation time and hence the time resolution depends on several factors. The positional variation of electron-ion pair creation, drift and diffusion of the electrons, gain of the detector, pressure and temperature, electronic noise (ENC) and responses of the electronics play roles in time resolution of a detector. A model simulation of the time resolution are performed to estimate the time resolution limit. The details about the simulation study are described in Section 4.3. In this section, the electronics setup and the obtained results of the time resolution measurement are described for the triple GEM detector.

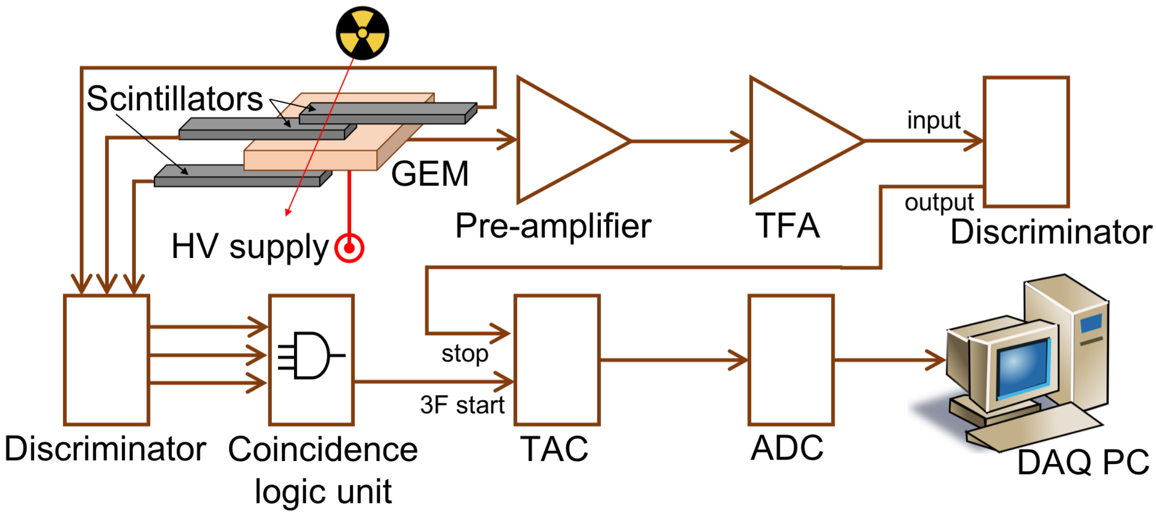

Figure 4.19: Schematic of the detector setup for the time resolution measurement.

The schematic of the detector setup for the time resolution measurement is shown in Fig. 4.19. ^{106}Ru-Rh is used as a trigger source in this measurement. The triple GEM detector signal is passed through the timing output of ORTEC 142IH pre-amplifier to a fast amplifier. Timing filter amplifier (TFA, model ORTEC-454) is used with integral and differential time both are set to 50 ns which is optimized to have a sharp clear signal with minimum noise fluctuation. The detector signal is amplified by 20X in the TFA module. The 3F scintillators signal provides *start* to the ORTEC 567 Time to Amplitude Converter (TAC) module. The amplified detector signal after discriminator is used as the *stop* signal for the TAC. The output amplitude of the TAC is proportional to the time difference between the *start* and the *stop* signals. The TAC output is fed to an ADC which provides the time spectrum.

The time resolution measurement of the triple GEM detector is performed at a gain $\sim 10^4$. The obtained time spectrum of the detector at 4450 V using Ar/CO_2 70:30 gas is shown in Fig. 4.20. Time resolution (σ_t) as a function of HV is shown in Fig. 4.21. From the figure, it can be noticed that the resolution is almost constant over the voltages. The obtained time resolution of the detector is $\approx$ 10 ns. The error bar in the figure is corresponding to the statistical uncertainty.

In the measured time resolution (σ_M) from the spectrum has the contribution from both the detector under study and scintillators used for a 3F trigger. The corrected time resolution (σ_t) can be expressed as,

$$\sigma_t = \sqrt{\sigma_M^2 - (\sigma_{SC1}^2 + \sigma_{SC2}^2 + \sigma_{SC3}^2)}, \tag{4.7}$$

where σ_{SCi} are the time resolution of the scintillator detectors. In this measurement, time correction due to the scintillators are considered.

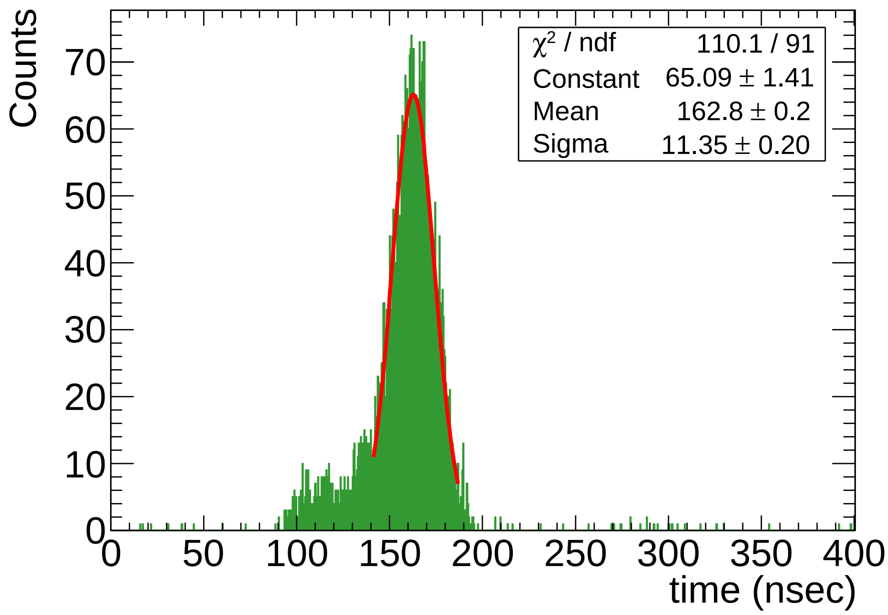

Figure 4.20: Time spectrum of the triple GEM detector at 4450 V in Ar/CO_2 70:30 gas.

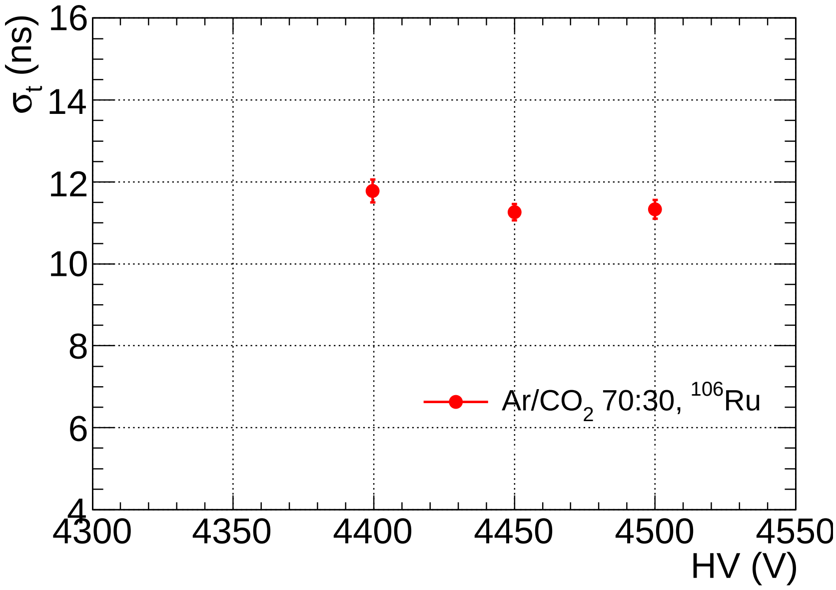

Figure 4.21: Time resolution of the triple GEM detector as a function of applied HV. Statistical errors are small and within the symbol size.

4.1.7 Spatial uniformity study

New generation high energy physics experiments require large area detectors. The overall performance of these detectors depends on the uniformity of the gain, energy resolution and efficiency over the entire active region. Several factors, like variations of the hole diameter due to inaccurate etching, nonuniform gas flow, variations in gas gap due to imperfect stretching, spatial variation of the electric field, etc., can lead to nonuniform performances over the area of the detector [67, 68]. Thus it is found essential to measure the variation of gain, energy resolution and efficiency over the entire surface area.

In this work, a method has been developed to scan for the gain, energy resolution and efficiency over the whole area of the detector. The results obtained across the different position of the detector have been compared. In this test setup, a thick ($\sim$ 3 mm) G10 plates with the hole matrices 4×4 and 7×7, divide zones of equal area, are cover from the top of the detector as shown in Fig. 4.22. The ^{55}Fe source was placed on the center of each zone so that the X-ray pass through the holes. The HV is set to 4400 V to obtain energy spectrum for all the specified zone. The signal from both the $x-$ and $y-$sum-up connectors, associated to each zones, are added together for the energy spectrum measurement. But, the zones associated to the middle row and middle column of the 7×7 matrices, as highlighted in the lower panel of Fig. 4.22, have charge spread in all four readout connectors. To keep the test condition same, therefore, those zones are excluded from the measurement.

The yield distribution of the effective gain for different zones is shown in Fig. 4.23 for 36 zones of study in 7×7 matrices. The mean value of the obtained gain is 10030 at 4400 V. The gains of the individual zone are normalized by dividing the mean gain. A 2D normalized gain map of the detector is shown in Fig. 4.24 [61, 69]. The relative gain values of each zone are mentioned in the figure. Both the gain plots in Fig. 4.24 have a similar trend of the obtained results. The RMS variations of the gain are found to be 6.6% and 8.8%, respectively, for 16 zones and 36 zones of study. The results of the gain uniformity have a good agreement with the literature [70]. The energy resolutions for all the 36 zones are calculated form the obtained ^{55}Fe energy spectra. The distribution of energy resolutions for 36 zones are shown in Fig. 4.25. The mean value of the energy resolution (FWHM) is 21% with an RMS of 6.7%.

The uniformity of the efficiency is also measured by dividing the active area of the detector into 16 zones of equal area. A three-fold scintillator setup is used separately for all the different zones under study. The ^{106}Ru-Rh source is used as a trigger source for efficiency measurements. The efficiency distribution for all the 16 zones are shown in Fig. 4.26. From the figure we found that efficiency is quite uniform over the area, having an RMS of 1.9%.

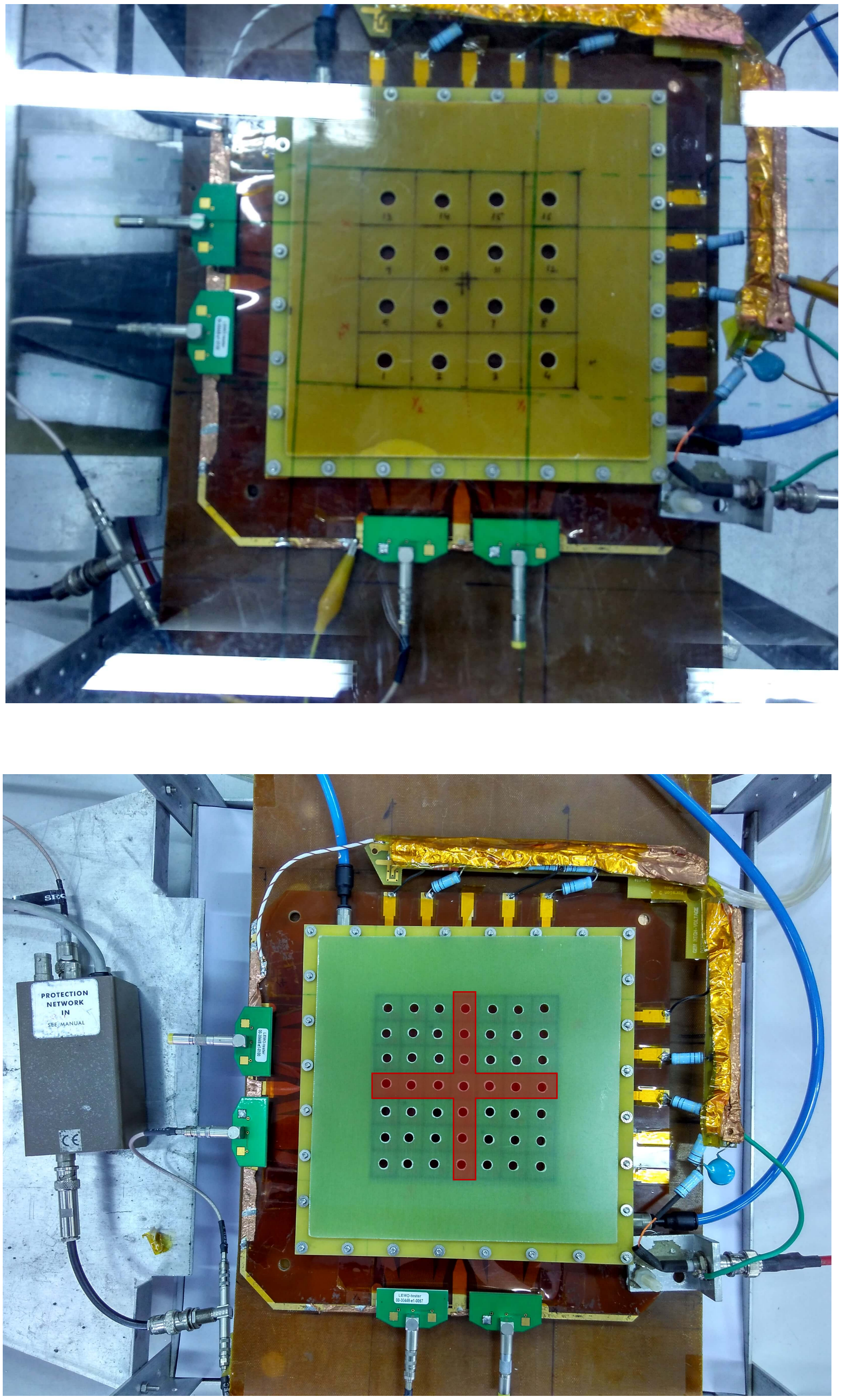

Figure 4.22: Photograph of the detector setup for uniformity measurement of the triple GEM detector. The upper panel is for 4×4 hole matrices and the lower panel is for 7×7 hole matrices.

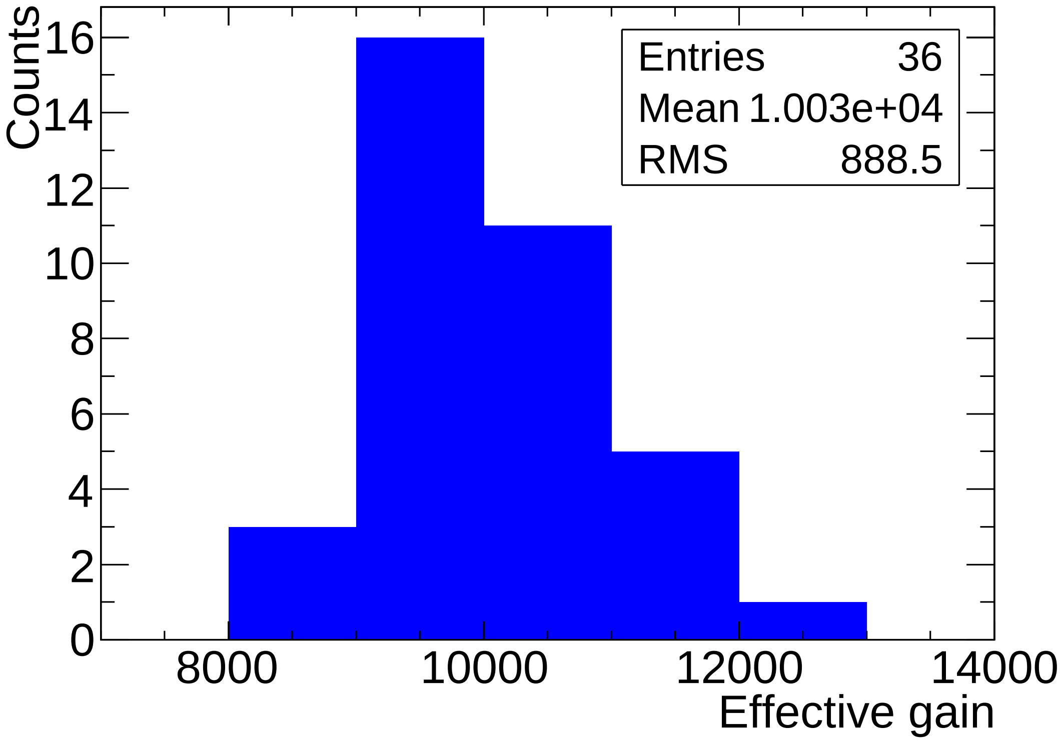

Figure 4.23: Distribution of the effective gain for 36 zones of the triple GEM detector at an applied voltage of 4400 V for 7×7 matrices.

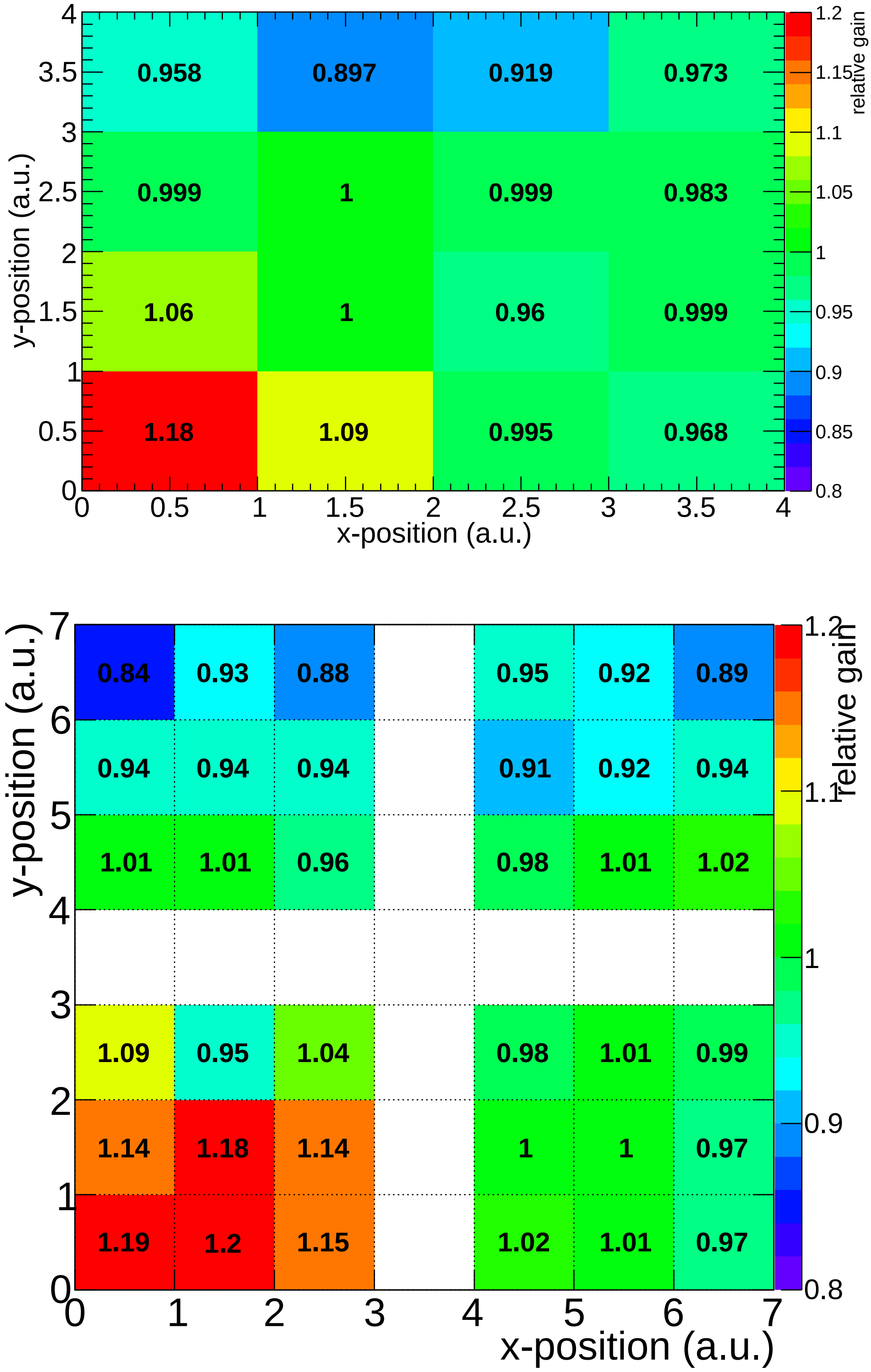

Figure 4.24: 2D mapping of the relative gain distribution. The upper panel is for the 4×4 matrices and lower panel is for 7×7 matrices.

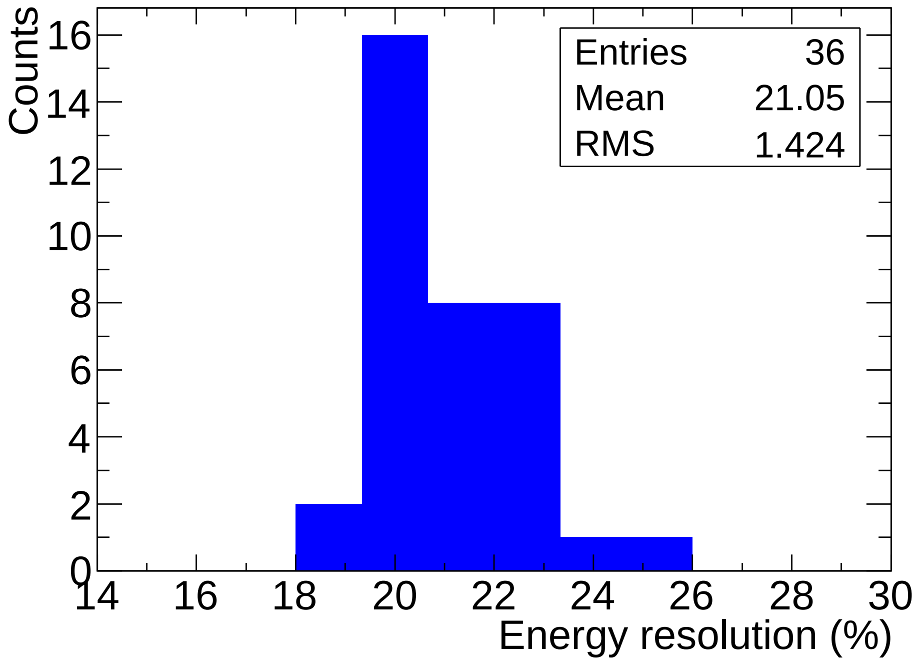

Figure 4.25: Distribution of energy resolution for the 36 zones of the GEM detector at an applied voltage of 4400 V for 7×7 matrices.

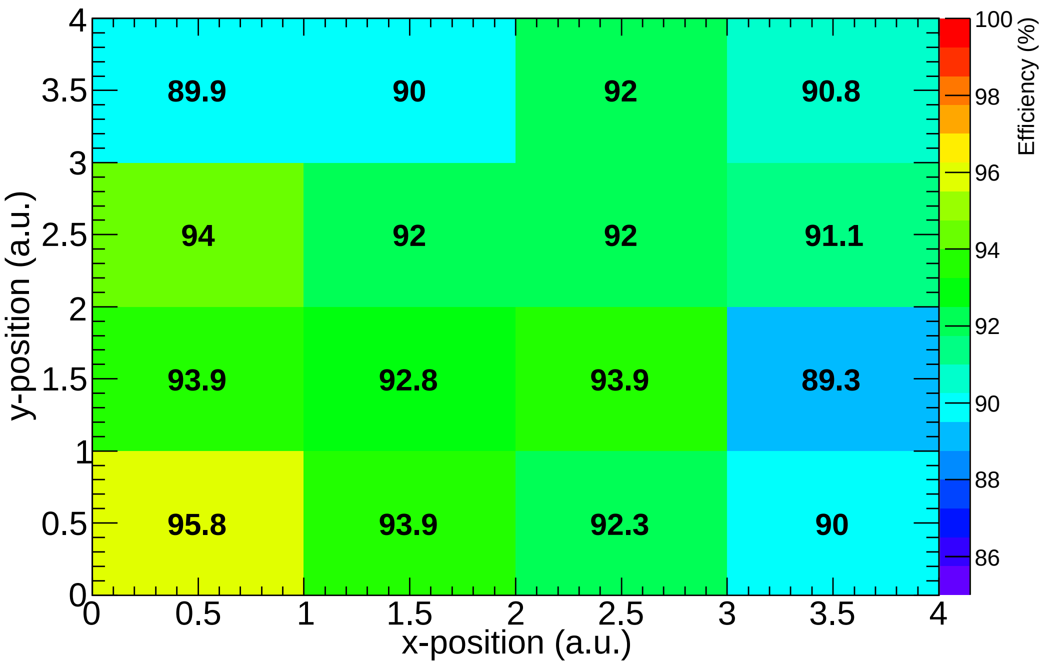

Figure 4.26: 2D mapping of the efficiency measurement of the triple GEM detector for the 16 zones at an applied voltage of 4400 V for 4×4 matrices.

4.2 Quadruple GEM detector

Most of the studies found in the literature are based on the single GEM, double GEM and triple GEM detectors. Over these years, most experiments have almost settled for triple GEM configuration for the detection of charged particles, as can be seen in both existing and planned future experiments [71–79]. Investigation of the detectors with more than 3 GEM foils has been focused towards specific applications, like photon detection using CsI cathode [80], making a gaseous photomultiplier tube by Breskin's group [81–83], in RICH application [84]. Quadruple GEM has very low ion backflow (IBF) $\sim 1-5\%$ in comparison to triple GEM detector [81, 85–87]. The other notable feature of quadruple GEM is low discharge probability. Triple GEM detector has three orders of higher discharge probability compared to the quadruple GEM configuration as reported in [88]. Quadruple GEM makes a very viable choice for large drift volume detectors (like the TPC) because of its low IBF and low discharges. The ALICE TPC is settled on with quad-GEM with very specific configurations for its upgrade [45].

The characteristic study of a quadruple GEM detector is performed keeping in mind ALICE TPC upgrade. The detector assembly and many test procedures are similar to the triple GEM detector. The characteristic study results are presented and also compared with triple GEM [62].

4.2.1 Quality assurance of the GEM foils

All the components and the GEM foils are procured from CERN, Geneva. Before starting the detector assembly, the quality assurance (QA) tests of all the GEM foils are performed. In the QA test procedure, all the GEM foils are kept in a Nitrogen environment so that the foils are dry enough (RH $< 10\%$). A Keithley 6487 pico-ammeter is used for the low current measurement of the GEM foils. The leakage current measurement setup of the GEM foils is shown in Fig.4.27. A voltage difference of 500 V is applied across the individual foils using the Keithley current meter which also provides DC voltages. The leakage current of the GEM foils is measured for 30 min. Keithley current meter is interfaced with the PC using RS-232 bus for remote monitoring. The LabVIEW software was used for successfully data capturing. The leakage current measurement of the GEM foils is shown in Fig. 4.28. All the GEM foils having leakage current below 500 pA without any major spark during the test are considered for the assembling the chamber.

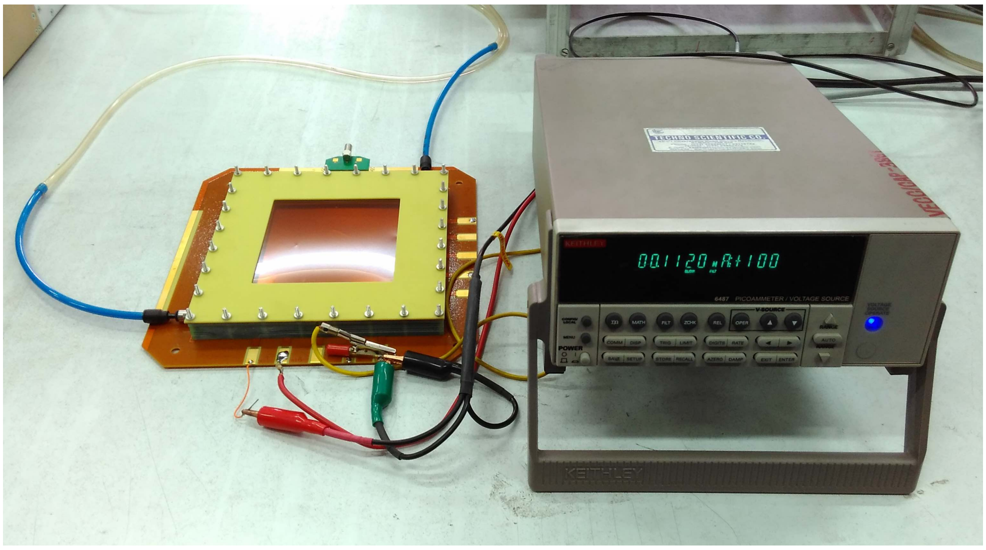

Figure 4.27: Photograph of the leakage current measurement setup of the GEM foils.

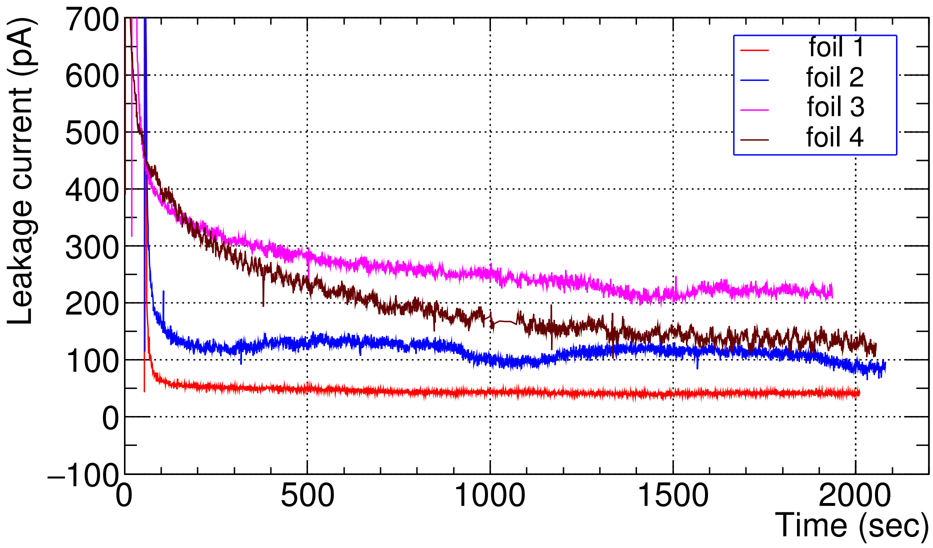

Figure 4.28: Leakage current measurement of the GEM foils.

4.2.2 Assembly of the quadruple GEM detector

A quadruple GEM detector has been assembled at Variable Energy Cyclotron Centre, Kolkata, India, in our lab., for its detailed characteristics study. All the four good GEM foils, those passed the QA test, with active area 10×10 cm^2 are used in the quadruple GEM detector assembly. The different components and the gas gaps of the detector are shown in schematic Fig. 4.29. In the assembly procedure, a stack of four GEM foils is placed on top of the readout PCB. The arrangement is covered by a drift plane (cathode) from the top as shown in the figure. The readout plane (anode) of the area of 10×10 cm^2 is divided by 120 pads of equal area for picking up the signals. The drift plane, GEM foils, and the readout plane are covered by an edge frame made of G10 material and a kapton window from the top for gas tightness. The gas tightness of the

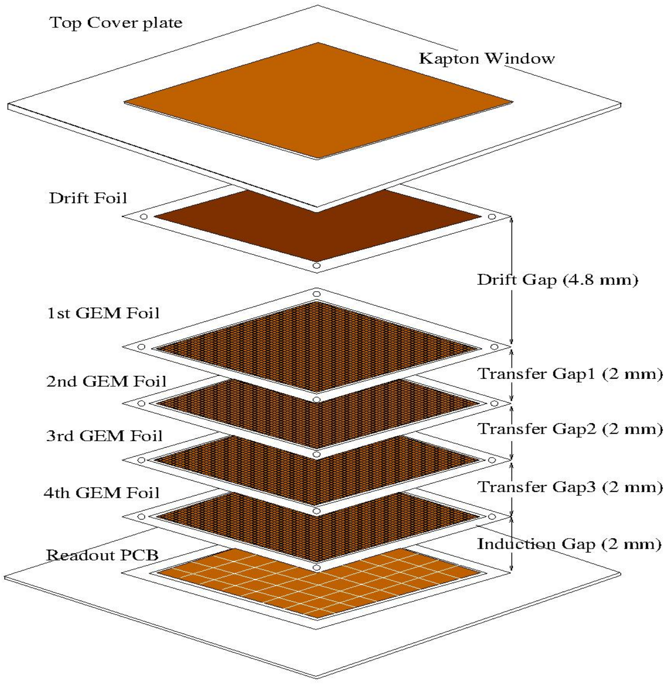

Figure 4.29: Schematic design of the quadruple GEM detector. Different components and the gas gaps are as labeled in the figure.

detector is confirmed by the leakage test using a CO_2 gas detector. The drift gap, transfer gaps and the induction gap of the detector are $4.8-2-2-2-2$ mm, respectively, as shown in Fig. 4.29. The present detector configuration is different from the one employed in the ALICE TPC [45], where the middle two GEM foils have large pitch (LP, 280 μm) and the other two GEM foils have small pitch (SP, 140 μm) and also in other multi-GEM detectors reported in literature [81, 84].

Voltage divider resistor chain

The voltages across the GEM foils and within the gaps are applied using a voltage divider resistor chain. Equal voltages (ΔV, $250-300$ V) to all four GEMs with a moderate electric field ($1-3$ kV/cm) in the gaps are applied in the *standard* field configuration. The voltage divider resistor chain for the *standard* field setting is shown in Fig. 4.30. In this setting, only a single HV channel is required for biasing the detector. The test results will be presented with mentioning total GEM voltage $\Delta V_{GEM-tot}$ or single GEM voltage $\Delta V_{GEM-single}$ instead of the applied HV. It is found that the comparison of the triple GEM and quadruple GEM detectors can be understood better as GEM voltages. All the measurements are performed with the application of Ar/CO_2 90:10 and 70:30 gas mixtures.

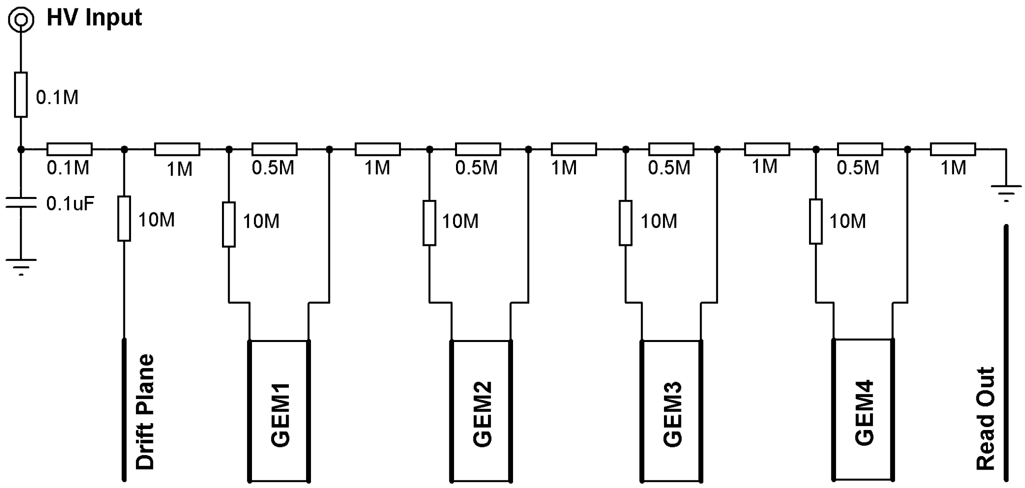

Figure 4.30: The voltage divider resistor chain used for *standard* field configuration of the quadruple GEM detector. The resistors' value in unit of MΩ.

4.2.3 Energy spectrum study

Test of the detector is begun with the energy spectrum measurement of the X-ray and β^--source. The measurement setup is same as mentioned in Fig. 4.5 in Section 4.1.2. The energy spectrum of ^{55}Fe X-ray source as shown in Fig. 4.31 is obtained at $\Delta V_{GEM-tot}$ = 1275 V in Ar/CO_2 70:30 gas mixture. The main photopeak of 5.89 keV and Ar escape peak can be distinguished clearly. An asymmetric broadening of the peak is observed, which could arise because of detector effects.

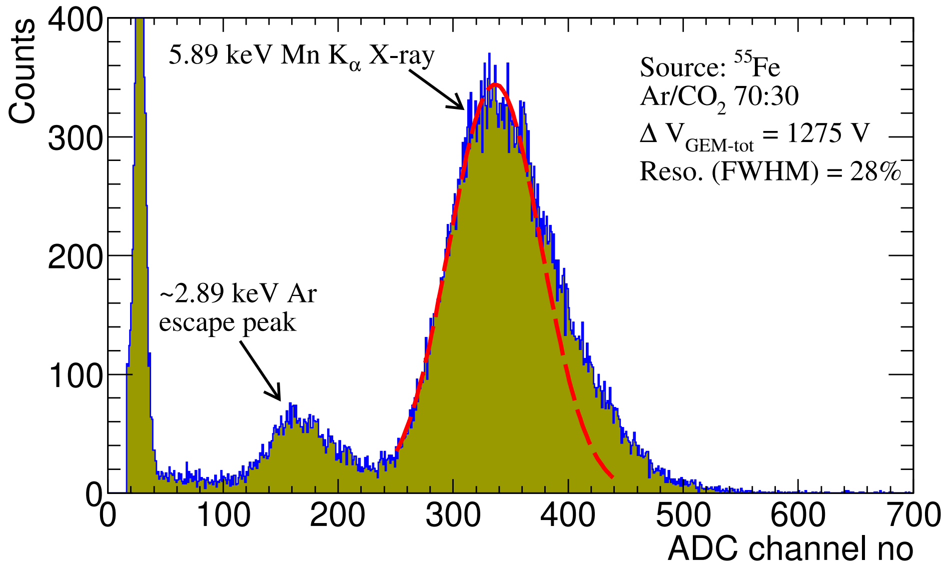

Figure 4.31: The energy spectrum of the quadruple GEM detector using the ^{55}Fe X-ray source. The peak at 2.89 keV corresponds to the Ar escape peak. The main photo peak corresponds to the X-ray of energy 5.89 keV.

The next set of tests have been performed by exposing the GEM detector to ^{106}Ru-Rh β^--

source. The resulting spectrum, taken at $\Delta V_{GEM-tot} = 1316$ V in Ar/CO_2 70:30 gas mixture, is shown in Fig. 4.32. The β^{-}-spectrum is continuous with a long tail extending to a large ADC value.

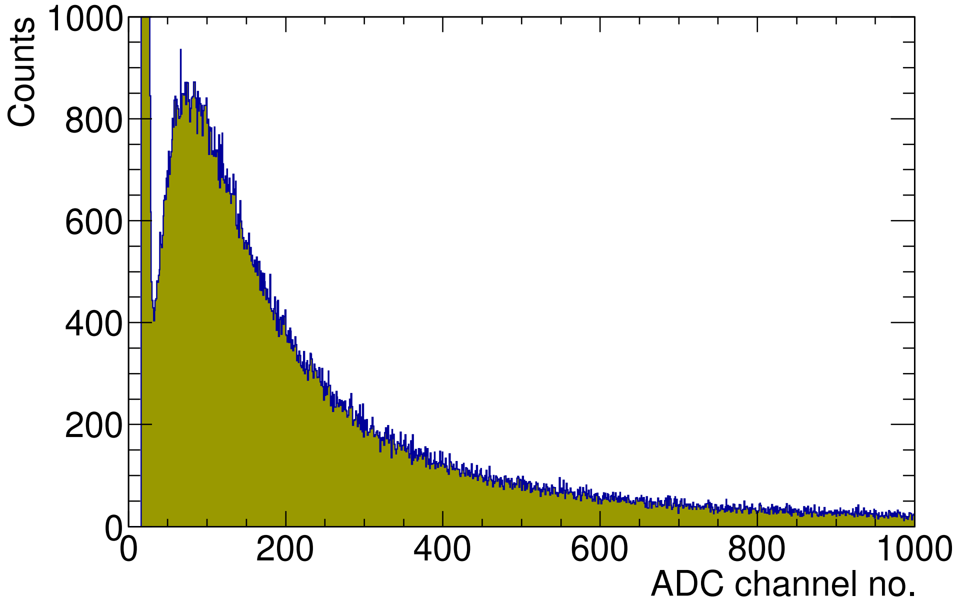

Figure 4.32: The energy spectrum of the quadruple GEM detector using ^{106}Ru-Rh β^{-}-source at $\Delta V_{GEM-tot} = 1316$ V with Ar/CO_2 70:30 gas.

4.2.4 Efficiency measurement

The electronics setup of the efficiency measurement of the quadruple GEM detector is similar to the triple GEM efficiency setup as shown in Fig. 4.12 in Section 4.1.4. The efficiency setup picture of the quadruple GEM detector is shown in Fig. 4.33. ^{106}Ru-Rh is used as a trigger source in efficiency measurement. The variation of the efficiency as a function of applied GEM voltage ($\Delta V_{GEM-tot}$) for both the gas mixtures are shown in Fig. 4.34. Efficiency increases with GEM voltage and then reach a plateau. The plateau region and hence the operational voltages of the quadruple GEM detector starts from 1120 V and 1300 V, respectively, for Ar/CO_2 90:10 and 70:30 gas mixtures. The efficiency at the plateau is $\approx 94\%$. The absolute value of the efficiency depends on the sensitivity of the electronics and noise performance of the detector. The ADC module used in this measurement was insensitive below 40 mV. Therefore, it might be the reason for some loss of efficiency.

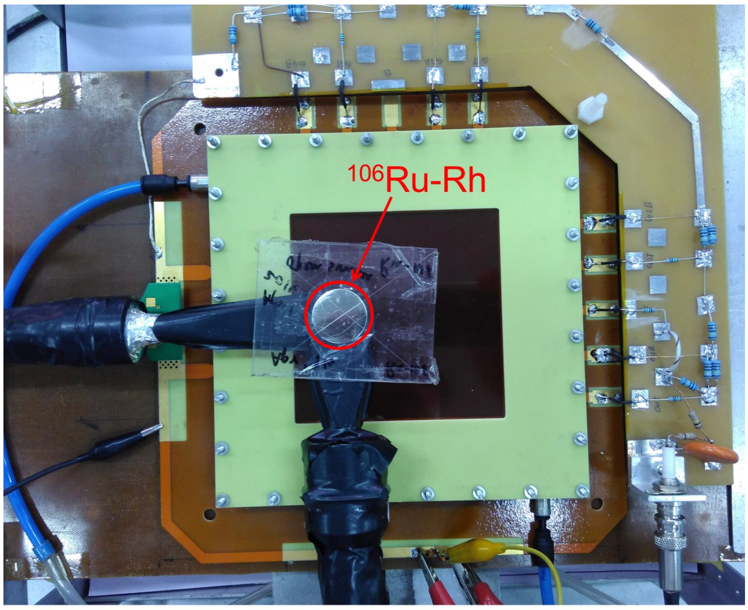

Figure 4.33: Photograph of the efficiency measurement setup of the quadruple GEM detector.

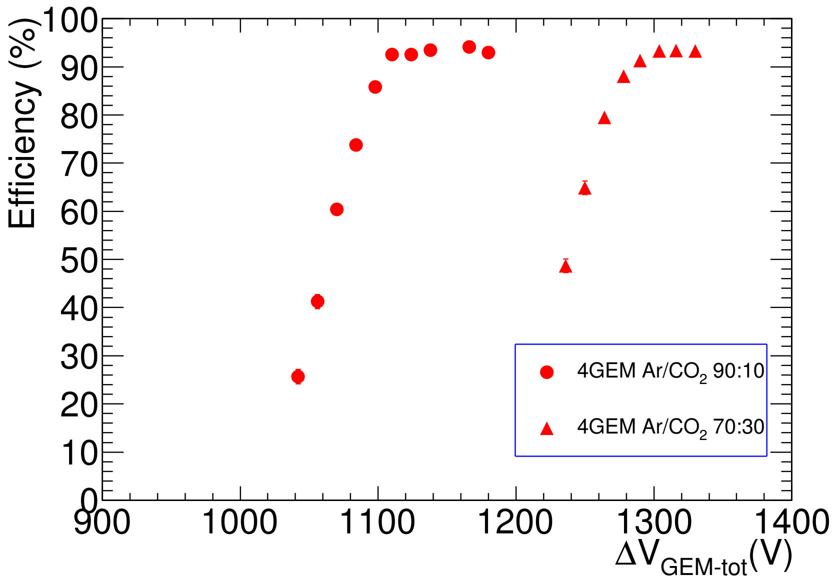

Figure 4.34: Efficiency of the quadrupole GEM detector as a function of $\Delta V_{GEM-tot}$ is presented for both the Ar/CO_2 gas mixtures. Statistical errors are small and within the symbol size.

4.2.5 Gain and energy resolution measurement

Gain and energy resolution measurement procedure is followed similar to Section 4.1.5 as explained in triple GEM detector study [61]. Effective gain is plotted as a function of the GEM voltages for both the gas mixtures, as shown in Fig. 4.35. For a given value of the GEM voltage ($\Delta V_{GEM-single}$), the gain for 90:10 gas mixture is much larger compared to that of the 70:30 gas mixture. For comparison, results of the triple GEM detector [61, 65] are also included in the same figure. It is important to notice that for the similar gain the individual GEM voltage (ΔV) required in case of triple GEM detector is higher than that for the quadruple GEM.

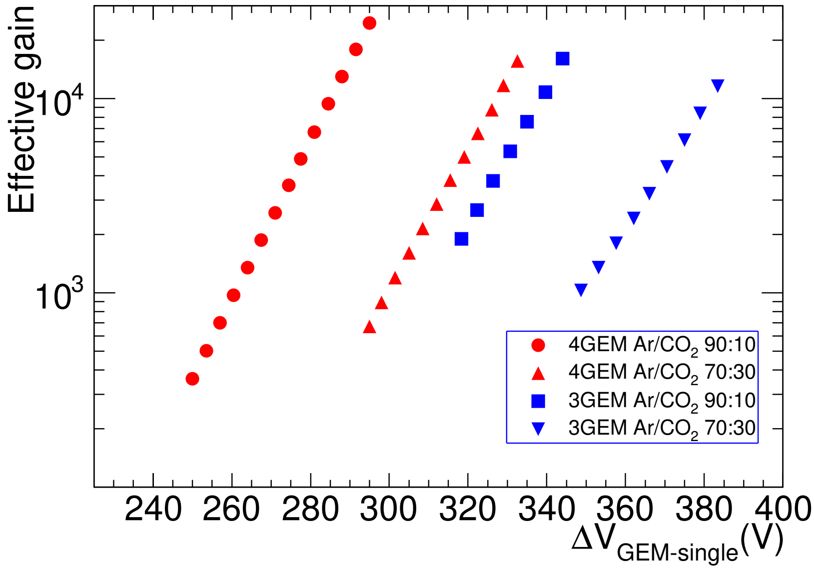

Figure 4.35: Effective gain as a function of $\Delta V_{GEM-single}$ with different Ar/CO_2 gas mixtures for the quadruple GEM and triple GEM detectors. Statistical errors are small and within the symbol size.

Discharge of a GEM detector is related to the gain and hence, GEM voltages ΔV. Operation of the GEM detector with the low voltage across the GEM foils are preferable for the stable operation against discharge. Discharge study of multi GEM detector is reported by Bachmann *et al.* [90]. The study results conclude that the application of multiple GEM foils has advantages against discharge with higher gas gain, as shown in Fig. 4.36. Discharge probability is further studied

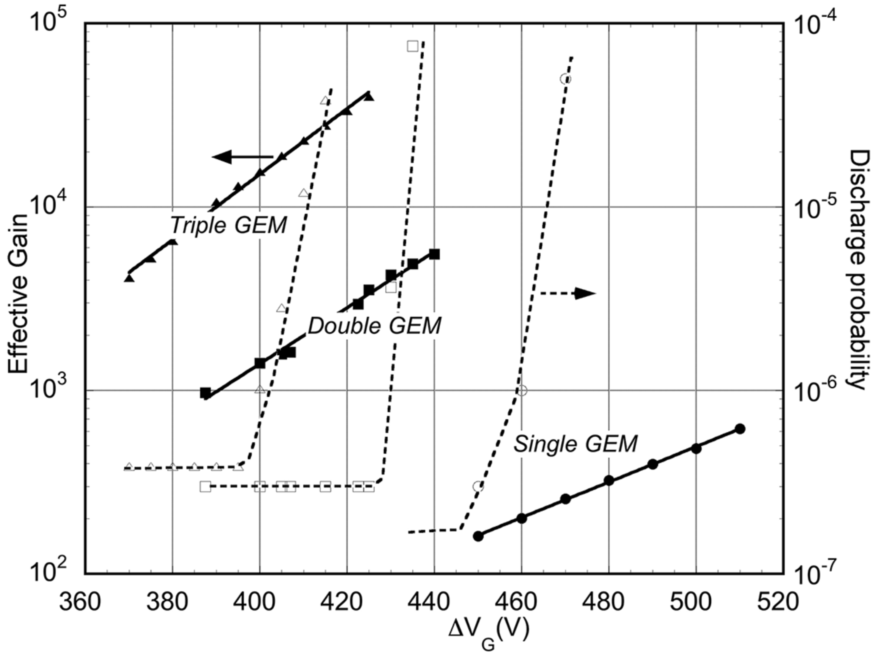

Figure 4.36: Gain and discharge probability variation with GEM voltages for a single, double and triple GEM detectors using α-particle in Ar/CO_2 70:30 gas mixture [90].

by ALICE TPC upgrade collaboration. The report [46, 88] has summarized that the triple GEM detector with ion backflow field setting leads to an increase of the discharge probability by three orders of magnitude than ALICE TPC quadruple GEM detector. More about discharge study for ALICE TPC upgrade can be found in Section 6.3.3.

The energy resolution (FWHM) of the quadruple GEM detector as a function of the individual GEM voltage is shown in Fig. 4.37 for both the gas mixtures. The resolution of the triple GEM detector with the same experimental condition is also included in the figure for direct comparison. The energy resolution of the quadruple GEM is found better for 90:10 gas mixture compared to 70:30. For both gas mixtures, the energy resolutions in case of quadruple GEM detector are poorer compared to those of the triple GEM detector. Similar results have also been reported in a previous study of quadruple GEM detector for ALICE TPC [45], where the effect has been attributed to low IBF in case of quadruple GEM detector.

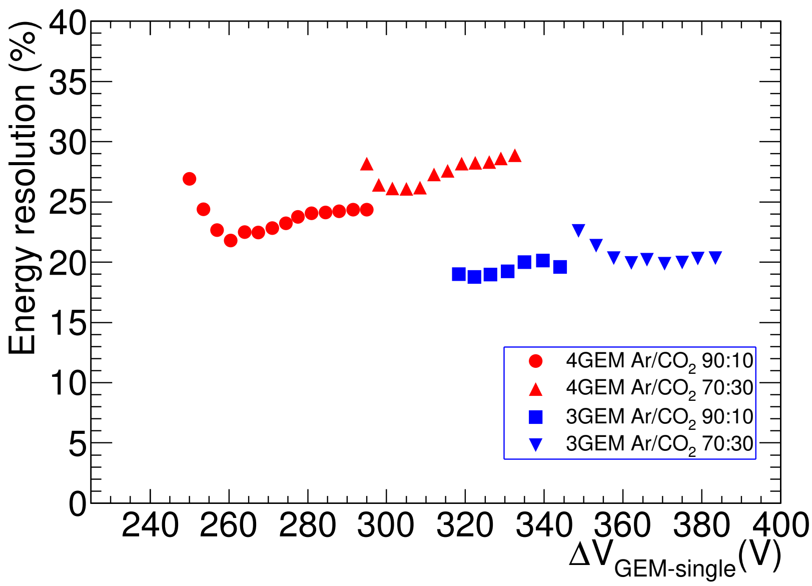

Figure 4.37: Energy resolution as a function of $\Delta V_{GEM-single}$ with different Ar/CO_2 gas mixtures. Statistical errors are small and within the symbol size.

4.2.6 Gain and energy resolution measurement using IBF field setting

The detector is also tested with a special electric field setting, *IBF* field configuration [89]. The *IBF* setting is very different than the *standard* one and with a similar philosophy of the ALICE TPC quadruple GEM field settings. The resistors used in the *IBF* field setting along with *standard* setting are shown in Fig. 4.38. In the *standard* setting, equal voltages (ΔV, $250-300$ V) to all four GEMs with a moderate electric field ($1-3$ kV/cm) in the gaps were applied. For *IBF* setting, the electric field was similar to the ALICE-TPC as given in Table 6.2. In this setting the applied ΔV

for GEM1 (258 – 300 V), GEM2 (220 – 255 V) and GEM3 (270 – 315 V) are low in comparison to GEM4 (345 – 400 V). Higher voltage in GEM4 is purposed to have maximum avalanche in the last stage of the charge amplification. Drift field is kept low ($\approx$ 400 V/cm) to stop ions movement into the drift gap. Low field ($\sim$ 100 V/cm) in transfer gap-3 is maintained to stop a large fraction of ions produced in GEM4.

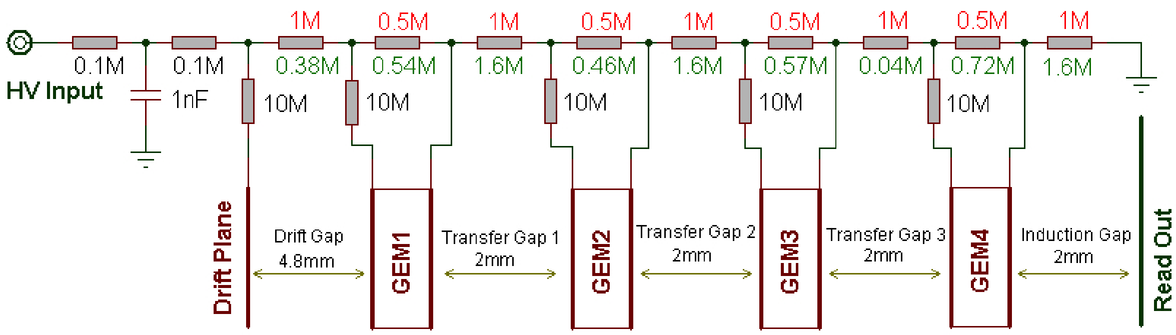

Figure 4.38: Voltage divider resistor chain. Values (in MΩ) in red upper are for *standard* and in green lower are for *IBF* settings. Resistors of drift and transfer gap-3 are changed with 1 and 0.34, respectively for Ar/CO_2 70:30 in *IBF* setting.

The effective gain of the detector for two different field configurations as a function of total GEM voltage ($\Delta V_{GEM-tot}$) is shown in Fig. 4.39. It is found that for the same $\Delta V_{GEM-tot}$, the *IBF* configuration has lower gain compared to the *standard* field setting. The reason behind low gain in *IBF* case is limited electron multiplications for other GEM foils except for the fourth GEM and also the low electric field of transfer gap-3.

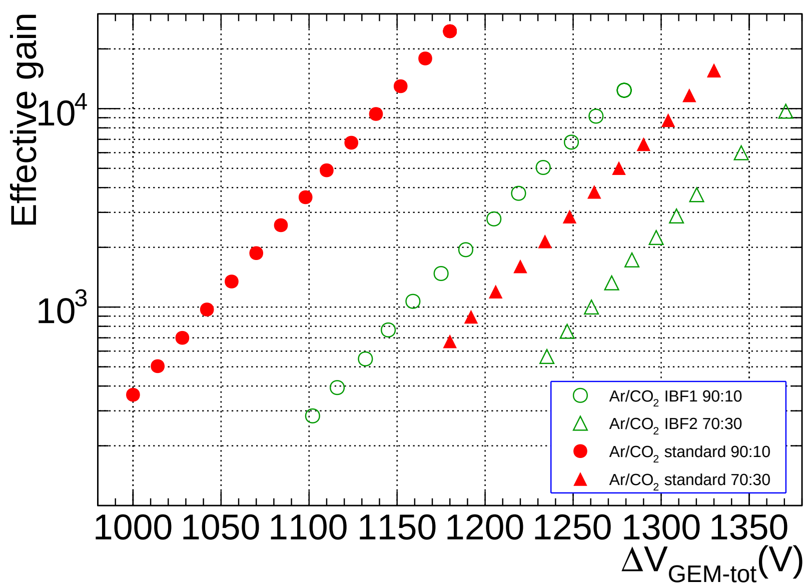

Figure 4.39: Effective gain as a function of total GEM voltage ($\Delta V_{GEM-tot}$) with different field settings of the quadruple GEM detector. Results with *IBF* field setting are in open bullets and *standard* setting are in solid bullets. Statistical errors are small and within the symbol size.

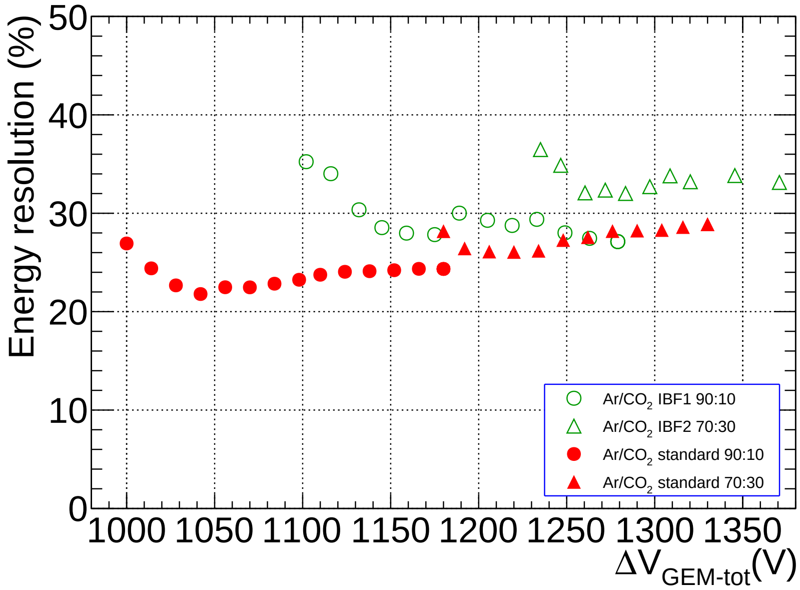

Figure 4.40: Energy resolution as a function of total GEM voltage ($\Delta V_{GEM-tot}$) with different field setting of the quadruple GEM detector. Results with *IBF* field setting is in open bullets and *standard* setting is in solid bullets. Statistical errors are small and within the symbol size.

The energy resolution of the quadruple GEM as a function of $\Delta V_{GEM-tot}$ is shown in Fig. 4.40 for both the electric field settings. It is observed that the energy resolution is worse in the *IBF* setting compared to the *standard* case. Electron amplification in the first GEM plays a significant role in energy resolution of the GEM detector [45]. In the *IBF* setting, the first GEM foil is kept at a lower voltage for stopping the motion of the ions into the drift volume. As a consequence electron transmission gets reduced and some of the primary electrons may get lost instead of producing an avalanche.

4.2.7 Relation between efficiency and effective gain of the GEM detectors

The efficiency of the GEM detectors is reached to a plateau where the signal amplitude is high enough then the noise level. The signal amplitude of the detector depends on the amount of charge collected by the readout pads and hence on the factors like the number of primary ionization, gain and sensitivity of the electronics. For a fully absorbed ^{55}Fe X-ray the number of primary ionization produced within the drift volume slightly depends on the gas mixture. The number of primary ionization produced by a MIP is almost had same value for different gases. The readout electronics have been used for the study of both the triple GEM and quadruple GEM detectors are same. Thus the gain should be the only determining factor for efficiency irrespective of the kind of the detector and gas mixtures used.

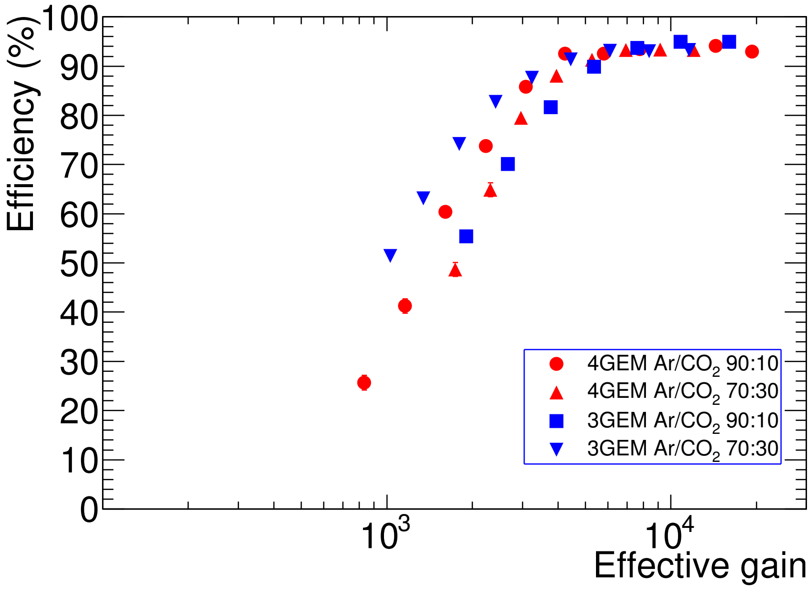

Figure 4.41: Variation of the efficiency as a function of effective gain with different Ar/CO_2 gas mixtures for both the triple GEM and the quadruple GEM detectors. Statistical errors are small and within the symbol size.

For a given applied voltage $\Delta V_{GEM-single}$, the gain of the detectors have been measured using ^{55}Fe source and the data is shown in Fig. 4.35. The efficiency value can be taken from Fig. 4.34 for the same value of $\Delta V_{GEM-single}$. Similarly, gain and efficiency data can be obtained from the triple GEM measurements [61]. The compilation of the two data sets for efficiency as a function of effective gain has been presented in Fig. 4.41. From the figure, one can observe the efficiency increases with effective gain of the detector and then reach a plateau. It is to be noted that the efficiency plateau begins at the same gain in all four cases, irrespective of the kind of the GEM detectors and its gas compositions. The efficiency reaches a maximum value at the gain $\sim$ 5000 for both the detectors. From the Fig. 4.41, one can conclude that the gain of the detector is the principal factor in efficiency measurement [62].

4.2.8 Drift field effect in GEM characterization

The characteristics of a GEM detector highly depend on electric field configurations. The significance of different fields in gain and energy resolution measurement are discussed before in this section. The importance of the drift field (E_d) on the performances of the quadruple GEM detector is studied separately for both the gas mixtures using the ^{55}Fe source. A voltage divider resistor chain with two HV inputs as shown in Fig. 4.42 is used to change the drift field and GEM voltages independently. The obtained results are explained using *electron transparency* across the first GEM foil. *Electron transparency* of the detector is defined as the ratio of primary electrons

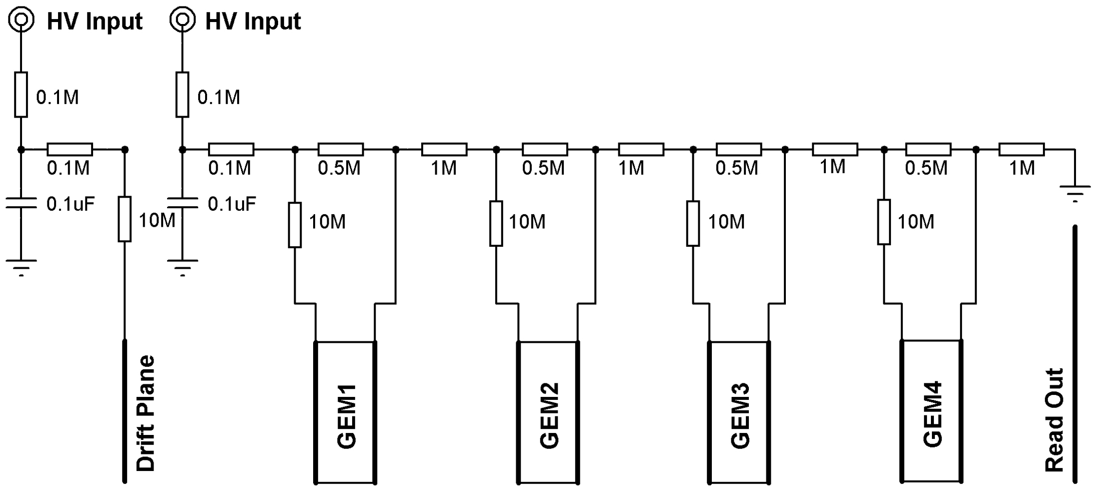

Figure 4.42: Voltage divider resistor chain for independent drift field (E_d) configuration.

collected into the first GEM and the number of primary electrons created within the drift volume.

$$Electron\ transparency = \frac{no.\ of\ primary\ electrons\ goes\ into\ first\ GEM}{no.\ of\ primary\ electrons\ created\ in\ the\ drift\ volume} \tag{4.8}$$

Effective gain of the detector is calculated using the ^{55}Fe source at different E_d keeping GEM voltages constant. The electron multiplication across the GEMs are expected to have uniform values since the GEM voltages are set to a constant. However, different gain with the variation of the drift field is observed for constant GEM voltages. The results are normalized to unity for comparison with the assumption that full transparency is reached at the plateau region. *Electron transparency* as a function of E_d is shown in Fig. 4.43. The measurements are performed for three different sets of the GEM voltages. The values of transparency increase with E_d attain an optimum value and afterward, it decreases again. The optimum transparency of the electrons is found in the drift field (E_d) range of $750 - 1000$ V/cm and 1000–1500 V/cm for the Ar/CO_2 90:10 and 70:30 gas mixtures, respectively. The gain plot in Fig. 4.35 is showing that GEM has lower operating voltage in Ar/CO_2 90:10 in comparison to 70:30 gas. As a consequence, a high field within the GEM in Ar/CO_2 70:30 gas is expected. The drift electrons will be more focused and efficiently collected in Ar/CO_2 70:30 gas even at a higher drift field.

The *electron transparency* study presented in this thesis is in qualitative agreement with similar studies for a single GEM carried out by S. Bachmann *et al.* [91]. The *electron transparency* or collection efficiency increases initially, attain a plateau and decreases after that. Low collection efficiency at lower field value might occur because of losses of electrons due to diffusion, recombination or attachment of the electrons with the contaminant of the gas. However, at higher drift field the electric field lines are terminated at the top conducting surface of the first GEM. Some

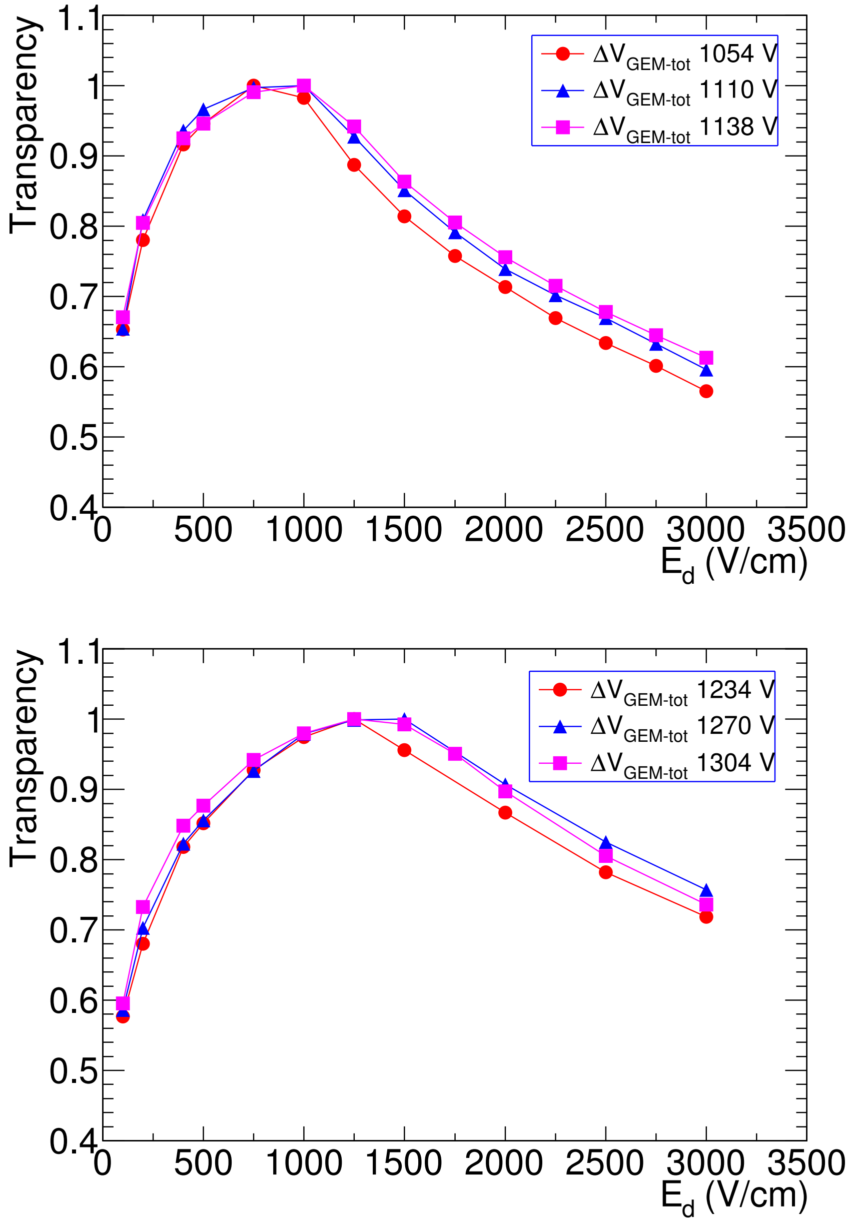

Figure 4.43: Electron transparency as a function of drift field (E_d). (Top) Ar/CO_2 90:10 and (bottom) 70:30 gas mixtures with different $\Delta V_{GEM-tot}$ sets. Statistical errors are small and within the symbol size.

drift electrons might be lost due to the collection on the GEM surface.

The importance of the drift field on the operation of a GEM detector has been further explored. The effective gain of the quadruple GEM detector is measured by varying the GEM voltages with different drift field (E_d) sets. The result is shown in Fig. 4.44. The highest gain of the detector is corresponding to $E_d = 1000$ V/cm, which is in the range of drift field for maximum transparency of both the gas mixtures (see Fig. 4.43). The larger differences in gain are found at lower GEM voltages. However, the gain difference narrows down with increasing $V_{GEM-tot}$. The reason for this is that the transparency depends on both the electric field of the first GEM and the drift field.

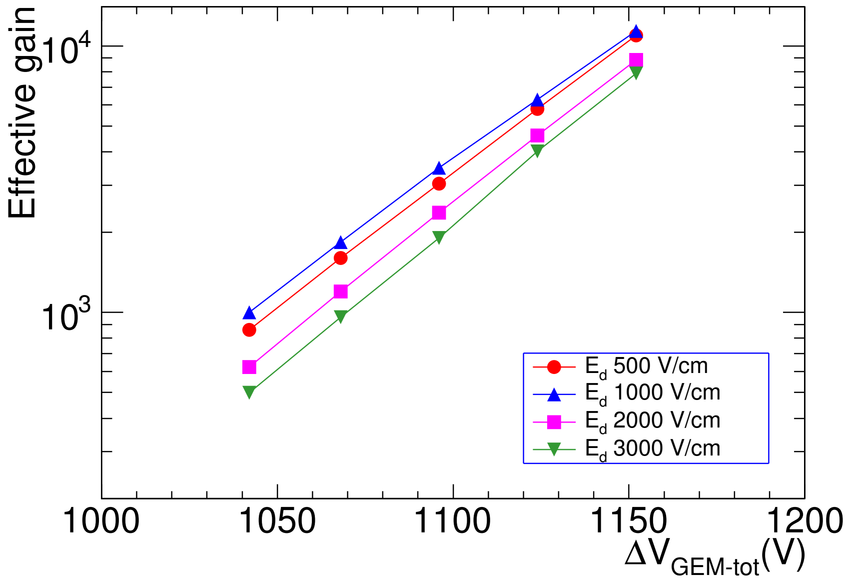

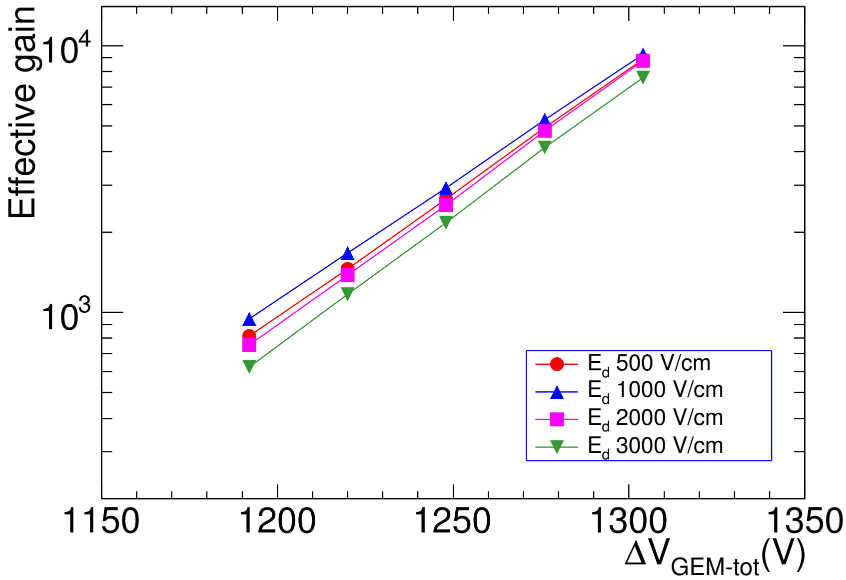

Figure 4.44: Gain variation as a function $\Delta V_{GEM-tot}$ with different drift field (E_d) sets. (Top) Ar/CO_2 90:10 and (bottom) 70:30 gas mixtures. Statistical errors are small and within the symbol size.

At lower GEM voltages, the drift field effect is quite strong as seen in the gain value. However, at higher GEM voltages, the electric field across GEM is so large that a significant fraction of the electrons are focused through the holes then the transparency increases. So the drift field becomes less important and the gain values converge to a single value. From Figs. 4.43 and 4.44 it can be concluded that both drift field and field across the holes of the first GEM have important roles in electron transparency study. Depending on the range of the field, at low GEM field the drift field is dominating and vice versa.

4.2.9 Drift field dependency on time resolution study

The time resolution of the quadruple GEM detector is measured with different drift field (E_d). The electronics setup for the time resolution measurement is similar to the setup of the triple GEM detector as shown in Fig. 4.19. The resistor setup for applying HV is the same as in Fig. 4.42. The measurement is performed with Ar/CO_2 70:30 gas mixture. In this study, the detector gain was set to $\sim 10^4$ and the GEM voltages were also kept constant throughout the measurement. The time spectrum obtained for the quadruple GEM is shown in Fig. 4.45. Time resolution

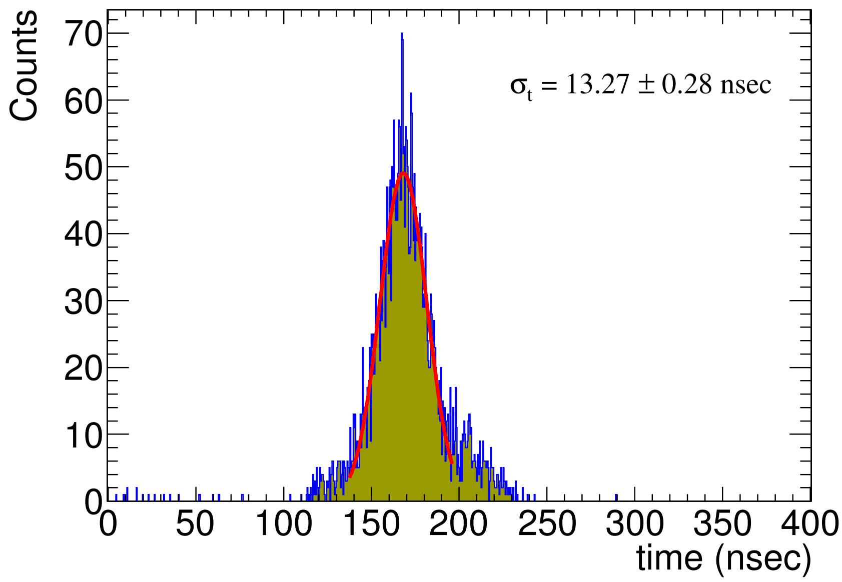

Figure 4.45: Time spectrum of the quadruple GEM detector with Ar/CO_2 70:30 gas mixture.

(σ_t) of the detector is measured with the variation of the drift field as shown in Fig. 4.46. It is observed that time resolution decreases with drift field and remains almost constant at high field values. The time resolution of a gas detector depends on how fast the primary electron cluster reaches the readout. The fastness of reaching of the electrons on the readout depends on the drift velocity of the electrons. In Ar/CO_2 70:30 gas mixture, the drift velocity increases with the electric field and remains almost constant above 2 kV/cm as shown in Fig. 4.47. The time resolution decreases with drift field and does not improve much with further increasing the field above 2 kV/cm. The optimum value of the time resolution, $\approx$ 13 ns has been obtained with the present setup. In this measurement, scintillators timing correction is also considered. It is to be noted that in this measurement time walk correction could not be taken care of. The time resolution of the quadruple GEM detector is slightly worse than the measured value of the triple GEM [61, 71].

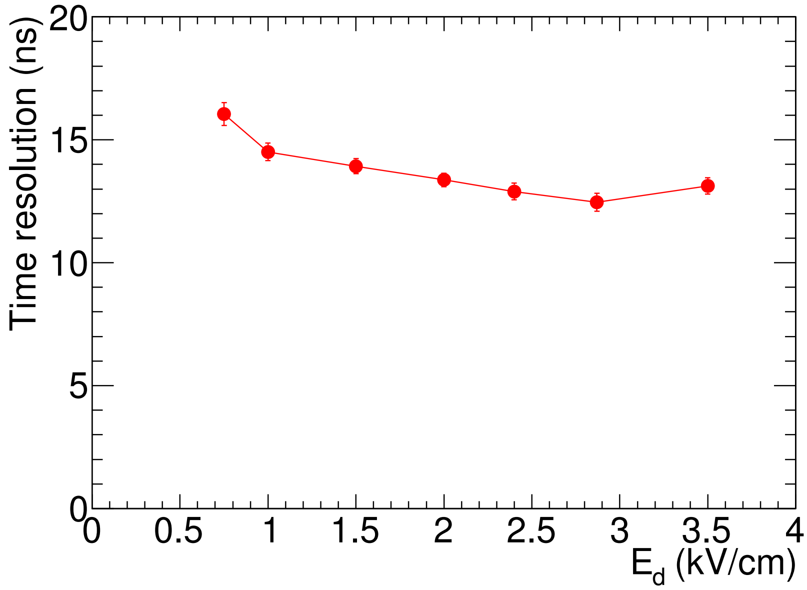

Figure 4.46: Time resolution as a function of drift field of the quadruple GEM detector. Applied gas is Ar/CO_2 70:30. Statistical errors are small and within the symbol size.

4.3 A model simulation of time resolution for the GEM detector

The time resolution of a gas detector depends on the factors, the electrons drift and diffusion, positional fluctuation of the electron-ion cluster creation and the electronic noise charge (ENC). In this section, a review on theoretical approach for time resolution will be described [92, 93]. I will approach a simulation model based on Garfield [59, 60] software to estimate the limiting value of the time resolution of the GEM detector. The simulation results will also be compared with the theoretical values.

4.3.1 Theoretical approach of time resolution

When a charged particle is passing through the gas volume (or drift volume), it produces a small number of electron-ion pairs which is following Poisson-like distribution. The average number of primary electrons is n, and the actual number of primary electrons produced in an event is k then the probability,

$$P_k^n = \frac{n^k}{k!} \exp^{-n} . \tag{4.9}$$

The inefficiency of the detector is, $k = 0$,

$$P_0^n = \exp^{-n} . \tag{4.10}$$

For example, in a 1 cm thick Ar/CO_2 70:30 gas, a MIP can produce number of primary ionizations $n = n_P = 28$ and total electrons $n_T = 100$. Therefore, the statistical limitation of detecting a particle, *i.e.,* inefficiency, in a 1 mm thick ($n_P = 2.8$) gas volume is 6%. For example in a GEM detector of 3 mm thick drift volume would have 0.02% inefficiency due to statistics which is negligible.

The primary ionizations encountered in a gas volume also have a probability distribution in space. In an event k number of electron-ion pairs are produced, with each pair j ($1 \leq j \leq k$) will follow the distribution in normalized space x ($0 \leq x \leq 1$),

$$D_j^k(x) = \frac{k!}{(k-j)!\,(j-1)!}\,(1-x)^{k-j}x^{j-1}. \tag{4.11}$$

The distribution in space with an average number of primary electron-ion pairs n will be,

$$A_j^n(x) = \sum_{k=j}^{\infty} P_k^n D_j^k(x) = \frac{x^{j-1}}{(j-1)!}\,n^j \exp^{-nx}. \tag{4.12}$$

In particular, for the first cluster which is closer to the charge collecting component is

$$A_1^n(x) = n.\exp^{-nx}. \tag{4.13}$$

The arrival time distribution of the electron clusters are

$$P_j(t_d) = v_d.A_j^n(v_d t_d). \tag{4.14}$$

For the first cluster it will be,

$$P_1(t_d) = v_d.n\exp^{-nv_d t_d}, \tag{4.15}$$

which is nothing but a Poisson distribution with the standard deviation,

$$\sigma_1(t) = \frac{1}{nv_d}. \tag{4.16}$$

The electrical signal will have a stepwise rising edge. Each step is corresponding to the convolution of a single electron cluster with its avalanche. If the time of detection is the time of arrival of the electron cluster closest to the GEM then the ionization distribution in space is obviously the limiting value of the time resolution of the GEM. In an ideal situation when the closest electron cluster to GEM always provides the trigger, the time resolution σ_t is limited by the statistical fluctuation of the first electron cluster position. The average number of primary electro clusters

(n) is roughly linearly proportional to the average atomic number of the gas [92]. In order to optimize the time performance of the GEM detector, high drift velocity and large average atomic number gas mixture are required. The accurate estimate of n (or n_P) is difficult in the experiment; however, it depends on experimental conditions like pressure as well as on the temperature. But the estimated values n_P are always within $10 - 20$ % variation. The limiting value of time resolution σ_t can be calculated using the existing reference values of n [94] and v_d.

4.3.2 Model simulation of time resolution

A simulation is performed using Garfield software to estimate the limiting value of the time resolution for the GEM detector. In Garfield simulation, a 3 mm thick gas gap of different gas mixtures are considered. High energy electrons (*i.e.,* MIP) are shoot through the gas so that it produces electron-ion pairs in its traverse. The interaction of the charged particles with the gas and ionization information are provided by Heed [95, 96] in Garfield. A simplified geometry with a thin parallel plate gas volume is used as an ionization chamber. The detail GEM like geometry with all the gaps are not required since the distribution of the primary electron clusters in the drift gap is the main concern. The dynamics of the electrons through all the gaps of the GEM detector can be calculated from the drift and diffusion parameters that can be obtained from the Magboltz [97, 98]. The drift velocity and diffusion of the electrons depend on the gas mixtures and electric field. The drift velocity (v_d) and longitudinal diffusion (D_L) for some useful Argon based gas mixtures have been calculated using Magboltz [97, 98] are shown in Fig. 4.47.

A charged particle produces electron-ion clusters when it passes through the gas. In such an event, the total number of charge clusters produced is denoted by N, the cluster closest to the anode is considered as the first cluster and the cluster with the largest distance from the anode is denoted as N^{th} cluster. The schematic and the cluster labeling conventions used in this simulation model are shown in Fig. 4.48. The first electron cluster bears the time information providing signal detection. The spatial distribution of the clusters are basically the realization of time resolution.

The distribution of the primary electron clusters closest to the anode plane for Ar/CO_2 70:30 gas mixture at normal temperature and pressure is shown in Fig. 4.49. From the figure, it can be observed that the mean ($\bar{x}_d$) and standard deviation (Δx) of the position distribution have a minimum value for the single electron collection. Δx increases with increasing the number of electrons collection. The total electrons production efficiency is 100% almost in all the cases. Therefore, to have the best time resolution of a detector, high charge avalanche and good electronics sensitivity are required to trigger the single electron cluster.

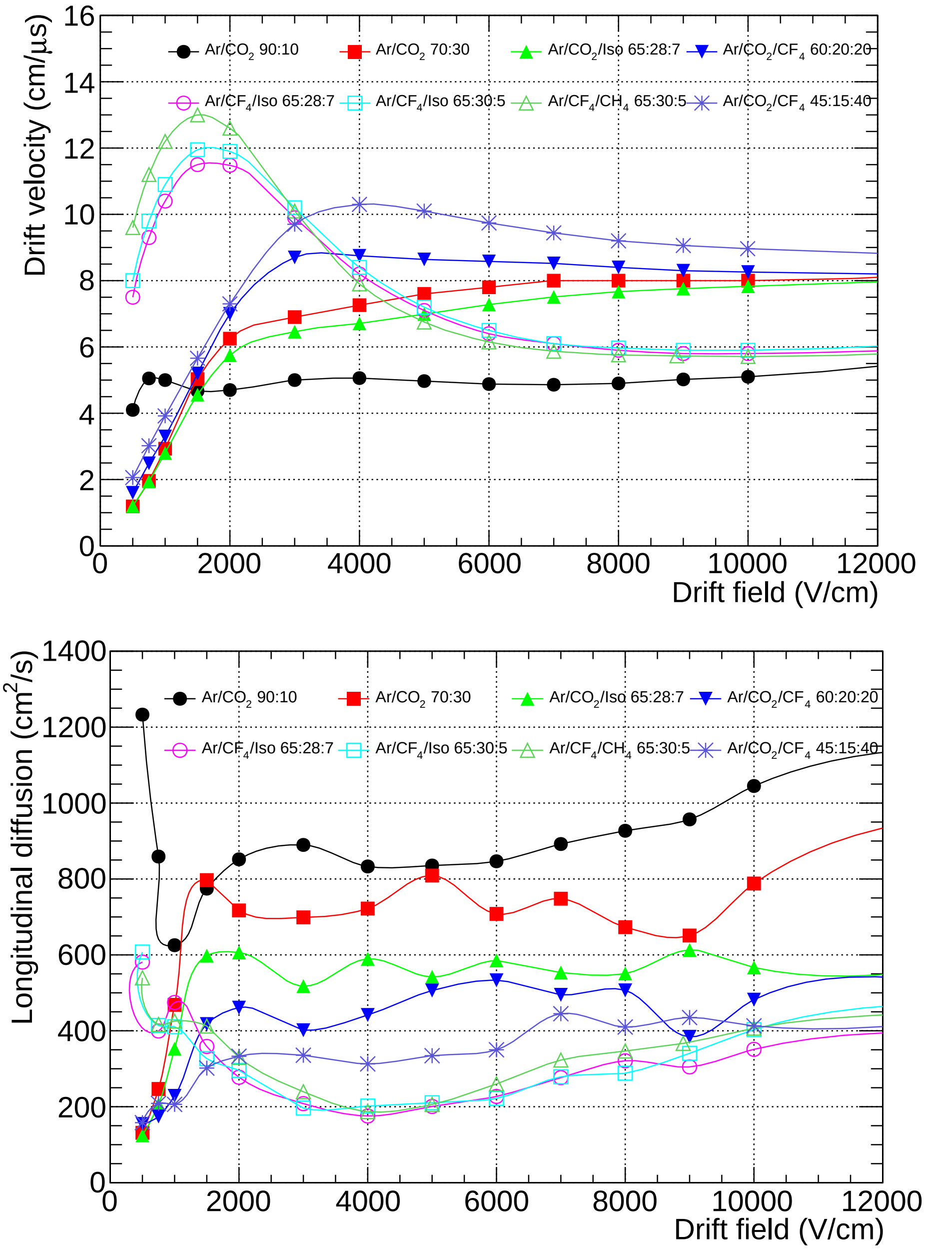

Figure 4.47: Variation of the electron drift velocity (top panel) and longitudinal diffusion (bottom panel) with electric field for different Argon based gas mixtures.

The uncertainty in arrival time of the electron is

$$\Delta t_x = \frac{\Delta x}{v_d}. \tag{4.17}$$

The diffusion of the electrons along its path also contribute to the time resolution as

$$\Delta t_{diff} = \frac{\sigma_{diff}}{v_d}, \tag{4.18}$$

where σ_{diff} is the total longitudinal diffusion due to drift of the primary electron from the drift

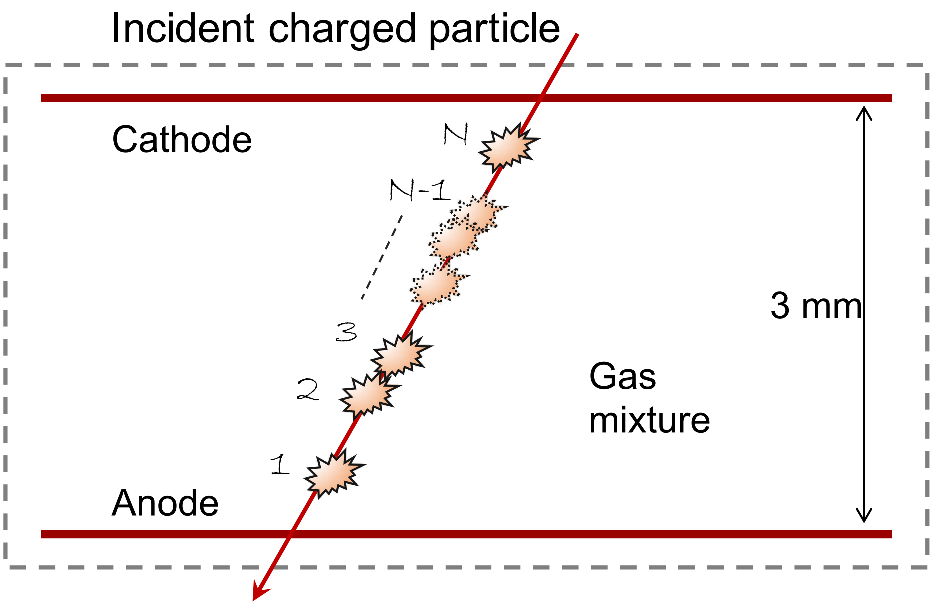

Figure 4.48: Schematic geometry of the time resolution simulation.

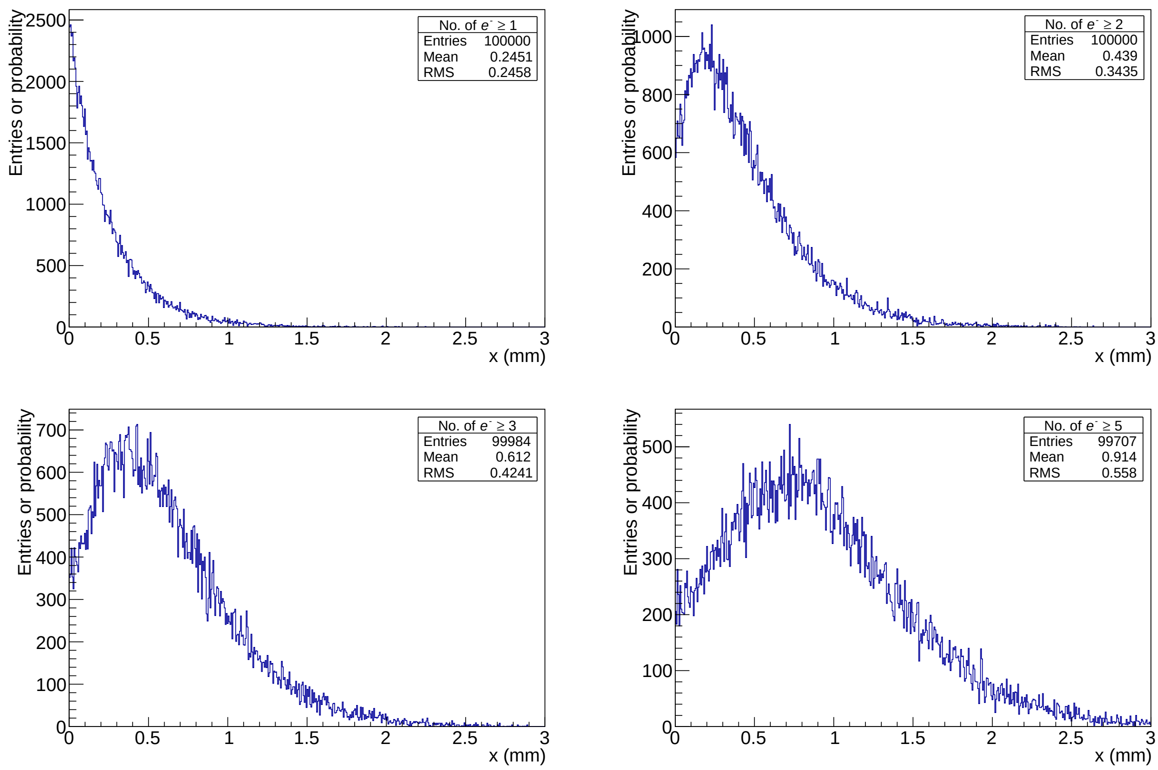

Figure 4.49: Simulation of primary electron clusters distribution in a 3 mm thick Ar/CO_2 70:30. The figures are corresponding to the position distribution of the clusters with total electrons 1, 2, 3 and 5.

gap to induction gap.

$$\sigma_{diff}(x) = \sqrt{\frac{2D_l}{v_d}(\bar{x}_d + L)}, \tag{4.19}$$

where $\bar{x}_d + L = (\bar{x}_d + d_{tr1} + d_{tr2})$ is the total drift length of the electron before inducing a signal.

The thickness of the GEMs are hundred order of magnitude less than the gaps; therefore, those are excluded in the model for simplicity. Drift velocity (v_d) is taken the same for all the gaps in the calculation. Total time variation (Δt_{pos}) due to uncertainty in the position of the clusters can be written as,

$$\Delta t_{pos} = \sqrt{(\Delta t_x)^2 + (\Delta t_{diff})^2}. \tag{4.20}$$

Electronic Noise: The signal of the detector can fluctuate because of the noise sources, external interference, electronics noise in addition to the spatial uncertainty of the clusters. The electronic noise is the cause of the baseline fluctuation. The rising edge and the amplitude both of the signal are altered because of the superimpose the signal with the baseline noise. Electronic noise charge (ENC) is the most convenient measurement of the system noise and provides the limiting value. Electronic noise is insignificant for the scintillator detector where the statistical fluctuation of the charge is so high (σ_Q) compare to the ENC. However, noise fluctuation has a significant effect on the silicon detector and for the proportional gas chamber where statistical fluctuation of the charge is less or comparable to the ENC.

The uncertainty in time measurement due to electronic noise can be expressed as,

$$\Delta t_{ele} = \frac{ENC}{dQ/dt} = \frac{ENC}{Q/t} = \frac{ENC}{(G.n_p)/t}, \tag{4.21}$$

and the total time uncertainty in this simulation is,

$$\Delta t_{simu} = \sqrt{(\Delta t_x)^2 + (\Delta t_{diff})^2 + (\Delta t_{ele})^2}, \tag{4.22}$$

where $Q = G.n_p$ is the total charge. Gain, G of the detector is $\sim 10^4$ and shaping time is $t = 20$ ns in general considered. ENC has the value of range $600 - 1000e$ depending on specific electronics. Therefore, for the single electron detection, the noise fluctuation has the value $\Delta t_{ele} \approx 2$ ns.

n_i	E kV/cm	v_d cm/μs	L mm	$\bar{x_d}$ μm	Δx μm	Δt_x ns	Δt_{diff} ns	Δt_{ele} ns	Δt_{simu} ns
1				245	246	3.5	1.33	2.0	4.27
2				439	344	4.9	1.36	1.0	5.22
3	3	7	4	612	424	6.1	1.38	0.67	6.28
4				770	494	7.1	1.41	0.5	7.25
5				914	558	8.0	1.57	0.40	8.18

Table 4.1: Time resolution simulation of GEM detector for Ar/CO_2 70:30 gas of different charge collections.

In this study, position distribution of electron clusters, drift velocity and diffusion have been simulated for some of the highly used Argon based gas mixtures in GEM detector. The temperature and pressure kept unchanged for all the gases study. We found that the mean ($\bar{x}_d$) and standard deviation (Δx) of the clusters positions have almost same value independent of the gas type. However, the temperature and the pressure dependency of the ($\bar{x}_d$) and (Δx) are found.

The simulation results for a triple GEM like geometry is summarized in Table 4.1 for Ar/CO_2 70:30 gas mixture with a different number of electrons collection on the anode. The table shows that with increasing the electron clusters (*i.e.,* charge collection time), the time resolution of the detector degrades though the uncertainty in the time measurement of the electronics decreases. The diffusion and electronic noise increases the time resolution value ≈ 30% for the single electron cluster.

Gas mixtures	**D** cm^2/s	**E** kV/cm	$\boldsymbol{v_d}$ cm/μs	$\boldsymbol{\Delta t_x}$ ns	$\boldsymbol{\Delta t_{diff}}$ ns	$\boldsymbol{\Delta t_{simu}}$ ns
Ar/CO_2 90:10	808	1.5	4.7	5.2	2.56	6.12
	879	3.0	5.0	4.9	2.42	5.78
Ar/CO_2 70:30	808	1.5	5.2	4.8	2.24	5.64
	700	3.0	7.0	3.5	1.33	4.27
Ar/CO_2/CF_4 45:15:40	258	1.5	5.8	4.2	1.06	4.81
	332	3.0	9.7	2.5	0.56	3.29
Ar/CO_2/CF_4 60:20:20	369	1.5	5.4	4.6	1.4	5.17
	435	3.0	8.7	2.9	0.75	3.56
Ar/CF_4/Iso 65:28:7	367	1.5	11.4	2.2	0.46	2.97
	222	3.0	10	2.5	0.43	3.2

Table 4.2: The limiting value of the time resolution for different useful gas mixtures of GEM detector. Total transfer gaps $L = 4$ mm, $\bar{x}_d = 245$ μm and $\Delta x = 246$ μm are take for all gas mixtures.

Table 4.2 summarized the limiting value of time resolution for different useful Argon based gas mixtures at normal temperature and pressure. The resolution is calculated for single electron collection in two different electric field setting, 1.5 kV/cm and 3.0 kV/cm. The mean ($\bar{x}_d$) and standard deviation (Δx) of the clusters positions are taken as $\bar{x}_d = 245$ μm and $\Delta x = 246$ μm.

The time resolution calculated by theoretical approach and model simulation is compared in the Table 4.3. The results from experimental measurements for triple GEM detector is also included in the table for comparison, wherever the test data found. The table indicates a little deviation of the theoretical value from the simulation one. However, the experimentally measured values (Δt_{ex}) are quite far from the limiting value.

This chapter can be summarized as a triple GEM detector and a quadruple GEM detector

Gas mixtures	$\boldsymbol{n_P}$ cm^{-1}	**E** kV/cm	$\boldsymbol{v_d}$ cm/μs	$\boldsymbol{\Delta t_1}$ ns	$\boldsymbol{\Delta t_{simu}}$ ns	$\boldsymbol{\Delta t_{ex}}$ ns
Ar/CO_2 90:10	26	3	5.7	7.6	5.78	–
Ar/CO_2 70:30	28	3	7.0	5.1	4.27	9.7
$Ar/CO_2/CF_4$ 45:15:40	41.7	3	9.7	2.5	3.29	–
$Ar/CO_2/CF_4$ 60:20:20	34.6	3	8.7	3.3	3.56	5.3
Ar/CF_4/Iso 65:28:7	40.2	3	10.0	2.5	3.2	4.5

Table 4.3: The limiting value of the time resolutions are compared for the theoretical obtaining and model simulations for different gas mixtures. The time resolutions obtained experimentally are also noted wherever they are available. n_P is taken from [94].

are assembled and detail characterization has been performed for the development of the GEM detector for ALICE TPC upgrade. Comparison of the results from both the detectors shows that the quadruple GEM detector can operate at a lower GEM voltage ($\Delta V_{GEM-single}$) which is preferable for longterm stable operation whereas the triple GEM detector has better energy resolution. A new method of uniformity study has presented with the uniformity results. The importance of electric field optimization for the GEM performances is also discussed in the chapter. The Garfield based gas simulation is performed to understand the time resolution mechanism of the GEM detector. The simulation results are compared with the theoretical calculation and experimental results.

Chapter 5

Characteristic study of MWPC

The invention of Multi-Wire Proportional Chamber (MWPC) in 1968 [99] by Charpak and his collaborators at CERN gave a breakthrough in nuclear physics experiments and High Energy Physics (HEP) experiments. Proportional counter has been widely used where energy information is essential, but that failed to restore particle tracking information. Charpak showed that an array of many parallel anode wires closely spaced in the same chamber could be a realistic detector for position sensing. It is found that the MWPC has good position precision, higher efficiency, better resolving time and shorter dead time than spark chamber. This classical kind of detector is successfully using in many HEP experiments till date [28, 30, 31, 100]. The detector is also found in other applications as X-ray and medical imaging [101, 102].

In this chapter will be discussed about the assembly and test results of the MWPC performed at VECC, Kolkata laboratory. All the measurements of the MWPCs have performed using Ar/CO_2 90:10 and 70:30 gas mixtures where for the signal reconstruction NIM and MANAS electronics have been used.

5.1 Design of MWPC detector

The simplified design of MWPC is shown in Fig. 5.1 where an anode wire plane is separated by two cathode planes, namely cathode or drift plane and readout plane. The anode wire plane consists of many thin Au-plated tungsten wires. The diameter of the anode wires is 20 μm with a wire spacing of 2.8 mm. The cathode plane is made of a copper coated thin insulator sheet. The gap between cathode and anode and readout plane and anode both are maintained 3 mm. A positive high voltage is applied to the wire plane where as the cathode and the readout planes are at the ground potential. The primary electrons are drifting in the field and have avalanches within few wire diameters from the anode, where the electric field is $\propto 1/r$. Electric field variation and the

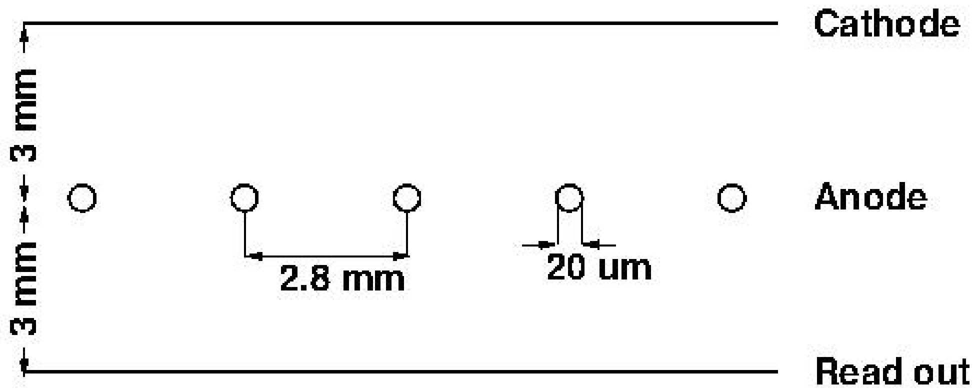

Figure 5.1: Schematic design of the MWPC detector.

drift of the electrons are simulated using Garfield software [59, 60] as shown in Fig. 5.2. From the figure, it can be seen that at very close to the anode wire a high electric field about a few tens of kV/cm can be developed to have an avalanche.

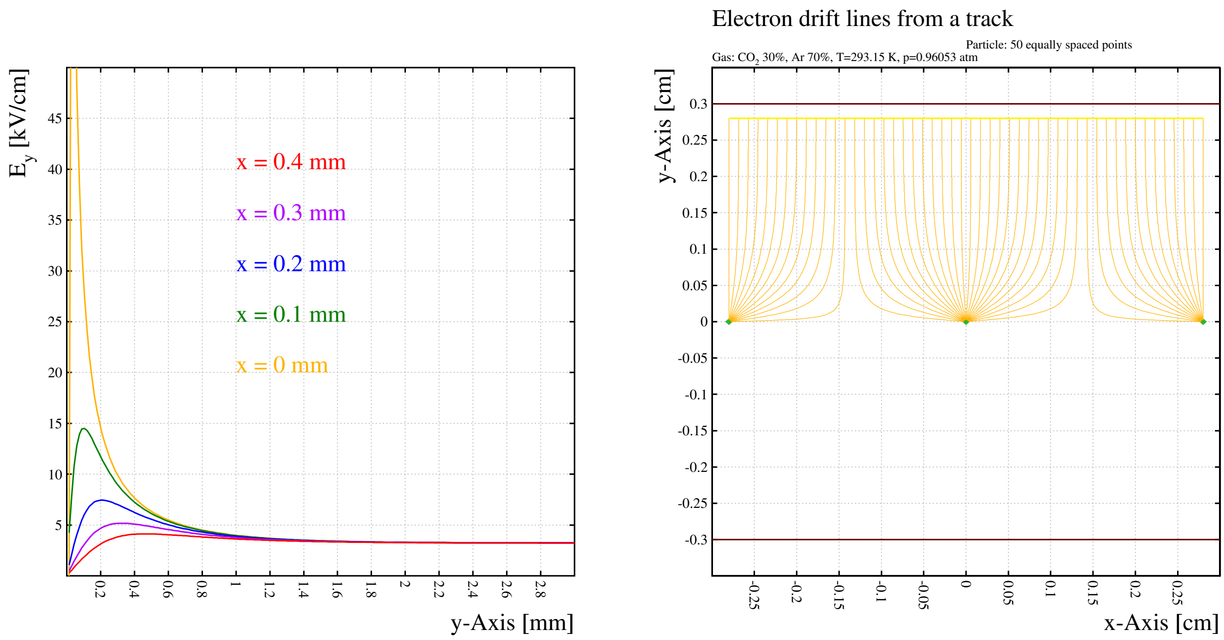

Figure 5.2: Variation of the electric field in space in left panel. Drift line following by the electrons are shown in right panel.

The detector is tested using Ar/CO_2 gas mixture having 70:30 and 90:10 ratio in flow mode at laboratory temperature and pressure.The summed up signal of the readout pads are used for further processing. The detector is tested using conventional NIM as well as with MANAS electronics. In the below section, the specification of the MANAS ASIC and its electronics setup are discussed.

5.1.1 Electronics setup using MANAS electronics

The Multiplexed ANAlog Signal Processor (MANAS) chip has successfully used in Front End Electronics (FEE) board of PMD and Muon spectrometer detector in ALICE experiment [103, 104]. The MANAS chip is fully developed by Semiconductor Complex Limited, Chandigarh, India. MANAS ASICs incorporate 16 channels pulse processing along with analog multiplexed output. Four such chips are embedded on MANAS NUmérique (MANU) board. These boards ensure the digital conversion and the data transmission through a 64 channels Muon Arm Readout Chip (MARC) ASIC. The specification of the MANAS ASIC is given in Table 5.1. The picture of a FEE board with four MANAS and MARC chips are shown in Fig. 5.3.

Noise at 0 pF (E_d)	500 rms electrons
Noise slope	$11.6e^-$/pF
Linear dynamic range	+500 fC to -300 fC
Conversion gain	3.2 mV/fC
Peaking time	1.2 μs
VDD/VSS	$\pm$ 2.5 V
Analog readout rate	1 MHz
Power consumption	9 mW/channel
Technology	1.2 μm CMOS N-well

Table 5.1: Specification of the readout ASIC MANAS.

Figure 5.3: Photograph of a FEE board with MANAS and MARC chips.

MANAS electronics can operate with both positive and negative input signals provided with trigger signals. In our setup, the trigger was provided by the anode signal and the readout pad signals are considered for the energy spectrum. The operation of the MANAS ASIC was controlled by using a DAQ PC.

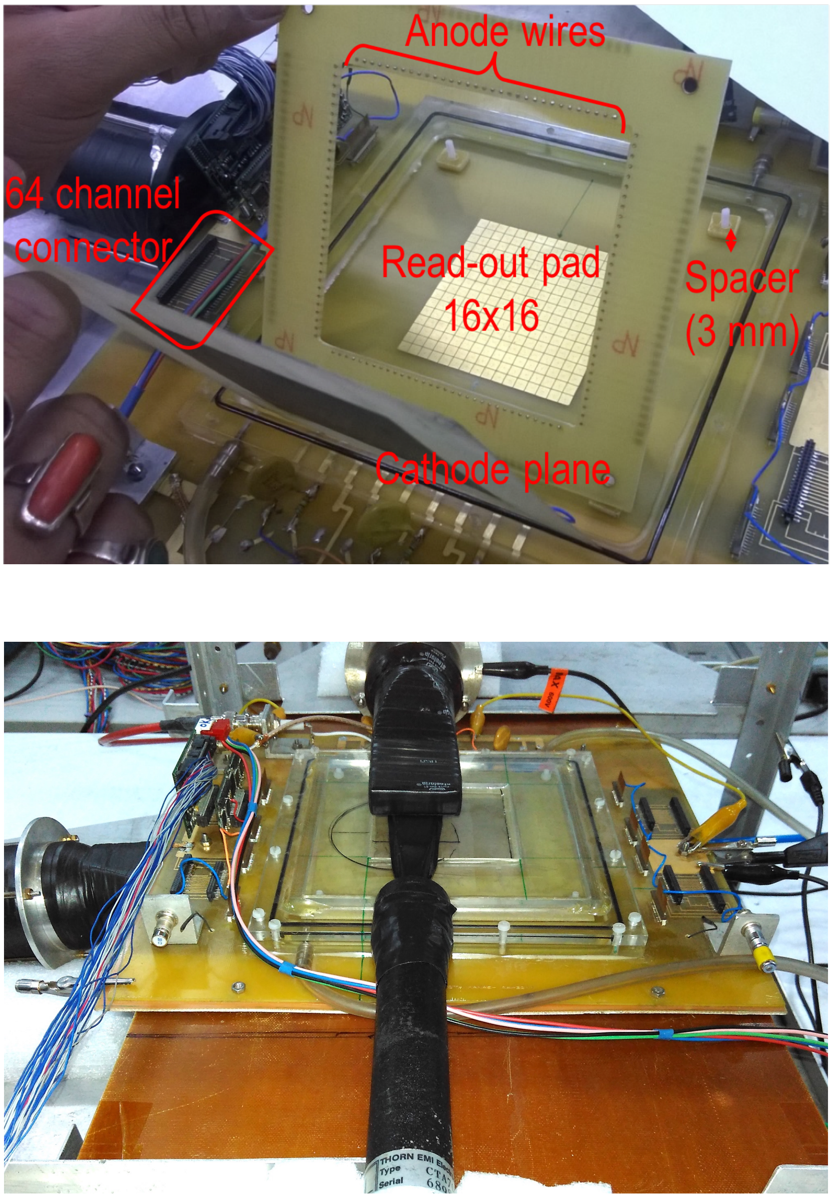

Figure 5.4: Components of the MWPC detector are labeled in upper panel. Laboratory setup picture of the MWPC in lower panel.

5.2 Test setup

Two MWPC detectors, labeled as MWPC-1 and MWPC-2, are tested in our laboratory for its characterization. Different components of the detector and the experimental setup are shown in Fig. 5.4. The detectors are tested with the ^{55}Fe X-ray source, β^{-}-source and cosmic muons radiations. The gain, energy resolution, fraction of charge sharing, efficiency and time resolution of the detectors are measured. The electronics setup of the MWPC detector using the NIM electronics is very similar to the setup of the GEM detector as described in Chapter 4. The detector signal from the anode wires and the induced signal from the readout pads both are considered in the measurements.

5.3 MWPC-1 detector test results

The detector is tested using both NIM and MANAS electronics [105]. The test results obtained from the detector are discussed below.

5.3.1 Energy spectrum and charge sharing

The MWPC-1 detector is tested using Ar/CO_2 70:30 gas in flow mode. The energy spectrum of the ^{55}Fe X-ray source is obtained for both the anode and pad signals using NIM electronics setup. Figure 5.5 shows the ^{55}Fe spectrum at 1800 V from the anode signal. The energy spectrum of the

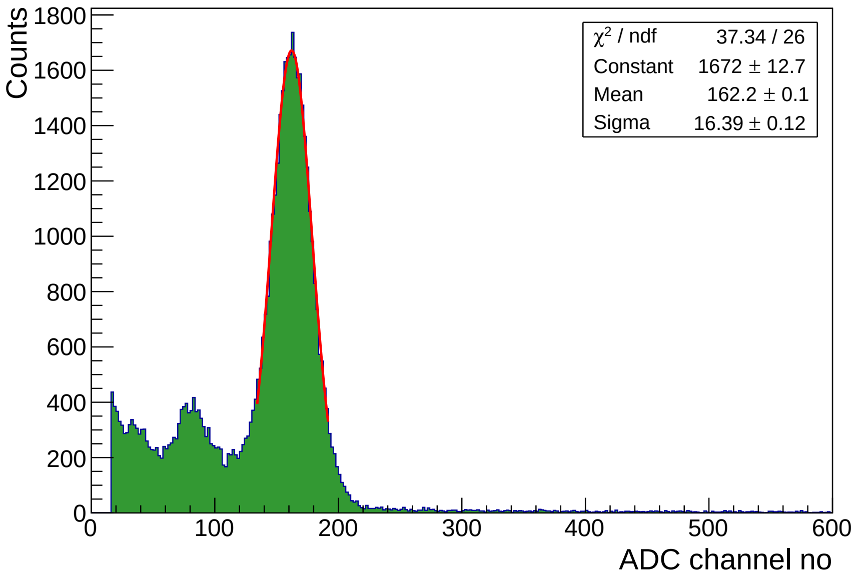

Figure 5.5: Energy spectrum of ^{55}Fe X-ray source of the MWPC-1 detector operated at 1800 V. The spectrum from anode signals using NIM electronics.

^{55}Fe radiation is also obtained using MANAS electronics setup, but here the spectrum is only from the pad. Since MANAS operates with a trigger, the anode signal is used to provide the trigger. However, the cosmic muons spectrum can be obtained from both anode and pad signals using MANAS. For the cosmic study, the trigger is provided using an external 3F scintillators setup as shown in Fig. 5.4. Cosmic muon spectrum as obtained from the anode and pad signals are shown in Fig. 5.6. The figure shows a good fitting with the Landau distribution. The MPV values of the spectrum in Fig. 5.6 shows that anode signal has a higher amplitude than the pad signal. From the figure, it is also notable that in the anode spectrum a small peak around 1600 ADC channel is found which is corresponding to the charge saturation of MANAS.

The variation of the mean value of the ADC, which is proportional to the detector gain, corresponding to the 5.9 keV X-ray peak as a function of HV is shown in the left panel of Fig. 5.7.

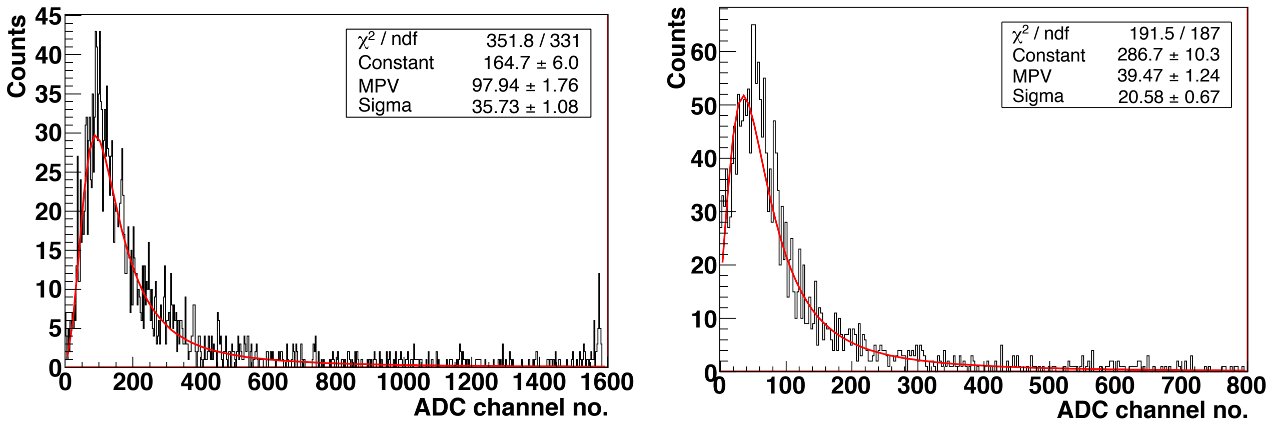

Figure 5.6: Cosmic muon spectrum of the MWPC-1 detector using MANAS electronics operated at 1850 V. The spectrum from anode in left panel and spectrum from pad in right panel.

The data points of the figure are fitted using an exponential function, which is characteristic of any gas detector in the proportional region. The mean ADC values of the readout pad are found

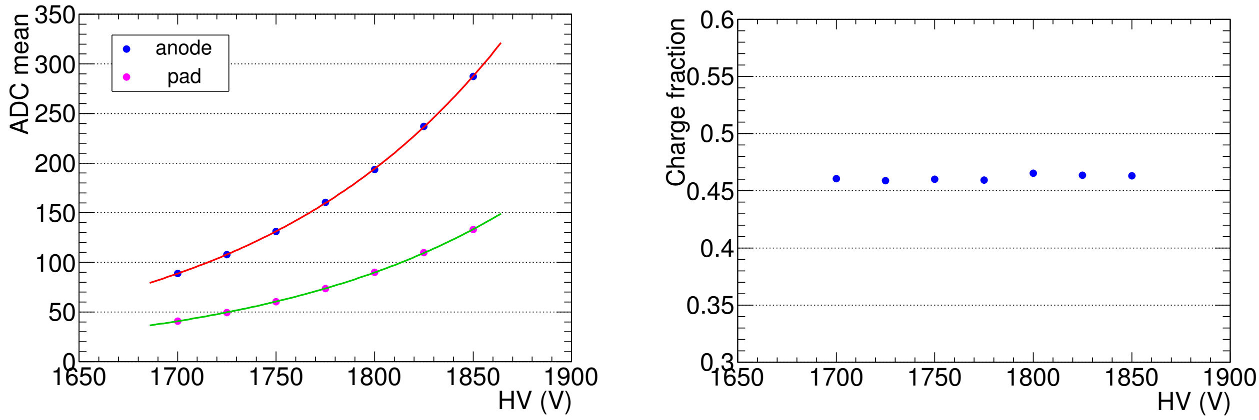

Figure 5.7: The variation of the ADC mean of the ^{55}Fe photopeak as a function of HV using NIM electronics in left panel and fraction of the avalanche charge induced in pad plane as a function of HV in right panel for MWPC-1 detector.

almost half of the mean ADC values of the anode. The reason for the low ADC value in the readout pad is equal sharing of the induced charge in between the drift plane and the readout pad plane. The fraction of the avalanche charge induced in the readout pad is shown in the right panel of Fig. 5.7. The observed value of charge fraction from the figure is $\approx 46\%$.

5.3.2 Gain and energy resolution measurement

The gain of the MWPC-1 is calculated from main the photopeak of the ^{55}Fe spectrum using both NIM and MANAS electronics. The anode spectrum of the NIM electronics and the pad spectrum of the MANAS electronics are used in the gain calculation. The obtained gain using both the electronics are shown in the left panel of Fig. 5.8. The gain estimation using the MANAS electronics is shown with two sets of threshold voltages $V_{th} = 60$ mV and $V_{th} = 80$ mV. It is found that with the $V_{th} = 80$ mV the gain values are deviating from the exponent nature at lower HV. But, with the $V_{th} = 60$ mV setting the exponential nature of the gain is maintained at the lower side of the HV also. Here the argument is the signals are cutting off with the high threshold set at the lower side of the HV. The obtained gain from the NIM and MANAS electronics are a bit different that might be due to a different setting and different environment (time) of the measurements. The energy resolution (in terms of FWHM) of the MWPC is calculated from the anode spectrum (in NIM) of ^{55}Fe as shown in the right panel of Fig. 5.8. The energy resolution of the detector is found almost constant about 24% for 5.9 keV X-ray.

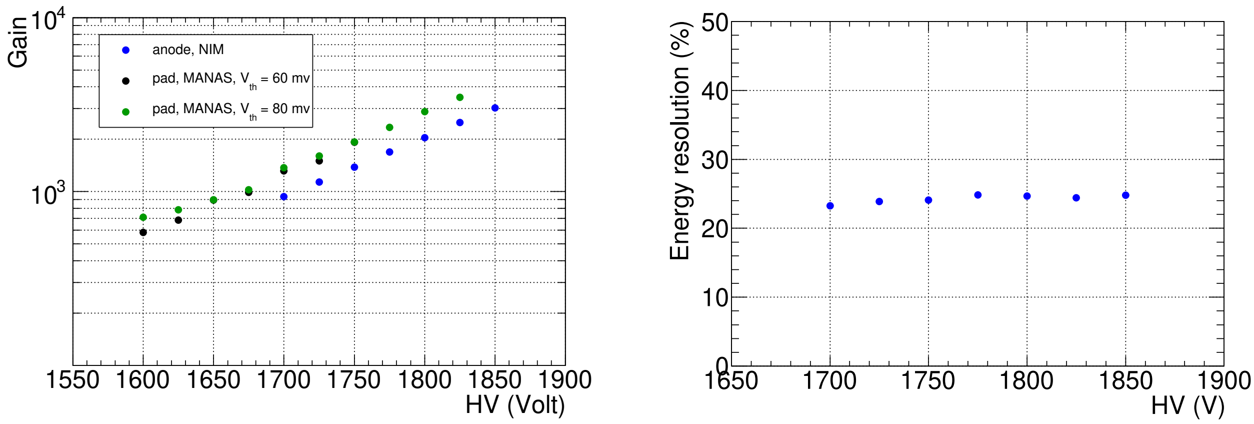

Figure 5.8: Measurement of gain using NIM and MANAS electronics in left panel and energy resolution (FWHM) of ^{55}Fe energy spectrum as a function of HV in right panel for the MWPC-1 detector. The measurements with Ar/CO_2 70:30 gas.

5.4 MWPC-2 detector test results

In the MWPC-1 detector, the drift plane was made of copper cladding glass epoxy of thickness 1.5 mm. In addition, for the solid support and noise shielding both side copper laminated FR4 plate of thickness 2.6 mm was used as a base plate. Therefore, the overall material budget of the detector was high enough to get an external trigger using the β^--source. Therefore the efficiency and time resolution measurements were not possible using the β^--source with this detector.

We fabricated MWPC-2 detector with low material budget. The thick drift plate is replaced by a copper clad kapton foil of thickness 100 μm and the additional base plate is removed. The efficiency and time resolution using the β^--source are successfully measured with this new detector. All the tests of the MWPC-2 are performed using Ar/CO_2 gas mixture of 70:30 and 90:10 ratio in flow mode at laboratory temperature and pressure. All tests are performed using standard NIM electronics only. The test results of the detector as discussed below are reported in Ref. [106].

5.4.1 Efficiency measurement

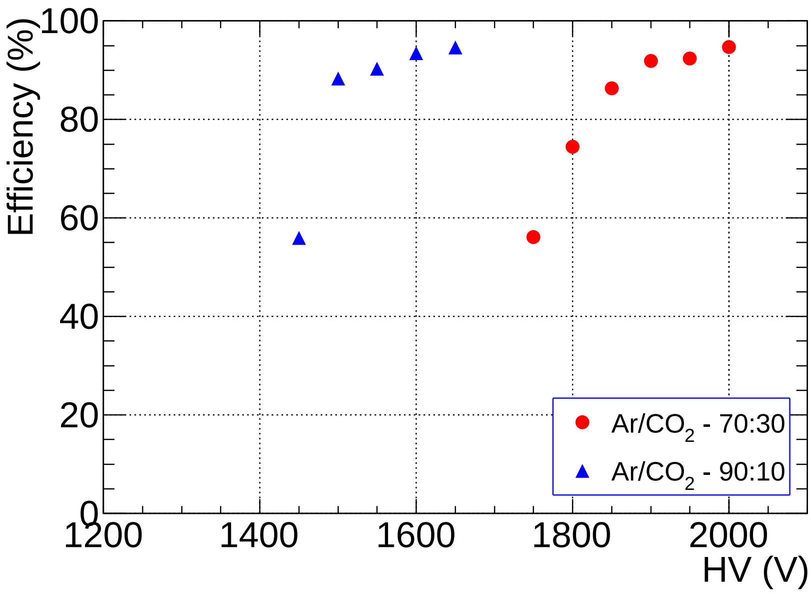

Figure 5.9: Efficiency as a function of HV of the MWPC-2 detector. The measurement performed using Ar/CO_2 70:30 and 90:10 gas mixtures.

The efficiency of the detector is measured using a ^{106}Ru-Rh β^--source. A 3F scintillators setup is used for providing the trigger in efficiency measurement. Efficiency as a function of applied HV is shown in Fig. 5.9. The efficiency at the plateau is $\approx$ 94% for both Ar/CO_2 gas mixtures. The voltage corresponding to the plateau region in the efficiency plot is the operating voltage of the detector.

5.4.2 Gain and charge fraction study

The gain measurement of the MWPC-2 is also performed, similar as MWPC-1, using spectrum analysis of ^{55}Fe source. The gain variation of the detector as a function of HV is shown in the right panel of Fig. 5.10. High gain value at low HV is found for the Ar/CO_2 90:10 gas in comparison to Ar/CO_2 70:30. The difference in the gain of the gas mixtures is due to the different percentages of the quencher are added in the gas mixtures. The fraction of avalanche charge induced in readout pads is found to be about 47% and 48%, respectively, for Ar/CO_2 90:10 and 70:30 gas mixtures as shown in the right panel of Fig. 5.10.

The correlation plot between the gain and efficiency of the MWPC detector is shown in Fig. 5.11. From the figure, it is found that the detector has efficiency plateau at a gain value $\approx$ 5000 irrespective of the type of the gas mixtures used. The result is found very similar to our GEM studies. Therefore,one can conclude that the efficiency depends only on the gain of the

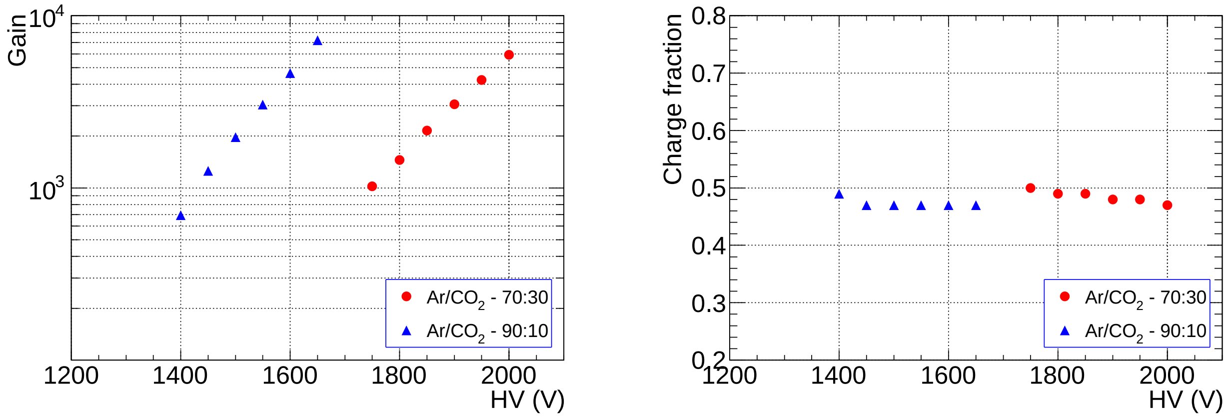

Figure 5.10: The gain as a function of HV for Ar/CO_2 90:10 and 70:30 gas mixtures in left panel and the fraction of the avalanche charge induced in the pad as a function of HV in right panel for the MWPC-2 detector.

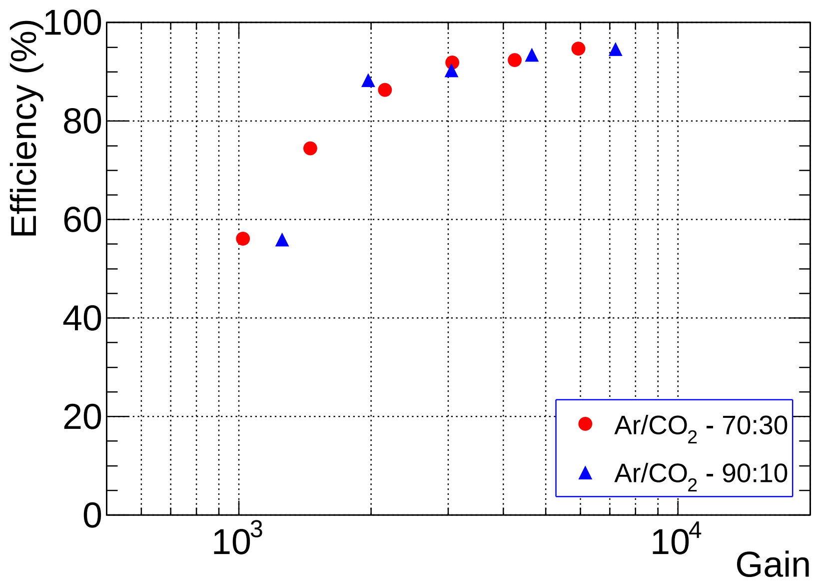

Figure 5.11: Efficiency as a function of Gain of MWPC-2 detector.

detector irrespective of the gases applied. The critical value of the gain at the efficiency plateau might depends on the readout electronics.

5.4.3 Time resolution measurement

The electronics modules and the setup for the time resolution measurement are similar as described in Section 4.1.6. The ^{106}Ru-Rh β^--source is used for the 3F external trigger which provides the start signal and the detector signal from a TFA output is used as the stop signal for the ORTEC 567 Time to Amplitude Converter (TAC) module. The time spectra of the MWPC are taken at different voltages and with both the gas mixtures. The obtained time spectrum at 2075 V for Ar/CO_2 70:30 gas is shown in the left panel of Fig. 5.12. The time resolution as a function of HV is shown in the right panel of Fig. 5.12. The best value of time resolution (σ_t) $\approx$ 10 ns is obtained with our detector. The resolution may be further improved using the time walk correction; however, that could not be implemented with the electronics used in the measurement.

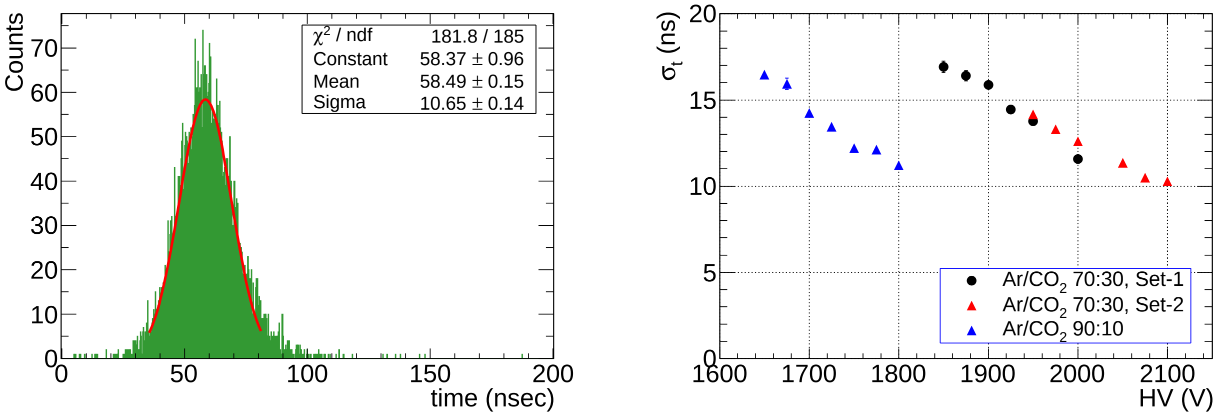

Figure 5.12: Time spectrum of MWPC-2 at 2075 V for Ar/CO^2 70:30 gas in left panel. Time resolution variation as a function of applied HV for Ar/CO_2 90:10 and 70:30 gas mixtures in the right panel.

This chapter can be summarized as fabrication and characterization of the MWPC detectors are performed. The gain, energy resolution and time resolution have been measured with two MWPC detectors. The detectors are tested using the standard NIM and MANAS electronics setup. The fraction of the charge sharing measured in both the MWPCs have very similar results. The gain *vs* efficiency plot has good agreement with the results obtained for the GEM detector.

Chapter 6

Towards ALICE TPC upgrade

The Time Projection Chamber(TPC), invented by D. R. Nygren in 1974 [107], is a charged particle tracking detector. TPC is useful for three-dimensional vertexing of the charged particles. In particle physics experiment [30, 100, 108–111], rare event search in dark matter experiments [112, 113] and for neutrino search [114–116] TPC has been used. The cylindrical design TPC is considered in most experiments, though, a cuboid shape is also found useful. The sensitive volume of the TPC is filled with a gas or liquid. In this chapter, I will discuss about the current ALICE TPC detector, its performances with MWPC and gating grid based readout, limitation of the existing TPC readout system, upgrade of the TPC detector to cope up with LHC Run-3 collision rate. GEM is chosen for the low IBF and low discharge probability of the TPC whereas the proper gas choice for future TPC is also very crucial. All of those will be discussed in detail in this chapter.

The main activity of the TPC upgrade is its chamber production and test performances. All the basic and advanced quality assurance tests of the GEM foils, its framing, chamber assembly and test methods are quite interesting. The chamber production and test results are discussed in detail in the section.

6.1 Working principle of a Time Projection Chamber

The schematic design of a cylindrical TPC detector is shown in Fig. 6.1. In one end of the TPC has a cathode plane, and on the other end it has an anode plane with 2D ($r, \phi-$plane) readout. When an energetic charged particle is passing through the TPC volume, it ionizes the gas along its path. With the application of -HV on the cathode plane a drift electric field of a few 100 V/cm is produced in parallel to the axis of the cylinder. The primary electrons drift towards the anode following the drift electric field. The electrons have charge amplification close to the readout anode. Wire plane or other micro-patter elements like GEM or Micromegas are useful for electron amplification. The induced signal of charge amplification provides 2D position (x, y or r, ϕ) information. The $z-$coordinate of the ionization is calculated from the drift time t of the electrons,

$$z = (t_a - t_0)\, v_d, \tag{6.1}$$

where, t_a is the time of arrival at anode plane, t_0 is the time of the incident particle passed through the TPC (trigger time) and v_d drift velocity of the electron in TPC gas. In particle physics experiment the collision time is taken as t_0. A high magnetic field $\vec{B}$ in parallel to the electric field $\vec{E}$ is also applied for the momentum measurement of the incident particle. The charge and momentum of the particle are calculated from the curvature of the track and $\vec{B}-$field. The dynamic of a charged particle in the presence of $\vec{E}-$ and $\vec{B}-$field is given by the *Langevin's equation*,

$$\vec{u} = \frac{e}{m}\tau|E|\,\frac{1}{1+\omega^2\tau^2}\left(\hat{E} + \omega\tau\left(\hat{E}\times\hat{B}\right) + \omega^2\tau^2\left(\hat{E}.\hat{B}\right).\hat{B}\right), \tag{6.2}$$

where e and m are the charge and mass of the particle, respectively. τ is the mean collision time and $\omega = \frac{e}{m}B$ is the *Larmor frequency*.

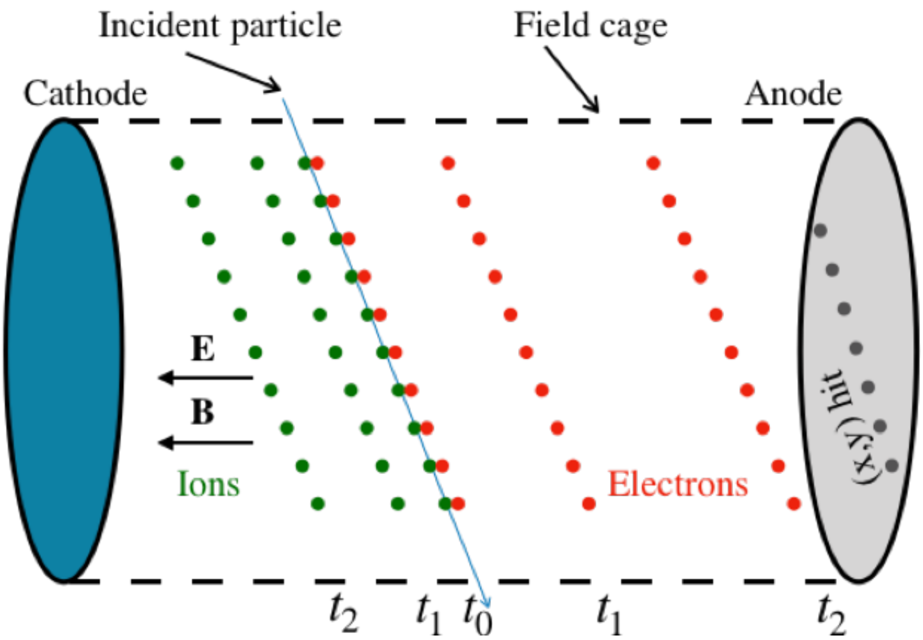

Figure 6.1: Schematic of the TPC detector. The red and green bullets are corresponding to the electrons and ions. Positions of the electrons at different time $t_2 > t_1 > t_0$.

The drift length of the TPC can be as long as a few hundreds of cm (in ALICE TPC 250 cm). A field cage, which consists of conducting rings around the cylinder, is used from cathode to anode. The usefulness of the field cage is to maintain uniform electric field between cathode and anode so that distortion in electrons drift track is minimum. The drift velocity v_d and hence the determination of the particle position has dependency on the electric field.

TPC fill with gas is useful for tracking and momentum measurement where the low material budget is the primary interest. Gas-filled TPCs already have been used in many experiments for examples PEP-4 [108], ALEPH [109], DELPHI [110], NA49 [111], and are presently being employed, e.g., in STAR [100] and ALICE [30]. Nobel liquid (ex. liquid Ar), as well as liquid and gas (dual phase), are also used as an active medium in TPC [114–117]. Such TPC works with the same principle as described for the gas-filled TPC. Here much denser material (1000X than noble gas) is used for searching rarely interacting particles. Liquid TPC is being used for rare event search in dark matter experiment, neutrino detection study [112–117].

6.2 ALICE TPC detector

ALICE is a dedicated experiment at CERN for heavy-ion physics program. The main objective of ALICE is searching QGP and its associated physics. The main central barrel detectors are ITS which is a silicon detector and TPC. The schematic layout of the ALICE experiment is as shown in Fig. 2.1. It can be found in the figure that the TPC is a hollow cylindrical detector positioned just outside covering the ITS. TPC is the main charged particle tracking device in ALICE. A brief about the ALICE TPC is described in this section. However, the detailed about it can be found elsewhere [30].

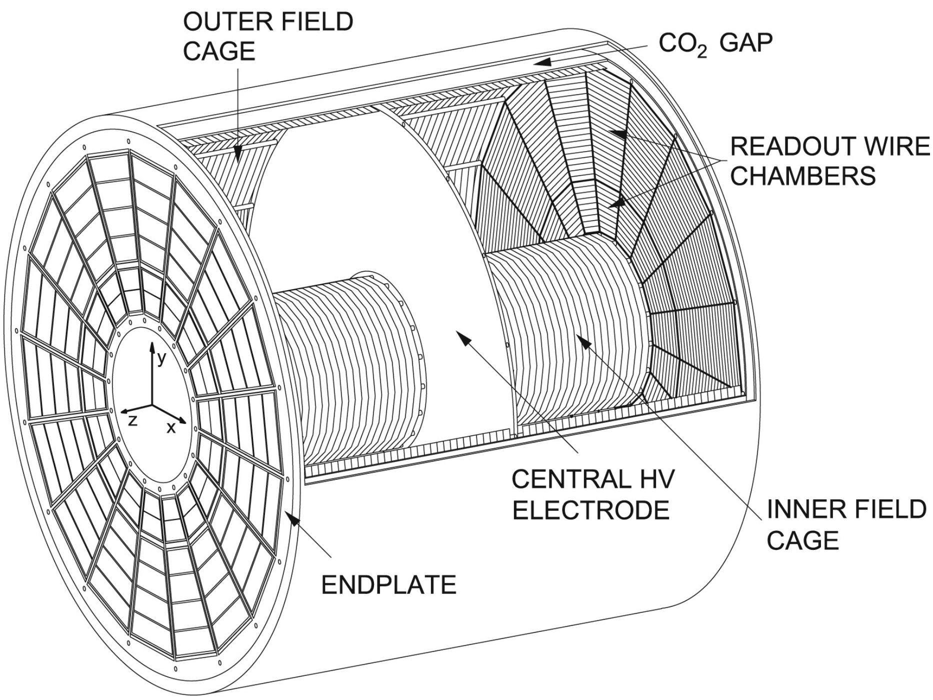

Figure 6.2: Schematic 3D design of the ALICE TPC detector. The high voltage electrode is located at the center of the drift volume. The endplates with 36 (18 × 2) readout chambers on each end are shown. The figure is adopted from [118].

6.2.1 TPC geometry and environment

The schematic design of the ALICE TPC detector is shown in Fig. 6.2. The inner and outer radii of the TPC is 85 cm and 2.5 m, respectively, with a length of about 5 m. The detector has a gas volume of $\approx$ 90 m^3. On both the endplates of the TPC, it has trapezoidal shape readout chambers (ROCs) each has 20^o azimuthal coverage. *Inner ReadOut Chambers* (IROCs) and *Outer ReadOut Chambers* (OROCs) are mounted on the inner side and outer side of both endplates. The total number of chambers are 2×18 for each side. The ROCs are using MWPCs currently. A central cathode plane (in $r, \phi-$plane) of the TPC divide the gas volume into two halves with drift length of 2.5 m in each. The anode consists of wire planes followed by the pad plane for the signal induction. The drift gas Ne/CO_2/N_2 90:10:5 (in 2009 – 2010), Ne/CO_2 90:10 (in 2011 – 2013) in Run-1 and Ar/CO_2 88:12 (in 2015 – 2018) in Run-2 have been used. A high voltage of 100 kV is applied to have drift field 400 V/cm for drifting the electrons towards the anode. A circular field cage from the cathode to anode is required to maintain uniform field throughout the drift volume as shown in Fig. 6.1. A constant magnetic field $B = 0.5$ T in parallel to beam axis is applied for the charged particle bending. Constant pressure and temperature throughout the drift volume are also very crucial since drift velocity depends on those parameters.

6.2.2 Gating grid and limitation on data taking rate

The electrons drift to the anode plane where they have an immediate avalanche. An induced signal associated with the avalanche is formed in the readout pads. A total of 0.55 million readout pads cover the full azimuth for data taking. The electrons are immediately collected to the anode wires whereas ions start to drift back to the central cathode. A gating grid (GG) technology has been used to stop the slow ions before they enter into the drift volume. GG is kept open for drifting electrons from cathode to anode whereas it is kept close to stop the ions moving into the drift volume. The open-and-close technique of the GG has successfully avoided the field distortion, which is generated by the slow ions, in the current TPC. More detail about the working method of GG, its position and bias voltage can be found in [30]. The maximum data taking rate of about 3.3 kHz can be reached with the GG. Since the electrons take maximum drift time $\approx$ 95 μs to travel the distance 2.5 m and the ion has a drift time $\approx$ 200 μs for moving from the anode to GG. It is already mentioned that the future ALICE goal is to increase Pb-Pb collision rate to 50 kHz in Run-3 and Run-4 to pursue its physics goals. The GG-based TPC will be replaced by GEM readout to achieve the future collision rate. The TPC with GEM readout will be discussed in detail in Section 6.3.

6.2.3 Performances of current TPC

ALICE TPC detector has a pseudorapidity $|\eta| < 0.9$ and full azimuthal coverage. Charged particle identification in TPC is possible from simultaneous measurement of the specific energy deposition dE/dx and its momentum. The momentum and charge sign of the particle can be calculated from the helix of the track in the presence of the B-field. Particle identification performances of the ALICE TPC is shown in Fig. 6.3. The dE/dx resolution ($\sigma_{dE/dx}$) of the ALICE TPC is

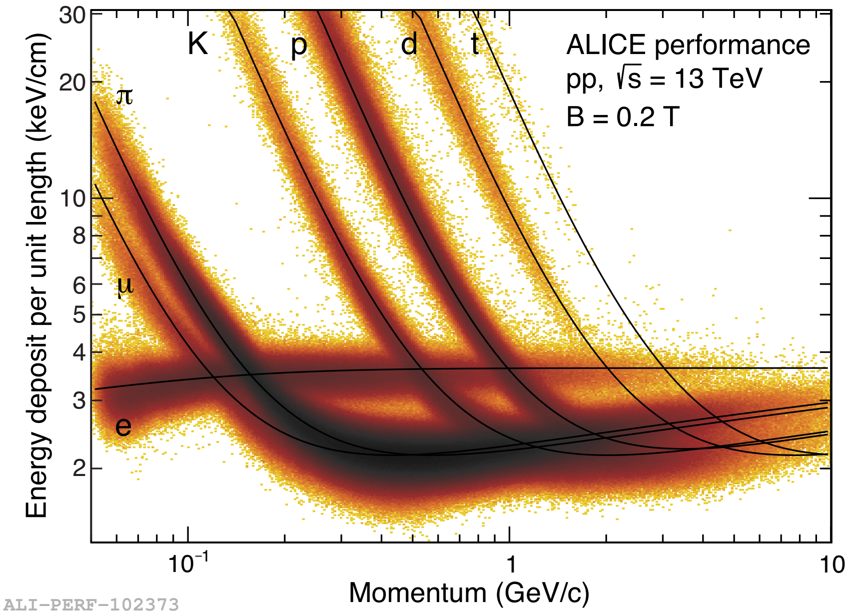

Figure 6.3: Particle identification performances of the ALICE TPC. Specific energy deposition dE/dx as a function of particle momentum [119].

5.2% and 6.5%, respectively, for the pp and Pb-Pb most central collision ($0-5\%$ centrality) [120]. dE/dx is calculated from the total charge integration on the readout. In Pb-Pb high multiplicity event $\sigma_{dE/dx}$ deteriorate because of the charge clusters overlapping. ALICE TPC has transverse momentum (p_{T}) resolution better than 7% for the particle with momentum 10 GeV/c. The p_{T} resolution can reach 2% for the particle of momentum 2 GeV/c [118]. However, particle identification becomes impossible for momentum < 200 MeV because of difficulties in track reconstruction due to multiple scattering.

6.3 ALICE TPC upgrade in LHC Run-3

The Pb-Pb collision rate limitation of the running TPC is about 3.3 kHz. Whereas, ALICE is going to increase Pb-Pb collision rate to 50 kHz to accumulate high statistics data for precise measurement of the rare probe physics [45]. The GG-based MWPC cannot overcome this high rate data taking challenge for LHC Run-3 and Run-4 starting from 2021. GEM [57] technology got immediate attention as a new readout solution for its intrinsic ion suppression facility [86, 87, 121, 122].

A prototype GEM-based TPC detector is proposed by the ALICE TPC Collaboration and tested in FOPI experiment, GSI, Darmstadt [122, 123]. Based on this results the collaboration pushed forward towards the development of the continuous readout for the ALICE TPC and ALICE TPC upgrade collaboration is formed [30]. Many R&D has been performed with prototype GEM detectors, simulation study and full-size IROC testing with test beam for the optimization of the future TPC chamber [75, 87, 88, 122, 124, 125].

A GEM-based TPC detector can handle high collision rate of LHC in Run-3. Whereas, the performances of the detector as dE/dx resolution and momentum resolution will be restored as the current MWPC based TPC. The energy resolution $(\sigma_E/E) \leq 12\%$ for X-ray of energy 5.9 keV at a gain of 2000 with IBF $< 1\%$ is optimized as an operational condition for the TPC. At recent, we have dE/dx performances of a full-size IROC prototype with test beam at the Proton Synchrotron (PS) at CERN. The test beam results of the IROC prototype with TPC operating conditions were satisfactory [126] which make confident for the chambers production towards TPC upgrade.

6.3.1 Gas choice

For the gas selection of the TPC, both the noble gases Argon and Neon with 10% CO_2 as a quencher have similar momentum and dE/dx resolutions. Where the space charge distortion is an essential concern for the TPC, Ar/CO_2 mixture is excluded. The mobility of Ar^+ ions in Ar gas is 1.52 $cm^2V^{-1}s^{-1}$, about three times lower than Ne^+ ions in Ne 4.08 $cm^2V^{-1}s^{-1}$. The presence of CO_2 in the gas mixture is not considered. Although both the gas mixtures have similar ion backflow (explained in next paragraph), because of the low mobility of Ar^+ large space charge distortion is observed even at two factors less gas gain [87]. The Ne/CO_2 90:10 gas starts amplification at the field around 4 kV/cm as shown in Fig. 6.4. Which cannot be stopped by further addition of CO_2 as a quencher because of electrons drift velocity rapidly decreases with increasing CO_2 percentage. Therefore, addition a little fraction of N_2 can solve both issues. $Ne/CO_2/N_2$ in 90:10:5 is chosen as the final TPC gas which has very similar gas property as Ne/CO_2 90:10 [30]. An admixture of CF_4 with Ne is also found a valid option. This is a very fast gas, which will reduce events pile up certainly. But thoroughly validated for compatibility with all materials of the detector and the gas system is yet to confirm. Some properties of a few useful gas mixtures which could be used in modern TPCs is shown in Table 6.1.

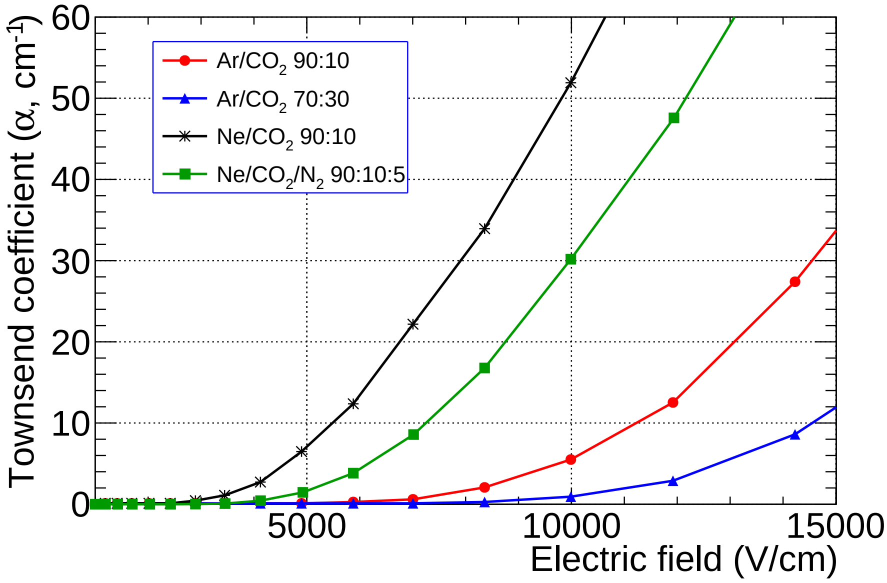

Figure 6.4: Townsend coefficients in different Argon and Neon-based gas mixtures as a function of the electric field is calculated using Magboltz software [97]. The avalanche shifted by 1 kV/cm upward with the admixture of N_2. The avalanche of Argon is sustainable away.

Gas	v_d (cm/μs)	D_L ($\sqrt{\text{cm}}$)	D_T ($\sqrt{\text{cm}}$)	$\omega\tau$	W_i (eV)	N_p (cm^{-1})	N_t (cm^{-1})
Ne-CO_2-N_2 (90:10:5)	2.58	0.0221	0.0209	0.32	37.3	14.0	36.1
Ne-CO_2 (90:10)	2.73	0.0231	0.0208	0.34	38.1	13.3	36.8
Ne-CF_4 (90:10)	8.02	0.0152	0.0131	1.77	37.7	15.7	42.7
Ne-CF_4 (80:20)	8.41	0.0131	0.0111	1.84	37.3	20.5	54.1
Ar-CO_2 (90:10)	3.31	0.0262	0.0221	0.43	28.8	26.4	74.8

Table 6.1: Properties of some useful gas mixtures which may be appropriate in modern TPCs: drift velocity v_d and longitudinal and transverse diffusion coefficients D_L and D_T , evaluated at a field of 400 V/cm; $\omega\tau$ factor, effective ionization energy W_i , number of primary electrons per MIP N_p, and total number of electrons per MIP N_t [30].

6.3.2 Ion backflow (IBF)

Stopping the ion backflow is the main challenge of the GEM readout TPC. Many groups have performed IBF studies with triple GEM detector. Ion backflow studied of the single and double GEM detector by Bachmann *et al.* [91]. IBF study performed for the triple GEM detector shows drastically drop-down of the IBF $\approx$ 4% as reported in [121]. In more recent time IBF study using standard triple GEM is performed dedicatedly for ALICE TPC upgrade [87, 122]. The measurements have been done for both Argon and Neon-based gas mixtures. The most suitable choices in the gases are found Ar/CO_2 90:10, Ne/CO_2 90:10 and Ne/CO_2/N_2 90:10:5 having similar IBF performances ($\approx$ 3%) [87]. However, Ar/CO_2 gas mixture is discarded because of the significant space charge distortion due to low ion mobility. Ne/CO_2/N_2 90:10:5 gas has been chosen because of high mobility and stable operation. From the simulation study, it is found that adding the fourth GEM foil IBF can reduce to TPC requirement limit. Two large pitch (LP, 280 μm) GEMs are placed between the standard pitch (SP, 140 μm) GEMs with a gap of 2 mm in between the foils. The LP foils stop a significant fraction of the ions successfully. This spacial quad GEM stack, SP-LP-LP-SP, allowed to reach the IBF $< 1\%$ with $\sigma_E/E \leq 12\%$ for 5.9 keV X-ray at a gain of 2000. The GEM voltage setting and the electric field in the gaps for the ALICE TPC are summarized in Table 6.2. The results of IBF measurement using a quad GEM is shown in Fig. 6.5.

Drift field (E_d)			0.4 kV/cm	
		U_{GEM1}		270 V
Transfer field 1 (E_{tr1})	2 mm		4.0 kV/cm	
		U_{GEM2}		250 V
Transfer field 2 (E_{tr2})	2 mm		2.0 kV/cm	
		U_{GEM3}		270 V
Transfer field 2 (E_{tr3})	2 mm		0.1 kV/cm	
		U_{GEM4}		340 V
Induction field (E_{ind})	2 mm		4.0 kV/cm	

Table 6.2: Typical GEM voltages and electric field settings in a quadruple GEM in $Ne/CO_2/N_2$ (90:10:5) at an effective gain of 2×10^3. Note the high transfer field in the 1^{st} and 2^{nd} gap, whereas E_{tr3} is very low. The potential of GEM4 is high compared to others.

The movement of electrons and the ions are highly depended on the electric field configurations. To stop the ions drift back to the drift volume, it is also necessary to have low U_{GEM1} and high field in transfer gap 1. The idea is to produce minimum ions within GEM1 and maximum transfer of the electrons to GEM2 for the second stage of amplification. Ion backflow and energy resolution as a function of GEM1 voltage are shown in Fig. 6.6. It is observed that the voltage of GEM1 U_{GEM1} has a significant role in energy resolution as well as ion backflow determination.

6.3.3 Discharge study

It is observed that the GEM detector has very low discharge probability with increasing the number of GEM stacks. A dedication discharge study performed especially for the ALICE TPC detector keeping in mind long-term operation in high radiation environment [46, 88]. Here the study is conducted using triple GEM and quadruple GEM detectors. Discharge of the triple GEM is measured using *standard setting*, where the electric field and GEM voltages have nominal values

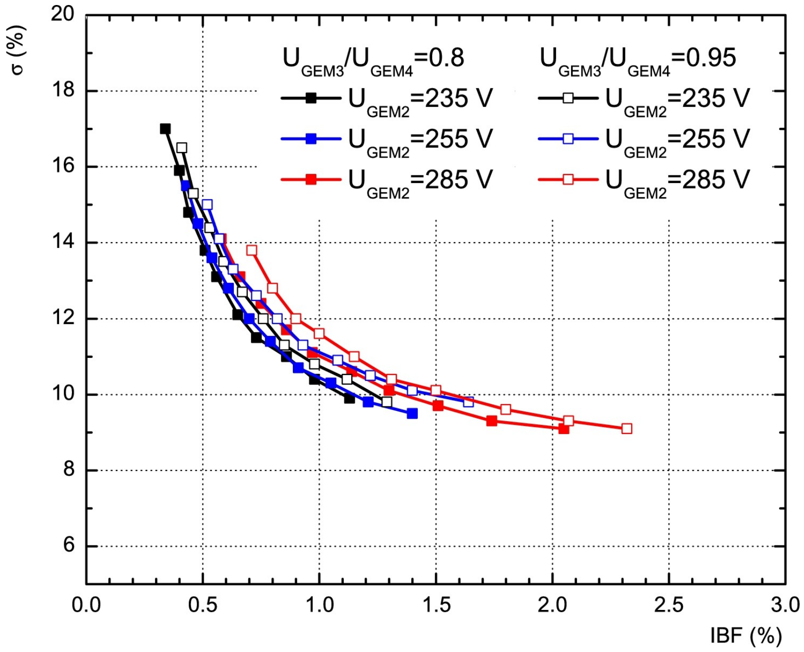

Figure 6.5: Correlation between ion backflow and energy resolution in a quadruple S-LP-LP-S GEM configuration in $Ne/CO_2/N_2$ 90:10:5 for various settings of ΔU_{GEM2}. The voltage on GEM1 increases for a given setting between 225 and 315 V from left to right. The voltages on GEM3 and GEM4 are adjusted to maintain the gain of 2000 while keeping their ratio fixed. The transfer and induction fields are 4, 2, 0.1 and 4 kV/cm, respectively [30].

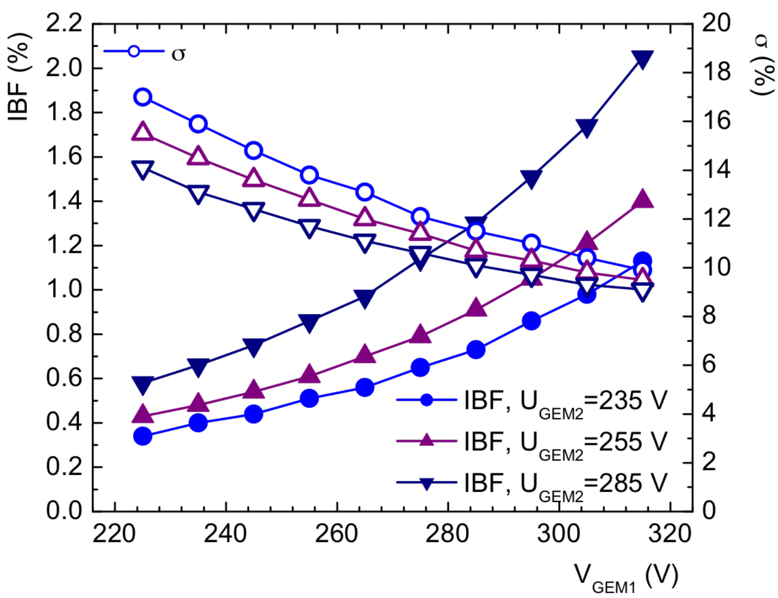

Figure 6.6: Ion backflow and energy resolution as a function of ΔU_{GEM1}, for various settings of ΔU_{GEM2}. The transfer and induction fields are 4, 2, 0.1 and 4 kV/cm, respectively, and the voltages on GEM3 and GEM4 are such that their ratio is 0.8 and the gain is 2000 [30].

and *low IBF setting* where field and GEM voltages are set for minimum ion backflow. From the results of Fig. 6.7, it is found that *low IBF setting* has a considerable degradation of detector stability, more than three orders of magnitude. The same measurement is performed for quadruple GEM detector in *low IBF setting* only. The results are shown in Fig. 6.8. The lowest possible

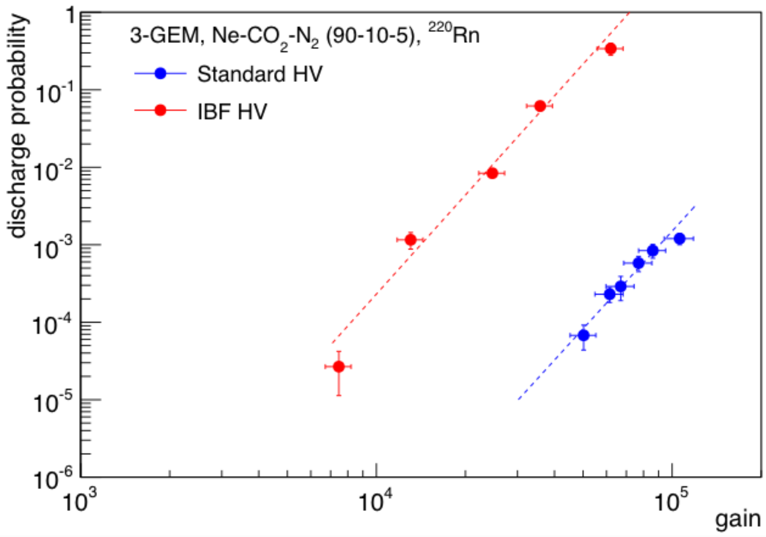

Figure 6.7: Discharge probability of a triple GEM detector measured for different HV settings. Dashed lines corresponding to power law function fits [88].

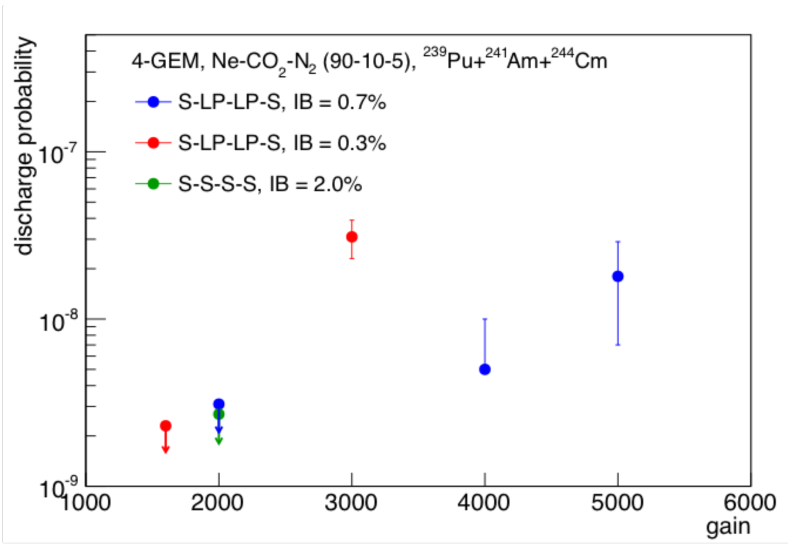

Figure 6.8: Discharge probability of a quadruple GEM detector measured for different gain. Corresponding values of ion backflow are indicated. Upper limits for discharge probability as indicated with arrows [88].

IBF ($\approx 0.3\%$) value will seriously affect the stability of the detector. From the results, it can be concluded that the 4-GEM configurations are more stable than the standard triple GEM operated in the low ion backflow mode. The upper limit of the discharge probability is 3×10^{-9} obtained for the SP-LP-LP-SP GEM configuration that is acceptable for TPC upgrade purpose.

6.4 Strategy of the readout chambers production for the TPC upgrade

Readout chambers (ROCs) production for the TPC upgrade contained many intense fabrication and test steps. All the steps in a single workstation are impossible as it requires many dedicated preparation and test systems and skilled manpower. As a practical solution, the total work-flow is distributed among many collaborative institutes; those have superior working people. The material flow of the ROC production among those institutes are shown in Fig. 6.9.

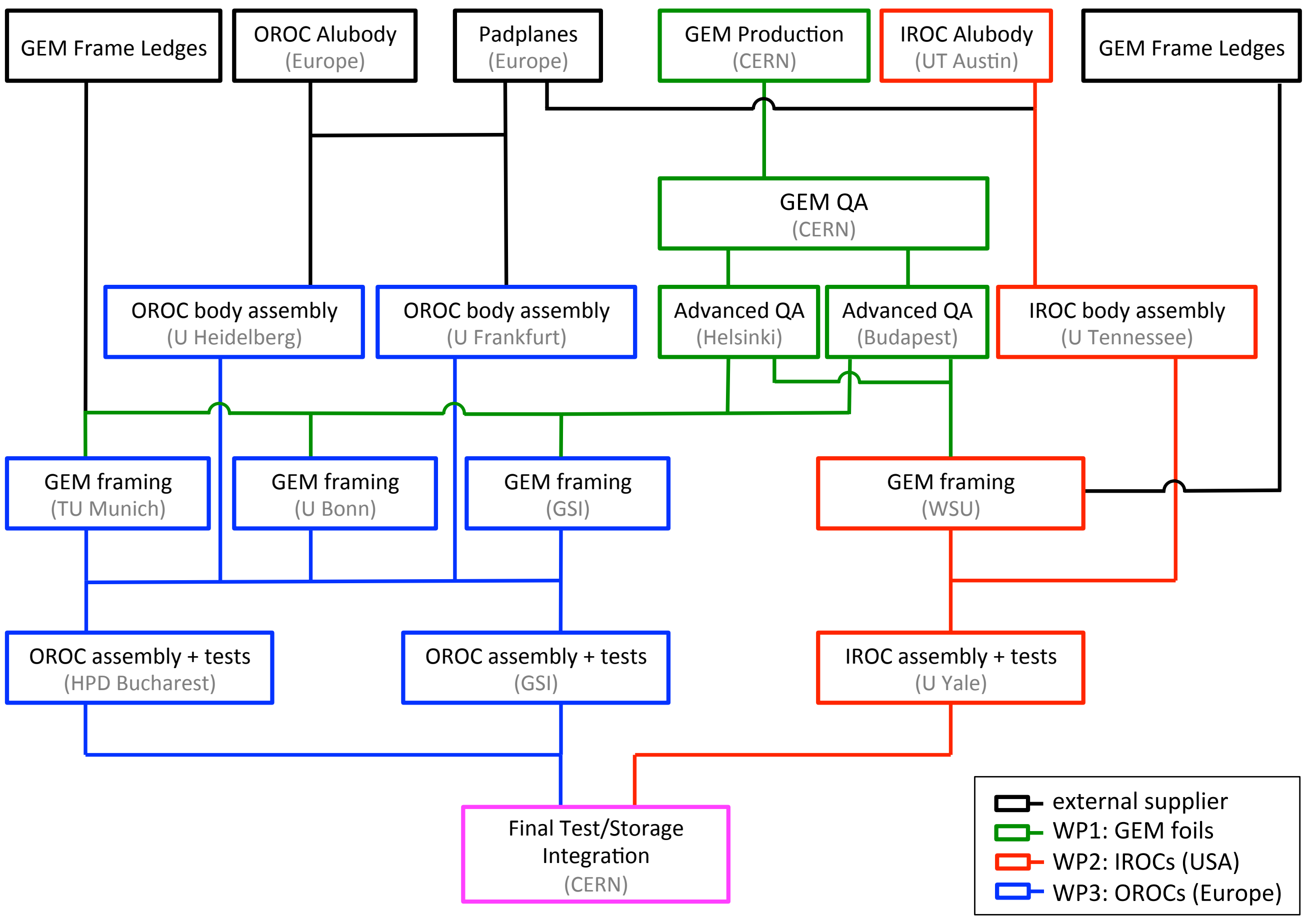

Figure 6.9: Material flow of the ALICE TPC readout chamber production. Picture adopted from ALICE TPC upgrade database.

6.4.1 A short description of preparation for the ROC assembly

GEMs are one of the main components of the TPC chamber production. All the GEM foils are produced in at CERN PCB lab. Due to the large size GEM foil production limitation, the OROC is physically divided into three sections named as OROC1, OROC2 and OROC3. A schematic design of the TPC ROC is shown in Fig. 6.10. All the GEM foils are segmented into an approximately equal area of 100 cm^2. The idea of segmentation is to localize the electrical short and protect the rest of the area from damage. A total of 576 GEM foils are required for the 36 chambers where 25% additional spares are also tested.

The quality assurance (QA) tests of the GEM foils is divided into two stages: *basic QA* test and *advanced QA* test. The purpose of the *basic QA* test is a quick inspection of the GEM foils locally (at CERN) and return the suspicious foils immediately to PCB lab. The *basic QA* test is involved in the visual inspection of the holes (accuracy $\approx$ 1 mm) for the chemical defect. The possible defects can be under etched, over-etched or missing of the holes. The next is HV cleaning and leakage current measurement for short-term (for 20 min). The HV (500 V) is provided to all the segments individually and the leakage currents of the corresponding are measured. The detailed procedure of the leakage current measurement is discussed in Section 6.5.1. The protection resistors mounting in between the HV line and GEM segments are also done at CERN. The nominal value of the resistors are 5 MΩ with a variation of 7% is accepted. It could be possible to have leakage current out of the limit, the electrical short or missing connection of the resistors. In either cases the foils are returned to CERN PCB lab for recleaning.

All the good foils that passed the *basic QA*, are transported to dedicated *advanced QA* centers. High definition (HD) optical scanning for the hole size distribution using an automated camera setup and long-term leakage current measurement for 5 hours test are considered in the *advanced QA*. All the foils passed *advanced QA* tests are mounted in a unique frame and stretched to ensure the flatness of the foil. The stretched foils are glued on a G10 frame. The details about GEM foil framing will be discussed in Section 6.5.2. The framed GEM foils are covered up by an envelope and stored inside a dry cabinet until the final use in the ROC assembly. The visual inspection and short-term current measurement are performed after each production steps and after the GEM transportation. The detailed discussion about the QA test and the ROC production can be found in [127, 128]. However, the production strategy is modified a little with time to time depending on urgency and new developments.

6.5 Production and test activity at GSI, Darmstadt

At GSI, Darmstadt, we dedicatedly perform the framing and QA tests of the GEM foils, assembly of the OROCs and then many different types of tests of the chambers. We received the GEM foils, which passed *advanced QA* tests in some other stations. The foils are stored into a dry cabinet to protect it from the environment. Before and after the framing the foils have to pass through a

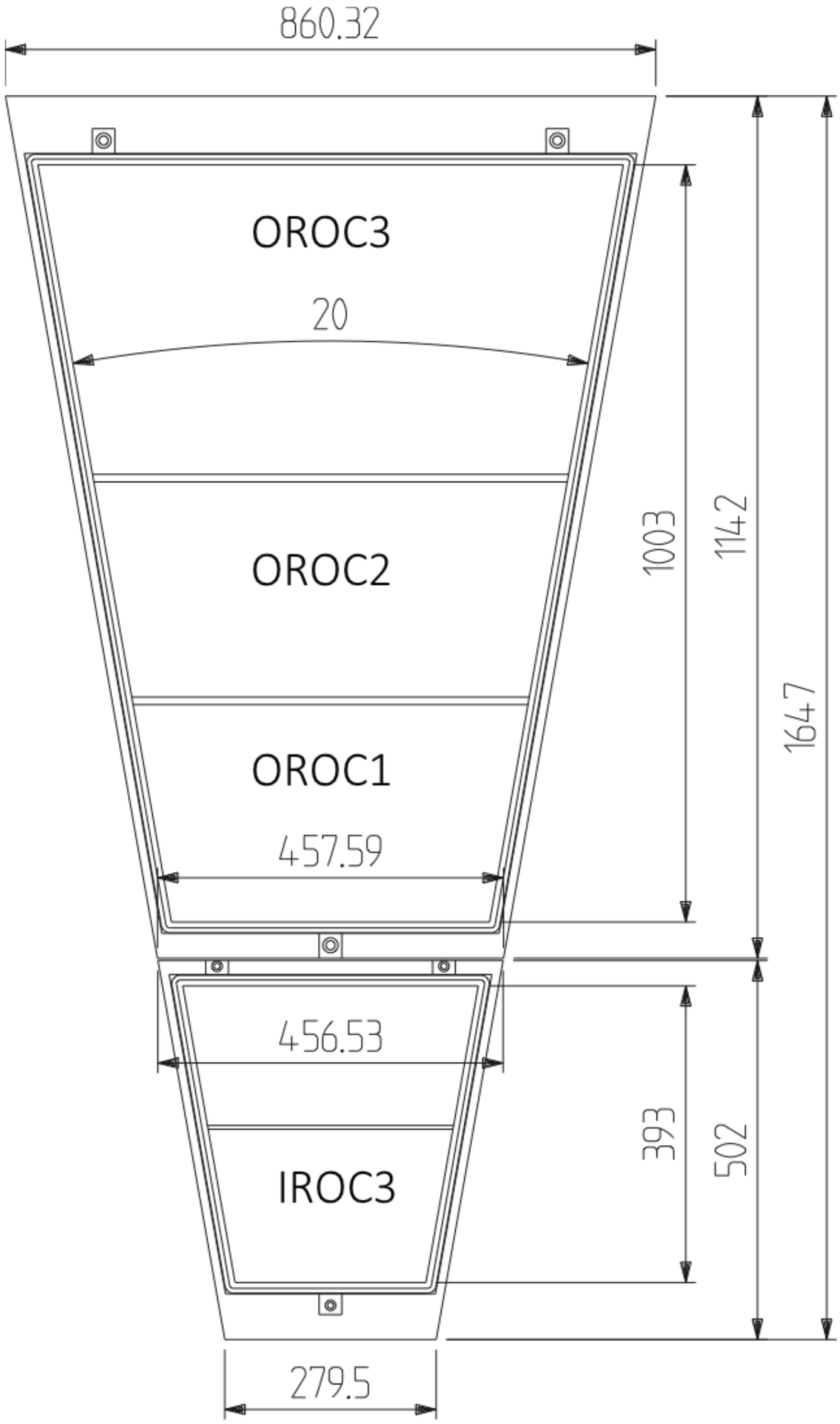

Figure 6.10: Design of TPC readout chamber. The dimension (mm) of the IROC and OROC are labeled. Each readout chamber cover 20^o. The figure is adopted from [30].

short-term leakage current test which ensures the electrical quality of the GEMs. Only the framed GEM foils, passed all the test steps that are used in OROC assembly.

6.5.1 Leakage current measurement of the GEM foils

The foils are cleaned from dust (or contaminants) using air blow before starting the leakage current measurement. The dust (or contaminants) might be attached on the foil during transportation and unpacking of the GEM foils. A dedicated HV box made of perspex is used for the leakage current measurement. Cleanness of the HV box and the HV drawer are ensured before placing the GEM foil inside the drawer. Good electrical connection of the HV pins with the GEM segments and resistor are checked using a multimeter. The resistance between the HV path and the GEM segments should be in the range of $4.65 - 5.35$ MΩ. Capacitance and resistance between the HV path and bottom side of the GEM (HV ground) are also measured to ensure no short. If the foils are found short or missing connection of the resistors, then those are sort out and send to CERN for repairing. If everything found normal, then the drawer with foil is placed inside the HV Box in N_2 environment. A hygrometer is put inside the box for monitoring the relative humidity. The GEM foil inside the HV drawer and the leakage current measurement setup inside the HV box is shown on the top and bottom panel in Fig. 6.11, respectively.

Preparation of the current measurement is begun once the relative humidity (RH) is below 10%. An HV of 500 V is applied immediately (without ramp up) across the GEM foil. The leakage current of all segments is read by Zagreb pico-ammeter, which measures very low current ($\sim$ pA) through the optical fiber. The duration of the short term current measurement is 1000 sec. Sometimes for the strategic change of the production, long-term current measurements for 5 hrs. also taking place in our station. Application of HV, current monitoring of individual segments and data capture are controlled using a LabVIEW based software. The LabVIEW based data monitoring and control window is shown in Fig. 6.12. The data are saved in an ASCII file for future analysis and uploaded in the common TPC upgrade database. After the measurement is completed, the foil is removed from the HV box carefully and put into a new envelope to store in the dry cabinet. However, there are many experiences with the foil having high leakage current in a particular sector. An attempt is always taken to bring back those sectors into good condition. The foils, cleaning by air blow or addition 100 V more than nominal voltage helped many times to recover the bad sector. One such example is shown in Fig. 6.13, which shows segment 22 of foil number O3-G1-23 had spurious current throughout the measurement. The leakage current becomes normal after cleaning the segment by air blow and applying 550 V. If still, the foil fails,

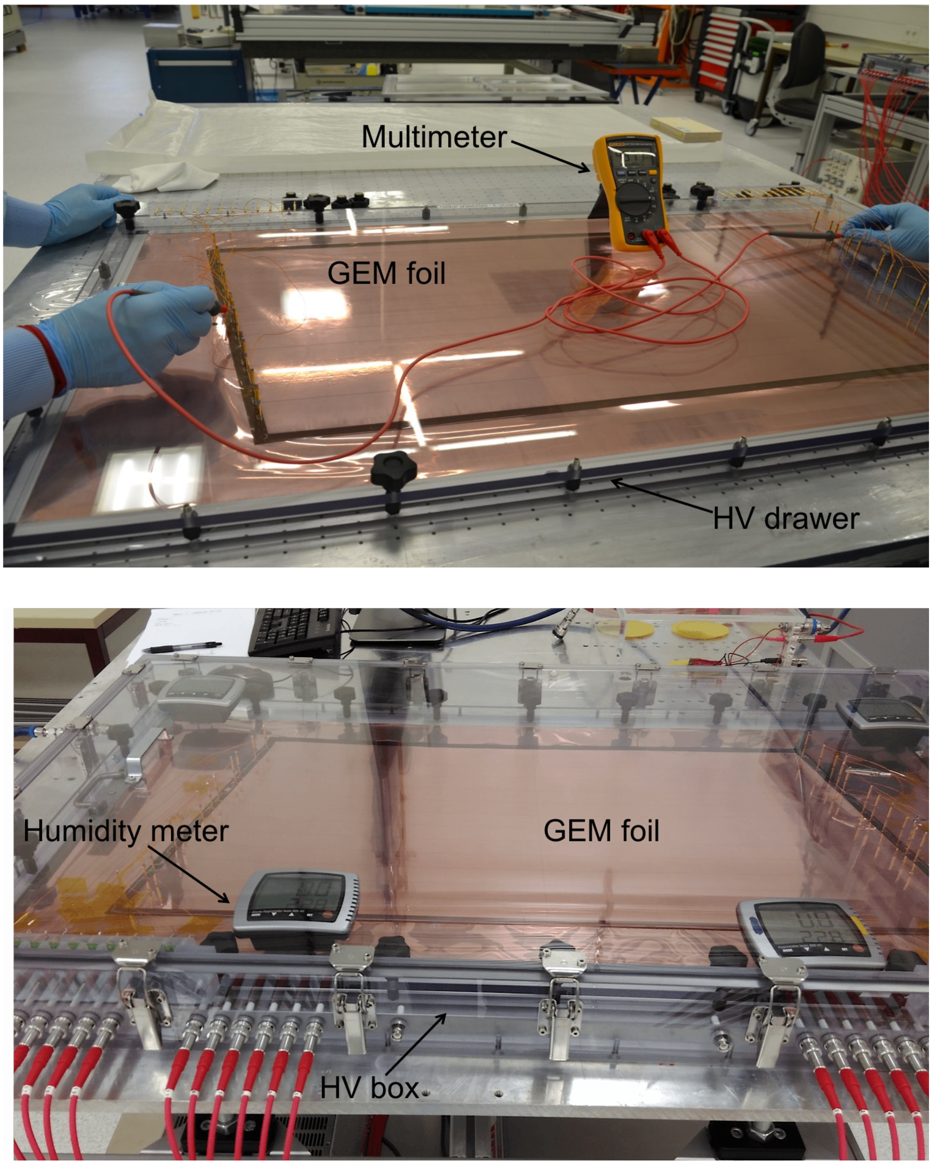

Figure 6.11: The resistance measurement of a GEM foil inside the HV drawer in top panel. Leakage current measurement of the GEM foil in HV box in bottom panel. Different components are labeled. N_2 gas flowed for dryness within the HV box.

then those are sort out and send back to CERN with comments for recleaning.

6.5.2 Framing of the GEM foils

We have a dedicated GEM framing tool at GSI. The ledges of the GEM frames are made of G10 material of thickness 2 mm. Four side ledges and two cross ledges are required for framing a single GEM foil. The ledges are checked about its appropriate fitting and cleaned by an ultrasonic bath in iso-propanal. The overlap area of the individual ledges are glued to a trapezoidal shape frame. The frame is left for 24 hrs. in a dry environment (N_2 gas flow) for good quality fixing of it.

The next step is to glue the GEM foil on the frame. The foil is put in a stretching frame to ensure sufficient flatness of the foil. The epoxy used is ARALDITE 2011. The glue is applied

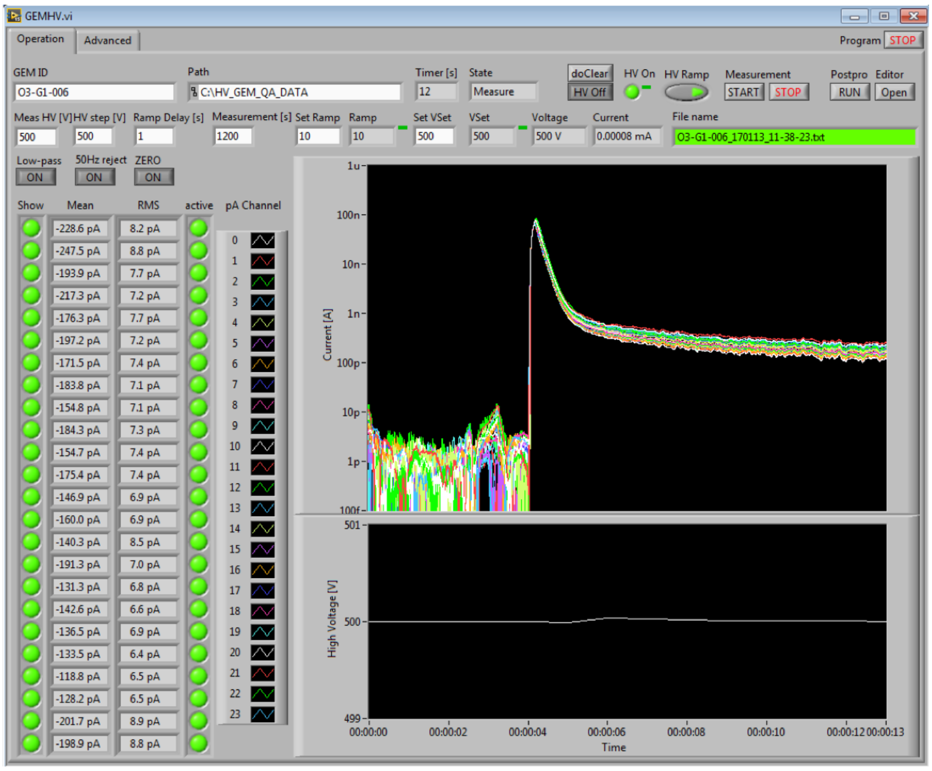

Figure 6.12: Current monitoring and data capture are done by LabVIEW software interface.

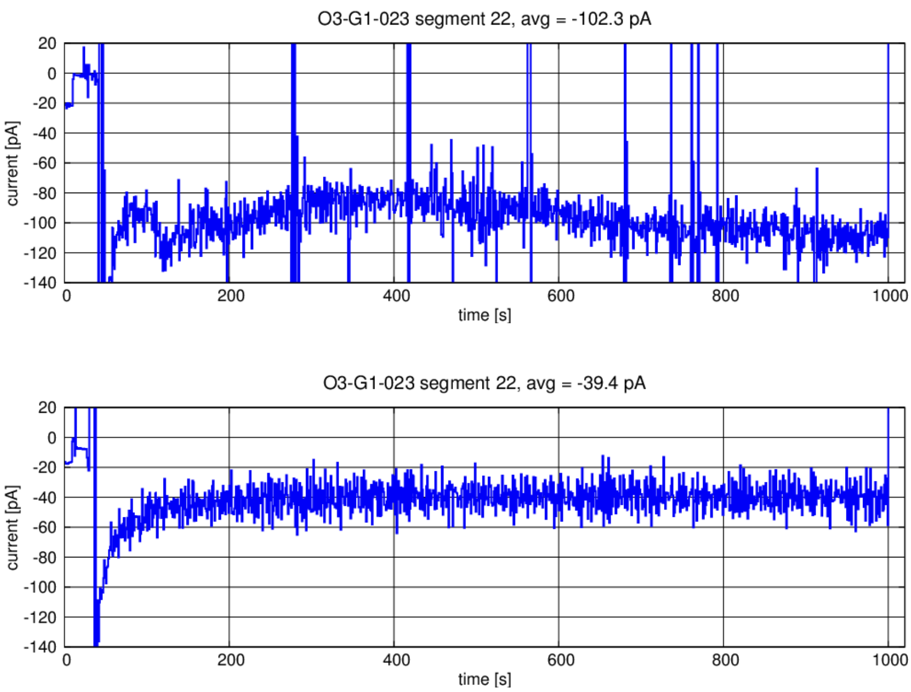

Figure 6.13: Sample plot, short-term leakage current measurement of individual GEM segment. The current plot on the top panel shows spurious current measurement. After recleaning the segment by air blow and tested with 550 V across it, current becomes normal as in the lower panel.

using a sticky roller on the correct side of the frame as shown in Fig. 6.14. Uniform distribution of glue over the frame is important. Attention required to refrain from over gluing, which might spread towards the active area of the foil and destroy the foil. Next, the GEM foil is put from

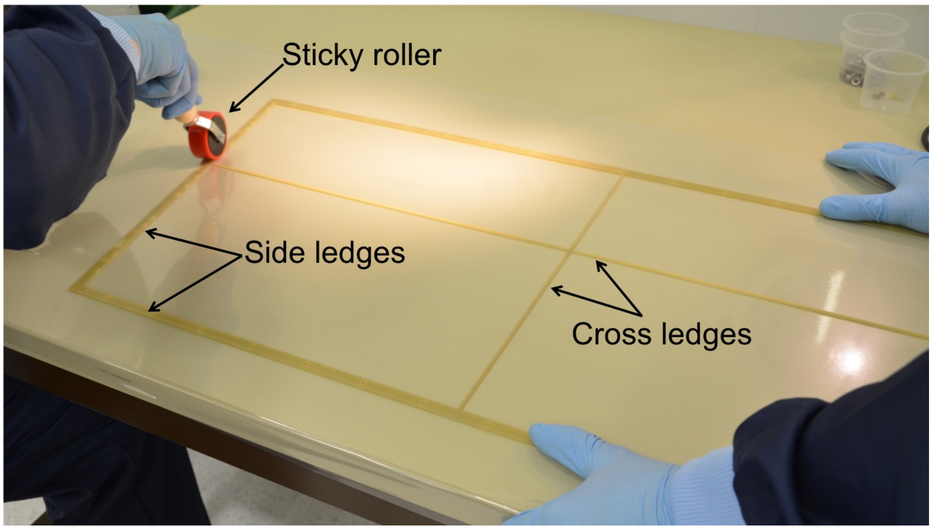

Figure 6.14: Gluing of the GEM frame.

the top on the glue side of the frame. The alignment of the foil and the frame is adjusted using a microscope from the top. With the help of steel bricks, a pressure about 0.5 kg/cm^2 is applied from the top for proper adhesive. The GEM framing procedure has to finish within ~ 15 min to prevent from humidity absorption of the glue. The GEM is covered by a big perspex box with N_2 flow to maintain dryness within the box and left for 24 hrs. as shown in Fig. 6.15. In the next day, the framed foil is removed carefully and short-term leakage current is measured. If everything seems fine, then the framed foil is stored inside a dry cabinet for future use in OROC assembly.

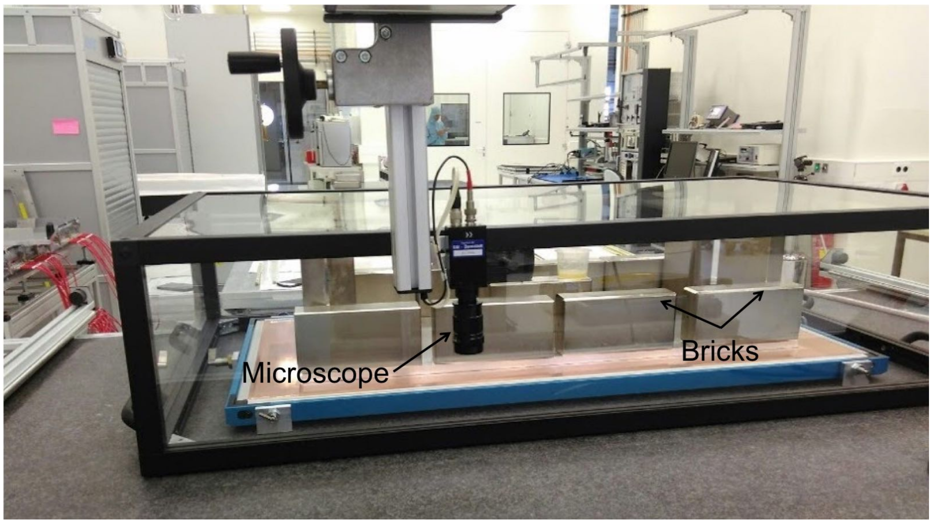

Figure 6.15: Gluing of the GEM foil. The foil is covered using a perspex box for keeping inside dry.

6.5.3 Assembling of the OROC

The readout pad plane along with a supportive aluminum flange is received from another institute. A special treatment is made to clean the flange and all the holes for tightening of the screws.

Throughout cleaning of the holes using iso-propanal, it has to be confirmed because metal dust can be found within the holes. The pad plane is cleaned by wiping with iso-propanal, air blow and sticky roller. All the pad connectors are plugged using the sorting cards into a single channel. Connectivity of the individual pads is checked. The HV tension test of the HV wires is also important. A voltage of 5 kV is applied to the individual HV wires in the air for electrical insulation test. The GEM foil is trimmed with a sharp scalpel keeping it slightly tilted for the sharp cutout at the frame. The outer cutoff part of the GEM is removed carefully. The frame might scrap during trimming, so the special care is taken for cleaning the edges of the frame using iso-propanal and air blow. GEM trimming example is shown in Fig. 6.16. Next is the

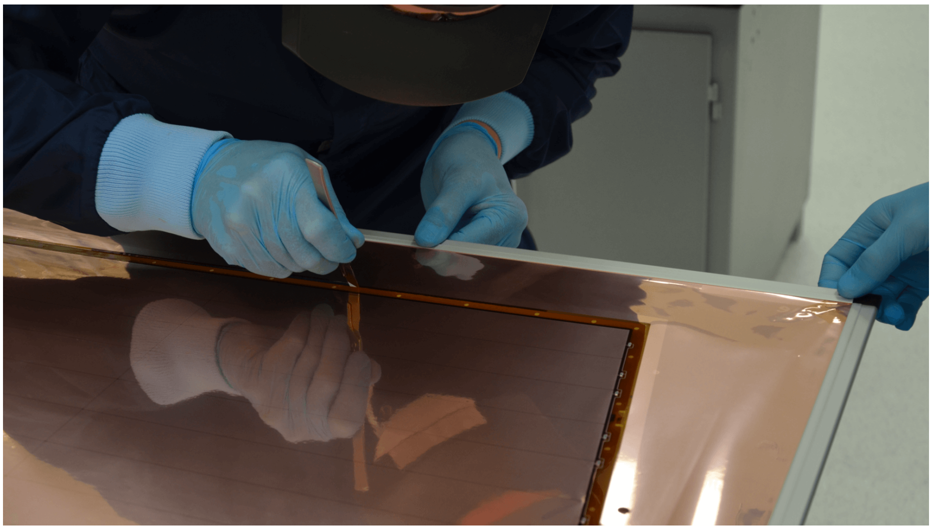

Figure 6.16: Cutout of the active area of a GEM foil.

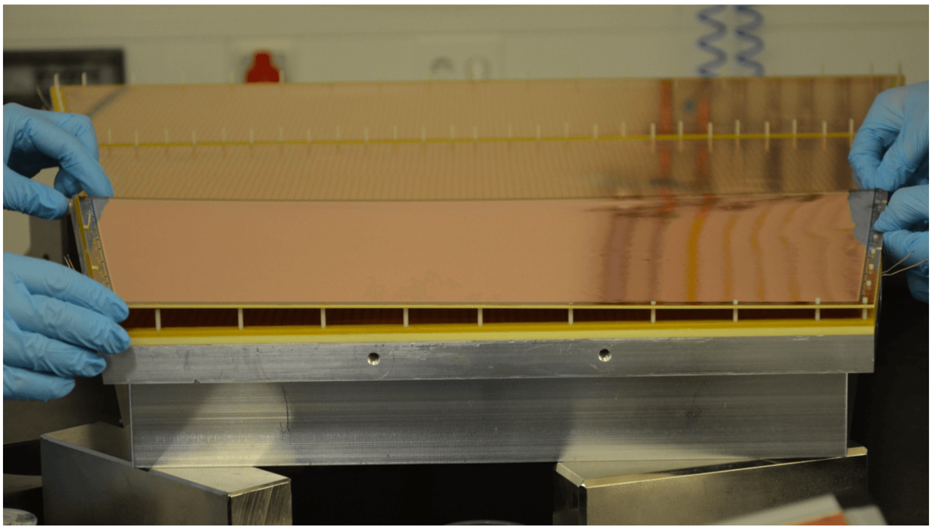

Figure 6.17: Stack of the GEM foils. Frame holes are aligned with the screw pillar.

mounting of the foil on the pad plane with proper alignment of the holes with nylon screws as shown in Fig. 6.17. Before that, the foil and the pad plane surface are checked with UV light

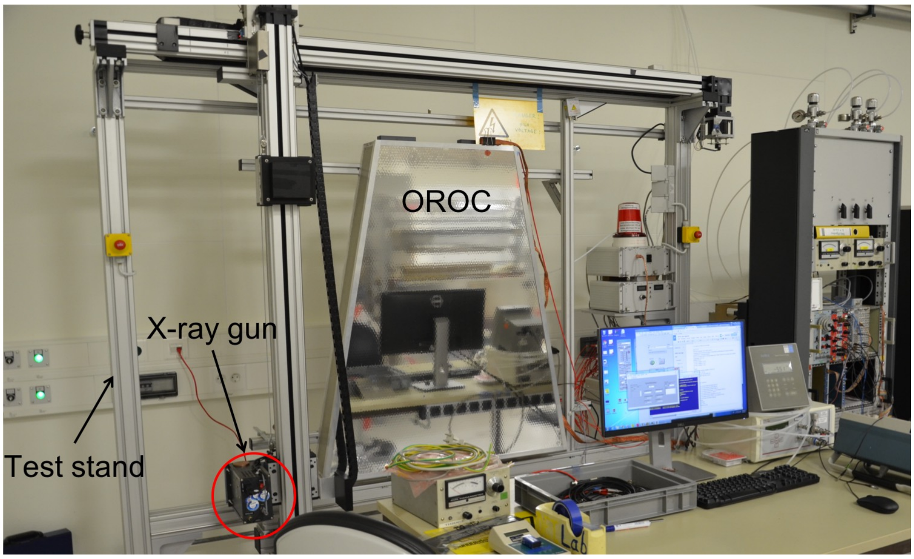

Figure 6.18: X-ray test station of the OROC.

test. Correct side of the foil must be noted. HV connection of the foil is made by soldering the HV wires. The procedure is followed in case of other three GEM foils also. By the mean time of cutout the foils, the readout chamber is covered by an aluminum plate to protect it from any mechanical damage or dust. Once all the four GEM foils are placed with correct order, those are tightened using washers and nuts. All three segments, OROC1, OROC2, OROC3, are assembled following the same processes. The readout chamber is then covered with a test box from the top and special care is taken during the tightening of the box for the gas tightness. After the chamber is assembled, it is moved to the testing station and hanged on to the X-ray test-stand as shown in Fig. 6.18.

6.5.4 Testing of the OROC

All the testing steps with the results of the OROCs are discussed in this section. At very first the chamber is kept in N_2 gas flow with a rate about 20 l/hr for few hours (exact time depends on the level of oxygen) to remove oxygen from it. Once the O_2 level is reached to $\lesssim$ 100 ppm, the gas is switched to Ne/CO_2/N_2 90:10:5 gas flow of rate about 10 l/hr. Before starting the X-ray test, the leakage current of the individual foils is measured at a voltage difference -250 V. The expected value of the leakage current is $\leq$ 1000 pA. However, the leakage current of the foils is found $\geq$ 2000 pA in some cases. We found that the gas flushing of the chamber for a longer time is helpful to bring down the leakage current below the limiting value. If the current is constantly out of the limit, then the foil is required to replace.

Once the leakage current measurement is found satisfactory, we did the X-ray test of the chamber. With the help of a robotic X-ray gun, the $x, y-$scan of the complete chamber area is performed. Readout pad (anode) current and the cathode current for the individual $x, y-$positions are noted. 2D current plot of the X-ray scan is shown in Fig. 6.19 for both the readout and cathode. In both the plots, there is a current drop in two places along the y-direction, those are because of the sector boundary of the chamber in between. Low ion backflow is the primary concern of

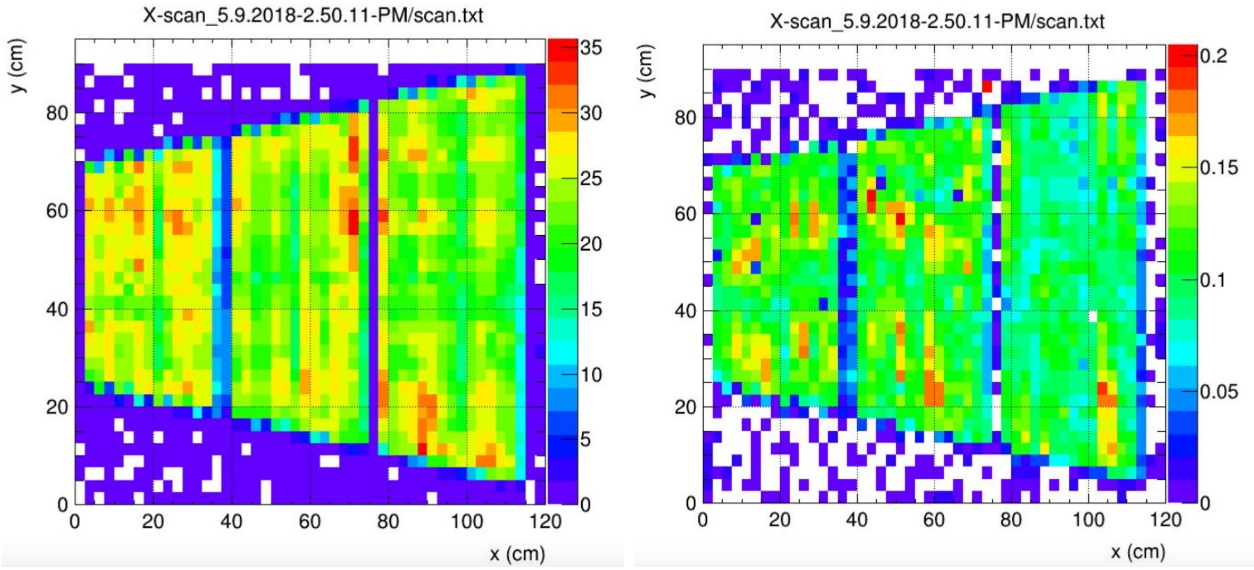

Figure 6.19: $x, y-$scan of the gain of an OROC using an X-ray gun. Readout pad current in the left panel and cathode current in the right panel.

chamber testing. Ion backflow of the chamber is calculated from the ratio of the cathode current to the anode (readout plane) current as shown in the formula,

$$IBF = \frac{I_{cathode}}{I_{anode}}. \tag{6.3}$$

The spatial variation of the IBF is shown in a 2D color plot in Fig. 6.20. The 1D histogram of the IBF distribution for all the three sectors (OROC1, OROC2 and OROC3) are shown in Fig. 6.21. The figure confirms the IBF $< 1\%$ in all the cases. The next level test is HV wire irradiation, gain measurement and the ^{55}Fe spectrum study. In HV wire irradiation test the wires are irradiated with application of the X-ray in the presence of the nominal voltages (voltage at gain 2000). The current of the wires is looked for any unusual responses due to insulation breakdown of the wires or ionization responses due to a high electric field. The gain of the chamber is calculated from the anode current and the corresponding rate of the absorbed X-rays. The X-ray absorption rate of the chamber is measured at a high gain so that the signal is well above the noise threshold. The gain measurement of the chamber is performed for a range of HV to cover the gain from a few 100 to about 10^4. The gain as a function of HV for all the three sectors is shown in Fig. 6.22. The current and the HV corresponding to the gain of 2000 is calculated from the gain curve. ^{55}Fe

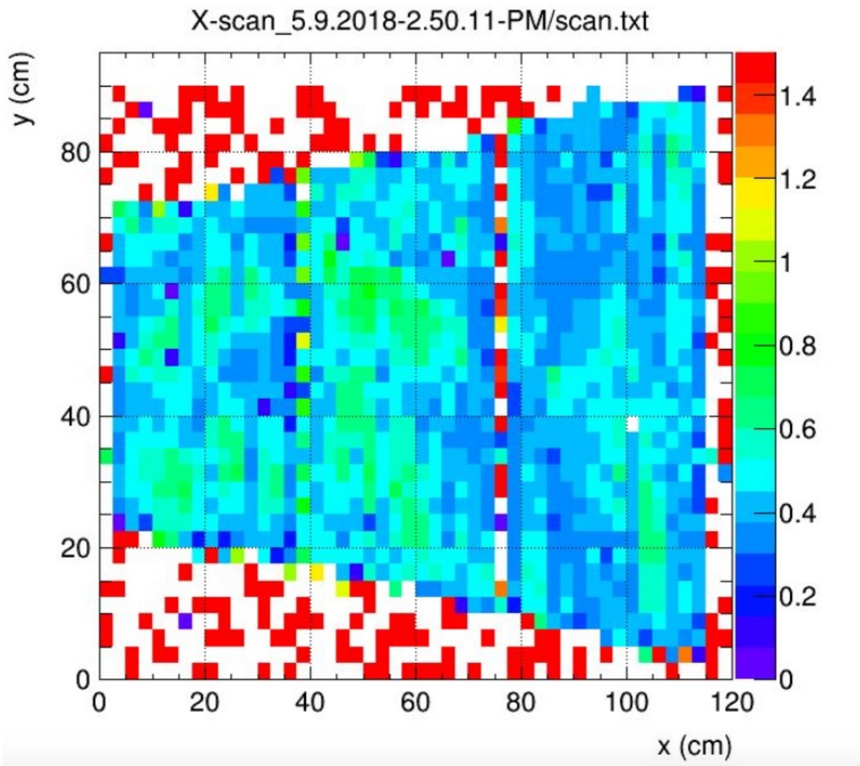

Figure 6.20: 2D distribution of ion backflow of a sample OROC.

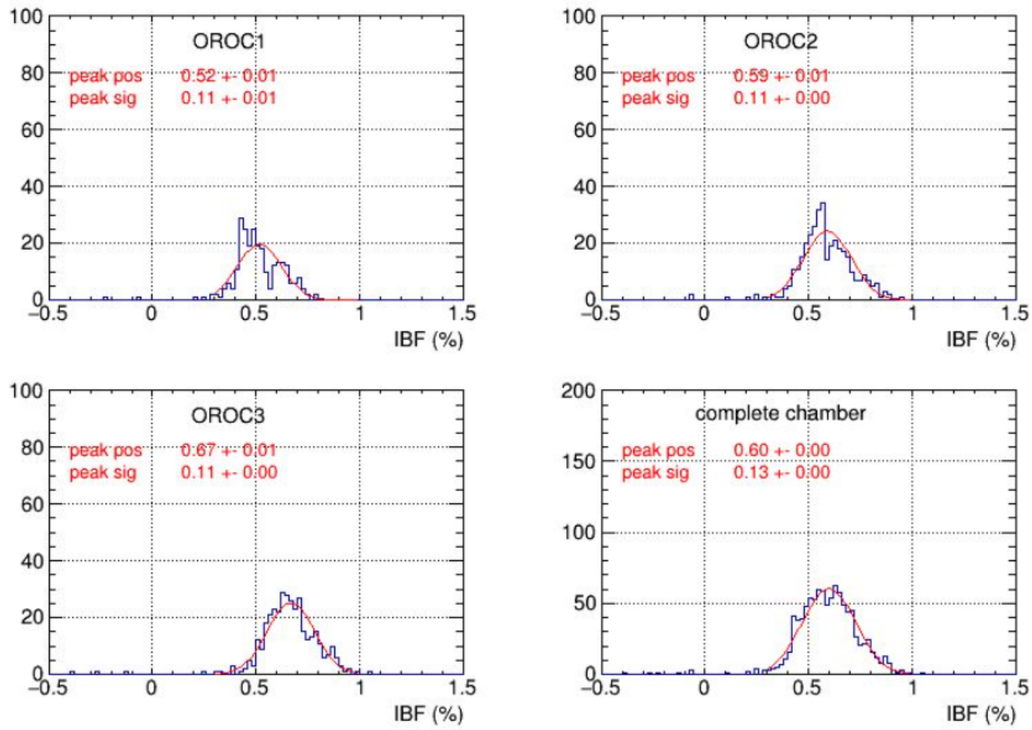

Figure 6.21: Ion backflow distribution of the OROC segments. The ion backflow is $< 1\%$.

spectrum and pedestal are taken at the HV associated to the gain of 2000. The energy resolution of the X-ray spectrum of the ^{55}Fe source for the Ne/CO_2/N_2 (90:10:5) gas is calculated. The pedestal subtracted data is considered in ^{55}Fe spectrum analysis. The ^{55}Fe X-ray spectrum in such an OROC at the gain of 2000 is shown in Fig. 6.23. The small peak at low ADC is the noise

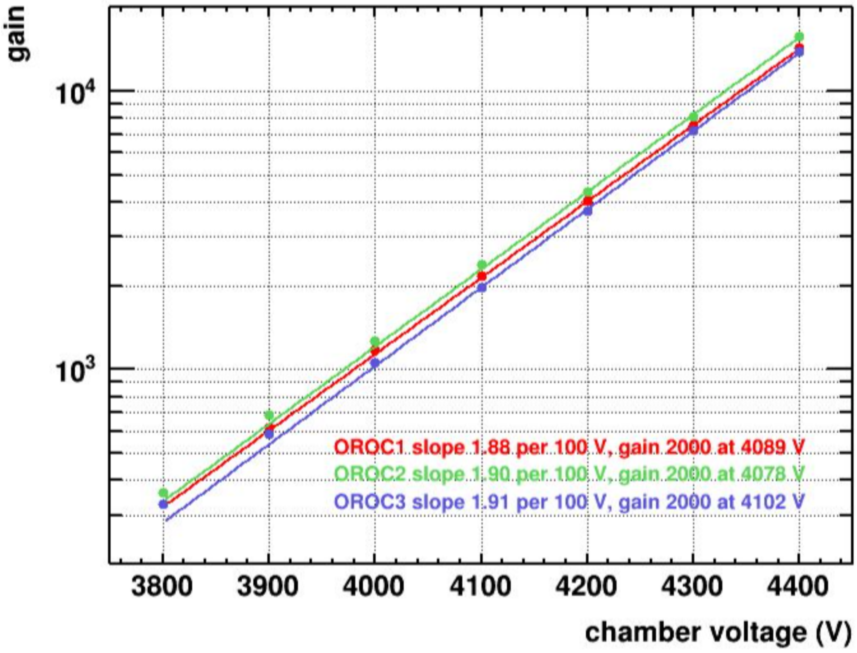

Figure 6.22: Effective gain variation as a function of applied voltage of the OROC. The voltage and the current associated with a gain of 2000 can calculate from the tangent of the fitting function.

peak whereas the main photopeak is corresponding to the 5.9 keV X-ray.

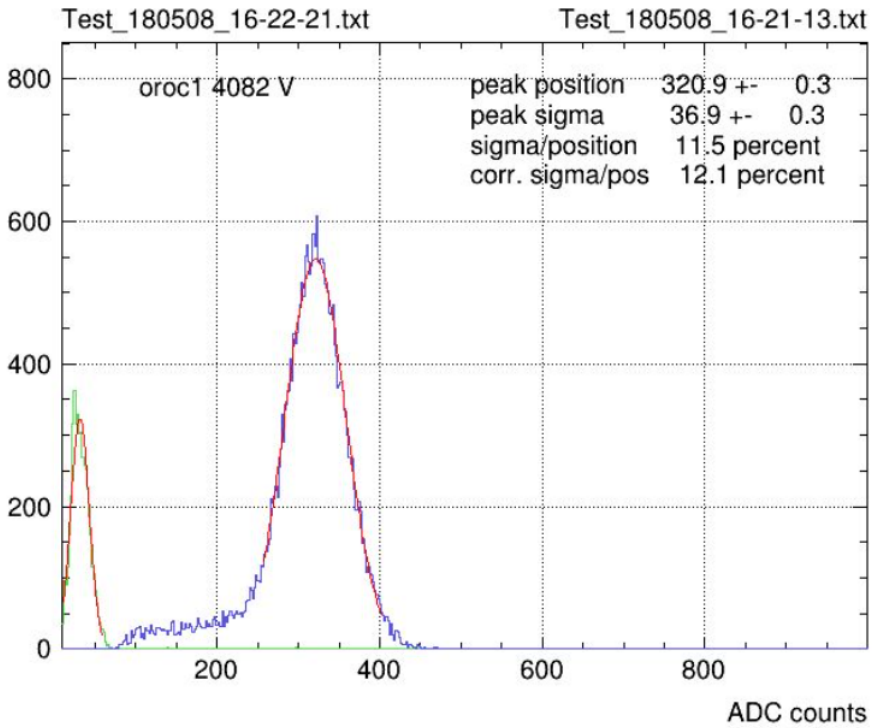

Figure 6.23: ^{55}Fe X-ray energy spectrum of the OROC in $Ne/CO_2/N_2$ (90:10:5) gas.

Next is the full area irradiation test using high-intensity X-ray guns. For this test, the chamber is moved inside a radiation shielded box. A high flux X-rays is projected to the whole chamber in this test. The gain of 4000 and the anode current about 10 nA/cm^2 are maintained for the irradiation test of the chamber. The stability performance of the chamber at high gain and high radiation environment is continued till 6 hrs. After the irradiation test is done, the leakage currents of all the GEM foils at -250 V are measured and compared with the previous one. If all the test results are satisfactory, then the OROCs are declared as test passed by the collaboration. The chambers are then transported to CERN for beam test and commissioning.

In this chapter, I have described current ALICE TPC, its readout and performances till LHC Run-2. The MWPC and gating grid based readout will be replaced with GEM readout because of the rate handling challenge. A quadruple GEM chamber is found as the optimum choice for the TPC upgrade; however, the present TPC performances will be restored in the future also. The IROCs and OROCs production and testing are the most important activity towards TPC upgrade during LHC LS2. I have reported the GEM framing, testing and the OROCs assembly and test results, those are done during my research.

Chapter 7

Particle production in Pb-Pb collisions at the LHC energies

According to Quantum Chromodynamics (QCD) normal nuclear matter undergoes a phase transition to a new state of matter, the quark-gluon plasma (QGP), where are quarks and gluons are deconfined. The formation of the QGP is characterized by a state of high temperature (T) and/or high energy density (ϵ) compared to the hadronic matter. Au-Au collisions have already established such a state where the T and ϵ have been above their transition values for the phase transition. In view of this, the Large Hadron Collider provides an excellent opportunity to study the QGP matter in great detail. The experiments at the LHC have collected pp, p-Pb, Xe-Xe and Pb-Pb data in Run-1 and Run-2. In Run-3, the collision energy and beam luminosity will be higher. So as a part of the thesis work, the particle productions for these collisions have been studied. Special attention has been given to Pb-Pb collisions as very large number of particles are produced in these collisions. As the ALICE experiment specializes on Pb-Pb collisions, the main focus will be on the measurements using central detectors in ALICE. I have studied the multiplicity distributions and momentum distributions of all charged particles and identified particles. From these, the initial energy densities have been extracted. The results are presented in this chapter.

7.1 Global property study in heavy-ion collisions

One of the primary motivation of all experiments and phenomenological models is to measure and understand the space-time evolution of the fireball created in high-energy heavy-ion collisions. The effective theories, such as relativistic hydrodynamic models and Monte Carlo models of parton and hadron transport in the medium, one needs the information about initial conditions of the parton production. The parton production is determined by the initial energy density or the temperature of the thermalized system. Experimental measurements of these initial quantities are not straightforward and need a connection to theoretical models. Global observables, charged particle multiplicity and transverse energy (E_{T}) distributions are connected with the initial energy density of the fireball produced in the collision. Both the observables depend on collision geometry (centrality) and beam energies. The charged particle multiplicity distributions as a function of pseudorapidity (η) over a large η range are needed to make the connection to initial states.

Event generators with simulation of particle production based on different models can provide insight into the possible range of multiplicity, the momentum of the emitted particles. A Multi Phase Transport (AMPT) model based simulation is performed to investigate the global properties of Pb-Pb collision at $\sqrt{s_{\mathrm{NN}}} = 5.5$ TeV. The main physics motivation of the AMPT model calculation is to estimate the global property in Pb-Pb collisions at LHC Run-3 energy. Multiplicity and rapidity study of all charged particles and identified particles, their transverse momentum spectra and initial energy density are obtained for most central collision ($0-5\%$ centrality) based on the AMPT simulation.

The multiplicity distributions in Run-3 and integrated multiplicity within the ALICE TPC acceptance ($|\eta| < 0.9$) have been obtained and presented.

7.2 Some useful kinematic variables in high-energy collision systems

In a high-energy collision, the general convention of the coordinate system is that the beam axis is along the z-axis and the collision takes place at $(x, y, z) = (0, 0, 0)$. The plane perpendicular to the beam axis (x, y) is the transverse plane. In a collision particle production in the transverse plane and its associated physics is the primary interest. Some useful definition of kinematic variables are given below.

• **Centre-of-mass energy**

Let us consider two particles moving in the laboratory frame with four-momenta $p_i = (E_i, \mathbf{p_i})$ collide with each other. In the center-of-mass (CM) frame, the four-momenta of the two particles are $p_i^* = (E_i^*, \mathbf{p_i^*})$. The sum of the four-momenta square is Lorentz invariant, denoted by s,

$$s = (p_1 + p_2)^2 = (p_1^* + p_2^*)^2 = (E_1^* + E_2^*)^2 = E_{cm}^2 = m_1^2 + m_2^2 + 2(E_1E_2 - \mathbf{p_1}.\mathbf{p_2}), \tag{7.1}$$

where $E_{cm}^2 = \sqrt{s}$ is the centre-of-mass energy of the collision system. For heavy-ion collisions, the collision energy is expressed by nucleon-nucleon centre-of-mass energy, denoted by $\sqrt{s_{\rm NN}}$.

• **Transverse momentum**

In high-energy collisions, the momentum of each particle is presented using two components, namely transverse momentum ($p_{\rm T}$) and longitudinal momentum (p_z). The transverse momentum is defined as,

$$p_{\rm T} = \sqrt{p_x^2 + p_y^2}, \tag{7.2}$$

where subscripts x and y are the x and y components of the particle momentum. $p_{\rm T}$ is the momentum of a particle in the transverse plane (xy-plane). The transverse momentum ($p_{\rm T}$) is a Lorentz invariant quantity. Therefore, it is an important property of particle under study. Another important variable used is transverse mass,

$$m_{\rm T} = \sqrt{p_{\rm T}^2 + m_0^2}, \tag{7.3}$$

where m_0 is the rest mass of the particle.

• **Rapidity**

Rapidity (y) of a particle is defined as,

$$y = \frac{1}{2}\ln\left(\frac{E + p_z}{E - p_z}\right). \tag{7.4}$$

Rapidity is a simple additive quantity, and invariant under Lorentz transformation. In the non-relativistic limits ($p << m_0$), rapidity is equivalent to the velocity of the particle.

• **Pseudorapidity**

Pseudorapidity (η) of a particle is the limiting case of rapidity, where particle momentum is very high ($p >> m_0$). The pseudorapidity is defined as,

$$\eta = \frac{1}{2}\ln\left(\frac{p + p_z}{p - p_z}\right) = -\ln\left(\tan\frac{\theta}{2}\right), \tag{7.5}$$

where θ is an angle relative to the beam axis. Therefore, η is a geometrical variable, which is often used to describe geometrical acceptance of the detector. Pseudorapidity (η) is useful where the particles are not identified. The region of $\eta \approx 0$ is called mid-η.

• **Particle multiplicity**

The multiplicity is defined as the number of particles produced in a single collision within a given acceptance. In the experiments, mostly charged particles are detected by tracking and triggering methods in detectors. Multiplicity is, therefore, referred to the charged particle multiplicity produced in an event.

• **Invariant yield**

The four-momentum, dp^3/E, is invariant under Lorentz transformation. Particle differential cross-section $Ed^3\sigma/dp^3$ can be expressed as,

$$E\frac{d^3\sigma}{dp^3} = \frac{1}{N_{evt}}E\frac{d^3N}{dp^3}. \tag{7.6}$$

Since, $dp^3 = p_{\mathrm{T}}dp_{\mathrm{T}}dp_z$ and $p_{\mathrm{T}}dp_{\mathrm{T}} = m_{\mathrm{T}}dm_{\mathrm{T}}$, the above relation can be decompose as,

$$\frac{1}{N_{evt}}E\frac{d^3N}{dp^3} = \frac{1}{N_{evt}}\frac{d^2N}{2\pi p_{\mathrm{T}}dp_{\mathrm{T}}dy} = \frac{1}{N_{evt}}\frac{d^2N}{2\pi m_{\mathrm{T}}dm_{\mathrm{T}}dy}. \tag{7.7}$$

The above relation is used to calculate collision cross-section experimentally.

• **Centrality of a collision**

In heavy-ion collisions, since nuclei are extended objects, the overlap area of a collision is quantified using impact parameter (b). A true head-on collision is of $b = 0$. Most central events have low b and collisions of large b are peripheral ones. More about centrality class determination is given in Section 7.4.1.

• **Units in high-energy physics**

In high-energy physics, the physical parameters are expressed in natural units *i.e.*, the velocity of light $c = 1$ and Planck constant $\hbar = 1$. Therefore, unit of energy and mass both are GeV in natural unit and the unit of length is GeV^{-1}. The use of natural units simplified the unit transformation of the kinematic variables and the observables in high-energy physics.

7.3 Event generation using AMPT

The AMPT [129–131] model has been widely used for the phenomenological study of partonic interaction and understanding the particle production mechanisms. The model can be divided into four main components: the initial conditions, partonic interactions, the conversion from the partonic to the hadronic matter, and hadronic interactions. The model works on two different modes: (a) default and (b) string melting (SM) [129]. In both the setting the initial conditions are taken from the HIJING [132] where the density profile of the two colliding nuclei are considered as Wood-Saxon type. The eikonal formalism governs the multiple scattering among the nucleons. In default mode, minijet partons are cascaded by Zhang's Parton Cascade (ZPC) model before the strings and partons are recombined. After that, the partons are recombined with their parent strings when they stop interacting, and the resultant strings are converted to hadrons by Lund string fragmentation function,

$$f(x) \propto z^{-1}(1-z)^a \exp(-bm_{\mathrm{T}}^2/z), \tag{7.8}$$

where a and b are the Lund string fragmentation parameters. The SM mode is based on the idea that once the energy density is above ~ 1 GeV/fm^3 then strings no longer hold the partons together (in hadrons). The strings are melt and produce a cascade of partons which follows ZPC afterward. The partonic matter then forms hadrons through the coalescence model and the hadrons subsequently interact themselves. In both the AMPT settings, total partonic scattering cross-section given by ZPC as,

$$\sigma_{gg} = \frac{9\pi\alpha_s^2}{2\mu^2}\frac{1}{(1+\mu^2/s)} \approx \frac{9\pi\alpha_s^2}{2\mu^2}, \tag{7.9}$$

where α_s is the strong coupling constant, s and t are the Mandelstam variables and μ is the Debye screening mass. The parameters setting in AMPT model is given in Table 7.1.

AMPT events using SM modes are generated for Pb-Pb collisions at $\sqrt{s_{\mathrm{NN}}} = 5.5$ TeV. The impact parameter set to minimum 0 fm and maximum of 3.5 fm corresponding to $0-5\%$ central collision in Pb-Pb [133]. These events are analyzed to extract multiplicity and momentum distributions of all charged particles and identified particles.

Parameter	Value
$\sqrt{s_{\mathrm{NN}}}$	5500 GeV
Frame	CMS
Projectile	Pb
Target	Pb
b$_{min}$	0.0 fm
b$_{max}$	3.5 fm
Mode	SM
NTMAX	3
a (PRAJ41)	0.3
b (PRAJ42)	0.15
μ Screening mass	2.2635
α_s	0.33

Table 7.1: AMPT parameters setting.

7.4 Charged particle multiplicity study

Charged particle multiplicity is one of the simplest observable in a high-energy experiment. But it provides important information about several observables and infers about particle production mechanism. The results of the multiplicity study provide constraints on the particle production models to reject it or to make further improvements. Particle multiplicity with a given η range depends on both the collision centrality and the centre-of-mass energy $\sqrt{s_{\mathrm{NN}}}$.

7.4.1 Collision centrality

In a heavy-ion collision, two nuclei overlap with each other and have impact parameter b from a value 0 to maximum $R_1 + R_2$, where R_1 and R_2 are the radii of the two colliding nuclei. A set of collisions with the range of the impact parameter $0 \leq b \leq R_1 + R_2$ are called *minimum bias* events. However, in the experiment, it is not possible to determine the impact parameter or initial geometry of the collision. To quantify the overlap region in an event, different *centrality* classes are found useful in the experiment.

The Monte-Carlo (MC) Glabour model simulates event-by-event collision of two nuclei composed of many nucleons. The overlap area can be calculated by the classification of the events according to the impact parameter. In a nuclear collision, overlap area of the two nuclei is expressed by the number of nucleons have one or more binary collisions, N_{part} and the spectators are expressed by the number of nucleons which do not have any interactions N_{spec}. These are related by $N_{spec} = 2A - N_{part}$, where A is the total number of the nucleons in a nucleus. Figure 7.1 shows the projection of the collision of two nuclei A and B in the $x, y-$plane. Collision centrality as a function of impact parameter b can be realized from the figure. In a collision, particle multi-

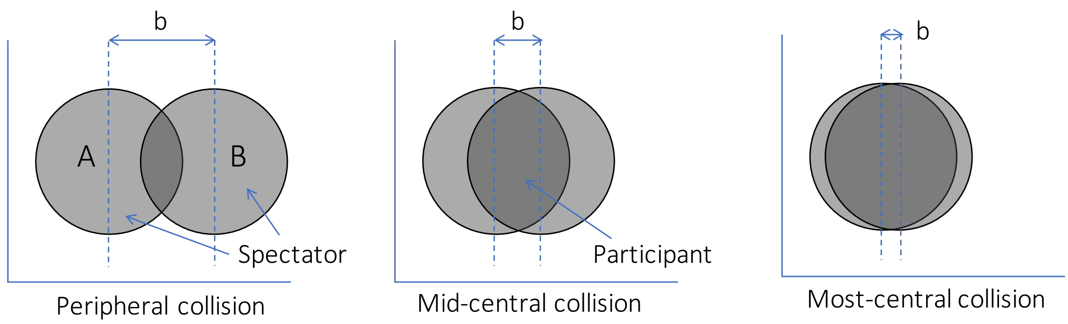

Figure 7.1: Projection of the collision of two nuclei in $x, y-$plane for different impact parameters.

plicity is proportional to the number of participating nucleons N_{part}. Therefore, multiplicity study allows us to know about the impact parameter of the collision. As an example, the amplitude (proportional to multiplicity) in the ALICE V0 detector is shown in Fig. 7.2. This distribution

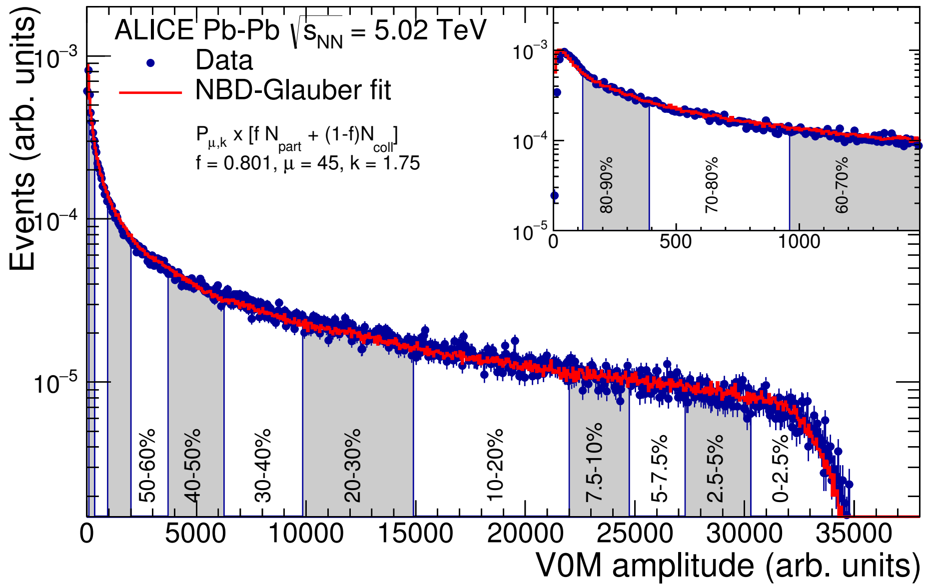

Figure 7.2: Collision centrality determination from the multiplicity measurement in ALICE. The distribution of the sum of the amplitudes in the ALICE V0 detector. The inset shows a zoom of the most peripheral region. The vertical lines separate the centrality classes. Figure is adopted from [134].

defines the centrality classes based on the percentage of the total distribution. These different centrality classes are labeled in the figure. Here, $0-5\%$ centrality meaning is the events of having the top 5% of N_{ch}. The centrality classes determined by experimental observables are compared with MC Glauber model [135] estimation as shown in the figure.

7.4.2 Particle multiplicity distribution

The experimental results of charged particle pseudorapidity density $dN_{ch}/d\eta$ distributions for central collisions in various collision energies are shown in Fig. 7.3 [136]. Here, the results of multiplicity are presented from the PHOBOS experiment [137] at RHIC for Au+Au collision of $\sqrt{s_{\rm NN}}$ = 19.6, 62.4 and 200 GeV, the ALICE experiment [138, 139] at LHC for Pb-Pb collision at energy $\sqrt{s_{\rm NN}}$ = 2.76 TeV along with the AMPT model calculation for Pb-Pb collision of $\sqrt{s_{\rm NN}}$ = 2.76 TeV as performed by [136]. The data presented for the ALICE and AMPT model is $0 - 5\%$ central whereas for PHOBOS is $0 - 6\%$ central. All the distributions are symmetry about the mid-rapidity region. AMPT model reproduces the data very well at mid-rapidity $|\eta| < 1$ region. This gives the confidence to predict these distributions using the AMPT event generator.

$dN_{ch}/d\eta$ distribution for $0-5\%$ central Pb-Pb collisions at $\sqrt{s_{\rm NN}} = 5.5$ TeV has been calculated using AMPT model, and is as shown in Fig. 7.4. $dN_{ch}/d\eta$ yields increase monotonically with the collision centre-of-mass energy $\sqrt{s_{\rm NN}}$. ALICE has reported the value of $dN_{ch}/d\eta$ for $|\eta| < 0.5$ is 1601 ± 60 for $0 - 5\%$ central Pb-Pb collisions at $\sqrt{s_{\rm NN}}$ = 2.76 TeV [140] whereas AMPT

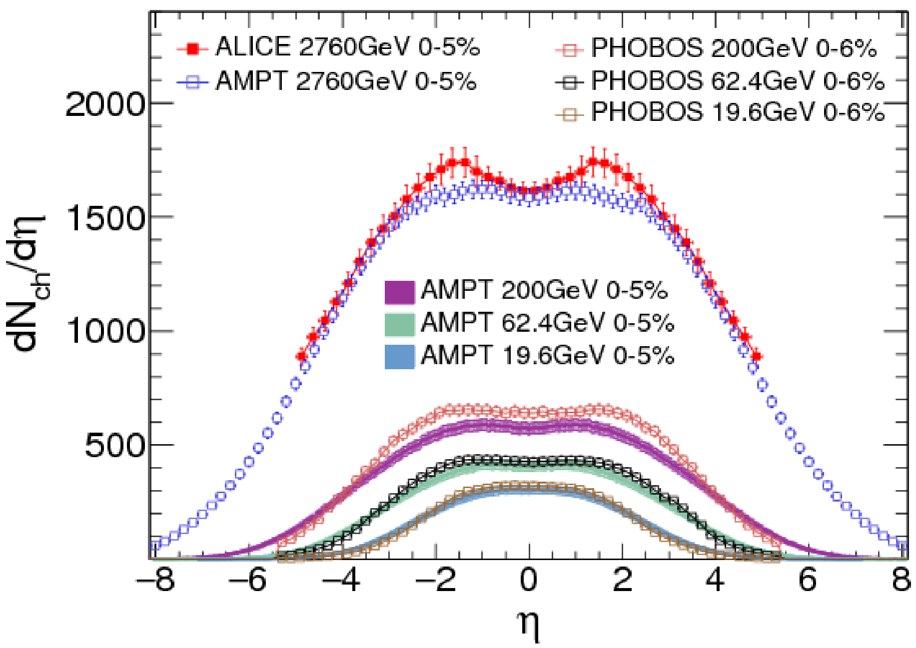

Figure 7.3: Beam energy dependency of charged particle pseudorapidity distributions. Results of most central collision from PHOBOS [137] and ALICE [138, 139] are shown along with calculations from AMPT model [136].

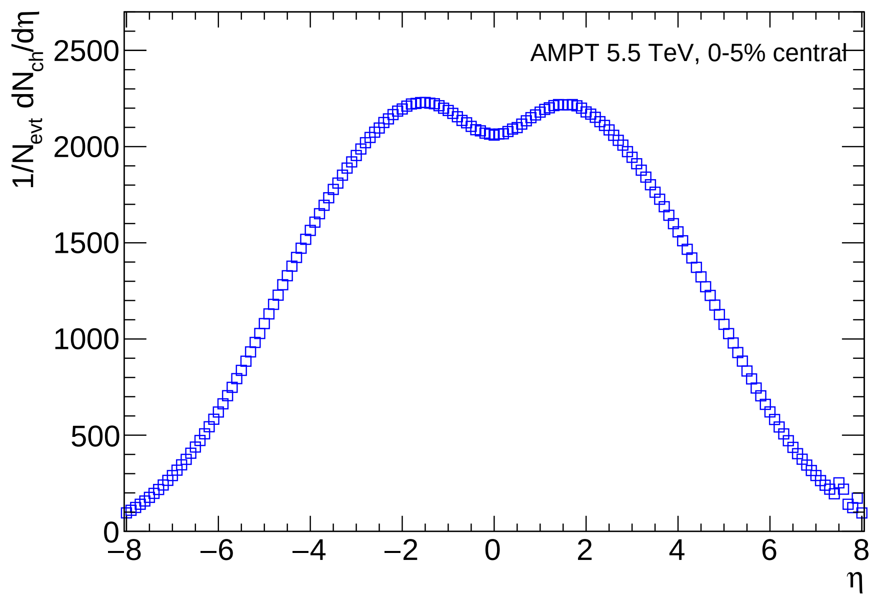

Figure 7.4: Charged particle pseudorapidity distributions. Result for Pb-Pb $0-5\%$central collisions of $\sqrt{s_{\mathrm{NN}}} =$ 5.5 TeV calculated using AMPT model, string melting mode.

model predicts $dN_{ch}/d\eta = 2080$ within $|\eta| < 0.5$ at $\sqrt{s_{\mathrm{NN}}} = 5.5$ TeV. A dip in the $dN_{ch}/d\eta$ distribution is found at $\eta \approx 0$ for both in experimental data and model calculation. The dip structure in $dN_{ch}/d\eta$ distribution becomes more prominent at the higher value of $\sqrt{s_{\mathrm{NN}}}$. The dip in pseudorapidity distribution arises due to mass effect of the particles. That can be realized from the mathematical relation,

$$\frac{dN}{d\eta} = \sqrt{1 - \frac{m^2}{m_{\mathrm{T}}^2 cosh^2 y}}\frac{dN}{dy}. \tag{7.10}$$

The dip in pseudorapidity density distribution is expected to be more prominent for proton than pion. The mass effect on $dN/d\eta$ distribution for the identified charged particle can be realized from the Fig. 7.5 as shown.

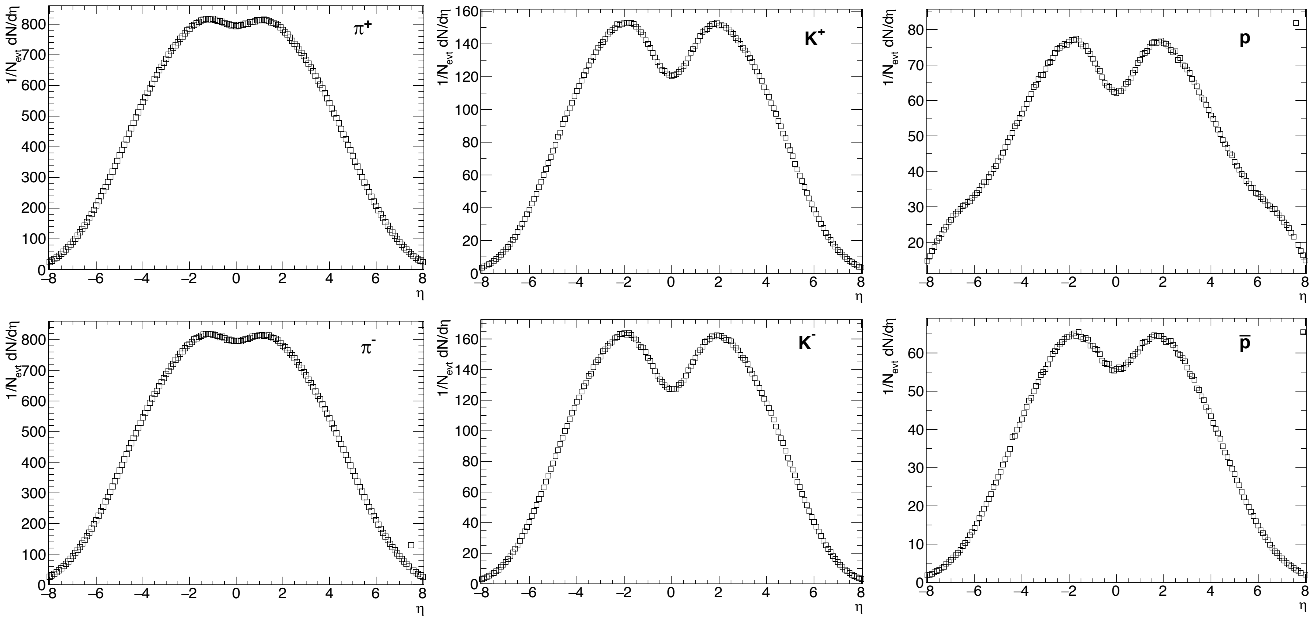

Figure 7.5: Pseudorapidity density distribution of $\pi^{\pm}, K^{\pm}, p, \bar{p}$ for $0-5\%$ central Pb-Pb collision at $\sqrt{s_{\mathrm{NN}}}$ =5.5 TeV. Results are from AMPT model calculation.

The charged particle rapidity distribution for identified particles π^+ and π^- are shown in Fig. 7.6. The results are based on AMPT model. It can be noticed that there is no dip at $\eta = 0$, unlike pseudorapidity distribution. The charged particle multiplicity density at mid-rapidity region $|\eta| < 0.5$ as found in AMPT model along with the ALICE measurement at $\sqrt{s_{\mathrm{NN}}}$ = 2.76 TeV and 5.02 TeV [21, 133] are summarized in Table 7.2. Different values of dN/dy at $|\eta| < 0.5$ is corresponding to different particle species in Table 7.2 can be understood because of there mass dependency in the particle production mechanism. The particle production from the thermalized QGP medium is mostly followed by the statistical (thermal) process. According to this process, light particles are most abundant whereas the heavy particles are produced in a small fraction.

In order to compare bulk particle production in different collision system and at different energies, particularly to compare with pp($\bar{p}$) collisions, the charged particle density is divided by the average number of participating nucleon pairs, $\langle N_{part}\rangle/2$. The N_{part} values can be calculated by MC-Glauber model for different centrality classes defined, classifying the events according to the impact parameter. For Pb-Pb $0-5\%$ central collisions, ALICE has reported $N_{part} = 385 \pm 3$

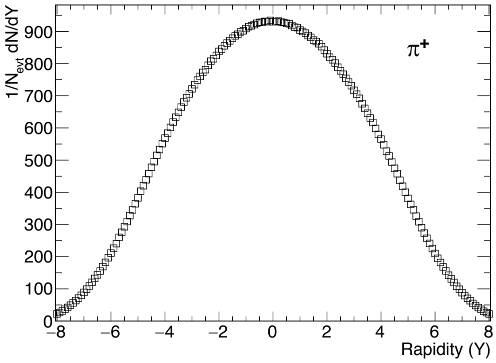

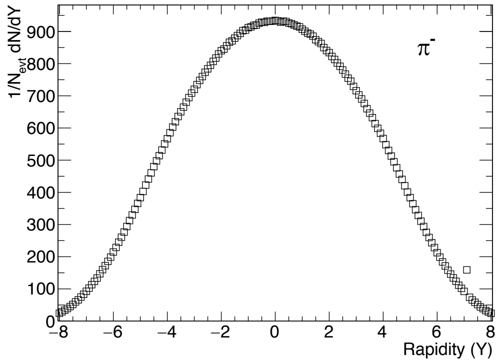

Figure 7.6: Rapidity density distribution of π^+ and π^- for $0-5\%$ central Pb-Pb collision at $\sqrt{s_{\rm NN}} = 5.5$ TeV. Results are from AMPT model calculation.

Source	$\sqrt{s_{\rm NN}}$	$dN_{ch}/d\eta$	$\frac{2}{\langle N_{part}\rangle}dN_{ch}/d\eta$	π^+	π^-	K^+	K^-	p	$\bar{p}$
AMPT	5.5	2305±4	10.8	930	930	165	175	103	85
ALICE data	5.02	1943±54	10.1±0.3	-	-	-	-	-	-
ALICE data	2.76	1601±60	8.4±0.3	733±54	732±52	109±9	109±9	34±3	33±3

Table 7.2: Charged particle multiplicity density $dN_{ch}/d\eta$ and identified particle rapidity yields dN_i/dy at $|\eta| < 0.5$ for Pb-Pb collision of $0-5\%$ centrality using AMPT model. For comparison ALICE data are taken from [21, 133].

and 382.7 ± 3.1 for $\sqrt{s_{\rm NN}} = 5.02$ TeV and 2.76 TeV, respectively [134, 140]. With changing the collision energy $\sqrt{s_{\rm NN}}$ from 2.76 Tev to 5.05 TeV, N_{part} does not have a significant change. In the AMPT model study, $N_{part} = 385 \pm 3$ has been considered for Pb-Pb $0-5\%$ central collisions at $\sqrt{s_{\rm NN}} = 5.5$ TeV. For $0-5\%$ centrality at $\sqrt{s_{\rm NN}} = 5.5$ TeV, it is found that the charged particle density per participant pair is $(2/\langle N_{part}\rangle)dN_{ch}/d\eta = 10.8$. In Fig. 7.7 the collision energy dependence of $(2/\langle N_{part}\rangle)dN_{ch}/d\eta$ is plotted for $(0-5\%)$ central Au+Au or Pb+Pb collisions as well as per pp collisions. The data presented in the figure are from the existing results for central Pb-Pb and Au-Au collisions from experiments at the LHC [140–142], RHIC [137, 143–146], and SPS [147]. The data of pp($\bar{p}$) [137, 148–152] collisions are included as a reference to present collisions system dependency of $(2/\langle N_{part}\rangle)dN_{ch}/d\eta$. The dependency of $(2/\langle N_{part}\rangle)dN_{ch}/d\eta$ on collision energy can be fitted with a power law of the form as^b. The power law fitting of A-A collisions data gives $b = 0.155 \pm 0.004$ [21]. Corresponding fit to the data for pp($\bar{p}$) collisions give $b = 0.103 \pm 0.002$. The A-A collisions have much stronger s dependence than pp($\bar{p}$). The expected value of $(2/\langle N_{part}\rangle)dN_{ch}/d\eta$ at $\sqrt{s_{\rm NN}} = 5.5$ TeV follow the extrapolated power law curve as shown in Fig. 7.7.

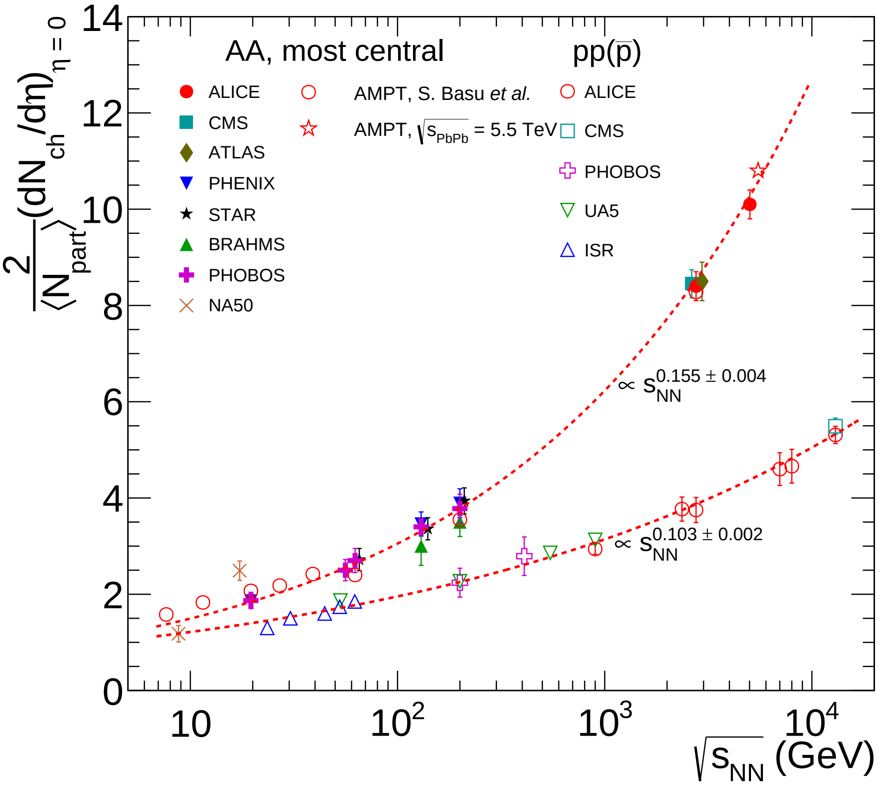

Figure 7.7: Variation of $(2/\langle N_{part}\rangle)dN_{ch}/d\eta$ for most central collision in A-A as a function of $\sqrt{s_{\rm NN}}$. Experimental data for central Pb-Pb [140–142, 147] and Au-Au [137, 143–146], and pp($\bar{p}$) [137, 148–152]. collisions. AMPT calculation from [136].

7.4.3 Charged particle multiplicity and the TPC limit

In this sub-section, the limit of the ALICE TPC for multiplicity measurement is discussed. The ALICE TPC is designed for its maximum acceptance of multiplicity, $dN_{ch}/d\eta \approx 8000$ at $\eta = 0$. ALICE has reported $\langle dN_{ch}/d\eta\rangle_{cent} \approx 1600$ and $\langle dN_{ch}/d\eta\rangle_{mb} \approx 400$ for central $(0-5\%)$ and minimum bias collisions, respectively, in Pb-Pb at $\sqrt{s_{\rm NN}} = 2.76$ TeV [140]. The AMPT model calculation shows that for Pb-Pb most central $(0-5\%)$ collision at the highest LHC energy of $\sqrt{s_{\rm NN}} = 5.5$ TeV is $\langle dN_{ch}/d\eta\rangle_{cent} \approx 2300$. The value of $\langle dN_{ch}/d\eta\rangle_{mb} \approx 500$ is expected for Pb-Pb minimum bias events at $\sqrt{s_{\rm NN}} = 5.5$ TeV.

In LHC Run-3, the collision rate will increase to 50 kHz. Within the time window of $t_d \approx 100\ \mu s$ (electrons drift time in TPC), the number of pile up events will be, $N_{pile} = 5$. The equivalent charged particle multiplicity in events pile up is $\langle dN_{ch}/d\eta\rangle_{eqiv} \approx 2500$. For the central event, out of these five events, one could be central and four minimum bias events. The equivalent piled up charged particle multiplicity in the central event is about 4300 ($\langle dN_{ch}/d\eta\rangle_{eqiv} \approx 2300$ for central + 4 minimum bias events 2000). This value of 4300 is still well below the design value of TPC for charged particle multiplicity (≈ 8000).

7.5 Study of particle momenta

The measurement of momenta of produced hadrons has the maximum utility in terms of understanding the particle production mechanisms. The physics of parton interactions and its dynamics can be addressed by measuring the transverse momentum (p_{T}) of the produced particles. Different underlying physics processes are reflected in the different ranges of transverse momenta, p_{T}. The ranges are classified as: low, intermediate and high p_{T}. A large fraction of the particles (more than 95%) are produced in low transverse momenta ($p_{\mathrm{T}} < 2$ GeV) regime, the particles produced in this p_{T} range are called *soft* particles. In this p_{T} range, the bulk matter dynamic is in good agreement with the statistical hydrodynamic model, which suggests that the fireball created in the heavy-ion collision has thermodynamic property. The inverse slope of exponent fit of the p_{T} (or m_{T}) spectrum infers temperature of the thermalized matter.

At the low p_{T} range information about parton distribution function and the deconfined state is lost. Particle production at intermediate momenta region between soft phenomena ($p_{\mathrm{T}} < 2$ GeV) and hard scattering ($p_{\mathrm{T}} > 6-8$ GeV), can be described by perturbative QCD. The transverse momentum spectrum as observed in Pb-Pb collision at $\sqrt{s_{\mathrm{NN}}} = 2.76$ TeV in ALICE is shown in Fig. 7.8 [153]. The trend of the transverse momentum distribution is at the low p_{T} region the distribution has a steeper exponential slope which becomes less stepper in the intermediated and high p_{T} range from which one can distinguish different p_{T} range. The particles at the intermediate p_{T} region infer about the interplay between hard and soft processes, carry the information about parton distribution function at the early phases. Whereas the high p_{T} particles production process is dominated by the hard scattering (parton scattering with large momentum transfer) at the initial stage.

7.5.1 p_{T} spectra for Pb-Pb collisions at $\sqrt{s_{\mathrm{NN}}} = 5.5$ TeV

The mean transverse momentum ($\langle p_{\mathrm{T}} \rangle$) of the outgoing hadrons provides bulk property of matter, such as the energy density and the temperature of the system. The $\langle p_{\mathrm{T}} \rangle$ of the identified particles can be obtained from the transverse momentum spectra. The $\langle p_{\mathrm{T}} \rangle$ of the spectrum depends on both, centrality classes and collision energy, $\sqrt{s_{\mathrm{NN}}}$, that can be realized from the ALICE results of the p_{T} spectra for the identified particles in Fig. 7.8.

Transverse momentum spectra for $\pi^{\pm}$, $\mathrm{K}^{\pm}$, p and $\bar{p}$ for $0-5\%$ central Pb-Pb collisions at $\sqrt{s_{\mathrm{NN}}} = 5.5$ TeV are shown in Fig. 7.9. The momentum spectra are obtained from the AMPT model simulations at mid-rapidity. The $\langle p_{\mathrm{T}} \rangle$ values are extracted from these spectra and are compiled in the Table 7.3. These values are compared to the data from the ALICE collaboration

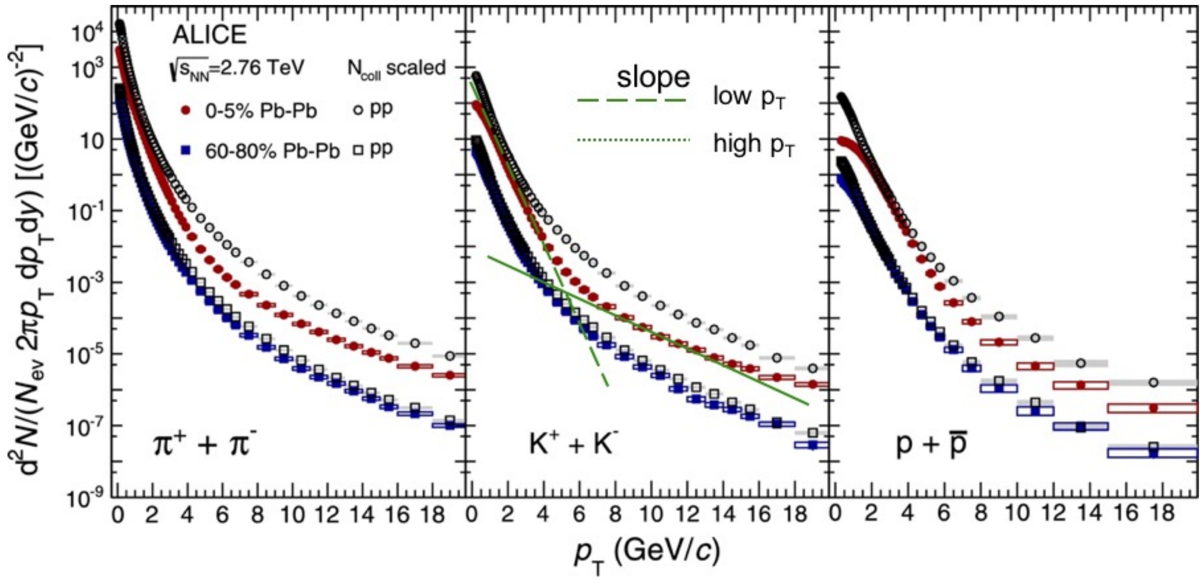

Figure 7.8: Transverse momentum distribution for the charged particles: $\pi^+ + \pi^-$, $K^+ + K^-$, $p + \bar{p}$. Two different slopes can be realized for the low and high p_T particles. The figure is adopted from [153].

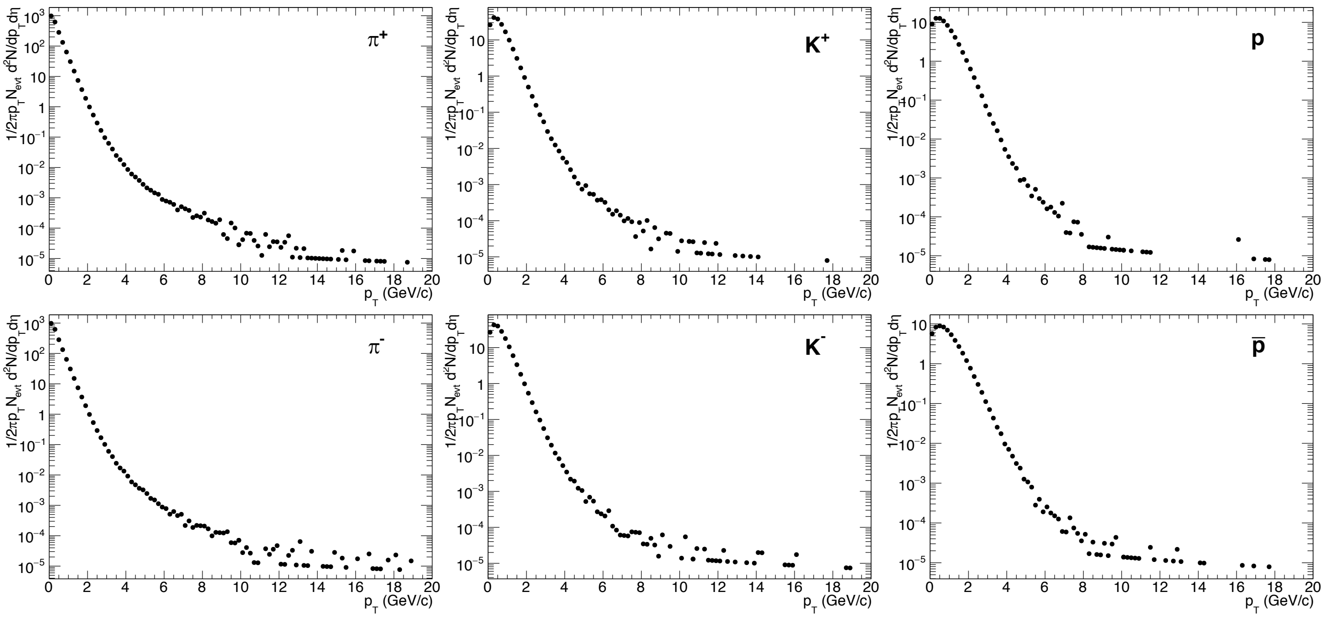

Figure 7.9: Transverse momentum spectrum of $\pi^{\pm}, K^{\pm}, p, \bar{p}$ at mid-rapidity ($\langle\eta\rangle < 0.5$) in most central $(0-5\%)$ Pb-Pb collision at $\sqrt{s_{\rm NN}} = 5.5$ TeV using AMPT model.

Source	$\sqrt{s_{\rm NN}}$	π^+	π^-	K^+	K^-	p	$\bar{p}$
AMPT	5.5	0.554	0.555	0.853	0.858	1.076	1.201
ALICE data	2.76	0.517±0.019	0.520±0.018	0.876±0.026	0.867±0.027	1.333±0.033	1.353±0.034

Table 7.3: $\langle p_T\rangle$ of the identified particle in $|\eta| < 0.5$ for Pb-Pb collision of $0-5\%$ centrality using AMPT model. For comparison ALICE data are taken from [133].

for Pb-Pb collisions at $\sqrt{s_{\rm NN}} = 2.76$ TeV [133]. We observe that the results obtained from AMPT are in close agreement to the experimental results from ALICE.

7.5.2 Calculation of initial energy density

The mean transverse energy per unit rapidity $\langle dE_{\mathrm{T}}/dy\rangle$ carry information about how much of the initial longitudinal energy carried by the colliding nuclei is converted into energy carried by the particle produced transverse to the beam axis. The transverse energy at mid-rapidity is, therefore, a measure of the stopping power of nuclear matter. The measurement of the energy density of the partonic medium based on Bjorken estimation [22] is as,

$$\epsilon_{Bj} = \frac{1}{A_T\tau}\frac{dE_{\mathrm{T}}}{dy}, \tag{7.11}$$

where τ is the formation time of the QGP, A$_T$ is the transverse overlapping area in the collision of the two nuclei. Most of the transverse energy E_{T} is carried out by the produced particles, $\pi^{\pm}, \pi^0, K^{\pm}, K^0, p, \bar{p}, n$, and $\bar{n}$. Here, we assume that all charged signs and its isospin state of each particle carry the same E_{T}, *e.g.*, $E_{\mathrm{T}}^{\pi^+} = E_{\mathrm{T}}^{\pi^-} = E_{\mathrm{T}}^{\pi^0}$, and E_{T} carried by the (anti)neutron equal to E_{T} carried by the (anti)proton. Then the transverse energy density term can be written as,

$$\frac{dE_{\mathrm{T}}}{dy} \approx \frac{3}{2}\left(\langle m_{\mathrm{T}}\rangle\frac{dN}{dy}\right)_{\pi^{\pm}} + 2\left(\langle m_{\mathrm{T}}\rangle\frac{dN}{dy}\right)_{K^{\pm},\ p,\ \bar{p}}. \tag{7.12}$$

Where $\langle m_{\mathrm{T}}\rangle$ is the mean transverse mass of the identified particles as shown in equation 7.3. The factors 3/2 and 2 compensate for the charge neutral particles. The formation time, τ, is typically taken as 1 fm/c, but there are many debates about its exact value. In the absence of experimental knowledge of τ, the energy density is expressed in terms of $\epsilon_{Bj}\tau$. For Pb-Pb collision at $\sqrt{s_{\mathrm{NN}}}$ = 5.5 TeV, I have calculated the Bjorken energy density $\epsilon_{Bj}\tau$ using AMPT model simulation. dE_{T}/dy is calculated from the dN/dy and mean p_{T} values of the identified particles as given in Table 7.2 and Table 7.3, respectively. $2/\langle N_{part}\rangle dE_{\mathrm{T}}/dy = 14.8$ GeV is found for the Pb-Pb $0-5\%$ central collision at $\sqrt{s_{\mathrm{NN}}} = 5.5$ TeV.

The energy density $\epsilon_{Bj}\tau$ as a function of collision energy $\sqrt{s_{\mathrm{NN}}}$ is shown in Fig. 7.10. The results presented in the figure are for different $\sqrt{s_{\mathrm{NN}}}$ from the experiments NA49 [154], STAR [146, 155], PHENIX [156–158], ALICE [23, 159] and CMS [160] collaborations. The energy density obtained using the AMPT model as reported in Ref. [136] is also presented in the figure. The experimental data of energy density $\epsilon_{Bj}\tau$ is following a power law function $a\,s_{\mathrm{NN}}^b$ [160]. The fitting parameter in the range of $17.2 \leq \sqrt{s_{\mathrm{NN}}} \leq 2760$ GeV is obtained as $a = 0.87 \pm 0.07$ and $b = 0.17 \pm 0.007$. In this work, the AMPT estimation of $\epsilon_{Bj}\tau = 17.53$ for $0-5\%$ central Pb-Pb collision at $\sqrt{s_{\mathrm{NN}}} = 5.5$ TeV is following nicely the extrapolation power law function.

This chapter can be summarized as global property of Pb-Pb collisions at $0-5\%$ centrality at

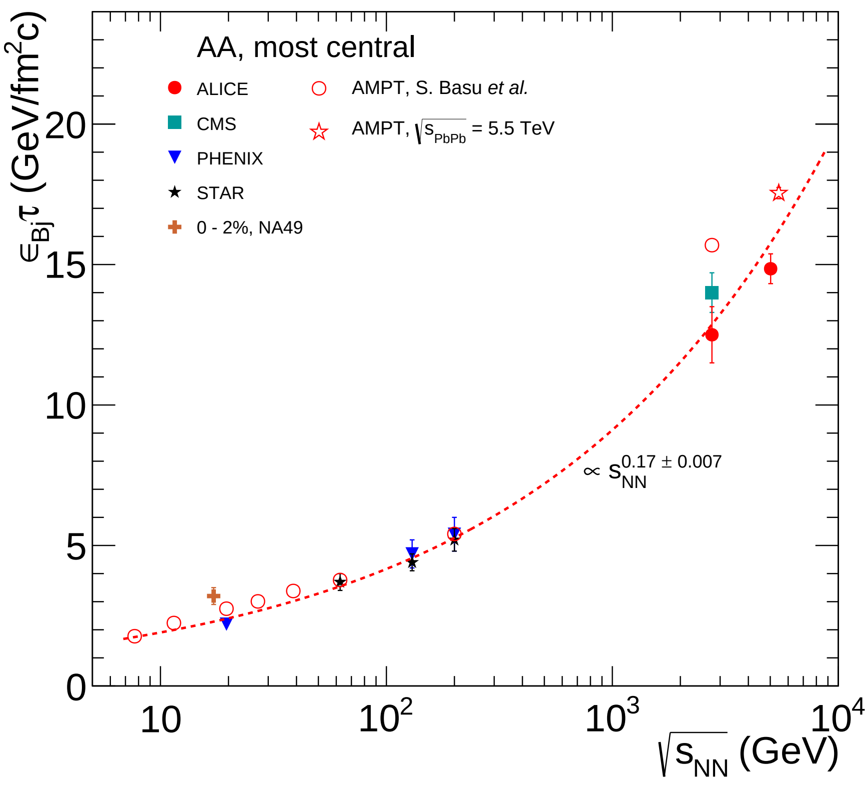

Figure 7.10: Variation of the Bjorken energy density $\epsilon_{Bj}\tau$ for most central A-A collisions as a function of $\sqrt{s_{\rm NN}}$. Experimental data for central Pb-Pb [23, 154, 159, 160] and Au-Au [146, 155–158]. AMPT calculation from [136].

$\sqrt{s_{\rm NN}} = 5.5$ TeV have been studied using AMPT model simulation. The charged particle density distribution $dN_{ch}/d\eta$ has been calculated in this simulation. $dN_{ch}/d\eta$ results confirms in LHC Run-3 the particle production is still well below than the TPC acceptance. The calculated charged particle density per participant pair $(2/\langle N_{part}\rangle)dN_{ch}/d\eta = 10.8$ follows the energy dependent power law extrapolation. The transverse momentum spectra of the identified particles are also shown, from which Bjorken energy density has been estimated. The Bjorken energy density is found following $\sqrt{s_{\rm NN}}$ dependent power law with a value 17.53 GeV/fm^{2}c.

Chapter 8

Summary

Research in high-energy physics experiments is progressing very aggressively in order to answer some of the most fundamental physics questions. Along with the LHC, there have been plans to build new accelerators worldwide. At CERN, the LHC will be upgraded to high Luminosity LHC and the proposal for the Future Circular Collider (FCC) has been submitted. Considerable development of particle detectors has been ongoing at the same time in order to cope up with the high energy and high luminosity offered by the accelerators. Micro-Pattern Gaseous Detectors have been found to be most acceptable in high rate and high radiation environment in large scale HEP experiments. The development and study of GEM detector have great importance because of its large scale usage in HEP and nuclear physics experiments. Several experiments are upgrading as well as planning to use GEM detectors as the most preferred choice. The ALICE TPC is going to replace the MWPC detectors with GEM readout for the high luminosity LHC Run3 and Run4 period. The primary goal of this thesis is the development and characterization of the GEM detector for ALICE TPC. Also as a part of this thesis, the particle productions in Pb-Pb collisions at highest LHC energy have been studied. The scientific findings from this thesis are summarized in this chapter.

The assembly and characterization of triple GEM detector and quadruple GEM detector are performed in VECC, Kolkata. Both the detectors are tested with Ar/CO_2 90:10 and 70:30 gas mixtures and the results are compared. Excellent separation between the main peak and Ar-escape peak of 5.9 keV X-ray energy spectrum is obtained from both the detectors. The efficiency measurement shows a plateau of efficiency $\approx 95\%$ at the operating voltages with a gain of ≥ 5000 for both the detector. We found that the efficiency measurement using ^{106}Ru-Rh β^{-}-source is much faster and convenient as compared to the use of cosmic muon triggers. The gain comparison study shows that quadruple GEM detector can operate at lower GEM voltages as compared to triple GEM detector. The advantages of low GEM voltages is long term stable operation. Whereas we found that triple GEM detector has better energy resolution ($\approx$ 20% in Ar/CO_2 70:30) performances as compared to quadruple GEM detector. For large area detectors (*e.g.,* ALICE TPC) in HEP experiments, uniform operation of the gain, energy resolution and efficiency over its active region are expected. In this thesis, a method has been developed for the spatial scan of the gain, energy resolution and efficiency of the detector. With the prototype triple GEM detector, we reported the spatial variation of the characteristic parameters with different test settings. The detector is also tested using the ALICE TPC GEM field setting, which is special for low ion backflow. We found that for the same gain, *IBF* field setting requires higher GEM voltages as compared to the *standard* field setting. The energy resolution is also deteriorated in *IBF* setting, which is understood because of the low gain of the first GEM foil. The quadruple GEM detector study is further extended for the importance of the drift field. A couple of interesting results are obtained in the electron transparency study as a function of the drift field and GEM voltages. We found that electron transparency, therefore, the gain of the detector depends on both the drift field and GEM voltages and optimization of the drift field is necessary for the best performances of the GEM detectors. Time resolution with the variation of the drift field (E_d) in the quadruple GEM detector shows a plateau for $E_d > 2$ kV/cm. Our measurement shows the time resolution of the quadruple GEM detector is $\approx$ 13 ns which is close to the triple GEM detector of $\approx$ 10 ns.

I have also performed a Garfield simulation using a model for time resolution estimation of the GEM detector and reviewed the theoretical aspects of it. It is found that the spatial distribution of the electron-ion clusters, electron drift and diffusions and ENC have important roles in the time performances of the gas detector. Here, the simulation is executed for the triple GEM geometry. The limiting value of time resolution obtained from simulation from different Argon based gas mixtures has a little deviation from the theoretical calculation. But the experimental results are quite far from the limiting value.

As a part of the gas detector study, we have fabricated and tested MWPC detectors. The tests of the MWPC detectors are done with two different electronics setup, namely standard NIM electronics and using MANAS ASIC. The results from both the setups are compared. The obtained gain of MWPC from both the setups are found similar. For the characterization of the detector, the energy resolution, fraction of charge sharing efficiency and time resolution are measured with Ar/CO_2 90:10 and 70:30 gas mixtures. The efficiency *vs.* gain plot shows the efficiency plateau at gain $\geq$ 5000 which is similar to the GEM measurements. The efficiency measurement using the ^{106}Ru-Rh source has become only possible for the MWPC with the low material budget. All the measurements are found important for comparing with the GEM detectors results.

The present ALICE TPC detector has an acceptance rate limit of 3.3 kHz in Pb-Pb collisions. In LHC Run3, the collision rate will be up to 50kHz. TPC upgrade using GEM readout can accomplish such a high collision rate. However, the performances will be retained as the current TPC. For which the operating condition require as IBF $< 1\%$ with energy resolution $\sigma_E/E \leq 12\%$ for 5.9 keV X-ray at a gain of 2000 that can be achieved using a stack of four GEM foils with a particular order, SP-LP-LP-SP. The TPC upgrade demands new chambers using GEM readout to be ready before its installation during LS2. During my Ph. D. period I have actively participated in large size GEM foils preparation, framing, chamber assembly and in test procedures. The long term and short term leakage current measurements, framing of the GEM foils and chambers test using a robotic X-ray gun are carried out very professionally. The detail procedures about the chamber production and test methods are described in Chapter 6 of the thesis.

The global property, multiplicity and momentum study in the heavy-ion collision at the highest LHC energy are performed. For the global property investigation, simulation based on AMPT model is performed for Pb-Pb collision at $\sqrt{s_{NN}} = 5.5$ TeV. The special attention has been given to $0-5\%$ central Pb-Pb collision which is the high multiplicity events. The charged particle pseudorapidity density per participant pair $(2/\langle N_{part}\rangle)dN_{ch}/d\eta$ follows the energy dependent power law quite well with the value of 10.8. The multiplicity distributions within the ALICE TPC acceptance ($|\eta| < 0.9$) has been obtained and found the value well below the the TPC limit. From the multiplicity and momentum calculation of the identified particles, the initial energy density $(\epsilon_{Bj}\tau)$ of the collisions are estimated. It is found that $\epsilon_{Bj}\tau$ follows the energy-dependent power law successfully with the value of 17.53 GeV/fm^{2}cm. In conclusion, global properties of the most central Pb-Pb collisions at LHC Run3 energy are predicted by using AMPT event generator.

Bibliography

[1] T. D. Lee and G. C. Wick, Phys. Rev. **D9** 2291 (1974).

[2] E. V. Shuryak, Quark-gluon plasma and hadronic production of leptons, photons and psions, Phys. Lett. B **78** 150 (1978).

[3] P. B. Munzinger and J. Stachel, The quest for the quark–gluon plasma, Nature **448** 302 (2007).

[4] ALICE Collaboration, ALICE Technical Proposal for A Large Ion Collider Experiment at the CERN LHC, CERN/LHCC 95-71 (1995).

[5] The ALICE experiment at the CERN LHC, JINST **3** S08002 (2008).

[6] S. L. Glashow, Nucl. Phys. **22** 579 (1961).

[7] A. Salam and J.C. Ward, Phys. Lett. **13** 168 (1964).

[8] S. Weinberg, Phys. Rev. Lett. **19** 1264 (1967).

[9] G. Aad *et al.* for ATLAS Collaboration, Phys. Lett. B **716** 1 (2012).

[10] W. Adam *et al.* for CMS Collaboration, Phys. Lett. B **716** 30 (2012).

[11] http://pdg.lbl.gov/2018/reviews/rpp2018-rev-qcd.pdf.

[12] D. J. Gross, F. Wilczek, Ultraviolet Behavior of Nonabelian Gauge Theories, Phys. Rev. Lett. 30, 1343 (1973); H.D. Politzer, Phys. Rev. Lett. 30, 1346 (1973).

[13] H. D. Politzer, Reliable Perturbative Results for Strong Interactions?, Phys. Rev. Lett. **30** 1346 (1973).

[14] J. C. Collins and M. J. Perry, "Superdense Matter: Neutrons Or Asymptotically Free Quarks?," Phys. Rev. Lett. **34** 1353 (1975).

[15] K. G. Wilson, Confinement of Quarks, Phys. Rev. **D10**, 2445 (1974).

[16] F. Karsch, Lattice results on QCD thermodynamics, Nucl. Phys. **A698** 199 (2002), arXiv:hep-ph/0103314.

[17] A. Bazavov, T. Bhattacharya, M. Cheng, C. DeTar, H. Ding, et al.,The chiral and deconfinement aspects of the QCD transition, Phys. Rev. D **85** 054503 (2012), arXiv:1111.1710.

[18] T. Matsui and H. Satz, Phys. Lett. B **178** 416 (1986).

[19] F. Antinori *et al.* for the NA57 Collaboration, J. Phys. G: Nucl. Part. Phys.**32** 427 (2006).

[20] https://cds.cern.ch/record/2636343.

[21] J. Adam *et al.* for ALICE Collaboration, Phys. Rev. Lett. **116** 222302 (2016).

[22] J. D. Bjorken, Phys. Rev. **D27** 140 (1983).

[23] J. Adam *et al.*, for ALICE Collaboration, Phys. Rev. C **94** 034903 (2016).

[24] K. Aamodt *et al.* for ALICE Collaboration, Phys. Lett. B **696** 30 (2011).

[25] J. Adams *et al.* for STAR Collaboration, Nucl. Phys. A **757** 102 (2005).

[26] B. Abelev *et al.* for ALICE Collaboration, Phys. Rev. Lett. **109** 072301 (2012).

[27] A. Adare *et al.* for PHENIX Collaboration, Phys. Rev. C **84** 054912 (2011).

[28] ALICE Collaboration, ALICE dimuon forward spectrometer: Technical Design Report, CERN-LHCC-99-022; http://cdsweb.cern.ch/record/401974; AL- ICE dimuon forward spectrometer: addendum to the Technical Design Report, CERN-LHCC-2000-046, http://cdsweb.cern.ch/record/494265.

[29] ALICE Collaboration, ALICE Inner Tracking System: Technical Design Report, CERN-LHCC-99-012, http://edms.cern.ch/file/398932/1.

[30] ALICE Collaboration, Technical Design Report of the Time Projection Chamber, CERN/LHCC 2000-001, 2000.

[31] ALICE Collaboration, ALICE Transition Radiation Detector: Technical Design Report, CERN-LHCC-2001-021, http://cdsweb.cern.ch/record/519145.

[32] ALICE Collaboration, ALICE Time-Of-Flight system: Technical Design Report, CERN-LHCC-2000-012; http://cdsweb.cern.ch/record/430132; ALICE Time-Of-Flight system (TOF): addendum to the technical design report, CERN-LHCC-2002-016, http://cdsweb.cern.ch/record/545834.

[33] ALICE High-Momentum Particle Identification: Technical Design Report, CERN-LHCC-98-019, http://cdsweb.cern.ch/record/381431.

[34] ALICE Collaboration, Technical Design Report of the Photon Spectrometer, CERN-LHCC-99-004, http://cdsweb.cern.ch/record/381432.

[35] ALICE Electromagnetic Calorimeter: addendum to the ALICE technical proposal, CERN-LHCC-2006-014, http://cdsweb.cern.ch/record/932676.

[36] ALICE Collaboration, ALICE Zero-Degree Calorimeter: Technical Design Report, CERN-LHCC-99-005, http://cdsweb.cern.ch/record/381433.

[37] ALICE Collaboration, ALICE Photon Multiplicity Detector: Technical Design Report, CERN-LHCC-99-032; http://cdsweb.cern.ch/record/451099; ALICE Photon Multiplicity Detector: addendum to the technical design report, CERN-LHCC-2003-038, http://cdsweb.cern.ch/record/642177.

[38] ALICE Collaboration, ALICE forward detectors: FMD, T0 and V0: Technical Design Report, CERN-LHCC-2004-025, http://cdsweb.cern.ch/record/781854.

[39] A. V. Tello for ALICE Collaboration, AD, the ALICE diffractive detector, AIP Conf. Proc. 1819, 040020-1–040020-4 (2016).

[40] Cosmic ray physics with the ALICE detectors, Czech. J. Phys. 55 (2005) B801; A. Fernandez et al., ACORDE a cosmic ray detector for ALICE, Nucl. Instrum. Meth. A572, 102 (2007).

[41] https://alice-figure.web.cern.ch.

[42] B. Abelev *et al.* for ALICE Collaboration, Int. J. Mod. Phys. A **29** 1430044 (2014).

[43] ALICE Collaboration. Upgrade of the ALICE Experiment: Letter Of Intent, CERN-LHCC-2012- 012 / LHCC-I-022. 2012.

[44] ALICE Collaboration, Technical Design Report for the Upgrade of the ALICE Inner Tracking System, CERN-LHCC-2013-024 (2013).

[45] ALICE Collaboration, Technical Design Report for the Upgrade of the ALICE Time Projection Chamber, ALICE-TDR-016, CERN-LHCC-2013-020, 2014.

[46] ALICE Collaboration, Addendum to the Technical Design Report for the Upgrade of the ALICE Time Projection Chamber, ALICE-TDR-016-ADD-1, CERN-LHCC-2015-002, 2015.

[47] ALICE Collaboration, Technical Design Report for the Muon Forward Tracker, CERN-LHCC-2015-001 (2015).

[48] T L Karavicheva for ALICE Collaboration, J. Phys. Conf. Ser. **798** 012186(2017).

[49] ALICE Collaboration, Technical Design Report for the Upgrade of the ALICE Read-out and Trigger System. ALICE-TDR-015, CERN-LHCC-2013-019, 2014.

[50] http://pdg.lbl.gov/2016/reviews/rpp2016-rev-passage-particles-matter.pdf

[51] P. Marmier, Kernphysik I, Verlag der Fachvereine, Zurich (1977).f

[52] G. Charpak *et al.*, Nucl Instr. and Meth. **62**, (1968), 262.

[53] H. Walenta, Phys. Scripta **23**, (1981), 354.

[54] A. Oed, Position-sensitive detector with microstrip anode for electron multiplication with gases. Nucl. Instr. and Meth. A, **263**, (1988), 351.

[55] R. Bouclier et al, Nucl. Instr. and Meth. A **323**, (1992), 240.

[56] Y. Giomataris et al., Micromegas: a highgranularity position-sensitive gaseous detector for high particle-flux environments. Nucl. Instrum. Meth. A **376**, (1996), 29.

[57] F. Sauli, Gem: A new concept for electron amplification in gas detectors, Nucl. Instr. and Meth. A **386** (1997) 531.

[58] S. Duarte Pinto et al., JINST 4, (2009) P12009.

[59] https://garfieldpp.web.cern.ch/garfieldpp/

[60] Rob Veenhof, Nucl. Instr. Meth. A 419 726 (1998).

[61] R. N. Patra *et al.*, Measurement of basic characteristics and gain uniformity of a triple GEM detector, Nucl. Instr. and Meth. A. **862** (2017) 25.

[62] R. N. Patra *et al.*, Characteristic study of a quadruple GEM detector and its comparison with a triple GEM detector, Nucl. Instr. and Meth. A. **906** (2018) 37.

[63] P.Busca, et al., Silicon drift photodetector arrays for the HICAM gamma camera, Nucl. Instr. and Meth. A **624** (2010) 282.

[64] http://pdg.lbl.gov/2018/reviews/rpp2018-rev-cosmic-rays.pdf.

[65] R. N. Patra *et al.*, Corrigendum to 'Measurement of basic characteristics and gain uniformity of a triple GEM detector [Nucl. Instrum. Methods A 862 (2017) 25]', Nucl. Instr. and Meth. A. **905** (2018) 199.

[66] R. N. Patra *et al.*, Study of a Triple GEM Detector Operated with Different Argon Based Gas, Springer Proceedings in Physics 203, (2018) 821-823. doi:10.1007/978-3-319- 73171 199.

[67] M. Abi Akl *et al.*, Nucl. Instr. and Meth. A **832** (2016) 1.

[68] Y. Maghrbi and O. Bouhali, Seventh International Conference on Sensing Technology (ICST), 10.1109/ICSensT.2013.6727768, page(s): 833.

[69] R. N. Patra *et al.*, Gain Uniformity and Characteristics Study of a Triple GEM Detector, IEEE (NSS/MIC/RTSD) 2016, Conference Record, doi:10.1109/NSSMIC.2016.8069752.

[70] F. Simon *et al.*, IEEE Trans. Nucl. Sci. **54** (2007) 2646.

[71] G. Bencivenni *et al.*, A triple GEM detector with pad readout for high rate charged particle triggering, Nucl. Instr. and Meth. A **488** (2002) 493.

[72] M. Bozzo *et al.*, Design and Construction of the Triple GEM Detector for TOTEM, Nuclear Science Symposium Conference Record, IEEE (2004) 477.

[73] A.K. Dubey *et al.*, Testing of triple-GEM chambers for CBM experiment at FAIR using self-triggered readout electronics, Nucl. Instr. and Meth. A **755** (2014) 62.

[74] M. Tytgat, *et al.*, Construction and performance of large-area triple-GEM prototypes for future upgrades of the CMS forward muon system, IEEE Nuclear Science Symposium N19 7 (2011) 1019.

[75] F.V. Böhmer *et al.*, Simulation of space-charge effects in an ungated GEM-based TPC, Nucl. Instr. and Meth. A **719** (2013) 101-108.

[76] A. Balla, *et al.*, Construction and test of the cylindrical-GEM detectors for the KLOE-2 Inner Tracker, Nucl. Instr. and Meth. A **732** (2013) 221.

[77] R. Arora, *et al.*, A Large GEM-TPC Prototype Detector for PANDA, Physics Procedia **37** (2012) 491.

[78] FGT Proposal, "Forward GEM Tracker (FGT) - A Forward Tracking Upgrade Proposal for the STAR Experiment", https://drupal.star.bnl.gov/STAR/system/files/fgt review 0.pdf.

[79] A. Adare, An Upgrade Proposal from the PHENIX Collaboration, arXiv:1501.06197.

[80] J. Va'vra and A. Sharma, Single electron detection in quadruple GEM detector with pad readout" Nucl. Instr. and Meth. A **478** (2002) 235.

[81] A. Breskin, *et al.*, Sealed GEM photomultiplier with a CsI photocathode: ion feedback and ageing, Nucl. Instr. and Meth. A **478** (2002) 225.

[82] A. Buzulutskov, *et al.*, The GEM photomultiplier operated with noble gas mixtures, Nucl. Instr. and Meth. A **443** (2000) 164.

[83] A. Buzulutskov, *et al.*, Further studies of GEM photomultiplier, Nucl. Instr. and Meth. A **442** (2000) 68.

[84] M. Blatnik *et al.*, Performance of a Quintuple-GEM Based RICH Detector Prototype, IEEE Transactions on Nuclear Science, V. **62** No. 6 (2015) 3256.

[85] A. Bondar, *et al.*, Study of ion feedback in multi-GEM structures, Nucl. Instr. and Meth. A, 496 (2003), 325.

[86] D. Mormann *et al.*, Evaluation and reduction of ion back-flow in multi-GEM detectors, Nucl. Instr. Meth. A **516** (2004) 315.

[87] M. Ball *et al.*, Ion backflow studies for the ALICE TPC upgrade with GEMs, JINST **9** (2014) C04025.

[88] P. Gasik for the ALICE TPC collaboration, Discharge probability studies with multi-GEM detectors for the ALICE TPC Upgrade, arXiv:1807.02979.

[89] R. N. Patra *et al.*, Characteristic study of a quadruple GEM detector in different electric field configurations, Nucl. Instr. Meth. A **936** (2019) 433.

[90] S. Bachmann *et al.*, Discharge studies and prevention in the gas electron multiplier (GEM), Nucl. Instr. and Meth. A **479** (2002) 294.

[91] S. Bachmann *et al.*, Charge amplification and transfer processes in the gas electron multiplier, Nucl. Instr. and Meth. A **438** (1999) 376.

[92] F. Sauli, "Principles of operation of multiwire proportional and drift chamber", CERN, Geneva, Switzerland, Rep. 77-09, 1977.

[93] W. Bonivento *etal.*, "A Complete Simulation of a Triple-GEM Detector", IEEE Trans. on Nucl. Science, Vol. **49**, no. 4, 1638 (2002).

[94] http://pdg.lbl.gov/2017/reviews/rpp2017-rev-particle-detectors-accel.pdf

[95] Heed online.

[96] I. Smirnov, "Modeling of ionization produced by fast charged particles in gases", Nucl Instr. Meth. A **554** 474 (2005).

[97] http://magboltz.web.cern.ch/magboltz/.

[98] S. F. Biagi, Nucl. Instr. Meth. A 421 234 (1999).

[99] G. Charpak, *et al.*, Nucl. Instr. and Meth. **62** (1968) 235.

[100] K. H. Ackermann *et al.*, The STAR time projection chamber, Nuclear Phys. A, **661** (1999) 681-685.

[101] W. T. Chu et al.., Proc. SPIE 03772, Physics and Engineering in Medical Imaging, (1982), 221; doi:10.1117/12.934519.

[102] Jeffrey L. Lacy, *et al.*, J Nucl. Med. **25** (1984) 1003-1012.

[103] ALICE Collaboration, The electronics of the Alice Dimuon Tracking Chambers, ALICE Internal Note, ALICE-INT-2004-026, 2004, hhttp://cds.cern.ch/record/1158633/files/p242.pdf.

[104] ALICE Collaboration, Addendum to the Technical Design Report of the Photon Multiplicity Detector (PMD), ALICE TDR 6, CERN/LHCC 2003-038, 2003, hhttp://cds.cern.ch/record/642177/files/cer-002399082.pdf?version=1i.

[105] R. N. Patra *et al.*, Study of Multiwire Proportional Chambers MWPC detector using NIM and MANAS electronics, Proceedings of the DAE-BRNS Symp. on Nucl. Phys. 61 (2016) 1052-1053.

[106] R. N. Patra *et al.*, Time Resolution and Characteristic Studies of MWPC Detectors with Argon Based Gas Mixtures, Springer Proceedings in Physics, 203 (2018) 509-512. doi:10.1007/978-3- 319-73171_119.

[107] D. R. Nygren, Proposal to investigate the feasibility of a novel concept in particle detection, LBNL Internal report (1974).

[108] R. J. Madaras *et al.*, Spatial resolution of the PEP-4 time projection chamber, IEEE Trans. Nucl. Sci. **30** (1983) 76-81.

[109] W. B. Atwood *et al.*, Performance of the ALEPH time projection chamber, Nucl. Instrum. Methods A, **306** (1991) 446-458.

[110] C. Brand *et al.*, The DELPHI time projection chamber, Nucl. Instr. Meth. A **283** (1989) 567-572.

[111] S. Wenig, Performance of the large-scale TPC system in the CERN heavy ion experiment NA49, Nucl. Instr. Meth. A **409** (1998) 100-104.

[112] C. Amsler *et al.*, First results on light readout from the 1-ton ArDM liquid argon detector for dark matter searches, JINST **5** (2010) P11003.

[113] E. Aprile *et al.*, Design and Performance of the XENON10 Dark Matter Experiment, Astropart. Phys. **34** (2011) 679.

[114] C. Rubbia, The Liquid-Argon Time projection Chamber: a new concept for Neutrino Detector, CERN-EP-INT-77-08 (1977).

[115] F. Arneodo *et al.*, Performance of a liquid argon time projection chamber exposed to the CERN West Area Neutrino Facility neutrino beam, Phys. Rev. D **74** (2006) 112001.

[116] B. Baaller *et al.*, Liquid Argon Time Projection Chamber research and development in the United States, JINST **9** T05005 2014.

[117] A. Badertscher *et al.*, First operation of a double phase LAr Large Electron Multiplier Time Projection Chamber with a 2D projective readout anode, Nucl. Instr. Meth. A **641** (2011) 48-57.

[118] J. Alme *et al.*, The ALICE TPC, a large 3-dimensional tracking device with fast readout for ultra-high multiplicity events, Nucl. Instr. Meth. A **622** (2010) 316-367.

[119] ALICE Collaboration, ALICE-PUBLIC-2015-004 (2015).

[120] The ALICE Collaboration, Performance of the ALICE experiment at the CERN LHC, International Journal of Modern Physics A **29** No. 24 (2014).

[121] F. Sauli *et al.*, Electron Collection and Ion Feedback in GEM-Based Detectors, IEEE Trans. Nucl. Sci **50** (2003) 803.

[122] B. Ketzer, For the GEM-TPC and ALICE TPC Collaborations, A time projection chamber for high-rate experiments: Towards an upgrade of the ALICE TPC, Nucl. Instr. Meth. A **732** (2013) 237.

[123] L. Fabbietti *et al.*, The PANDA GEM-based TPC prototype, Nucl. Instr. Meth. A **628** (2011) 204.

[124] A. Mathis on behalf of the ALICE collaboration, Study of dE/dx resolution of a GEM Readout Chamber prototype for the upgrade of the ALICE TPC, EPJ Web of Conferences **174**, (2018) 01002.

[125] A. Deisting *et al.*, Ion mobility measurements in Ar-CO_2, Ne-CO_2, and Ne-CO_2-N_2 mixtures and the effect of water contents, Nucl. Instr. Meth. A **904** (2018) 1–8.

[126] ALICE TPC Collaboration, Particle identification studies with a full-size 4-GEM prototype for the ALICE TPC upgrade, Nucl. Instr. Meth. A **903** (2018) 215–223.

[127] M. Ball *et al.*, Quality assurance of GEM foils for the upgrade of the ALICE TPC, JINST **12** (2017) C01081.

[128] E. Brücken and T. Hildén for the ALICE TPC Collaboration, GEM Foil Quality Assurance for the ALICE TPC Upgrade, EPJ Web of Conferences **174**, (2018) 03004.

[129] Z. W. Lin, C.M. Ko, B. A. Li, B. Zhang, S. Pal, Phys. Rev. C **72**, 064901 (2005).

[130] Z.W. Lin *et al.*, Phys. Rev. C **64**, 011902 (2001).

[131] B. Zhang *et al.*, Phys. Rev. C bf 61 067901 (2000).

[132] X. N. Wang, M. Gyulassy, Phys. Rev. D **44**, 3501 (1991).

[133] B. Abelev *et al.* for ALICE Collaboration, Phys. Rev. C **88** 044910 (2013).

[134] J. Adam *et al.* for the ALICE Collaboration, ALICE-PUBLIC-2015-008, arXiv: 1512:06104.

[135] M. L. Miller, J. Schukraft, and B. Wyslouch Ann. Rev. Nucl. Part. Sci. **57** 205 (2007).

[136] S. Basu *et al.*, Phys. Rev. C **93** 064902 (2016).

[137] B. Alver *et al.* for PHOBOS Collaboration, Phys. Rev. C **83** 024913 (2011).

[138] E. Abbas *et al.* for ALICE Collaboration, Phys. Lett. B **726** 610 (2013).

[139] J. Adam *et al.* for ALICE Collaboration, arXiv:1509.07299.

[140] K. Aamdot *et al.* for ALICE Collaboration, Phys. Rev. Lett. **106** 032301 (2011).

[141] G. Aad *et al.* for ATLAS Collaboration, Phys. Lett. B **710** 363 (2012).

[142] S. Chatrchyan *et al.* for CMS Collaboration, JHEP **08** 141 (2011).

[143] I. G. Bearden *et al.* for BRAHMS Collaboration, Phys. Lett. B **523** 227 (2001).

[144] I. G. Bearden *et al.* for BRAHMS Collaboration, Phys. Rev. Lett. **88** 202301 (2002).

[145] K. Adcox *et al.* for PHENIX Collaboration, Phys. Rev. Lett. **86** 3500 (2001).

[146] B. I. Abelev for STAR Collaboration, Phys. Rev. C **79** 034909 (2009).

[147] M. C. Abreu for NA50 Collaboration, Phys. Lett. B **530** 43 (2002).

[148] K. Aamodt *et al.* for ALICE Collaboration, Eur. Phys. J. C **77** 33 (2017).

[149] V. Khachatryan *et al.* for CMS Collaboration, Phys. Lett. B **751** 143 (2015).

[150] J. Adam *et al.* for ALICE Collaboration, Phys. Lett. B **753** 319 (2016).

[151] G. Alner *et al.* for UA5 Collaboration), Z. Phys. C **33** 1 (1986).

[152] W. Thome *et al.*, Nucl. Phys. **129B**, 365 (1977).

[153] B. Abelev *et al.* for ALICE Collaboration, Phys. Lett. B **736** 196 (2014).

[154] T. Alber *et al.*, Phys. Rev. Lett. **75** 3814 (2001).

[155] J. Adam *et al.* for STAR Collaboration, Phys. Rev .C **70** 054907 (2004).

[156] K. Adcox *et al.* for PHENIX Collaboration, Phys. Rev. Lett. **87** 054907 (2001).

[157] S. S. Adler *et. al.* for PHENIX Collaboration, Phys. Rev. **C71** 034908 (2005).

[158] J. T. Mitchell *et al.* for PHENIX Collaboration, arXiv: 1601:00904.

[159] Z. Jiang *et al.*, Pseudorapidity and initial energy densities in p+p and heavy ion collisions at RHIC and LHC, arXiv: 1806.05750v1.

[160] S. Chatrchyan *et al.* for CMS Collaboration, Phys. Rev. Lett. **109**, 152303 (2012).